DEPARTMENT OF MECHANICAL ENGINEERING

UNIVERSITY OF SOUTHAMPTON

THE VIBRATION CHARACTERISTICS OF HYBRID JOURNAL GAS BEARING SYSTEMS

by

NEVILLE TULLY

October 1965.

Presented for the Degree of Doctor of Philosophy.

LIST OF CONTENTS

PREFACE

The research reported in this thesis has been supported by D.S.I.R. and conducted within the Department of Mechanical Engineering. Gas lubrication studies at Southampton were started in 1959 by Dr. N. S. Grassam and have been largely concerned with externally pressurized bearings. The present work was begun in 1962, about which time evidence was becoming available that small clearance externally-pressurized bearings running at high speeds could have very significantly enhanced load capacity, due to the aerodynamic pressure generation. However the maximum speeds which could be run at were limited by self excited instability of the type widely reported for aerodynamic bearings. Little concrete evidence appeared to be available about the exact nature of this or about the general dynamic performance of these hybrid bearings, and the object of this investigation is to try to clarify some of these areas.

The author wishes to thank his supervisor Dr. Grassam for his valuable help and guidance in this project. Thanks are also due to Dr. K. R. McLachlan, Mr. A. J. Munday and Dr. J. W. Powell for many fruitful discussions concerning the work, and to the former for his advice and assistance on techniques of measurement. Except for the rotors, which were accurately ground by Dr. Powell's Company, the experimental rig has all been constructed by Mr. F. Kerens, whose

readiness to carry out the many modifications throughout the work has been greatly appreciated.

SUMMARY

The thesis contains an introduction to the field of lubrication in general and gas lubrication in particular. The steady state and vibration properties of both externally pressurised and self acting journal bearings are discussed and an exposition of recent theory concerned with unstable free vibrations in self acting bearings given. A new description of the general mechanism by which such vibrations arise is presented, and the implications of the theory are discussed in detail with particular reference to the hybrid type of bearing. It is found possible to give a concise explanation of the type of half speed whirl instability widely observed in these bearings.

The general principles of constructing an experimental test rig for examining the practical performance of hybrid bearings in the high speed range are given, together with a detailed description of the $\frac{3}{4}$ in. diameter, annular feed hole bearing rig used.

A method of examining the aerostatic performance of the bearing, under the conditions of variable supply pressure and clearance used, is developed from the work of Shires and Robinson. Experimental measurements of steady state stiffness are made and correlated to the theoretical prediction.

The free vibration response of the rotor to a shock load is examined, being a planar vibration with the rotor stationary, and an orbital motion with the rotor revolving. Simple analysis is developed

for each case and found to hold for large clearances. The unstable whirl condition is one of zero damping and an experimental method is described to determine the onset speed without running up to it, by observing the change of damping with increasing speed and extrapolating it to zero.

Finally the case of unbalance vibrations is considered for both hybrid and aerodynamic bearing operation. Theory is developed for each, but in the hybrid case is found only to give a quantitative idea of the change in performance with increasing speed.

Nomenclature

A	feed hole area
A	$= \gamma/\Lambda^2$
C	squeeze film damping
C'	overall damping to free vibrations
C^*	non-dimensional forced vibration damping
C_D	feed hole discharge coefficient
C_{L_o}	$= \frac{W}{(p_s - p_a)LD}$ aerostatic load coefficient
C_L	short bearing load coefficient
D	diameter of bearing
E	Youngs modulus
F_r	film force along displacement line
F_t	film force normal to displacement line
I_T	transverse moment of inertia of rotor
I_o	polar moment of inertia of rotor
J	half of bearing centre separation
K	stiffness
K	$= p_d/p_s$ pressure ratio
K_g	$= \frac{p_d - p_a}{p_s - p_a}$ gauge pressure ratio
K_{go}	gauge pressure ratio for concentric bearing
L	bearing length

L_s shaft length

M shaft weight

N rotor speed

N_c tangential damping coefficient

Q $= \frac{\omega_1}{\omega}$ frequency ratio

R bearing radius

R gas constant

T absolute temperature

W total load

W_s aerostatic load component) hybrid bearing

W_d aerodynamic load component)

a_{ij} etc. elements of matrices

a $= \frac{\pi D}{n}$ width of slot in aerostatic bearing

b unbalance mass centre shift

c radial clearance

d feed hole diameter

e = εc bearing/rotor centres deflection

f_n critical shaft bending frequency

g gravitational constant (386.4 in/sec/sec)

h local clearance

i $\sqrt{-1}$

k $= \frac{Kc}{\pi pRL}$ nondimensional stiffness

ℓ distance of plane of feed holes from end of bearing

m vibrating mass

n number of feed holes

n_c tangential force coefficient

p pressure (absolute)

p_a ambient pressure

p_d downstream pressure in aerostatic bearing

p_m mean pressure in hybrid bearing

p_s supply pressure

r distance of rotor mass centre from centre of bearing

t time

u, v, w velocity components

w_j feed hole gas flow

x displacement vector

x, y, z rectangular coordinates

α synchronous unbalance phase angle

β measured phase angle

$\gamma = \frac{M c\omega^2}{4\pi g p_a RL}$ translational stability parameter

$\varepsilon = e/c$ eccentricity ratio

ζ nondimensional length

θ angular position

μ viscosity

ξ damping ratio

ρ density

σ $\frac{12\mu\omega_1}{p_a}\left(\frac{R}{c}\right)^2$ squeeze number

ϕ)
ϕ_r) angular coordinates defined by fig. (3.2.1.b.)
θ)

ϕ attitude angle

ϕ_H attitude angle hybrid bearing

ω rotational angular frequency

ω_1 vibration frequency

ω_n natural frequency

Λ $= \frac{6\mu\omega}{p_a}\left(\frac{R}{c}\right)^2$ compressibility number

Λ_m hybrid compressibility number based on mean bearing pressure.

I.

GENERAL INTRODUCTION.

1.1. Lubrication.

Two surfaces which have to slide relative to one another present the engineer with two basic problems - friction which absorbs power and produces heat, and wear which causes changes in dimensions. Modern practice is reducing the magnitude of both of these, but the amount of money that they cost industry must, with expanding mechanization, still be increasing from an already staggering total.

It is possible to divide the methods of supporting one surface moving relative to another into fluid film lubrication, boundary lubrication, and the use of rolling elements. The fluid film type of bearing produces a complete film of lubricant between the two surfaces and can, under certain circumstances, be completely free from wear. The lubricating fluid can be any viscous fluid and generally the more viscous the lubricant, the greater the load which can be supported, but the higher the friction. A complete film of lubricant can be generated either by relative motion of the surfaces or by supplying fluid from an external source. These methods will be discussed in detail later. Boundary lubrication is the half way stage to the full fluid film type, and is used when the mechanism necessary to support a full film is not present. It relies on the ability of the lubricant to form a low friction film, strongly bonded to the

bearing surfaces. Here the main property required is not viscosity but what is known, for want of a better term, as 'oiliness' which is independent of viscosity. However, it was evident from discussion of this subject at the Lubrication and Wear Convention of the Institution of Mechanical Engineers at Bournemouth in 1963, that even a concise definition of boundary lubrication has not yet been accepted.

Clearly only certain classes of viscous full film lubricants will possess any significant boundary lubrication properties, and care has to be exercised not to let the bearing surfaces come into contact if these are not being used.

Rolling element bearings if supplied with a lubricant, can utilize both the above types of lubrication, but in principle should not be dependent on lubrication as only rolling motion is taking place. In practice pure rolling would not be expected and this lubrication plays an important part in reducing wear. This type of bearing is used for loads too heavy for film or boundary lubricated bearings and instead of bearings using high viscosity lubricants in high speed applications. It is very important to realize that any type of bearing represents a flexible support to the moving object, and this must be taken into account when considering the application.

1.2. Fluid Film Lubrication.

This is the most important type of lubrication and is widely used. In this case the moving surface is effectively floating directly on a film of the lubricant and does not come into contact with the stationary surface, which is on the other side of the film. This implies that the lubricating film must have a mean pressure above the ambient equal to the pressure exerted by the forces on the member supported.

Two mechanisms can be used to generate this pressure in the lubricating fluid - which may be anything from liquid metal to the lightest gas providing that it possesses viscosity. The first is to feed lubricant from an external source through restrictors in the bearing surface, in between the two surfaces.

The moving surface lifts providing a gap through which the pressurized fluid flows to the ambient conditions at the edges of the surface.

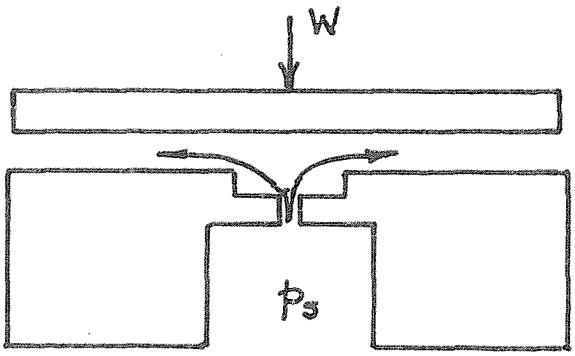

This is known as Hydrostatic Lubrication, and the first known example of a hydrostatic bearing was seen at the Paris Industrial exposition in 1878. This exhibition just consisted of a large block of metal supported on four hydrostatic bearing pads, which could be moved with virtually no effort. Subsequent development of the principle proved this to be more than a toy.

The hydrostatic bearing will maintain a complete film whether the surfaces are in relative motion or stationary. But with moving surfaces, when the relative velocity becomes great enough, another rather more subtle mechanism can become significant, which will create sufficient film pressure without the need for an external source. An additional condition necessary for this effect is that the shape of the gap is convergent in the direction of motion. This is commonly

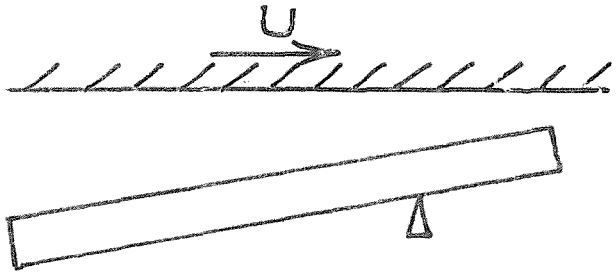

achieved by a tilting pad arrangement as shown or a journal positioned eccentrically in a sleeve (Fig. 3.2.1.b). The lubricant adheres to

each surface and thus the bulk of it is dragged through the converging wedge which due to the viscosity generates a pressure rise.

This effect is known as self-acting or Hydrodynamic lubrication and was first understood as such by Beauchamp Tower in 1883 when he obtained measurements of the pressure profile in a partial journal bearing. In the same year a Russian engineer Petrov, recognising the existence of the complete lubricating film, made the first analysis of the friction effect of the fluid in between two concentric cylinders.

At about this time Osburn Reynolds had been deriving a mathematical model for the hydrodynamics of viscous fluids in thin non parallel slots. On reading the report of Tower's experimental work on bearings, Reynolds realized that the conditions existing in Tower's journal bearing were of a similar nature to those for which the mathematical model had been propounded. He then set about obtaining a solution to his equations for this journal bearing, and in 1886 presented before the Royal Society in London[22]* the first description of the mechanism of full hydrodynamic lubrication.

1.3. The Use of Gas as a Lubricant.

In the previous section it has been stated that the lubricant can be any viscous fluid, and in the vast majority of bearings some type of lubricating oil is used. However during the last fifteen

* Reference Number

years the limitation of liquid lubricants in certain applications has lead to the development of bearings which run on a film of gas. The idea is not a new one and originated with a Frenchman, G. A. Hirn[12] in 1854 who was experimenting on the friction of lubricated bearings. During some tests he ran his apparatus without a liquid lubricant, and his bearings were sufficiently well made to generate a hydrodynamic air film, the effects of which he observed. It is doubtful if he would have understood why such a bearing might function prior to Reynolds work. This was the real start and in 1897 an American engineer, Kingsbury, built the first known air lubricated journal bearing and published some excellent experimental data which confirmed that the ideas of Reynolds applied satisfactorily to gaseous lubricants. In 1913 the first solutions to Reynolds equation for compressible lubricants in infinitely long slider and journal bearings were presented by W. J. Harrison[11].

It does not appear to be widely known that a very early application of air lubrication was made in England in 1905 by the electrical engineer S. Z. de Ferranti. His patent[6] of that year marked the commencement of several years development of self acting journal bearings for cotton spinning machinery. The original bearings consisted of thin rotating sleeves mounted vertically. The stators were mounted in rubber and this combined with the light sleeve mass delayed the onset of vibrational instability, which crippled so many

later projects, to above the 20,000 rpm operating speed. The machine which had many other revolutionery aspects was eventually abandoned because of its general complexity and cost, although the bearings functioned well.

The early work was all concerned with the self acting (now usually known as Aerodynamic) type of bearing, and very little further notice of air lubrication was taken until the late 1940's. During this period however the first externally pressurized or aerostatic bearings were used in ultracentrifuges although no theory was published for them. This did not come until 1949 when G. L. Shires at the National Gas Turbine Establishment published two papers [24, 25] containing theoretical and experimental data for feed hole type aerostatic journal bearings.

Gas bearings really came into large scale use when the U.K.A.E.A. gaseous diffusion plant was built at Capenhurst. These plants contain several thousand compressors and power consumption is a problem. Also since the gas circulated, UF_6, is radioactive and corrosive, the ability to use it as a lubricant makes an ideal application for gas bearings. Their inherent reliability is also important: once running no contact between rotor and sleeve occurs and no wear takes place. Experience at Capenhurst suggested the use of gas bearing circulators in nuclear reactor applications, since although the coolant gas is not itself radioactive, radiation conditions exist,

and again the need for seals is eliminated. Due to the stringent control of the amount of gas in the cooling circuit, aerodynamic bearings had to be used. The Dragon reactor project at Winfrith is the first to rely solely on gas lubricated circulators, commencing operation in 1964.

An added bonus in AGR reactor applications is that gas has a very small viscosity change with temperature, but one that increases, whereas liquids in general loose most of their viscosity at high temperatures. At the other end of the temperature scale gas lubrication plays an important part in the development of cryogenic techniques, being used in gas liquifying plant expansion turbines.

In the last fifteen years an immense amount of effort has been put into the analysis and development of gas lubrication. Outstanding contributions have been made in England by the following: Shires - externally pressurized bearings: Ford - aerodynamic bearing experiments: Whitley - nuclear plant bearings and seals: Powell - development of hybrid bearing machines: Marsh - analysis of instability effects. In the U.S.A. Ausman has provided valuable approximate solutions for self acting journal bearings, and Sternlicht and Gross have produced books in addition to extensive theoretical and experimental work. A recent survey indicates that gas bearing research is currently being conducted in at least 23 centres in Europe and 50 centres in America.

A close understanding of the nature of many apsects of gas lubrication has been reached during this period, which has far outstripped the knowledge of the parent liquid lubricated variety. This is because the gas bearing has a single phase lubricant, whereas the liquid bearing almost always operates with a two phase lubricant of liquid and vapour. However, the study of the single phase system offers a considerable insight into the mechanisms of, and the way to treat, the more complex two phase systems. It is also true to say that since liquid lubricated bearings could be made to perform their duties fairly readily using empirical methods, not such an intensive effort was made to obtain a full understanding of them. The same is perhaps true of aerostatic gas bearings, which in depth are also more complex than aerodynamic gas bearings.

1.4. Limitations of Gas Lubrication.

So far, much has been said of the merits of gas film lubricated bearings but nothing of their shortcomings. In general more precise bearing sizes and geometries have to be produced than are necessary for liquid bearings. Also the load capacity is small, leading to large bearing sizes compared to other types of bearing. Where numerous starts and stops are to be made with aerodynamic bearings, particular attention has to be paid to the choice of bearing materials, as no boundary lubrication is present.

A major limitation to the widespread use of gas lubricated journal bearings is their dynamic characteristics. It has been mentioned previously that the bearing forms a flexible element in the system, and in fluid film bearings is a prime factor in the study of rotor system stability. Thrust bearings do not in general suffer in this way but both aerodynamic and externally pressurized journal bearings exhibit a self excited orbital vibration due to shaft rotation effects. The precise mechanism of this is complex, and will be described in considerable detail in a later section. The occurrence of this instability in a pure aerodynamic journal bearing has been the subject of a recent doctoral thesis at Cambridge University by H. Marsh[14] who also examined the dynamic response of this type of bearing to imposed vibrations.

For the externally pressurized bearing however, very little conclusive information has been published on the dynamic response, which differs from the aerodynamic bearing in that it has stiffness and damping properties with no rotation and no forcing, and that it exhibits a natural frequency to out-of-balance forcing (which has not been reported experimentally for the aerodynamic bearing, although as shown later, is theoretically possible.) In this case the characteristics will be not only a function of rotor properties and gas film geometry, but also of the way in which the pressurized gas is fed into the bearing clearance.

This thesis is concerned with gas bearing vibrations including those caused by unbalanced rotors, with special reference to the externally pressurized hybrid bearing.

2.

THE STEADY STATE GAS BEARING.

2.1. Classes of Gas Bearing.

It has been stated already that bearings may be classed as either aerodynamic or aerostatic, and it is also possible for bearings to perform through a combination of these principles.

The aerodynamic bearing operates because of relative motion between the surfaces, either tangential, normal or more usually a combination of these. It is thus usual to subdivide into bearings which rotate, giving mainly tangential motion, and those which do not and are called squeeze film bearings. These latter, whilst not widely known, are likely to be of importance in applications where a gas film is required with zero rotation of the journal, and in circumstances which do not allow externally pressurized fluid to be supplied.

Aerodynamic thrust bearings dependent on tangential motion can be built utilizing either the converging wedge principle or a 'viscosity groove' in one of a pair of flat parallel plates. However, thrust bearings of either the aerostatic or aerodynamic type give few problems when compared to the journal bearing and this work will be concerned only with journal bearings unless specifically mentioned.

2.2. The Aerodynamic Rotating Journal Bearing.

Referring to the sketch below it may be seen that in order to form the converging wedge necessary for aerodynamic pressure generation from relative tangential motion, the journal centre must be displaced to an eccentric position within the sleeve. In fact two identical wedges are formed on either side of the position of minimum clearance, which give rise to pressure changes in the gas film having supplementary effects in supporting the load. The pressure is positive on the low clearance side of the bearing and negative on the large clearance side, as shown in the diagram.

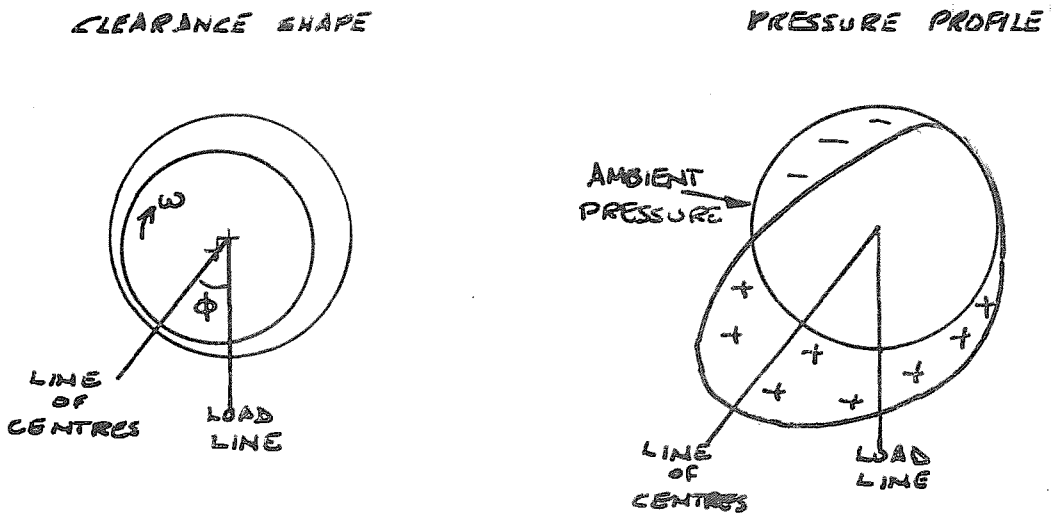

The pressure profile is such that the resultant pressure force does not act through the line of centres, but at an angle ϕ, known

as the attitude angle, the magnitude of which is dependent on speed in a gas bearing. The attitude angle starts at a theoretical 90^{o} leading the load line at zero speed, and reduces towards zero as the speed is increased.

It is worth noting at this point that journal bearings of the type described above usually have their performance described in terms of a parameter called the compressibility number Λ defined as

$$\Lambda = \frac{6\mu\omega}{p_a}\left(\frac{R}{c}\right)^2$$

where μ is the lubricant viscosity

ω is the rotational speed

R is the bearing radius

c is the radial clearance

p_a is the ambient pressure.

This is nondimensional and its origin will become clear in the section on bearing analysis.

The load supported by such a bearing is dependent on speed, clearance, bearing area, relative length to diameter, ambient pressure, viscosity and eccentricity. Performance curves are normally presented in the form shown

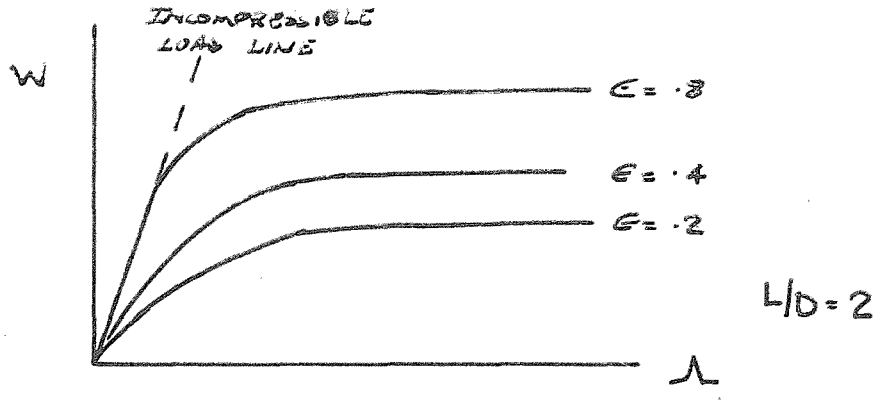

and cover a range of L/D values. A comprehensive set of such graphs has been published by Raimondi[21] and are reproduced in a number of text books e.g. refs (8 and 10).

It can be seen that at low values of Λ the performance is close to that of an incompressible lubricant, but as Λ increases the increase in load capacity falls away. Thus there is a region beyond which no useful purpose is served by achieving higher compressibility numbers. For long bearings this is approximately $\Lambda = 1$ and for short bearings in the region of $\Lambda = 10$. The maximum possible load capacity which could be achieved with a gas bearing is something like 95 Lb/sq.in. of projected area at 0.9 eccentricity but in practice due to a number of factors, principally starting torques, the usual loading is in the region of 3-4 Lb/sq.in. It has been mentioned that due to the change in the positions of the high and low pressure regions with Λ, the angle between the load

line and the line joining the centres of the two members changes. This is the other main design feature and is normally presented in a similar manner to load capacity. This property can

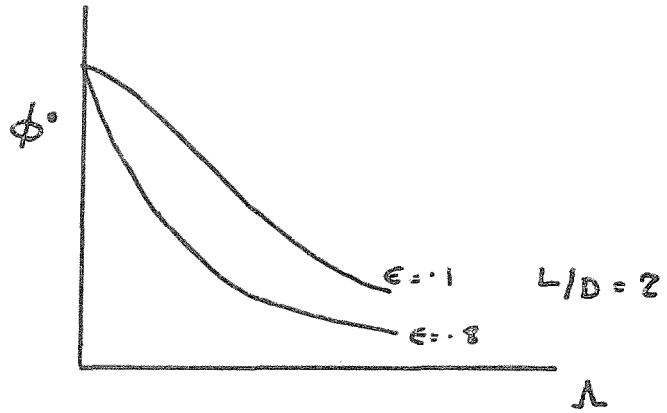

be important in certain gyroscope applications where the position of the journal centre must be accurately defined.

2.3. The Squeeze Film Journal Bearing.

The second possibility for aerodynamic pressure generation capable of supporting a load in a journal bearing is a relative plain vibration of the centres of the two members, with no rotation necessary. This is normally classed with unsteady bearing operation, in which it plays a very important part, but as a steady load can also be supported by vibrations alone, the mechanism is described in this section.

In this case, bearing performance is defined in terms of a non-dimensional 'Squeeze Number' σ

$$\sigma = \frac{12\mu\omega_1}{p_a}\left(\frac{R}{c}\right)^2$$

in which frequency of vibration ω_1 is the major variable.

At low values of Squeeze Number σ the gas is sucked in and pumped out of the clearance space, giving purely viscous effects [viscous damping]. As σ increases, the viscous forces opposing flow increase, and in the central region of the bearing compressibility effects begin to dominate - gas is compressed and expanded giving resistance or spring effects. The gas film now represents

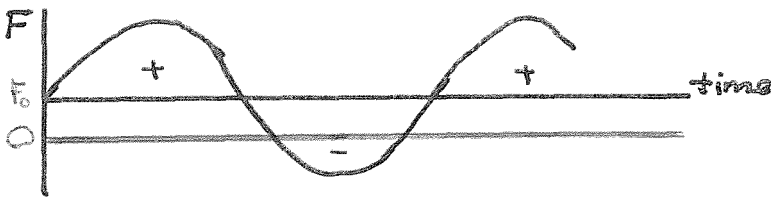

a spring damper combination, and due to the load the mean position of the free member is eccentric to the fixed member. Thus as pressure generation is a function of $\left(\frac{1}{h}\right)^2$ the pressure on the load side of the bearing is less than that opposite, giving a net load carrying capacity.

As $\sigma \to \infty$ the compressibility region tends to the outer edges of the bearings giving a pure spring action. In this limiting condition no flow takes place, and the system is analagous to a piston in a closed system. Now Boyles Law (pv = const) provides a close representation of gas behaviour.

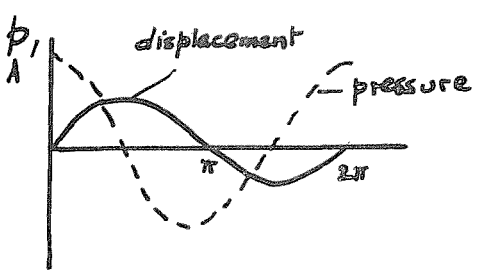

$\sigma \to 0$

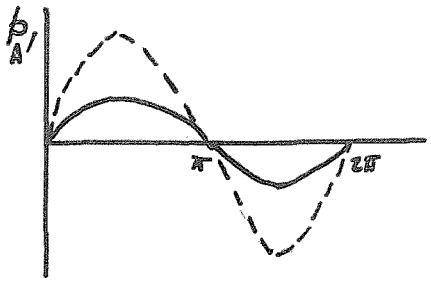

$\sigma \to \infty$

Squeeze Film bearings can also operate on liquid lubricants, but as these are almost incompressible, the principle of operation differs, and relies on the cavitation of the fluid in the low pressure regions.

The load bearing performance of squeeze film bearings can be presented in a similar manner to that for rotating journal bearings except that the squeeze number σ is used instead of Λ. As before there is an optimum design region

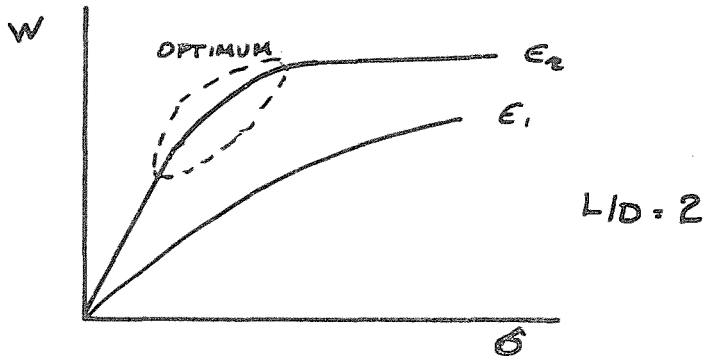

It is quite possible to build such a bearing using piezo-electric ceramic materials which when fed with an alternating voltage produce a corresponding normal deflection of the surfaces.

2.4. The Aerostatic Journal Bearing.

The term aerostatic for journal bearings only really applies for zero or low speeds of shaft rotation, i.e. very low Λ's. As Λ rises, the contribution from the aerodynamic effect becomes significant and bearing operation becomes what is called 'Hybrid'. The magnitude of this aerodynamic component of the load capacity is largely a function of the bearing size, compressibility number and eccentricity.

For the aerostatic bearing a source of pressurized gas is needed. This is metered into the bearing clearance through flow restrictors, which may be of the following types Fig (231a). (A) The annular orifice or inherent compensator which is a plain hole in the bearing wall, (B) the simple orifice in which the hole terminates in a pocket. The term 'simple' is used because a change in local bearing clearance does not change the flow area of the restrictor, (C) the capillary tube restrictor which is not widely used. Other methods of compensation include porous wall bearings and elastic orifii. The 'feed holes' are normally arranged in rows around the bearing each row containing between 3 and perhaps 16 holes. It is usual to have either one central row or two rows at quarter length stations of the bearing, although of course different arrangements can be used.

The mode of operation of the aerostatic bearing is illustrated by Fig. (231b) which shows a bearing with a single row of four feed

holes. Air is fed to an annular chamber at a pressure p_s from which it flows through the feed holes into the bearing clearance, and thence to atmosphere. Thus the air is subjected effectively to two flow resistances in series.

When the journal is concentric with the bearing sleeve, the flow through all feed holes is the same, and the pressure is uniform around the bearing. If the rotor is loaded towards one of the feed holes, the clearance restriction is increased and flow through the feed hole reduced. This results in a smaller pressure drop through the feed hole, and thus a higher pressure in the bearing clearance space on that side. The converse of this occurs on the opposite side resulting in lower pressures in the bearing clearance. These two effects combine to oppose the load and the journal will move within the clearance space until the pressure difference across it supports the load.

The load which can be supported by such a bearing is primarily a function of the supply pressure and bearing area. However, the other factors - Length/Diameter ratio, axial position of feed hole rows with two rows, and feed hole type, have optimum conditions for best load capacity. It is also important to match the two flow restrictions for optimum performance. This is done in terms of a bearing pressure factor $K_g = \frac{p_d - p_a}{p_s - p_a}$ which is often taken as 0.4-0.5

for maximum load capacity [see Fig. 622].

For medium eccentricities, the change in load capacity is of order 16% for values of K_g between 0.3 and 0.7 which allows a fair degree of lattitude in feed hole diameter.

In designs where stiffness is of prime importance, clearance is a major factor since the effective stiffness is the load capacity ÷ clearance. Thus the smaller the clearance the higher the stiffness, it being necessary only to make the feed holes smaller to keep the pressure factor at optimum value which is, however, not necessarily the same as that for maximum load. In practice the load-deflection relationship is usually linear only for eccentricities of up to 0.6, after which stiffness falls away.

The other factor which is usually of importance in aerostatic bearing design is air consumption. This can be reduced by keeping the feed hole rows away from the end of the bearing, at the expense of angular stiffness and possibly of load capacity. Also the smaller the clearance, the lower the air consumption, but the more costly the manufacture of the bearing.

The method of analysis of this type of bearing is given in Section 6 where the stiffnesses of the bearings used in the experimental work are calculated.

2.5. The Hybrid Bearing.

The last section on the aerostatic journal bearing was restricted to low or zero journal rotational speeds, i.e. low Λ's. In bearings where the clearance is small, speeds giving aerodynamic pressure generation which is significant compared to the aerostatic bearing pressures can be attained, and these have become known as hybrid bearings. Such bearings have many advantages where the weight of the rotor is the only load imposed at standstill, but where at the operating speed external loads are applied (such as in high speed cutting tools). Also very important is the stability of these bearings, which is generally much better than for pure aerodynamic operation. This will be discussed in a later section.

In practice, due to the general desire to preserve pressurized air almost all aerostatic journal bearings are designed with small clearances and become hybrid if run at speed. Thus in cases where bearing dynamics have to be considered, usually this has to be in terms of hybrid bearings.

The design load capacity of hybrid bearings can be achieved to a fair approximation by a superposition of aerostatic and aerodynamic characteristics, as proposed by Powell[19] for example. This is likely to be accurate over a fairly limited range of operating conditions, but a full analysis of Reynolds equation incorporating the feeding of pressurized air is likely to be too complex to make a

solution tractable, even if the conditions at entry to the gas film can be fully described. Progress is more likely to be made by continuous sophistication of correction factors to achieve the actual performance predictions.

3.

THE DYNAMIC CHARACTERICTS OF THE GAS JOURNAL BEARING.

3.1. Introduction.

With a system using gas lubricated journal bearings we are interested, not only in the ability of the bearings to carry specific steady loads, but also in the system's response to applied dynamic loading or vibration, and in the system's stability in respect of self excited vibrations. The response of the rotor must not be so large as to lead to the amplitude exceeding the bearing clearance, and in certain applications where an accurate axis of rotation is required, the restrictions are much more severe than this.

The most common applied dynamic load is due to rotor unbalance, which is at rotor frequency, increasing in magnitude as the square of speed. The rotor response under these conditions is discussed in detail in Section 9. Other sources of loading stem from the devices which the bearings are being used to support: e.g. turbines, grinding wheels etc. Vibrations are imposed on the system from the environment in which it is operating, and are transmitted to the rotor through the gas film, which may amplify or attenuate the vibration amplitude. The frequency spectrum of such vibrations may be extensive and capable of exciting any of the resonances which the system displays. We shall see that each type of bearing has one or more such dangerous resonances.

Considerably more important are the occurrence of self excited vibrations. One type occurs in externally pressurized bearings with pocketed feed holes and is known as Pneumatic Hammer. This can normally be overcome by correct design of the feed hole pocket. The other type which may occur in all film lubricated journal bearings with rotating shafts, is a self excited rotor whirl, which under normal circumstances leads to complete bearing failure. Close to the stability boundary, a small change in speed leads to a rapid transition from steady rotation of the shaft about its axis with a balanced shaft. or a steady synchronous whirl of the shaft axis about its mean position, into an unstable whirling mode at some frequency less than or equal to half the rotor speed. This is commonly known as 'Half Speed Whirl', although the ratio can differ considerably from one half.

The instability occurs in liquid lubricated as well as gas lubricated bearings, and was first described as such by Newkirk in 1924. Since that time many attempts have been made to solve the mathematical equations governing the fluid film behaviour under dynamic conditions and to predict the conditions which govern the onset of instability. The advent of high speed digital computers has lead to a number of recent numerical solutions for the aerodynamic bearings, the recent Cambridge thesis by Marsh[14] being the first to present an insight into the exact mechanism governing bearing instability, and to calculate accurate whirl onset speeds. This work was

done for gas lubricated bearings, which although complicated by compressibility effects do not exhibit the cavitation found in liquid film journal bearings. It is the definition of the liquid/vapour boundaries which is holding up further progress with the analysis of liquid film bearings, and indeed it looks possible that no solutions will be found. However, the analysis of the single phase gas lubricants provide valuable insight into liquid bearing phenomena, and in many cases will lead directly to solution of liquid bearing problems.

The dynamic characteristics of aerodynamic and aerostatic (including hybrid) bearings have certain similarities and certain fundamental differences, and the following sections will contain a guide to the analysis of bearing dynamics, and a description of their characteristics.

3.2. The Aerodynamic Journal Bearing Equations.

The basis of lubrication is the Navier-Stokes Momentum equations for laminar continuum fluid flow. These are complex, but for a thin film (Fig. 321a) it is possible to make the following assumptions: e.g. see Gross[10].

The y component of velocity is small compared to the x and z components.

Variation of velocities u and w in the x and z direction are small compared to that of v in the y direction.

Inertia terms are neglected for gaseous lubricants.

The equations then reduce to

$$\frac{\partial p}{\partial x} = \frac{\partial}{\partial y}\left(\mu \frac{\partial u}{\partial y}\right)$$

$$\frac{\partial p}{\partial y} = 0 \qquad 3.2.1.$$

$$\frac{\partial p}{\partial z} = \frac{\partial}{\partial y}\left(\mu \frac{\partial w}{\partial y}\right)$$

For the case of the journal bearing shown in Fig.3.2.1. , equations 3.2.1. may be integrated to give the velocity profiles along and around the bearing

$$u = \frac{1}{2\mu} y(y-h) \frac{\partial p}{\partial x} + \frac{Uy}{h}$$

$$w = \frac{1}{2\mu} y(y-h) \frac{\partial p}{\partial z} \qquad 3.2.2.$$

where h is the local clearance

U is the moving surface velocity.

The second equation of this film lubrication is the Continuity Equation. For a fixed volume in which fluid is neither created or destroyed, the mass of fluid entering per unit time must equal the mass of fluid leaving plus the stored mass.

For the bearing shown in Fig. 321b the circumferential distance is given by $x = R\phi$ and the axial distance $z = L\zeta$.

The equation of continuity for the element $hRL\delta\phi\delta\zeta$, is given by

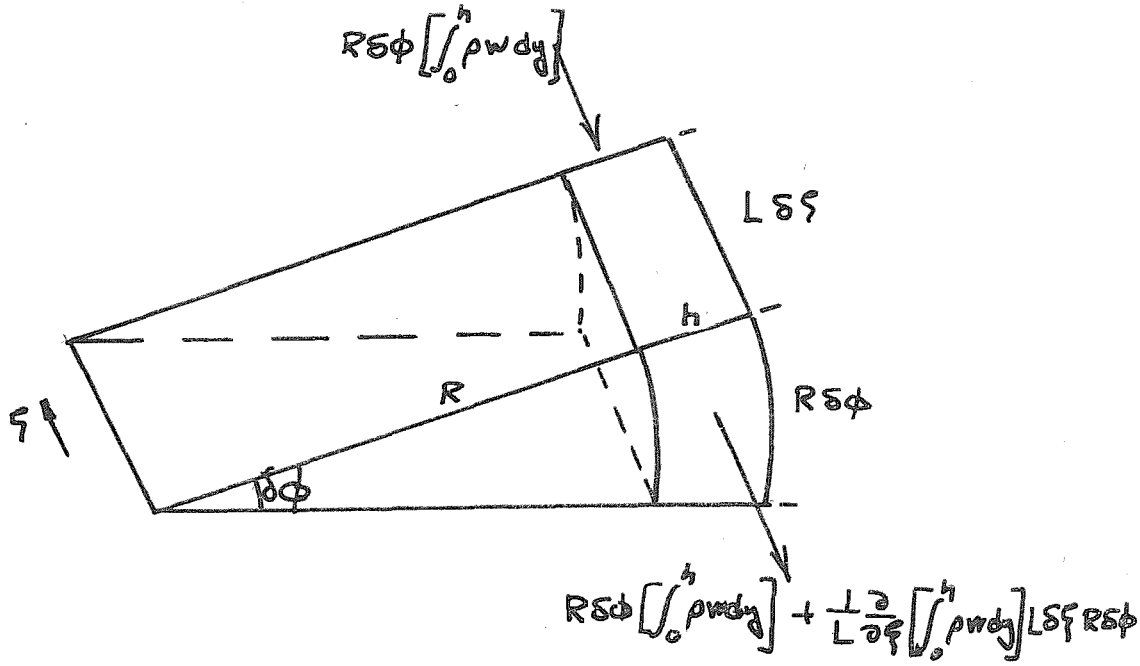

$$\frac{1}{R}\frac{\partial}{\partial\phi}\left[\int_0^h u\rho dy\right] + \frac{1}{L}\frac{\partial}{\partial\zeta}\left[\int_0^h w\rho dy\right] = -\frac{\partial}{\partial t}\left[\int_0^h \rho dy\right]$$

$$= -\frac{\partial(\rho h)}{\partial t} \qquad 3.2.3.$$

Now to a first approximation since c/R is very small

$$h = c\ (1 - \varepsilon \cos \phi_r)$$

also $$\phi_r = \phi - \theta(t)$$

Hence $$\frac{\partial(\rho h)}{\partial t} = h\frac{\partial\rho}{\partial t} + \rho\frac{\partial h}{\partial t}$$

$$= h\frac{\partial\rho}{\partial t} - \rho\{c\frac{d\varepsilon}{dt}\cos\phi_r + c\varepsilon\frac{d\theta}{dt}\sin\phi_r \qquad 3.2.4.$$

$c\frac{d\varepsilon}{dt}$ and $c\varepsilon\frac{d\theta}{dt}$ represent journal centre velocities along and perpendicular to the line of centres.

Substituting the velocity equation 3.2.2. the general form of the Reynolds equation is obtained

$$\frac{\partial}{\partial\phi}\left[\frac{h^3\rho}{\mu}\frac{\partial p}{\partial\phi}\right] + \left(\frac{R}{L}\right)^2\frac{\partial}{\partial\zeta}\left[\frac{h^3\rho}{\mu}\frac{\partial p}{\partial\zeta}\right] = 6\omega R^2\left\{\frac{\partial}{\partial\phi}(\rho h)\right.$$

$$\left. - \frac{2}{\omega}\rho c\frac{d\varepsilon}{dt}\cos\phi_r - \frac{2}{\omega}\rho c\varepsilon\frac{d\theta}{dt}\sin\phi_r + \frac{2h}{\omega}\frac{\partial\rho}{\partial t}\right\} \qquad 3.2.5.$$

The variables are written in nondimensional form

$$\bar{p} = p/p_a$$

$$\bar{\rho} = \rho/\rho_a$$

$$\bar{\mu} = \mu/\mu_a$$

$$\bar{h} = h/c$$

and for the gas film which operates under isothermal conditions $\bar{p} = \bar{\rho}$. and $\bar{\mu} = 1$.

The Reynolds equation which governs the gas film pressure distribution for a generalised journal centre movement is written

$$\frac{\partial}{\partial\phi}\left[\bar{h}^3\,\bar{p}\,\frac{\partial\bar{p}}{\partial\phi}\right] + \left(\frac{R}{L}\right)^2 \frac{\partial}{\partial\zeta}\left[\bar{h}^3\,\bar{p}\,\frac{\partial\bar{p}}{\partial\zeta}\right] = \Lambda\left\{\frac{\partial}{\partial\phi}\left[\bar{p}\bar{h}\right]\right.$$

$$\left. - \frac{2}{\omega}\,\bar{p}\,\frac{d\varepsilon}{dt}\cos\phi_r - \frac{2}{\omega}\,\bar{p}\varepsilon\,\frac{d\theta}{dt}\sin\phi_r + \frac{2\bar{h}}{\omega}\,\frac{\partial\bar{p}}{\partial t}\right\}$$

where $\Lambda = \dfrac{6\mu_a\,\omega}{p_a}\left(\dfrac{R}{c}\right)^2$ 3.2.6.

the Compressibility Number.

The boundary conditions for a plain journal bearing are

$$\bar{p} = 1 \quad \text{for } \zeta = \pm\, 1/2$$

and the pressure must be periodic in ϕ

$$\bar{p}\ (\phi) = \bar{p}\ (\phi + 2\pi)$$

This brief derivation of Reynolds Equation is repeated from reference (14) since it shows clearly in terms of fixed and relative coordinates the equation for any generalized motion of the journal bearing centre.

3.3. The Modifications for the Hybrid Bearing.

The above equation applies to aerodynamic operation, but the equations can be extended to cover the case of external pressurization. This involves modifying the continuity equation at the points at which gas is fed into the film. (ζ_n, ϕ_n) giving for the element $hR\delta\phi L\delta\zeta$ encompasing the point

$$\frac{1}{R}\frac{\partial}{\partial\phi}\left(\int_o^h u\rho dy\right) + \frac{1}{L}\frac{\partial}{\partial\zeta}\left[\int_o^h w\rho dy\right] = \frac{-\partial}{\partial t}\left(\int_o^h \rho dy\right) + w_j\Big|_{\zeta_n\ \phi_n} \qquad 3.3.1.$$

Where the source area is $R\delta\phi L\delta\zeta$, and the flow in is w_j $\frac{lb}{ft^2 sec}$

Reynolds equation becomes

$$\frac{\partial}{\partial\phi}\left[\bar{h}^3\bar{p}\frac{\partial\bar{p}}{\partial\phi}\right] + \left(\frac{R}{L}\right)^2\frac{\partial}{\partial\zeta}\left[\bar{h}^3\bar{p}\frac{\partial\bar{p}}{\partial\zeta}\right] = \Lambda\left[\frac{\partial}{\partial\phi}(\bar{p}\bar{h}) - \frac{2}{\omega}\bar{p}\frac{d\varepsilon}{dt}\cos\phi_r\right.$$

$$\left. - \frac{2}{\omega}\bar{p}\,\varepsilon\frac{d\theta}{dt}\sin\phi_r + \frac{2\bar{h}}{\omega}\frac{\partial\bar{p}}{\partial t}\right] - \Lambda\left|\frac{2w_j}{c\omega p_a}\right|_{\zeta_n\ \phi_n} \qquad 3.3.2.$$

and can be combined with the flow characteristic of the feeding restrictor, and solved analytically if the bearing is of the porous type, or by finite difference techniques assuming the source area to be the same area as the mesh used to define the pressure field. This has not been attempted except for a simplified analysis of squeeze film pressures using an idealized feeding source uniform around the bearing in the place of the feed holes, by Mullan and Richardson[17]. It seems probable that the value of such solutions would be limited as the flow conditions from the feed hole are known to be complicated, invalidating the basic assumption that fluid inertia can be neglected, and cannot be simply described mathematically.

The theory of Robinson and Sterry[23] which uses a jet and slot flow model for the aerostatic bearing, predicts steady load capacity quite well, and hybrid steady operation can be estimated as previously

indicated. However, this type of model is not much good for describing dynamic behaviour and it seems probable that the best way to derive design information will be from an experimental approach, based on the theoretical indications provided by the more tractable aerodynamic bearing dynamics.

3.4. The Stability of the Aerodynamic Bearing.

Rotor vibrations in one and two bearing systems can be classified into either a translational or conical mode

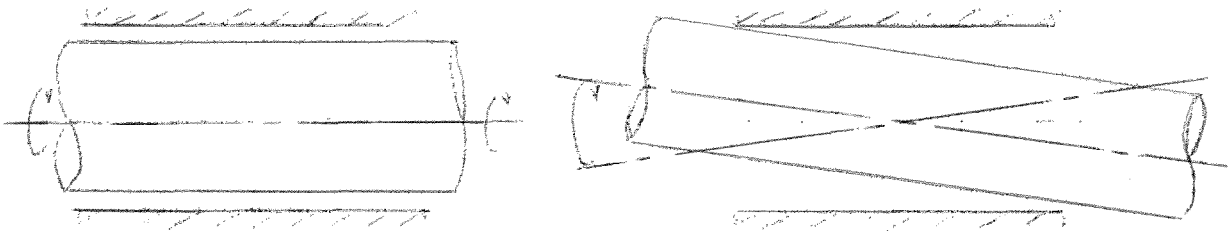

the axis of the rotor remaining parallel in the former, and describing a cone in the latter, the centre of which need not be within the bearing or bearings in a two bearing machine. However, for the case of self excited vibrations of a balanced symmetric rotor, the centre of conical whirl will lie at the centre of the system. The conical mode is complicated by the facts that gyroscopic forces come into play, and that in a two bearing machine, the motion is a combination of translational and conical motion. The operation of the system will normally be limited by the onset of one of the modes of instability and it is generally possible to ensure that the conical

mode is suppressed completely by making the transverse moment of inertia I_T more than twice the polar moment of inertia I_P.

To illustrate the form of analysis used by Marsh for dynamic characteristics, a simple case will be taken of a symmetric balanced rotor supported by a single plain aerodynamic bearing rigidly mounted. A translational mode of whirl will be considered, developing from a steady state position defined by the eccentricity ε_o and attitude angle θ_o, and the forces examined which result from an infinitesimal elliptic journal orbit at frequency ω_1 described by harmonic variations ε_1 and $\varepsilon_o\theta_1$.

Thus the generalised journal position is defined by

$$\varepsilon = \varepsilon_o + \varepsilon_1 e^{i\omega_1 t} \qquad 3.4.1.$$
$$\theta = \theta_o + \varepsilon_o\theta_1 e^{i\omega_1 t}$$

A fixed coordinate system is chosen such that the radial and tangential axes lie along and perpendicular to the steady state line of centres. The prediction of an unstable condition for the infinitesimal orbit does not necessarily imply that the bearing will still be unstable when a finite orbit is achieved, but experimental evidence indicates that for all practical purposes this is the limit of operation.

The pressure forces acting in a gas bearing may be resolved into components, acting radially and tangentially to the line of centres,

which are non linear functions of journal displacement. The method of analysis is to approximate the pressure field by the non linear steady state pressure $\bar{p}_o$ added to linearised pressure fields $\varepsilon_1\bar{p}_1 e^{i\omega_1 t}$ and $\varepsilon_o\theta_1\bar{p}_2 e^{i\omega_1 t}$ due to the vibrations.

The pressure field is now the first three terms of a Taylor series

$$\bar{p} = \bar{p}_o + \varepsilon_1\bar{p}_1 e^{i\omega_1 t} + \varepsilon_o\theta_1\bar{p}_2 e^{i\omega_1 t} \qquad 3.4.2.$$

By substituting this into equation 3.2.6. and eliminating terms of order $|\varepsilon_1^2|$ and higher a single equation is obtained of the form

$$\mathcal{R}(\bar{p}_o) + \varepsilon_1 e^{i\omega_1 t}[\mathcal{L}(\bar{p}_1)-F_1] + \varepsilon_o\theta_1 e^{i\omega_1 t}[\mathcal{L}(\bar{p}_2)-F_2] = 0$$

For the condition $|\varepsilon_1| << \varepsilon_o|$ and $|\varepsilon_o\theta_1| << |\varepsilon_o|$, this can be expressed as

$$\begin{aligned} \mathcal{R}(\bar{p}_o) &= 0 \\ \mathcal{L}(\bar{p}_1) &= F_1 \\ \mathcal{L}(\bar{p}_2) &= F_2 \end{aligned} \qquad 3.4.3.$$

where $\mathcal{R}(\bar{p}_o) = \frac{\partial}{\partial\phi}\left[\bar{h}_o^3\bar{p}_o\frac{\partial\bar{p}_o}{\partial\phi}\right] + \left(\frac{R}{L}\right)^2\frac{\partial}{\partial\zeta}\left[\bar{h}_o^3\bar{p}_o\frac{\partial\bar{p}_o}{\partial\zeta}\right] - \Lambda\frac{\partial}{\partial\phi}\left[\bar{h}_o\bar{p}_o\right]$

$$\mathcal{L}(\bar{p}_n) = \frac{\partial}{\partial\phi}\left[\bar{h}_o^3\frac{\partial}{\partial\phi}(\bar{p}_o\bar{p}_n)\right] + \left(\frac{R}{L}\right)^2\frac{\partial}{\partial\zeta}\left[\bar{h}_o^3\frac{\partial}{\partial\zeta}(\bar{p}_o\bar{p}_n)\right]$$

$$- \Lambda\frac{\partial}{\partial\phi}\left[\bar{h}_o\bar{p}_n\right] - i2Q\Lambda\bar{h}_o\bar{p}_n \qquad \text{for } n = 1,2.$$

$$F_1 = 3\{\frac{\partial}{\partial\phi}\left[\bar{h}_o^2\cos\phi\bar{p}_o\frac{\partial\bar{p}_o}{\partial\phi}\right] + \left(\frac{R}{L}\right)^2\frac{\partial}{\partial\zeta}\left[\bar{h}_o^2\cos\phi\bar{p}_o\frac{\partial\bar{p}_o}{\partial\zeta}\right]\}$$

$$- \Lambda\frac{\partial}{\partial\phi}\left[\bar{p}_o\cos\phi\right] - i2Q\Lambda\bar{p}_o\cos\phi$$

$$F_2 = 3\{\frac{\partial}{\partial\phi}\left[\bar{h}_o^2\sin\phi\bar{p}_o\frac{\partial\bar{p}_o}{\partial\phi}\right] + \left(\frac{R}{L}\right)^2\frac{\partial}{\partial\zeta}\left[\bar{h}_o^2\sin\phi\bar{p}_o\frac{\partial\bar{p}_o}{\partial\zeta}\right]\}$$

$$- \Lambda\frac{\partial}{\partial\phi}\left[\bar{p}_o\sin\phi\right] - i2Q\Lambda p_o\sin\phi$$

$$\bar{h}_o = (1-\varepsilon_o\cos\phi)$$

$$Q = \frac{\omega_1}{\omega} \quad \text{the whirl ratio}$$

$$i = \sqrt{-1}$$

Note that these equations are in terms of ϕ where

$$\phi = \phi_r + \theta_1 e^{i\omega_1 t}$$

The boundary conditions are

$$\left.\begin{aligned}\bar{p}_o &= 1\\ \bar{p}_1 &= \bar{p}_2 = 0\end{aligned}\right\} \quad \text{on } \zeta = \pm 1/2$$

and $\bar{p}_n(\phi) = \bar{p}_n(\phi+2\pi)$ for n = 0, 1, 2.

Also pressures are all symmetric about the bearing centre.

The solutions to these equations may be obtained by finite difference methods on a high speed digital computer, the pressure at each point in the grid being determined by the four pressures surrounding it. Marsh used a grid which divided up the bearing

surface into 12 parts in each direction, yielding a solution accuracy of 1%.

The first equation of 3.4.3. is nonlinear in $\bar{p}_o$ and the method of solution is to write it as two simultaneous equations

$$'A' \quad -R(\bar{p}_o) = \frac{\partial}{\partial\phi}\left(\bar{h}_o^3\bar{\rho}_o\frac{\partial\bar{p}_o}{\partial\phi}\right) + \left(\frac{R}{L}\right)^2\frac{\partial}{\partial\zeta}\left(\bar{h}_o^3\bar{\rho}_o\frac{\partial\bar{p}_o}{\partial\zeta}\right) - \Lambda\frac{\partial}{\partial\phi}\left[\bar{h}_o\bar{\rho}_o\right]\}$$

$$'B' \quad -$$

$$\bar{p}_o = \bar{\rho}_o$$

The density field $\bar{\rho}_o$ is guessed and equation 'A' solved for a pressure field $\bar{p}_o$. This is then made equal to $\bar{\rho}_o$ and a new solution obtained. Iteration is continued until a convergence criterion for $\bar{p}_o$ is satisfied. The other equations are linear but depend on the solution of $\bar{p}_o$.

The pressure fields so obtained are integrated around and along the bearing, and the radial and tangential components of resultant force obtained

$$\bar{F}_r = \frac{F_r}{\pi p_a RL} = -\frac{1}{\pi}\int_{-\frac{1}{2}}^{+\frac{1}{2}}\int_0^{2\pi}\bar{p}\cos\phi\,d\phi\,d\zeta$$

$$\bar{F}_t = \frac{F_t}{\pi p_a RL} = -\frac{1}{\pi}\int_{-\frac{1}{2}}^{+\frac{1}{2}}\int_0^{2\pi}\bar{p}\sin\phi\,d\phi\,d\zeta \qquad 3.4.4.$$

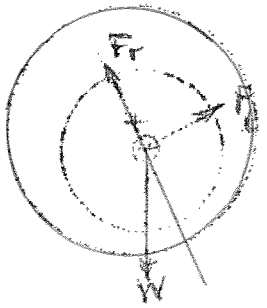

If friction forces are neglected it follows from equation (3.4.2.) that these two force components can be expressed by

$$\bar{F}_r = \bar{F}_{ro} + \left[\varepsilon_1 \frac{\partial \bar{F}_r}{\partial \varepsilon_1} + \theta_1 \frac{\partial \bar{F}_r}{\partial \theta_1}\right] e^{i\omega_1 t}$$

$$\bar{F}_t = \bar{F}_{to} + \left[\varepsilon_1 \frac{\partial \bar{F}_t}{\partial \varepsilon_1} + \theta_1 \frac{\partial \bar{F}_t}{\partial \theta_1}\right] e^{i\omega_1 t} \qquad 3.4.5.$$

$\bar{F}_{ro}$ and $\bar{F}_{to}$ are the steady state forces which combine to support the steady state load on the bearing.

The dynamic equations of motion of the journal are

$$-mc\omega_1^2 \varepsilon_1 e^{i\omega_1 t} = \pi p_a RLg \left[\varepsilon_1 \frac{\partial \bar{F}_r}{\partial \varepsilon_1} + \theta_1 \frac{\partial \bar{F}_r}{\partial \theta_1}\right] e^{i\omega_1 t}$$

$$-mc\omega_1^2 \varepsilon_o \theta_1 e^{i\omega_1 t} = \pi p_a RLg \left[\varepsilon_1 \frac{\partial \bar{F}_t}{\partial \varepsilon_1} + \theta_1 \frac{\partial \bar{F}_t}{\partial \theta_1}\right] e^{i\omega_1 t} \qquad 3.4.6.$$

These may be rewritten in matrix notation

$$\begin{bmatrix} -\frac{\partial \bar{F}_r}{\partial \varepsilon_1} - 4Q^2\gamma_1 & -\frac{1}{\varepsilon_o}\frac{\partial \bar{F}_r}{\partial \theta_1} \\ -\frac{\partial \bar{F}_t}{\partial \varepsilon_1} & -\frac{1}{\varepsilon_o}\frac{\partial \bar{F}_t}{\partial \theta_1} - 4Q^2\gamma_1 \end{bmatrix} \begin{bmatrix} \varepsilon_1 \\ \varepsilon_o\theta_1 \end{bmatrix} e^{i\omega_1 t} = 0$$

$$\text{or} \quad [A(Q) - 4Q^2\gamma_1 I]x = 0 \qquad 3.4.7.$$

where $A(Q) = \begin{bmatrix} \frac{\partial \bar{F}_r}{\partial \varepsilon_1}, & \frac{1}{\varepsilon_o}\frac{\partial \bar{F}_r}{\partial \theta_1} \\ \frac{\partial \bar{F}_t}{\partial \varepsilon_1}, & \frac{1}{\varepsilon_o}\frac{\partial \bar{F}_t}{\partial \theta_1} \end{bmatrix}$ the translational dynamic stiffness matrix at whirl ratio Q

$x = \begin{bmatrix} \varepsilon_1 \\ \varepsilon_o\theta_1 \end{bmatrix}$ the displacement vector

$\gamma_1 = \frac{mc\omega^2}{4g\pi p_a RL}$ the Stability Parameter

A self excited vibration can only exist if this matrix equation admits a non zero solution for the displacement vector x, which means in effect that a small input $(\varepsilon_1, \varepsilon_o\theta_1)$ does not die away. This only defines a condition of neutral stability, but it is found in practice that a very small increase in speed makes the bearing unstable.

Hence for $x \neq 0$

$$|A(Q) - 4Q^2\gamma I| = 0$$

This condition is found to exist only for one finite value of the whirl ratio Q_{c1} and one real value of the stability parameter, γ_{c1}. Thus at the onset of instability

$$\begin{aligned} Q &= Q_{c1} \\ \gamma_1 &= \gamma_{c1} \\ x &= x_{c1} \end{aligned} \qquad 3.4.8.$$

where x_{c1} is the critical eigenvector of equation 3.4.7.

Q_{c1} is found to be equal to or less than $\frac{1}{2}$ which is the half-speed whirl instability. The critical displacement vector is approximately

$$x_{c1} = \begin{bmatrix} 1 \\ -i \end{bmatrix}$$

which means that the journal centre traces an orbit nearly circular in shape. The translational whirl effects in a two bearing machine are directly additive and the criteria for the onset of instability is

$$\gamma_1 = 2\,\gamma_{c1}$$

whilst, as before

$$Q = Q_{c1}, \quad x = x_{c1}$$

The method used to obtain the critical parameters for a given bearing is to calculate values of the dynamic stiffness matrix A(Q) at three values of whirl ratio - 0.4, 0.45, 0.5. A parabolic interpolation is then used to determine the critical value Q_{c1}, and the critical stability parameter follows from the real eigenvalue $4Q_{c1}^2\gamma_{c1}$ of the matrix $A(Q_{c1})$. Results are presented on stability charts in the form of curves of $\sqrt{\gamma_{c1}}$ vs Λ for various eccentricity ratios, at each L/D ratio.

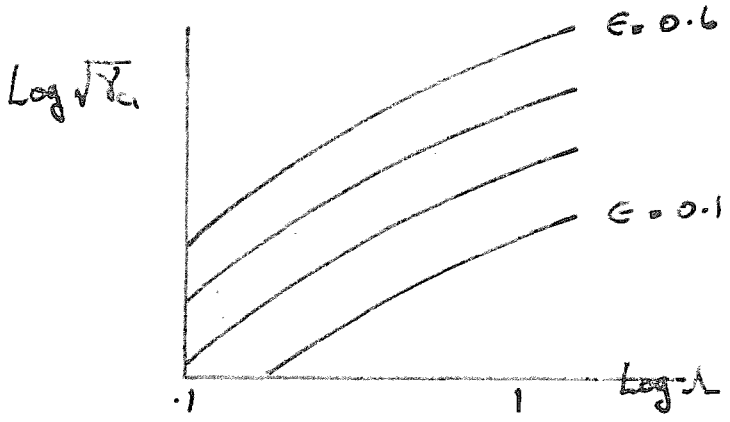

To test the stability of a specified bearing system at its running speed, the steady state operating eccentricity (ε_o) is calculated and the point (ε_o,Λ) plotted on the chart, giving the critical stability parameter γ_{c1}. The test is now made and for

$$\gamma_1 < \gamma_{c1}$$

the system is stable.

3.5. The Physical Interpretation of the Theory.

It is important to understand the physical significance of the unstable condition. If the journal performs a motion x, then the gas film forces acting on the journal are given by

$$\bar{F} = \begin{bmatrix} \bar{F}_r \\ \bar{F}_t \end{bmatrix} = - [A(Q)]x \qquad 3.5.1.$$

Now if it is possible to define a whirl ratio Q_{c_1} and an orbit x_{c_1} such that

$$\bar{F} = -\left[4Q^2_{c_1}\gamma_{c_1}\right] x_{c_1} \qquad 3.5.2.$$

then

$$[A(Q_{c_1})]x_{c_1} - [4Q^2_{c_1}\gamma_{c_1} I]x_{c_1} = [A(Q_{c_1}) - 4Q^2_{c_1}\gamma_{c_1} I]x_{c_1} = 0 \qquad 3.5.3.$$

If the critical frequency ratio and orbit are such that γ_{c_1} is real then from equation 3.4.9. the lubricating film is identical in behaviour with a spring of stiffness $\left[4Q^2_{c_1}\gamma_{c_1}\right]$.

Under these conditions there is no overall dissipation of energy by the gas film - a condition clearly necessary for the onset of a small self-excited vibration.

In the author's view a slightly more detailed description of the conditions existing at the onset of whirl might be of some value to its understanding. Fundamentally the feature of fluid film journal bearings

which leads to instability is that a deflection of the rotor, relative to the sleeve, produces a gas film force which does not act in the same direction but at the "attitude angle" to it. It can be considered that the force has components along the line of centres and perpendicular to it. It is this latter force which renders systems like this potentially unstable. The equations of motion governing the journal are given in 3.4.6. and represent respectively the forces acting along and normal to the line of centres. These are written in matrix notation in equation 3.4.7.

$$[A(Q) - 4Q^2\gamma_1 I]x = 0$$

It is seen from equations 3.4.3. that the coefficients of the matrix A(Q) are complex numbers and the A(Q) may thus be defined

$$A(Q) = \begin{bmatrix} a_{11} + ib_{11} , a_{12} + ib_{12} \\ a_{21} + ib_{21} , a_{22} + ib_{22} \end{bmatrix}$$

Thus equation 3.4.7. may be written

$$\left[(a_{11} + ib_{11})\varepsilon_1 + (a_{12} + ib_{12})\varepsilon_o\theta_1\right]e^{i\omega_1 t} = 4Q^2\gamma_1\varepsilon_1 e^{i\omega_1 t} \qquad 3.5.4.$$

$$\left[(a_{21} + ib_{21})\varepsilon_1 + (a_{22} + ib_{22})\varepsilon_o\theta_1\right]e^{i\omega_1 t} = 4Q^2\gamma_1\varepsilon_o\theta_1 e^{i\omega_1 t}$$

where $4Q^2\gamma_1\varepsilon_1$ and $4Q^2\gamma_1\varepsilon_o\theta_1$ represent the inertia forces along and perpendicular to the line of centres. It may be seen that the gas

film forces opposing the inertia force can be resolved into forces which act in phase, and at 90° phase shift in time, relative to the displacement vector. Thus in the first equation a force

$$a_{11}\varepsilon_1 + \imath\beta_{12}\varepsilon_o\theta_1$$

acts in phase with the inertia, and

$$ib_{11}\varepsilon_1 + a_{12}\varepsilon_o\theta_1$$

acts at 90° phase shift.

This equation might be thus considered analagous to a simple mass-spring-damper equation

$$m\ddot{x} + C\dot{x} + kx = 0$$

with a stiffness force kx in phase, with the displacement vector, and damping force $C\dot{x}$ at 90° phase shift.

The significance of the force produced in quadrature to the deflection is now seen. The force $\imath b_{11}\varepsilon_1$ is that primarily due to the velocity in the direction of displacement, and in a single degree of freedom system would constitute the total damping. But in this system, motion in the direction in quadrature to ε_1 gives rise to a force $a_{12}\varepsilon_o\theta_1$ in the direction of ε_1 but 90° lagging in time. This now acts against the velocity force and constitutes a negative damping component. Thus the overall damping in the plane containing ε_1 is the sum of these two components and may be positive or negative, depending on which dominates.

Any small vibrations will be at the resonant frequency and will die away at a rate dependent on the total damping. If the effective damping constant is zero, the vibrations are at the natural frequency governed entirely by the spring stiffness and do not die away. This is equivalent to a state of neutral stability.

In the gas film, for the general case of a rotor eccentric to the bearing, the equivalent gas film constants in the two planes will not be equal, leading to an elliptical free vibration orbit (ε_1, $\varepsilon_o\theta_1$) at whirl ratio Q, governed in part by the two spring stiffnesses and in part by the damping compoents. The stiffness and damping components are in turn functions of speed, frequency ratio and orbit. During stable operation damping is positive, but as the speed reaches the critical speed, the orbit and whirl ratio become such that the damping forces in each direction are exactly zero.

$$\begin{aligned} ib_{11}\varepsilon_1 + a_{12}\varepsilon_o\theta_1 &= 0 \\ a_{21}\varepsilon_1 + ib_{22}\varepsilon_o\theta_1 &= 0 \end{aligned} \qquad 3.5.5.$$

The rotor inertial force is now balanced exactly by the spring force

$$\begin{aligned} a_{11}\varepsilon_1 + ib_{12}\varepsilon_o\theta_1 &= \bar{m}\omega_1^2\varepsilon_1 \\ ib_{21}\varepsilon_1 + a_{22}\varepsilon_o\theta_1 &= \bar{m}\omega_1^2\varepsilon_o\theta_1 \end{aligned} \qquad 3.5.6.$$

where $\bar{m}$ is the non dimensional rotor mass.

With a further small increase in speed the damping which has reduced to zero becomes negative, and in practice the whirl amplitude normally increases rapidly until the rotor contacts the bearing wall. Stabilization sometimes occurs due to the non-linearities of the pressure field, but probably this only occurs when damping is changing magnitude slowly close to the critical speed condition.

The actual frequency of whirl ω_1 will fall in between the natural frequency of vibration of the rotor on the effective spring in each of the two directions, the gas film acting as though it were a symmetric linear spring of magnitude $\left[4Q^2_{c_1}\gamma_{c_1}\right]$. Increasing the eccentricity not only increases the overall magnitude of the two spring components, raising the frequency of vibration, but also increases the asymmetry of the system, which lowers the whirl ratio, the two factors being mutually beneficial to the whirl onset speed.

The simplicity of the matrix notation is illustrated by the fact that the four criteria given by equations 3.5.5, 3.5.6. are satisfied by the solution of

$$\left| A(Q) - 4Q^2\gamma_1 I \right| = 0$$

when it has a finite whirl ratio and a real value of the stability parameter.

It is important to note that the magnitude of each of the elements of the gas film force matrix is not directly dependent on its corresponding displacement or velocity, as assumed by some early authors.

3.6. An Experimental Method to Determine the Stability Parameter.

It has been noted above that if the rotor describes a critical orbit at the critical whirl ratio, the gas film is exactly analagous to a linear spring of stiffness $\left[4Q^2_{c_1}\gamma_{c_1}\right]$. The bearing is not unstable unless at the same time, the vibration frequency represents the natural frequency of the rotor mass on this spring.

Marsh[15] has proposed to use this property to determine the stability parameters of a bearing system for all operating conditions without the necessity to traverse the stability boundary. The author has thought it profitable to present a simple exposition of this.

If a journal bearing sleeve is forced into a critical orbit at a critical whirl ratio, the rotor now only supported by a linear spring of stiffness $\left[4Q^2_{c_1}\gamma_{c_1}\right]$ follows exactly the sleeve orbit and frequency but at a different amplitude, the relative motion still being a critical orbit.

A simple one dimensional spring analogy can be used

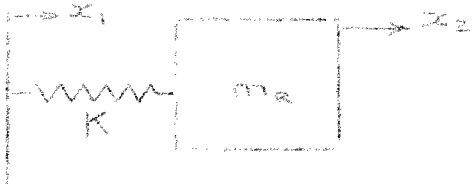

where $x_1 e^{i\omega_1 t}$ and $x_2 e^{i\omega_1 t}$ represent the orbits at frequency ω_1 of the rotor and journal respectively, and the stiffness K is written in non dimensional form as $k = \frac{Kc}{\pi p_a RL} = \left[4Q_{c_1}^2 \gamma_{c_1}\right]$

The equation of motion of the mass m_R is

$$m_R \ddot{x}_1 + K(x_1 - x_2) = 0 \qquad 3.6.1.$$

the steady state solution being

$$x_1 = \frac{Kx_2}{m_R}\left[\frac{1}{\frac{K}{m_R} - \omega_1^2}\right] \qquad 3.6.2.$$

$$\text{or} \quad \frac{x_1}{x_2} = \frac{\omega_n^2}{\omega_n^2 - \omega_1^2}$$

$$\text{where} \quad \omega_n = \sqrt{\frac{K}{m_R}}$$

Now the whirl ratio is given by

$$Q_{c_1} = \frac{\omega_1}{\omega}$$

where ω is the rotor speed.

But also

$$Qc_1 = \frac{\omega_n}{\omega_{cr}}$$

where ω_{cr} is the onset speed of whirl instability and ω_n is the frequency of the instability, representing the natural frequency of the rotor mass on a spring of stiffness $\bar{k} = \left[4Q_{c_1}^2 \gamma_{c_1}\right]$

Hence $\omega_n/\omega_1 = \omega_{cr}/\omega$

and $$\frac{x_1}{x_2} = \frac{\omega_{cr}^2}{\omega_{cr}^2 - \omega^2}$$

or $$\frac{x_1}{x_2} = \frac{\gamma_{c_1}}{\gamma_{c_1} - \gamma_{1R}} \qquad 3.6.3.$$

where $$\gamma_{1R} = \frac{m_R \, c \, \omega^2}{4\pi g \, p_a \, RL}$$

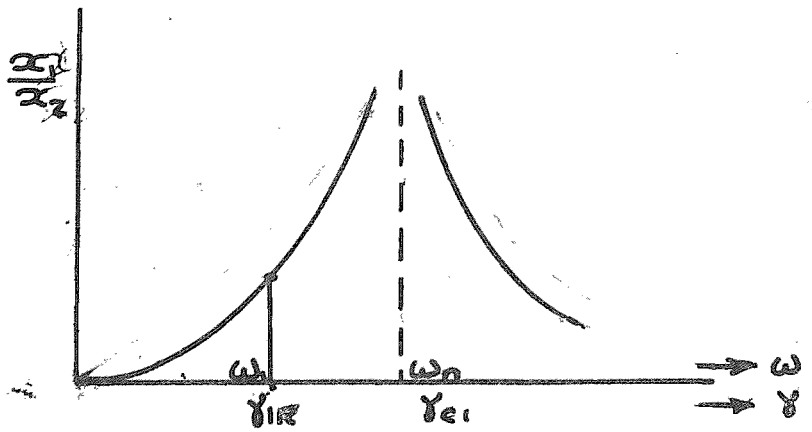

It follows that the relative motion can be written

$$(x_1 - x_2) = \frac{\gamma_{1R}}{\gamma_{c_1} - \gamma_{1R}} \, x_2 \qquad 3.6.4.$$

The experimental technique is to vibrate the sleeve in two planes, such that the orbits of the sleeve and rotor exactly match.

The system is then following a critical orbit at the critical whirl ratio. By measuring the absolute amplitude of the sleeve motion (x_2) and the relative amplitude between the sleeve and the rotor ($x_1 - x_2$), and the rotor speed, equation 3.6.4. may be used to determine the critical stability parameter for that speed and eccentricity.

The results are presented in exactly the same form as the stability chart shewn on page 34 produced from the numerical solution of Reynolds Equation.

The method is applicable for any type of bearing using any type of lubricant including non-Newtonian fluids, subject only to the provision that there exists a steady state operating condition. Thus the stability boundaries of bearings for which mathematical analysis is intractable, including nearly all liquid film bearings, may be quite simply determined.

3.7. Other Dynamic Considerations.

The above analysis has been developed for the translational mode of whirl, and the derivation for the conical mode is similar except that the gyroscopic forces must be included in the analysis. The principles underlying the instability are exactly the same as those stated above, and the stability conditions can be stated in the same way. It is usual to test the stability of a system both for the translational and conical modes, the maximum performance being limited

by the first mode of instability to occur.

It is quite common for bearing sleeves to be mounted in transkationally or conically flexible mountings. This provides an additional element of flexibility into the system and will obviously affect the conditions for instability. In this type of system there will be two conditions for which the system can be unstable. If the flexible mounting contains significant damping it may be possible to avoid the first onset speed of whirl altogether or to limit its amplitude until an offset speed is reached, giving a significant increase in speed range before whirl sets in again.

A method which has for some years been used, on an emperical basis, to curb half-speed whirl in self acting bearings is to lobe the surface, which has the effect of providing additional converging wedges to the one produced by eccentricity of the shaft within the bearing. This type of bearing offers the possibility of stable bearing operation in a zero 'g' environment which is impossible in a plain journal bearing. A second method of achieving this is by putting fine spiral grooves in one of the surfaces which pump gas into the centre of the bearing.

These methods are not easy to design, and extremely costly to manufacture and for applications where synchronous vibrations can be tolerated, rotor unbalance sufficient to produce a significant vibration eccentricity can result in an offset of half speed whirl.

Flexible mountings and lobed bearings have been theoretically analysed by Marsh[15]. Spiral grooved bearings have been the subject of a rather oversimplified report by Vohr and Pan[31], which predicted that the load capacity would increase in the same way as an incompressible fluid - linearly with Λ, and that the bearing could be completely stable to half speed whirl.

The last major method of modifying half speed whirl characteristics is by feeding pressurised air into the clearance. This has been used as a laboratory technique but as yet no work has been reported on determining the exact effects of just feeding external gas, as opposed to actually designing the bearing or hybrid operation i.e. capable of carrying a load under optimised conditions at standstill. It could be that this mode of design does not lead to optimised stability, although experimental evidence seems to indicate at present that it does. Once a pressurised gas system has been established, it would seem that for normal purposes there is little point in not designing the bearing for continuous hybrid operation. Hence the problem will be inverted and a look taken at the stability of aerostatic hybrid bearings.

4.

THE DYNAMIC CHARACTERISTICS OF THE EXTERNALLY PRESSURISED BEARING.

4.1. Introduction.

Essentially all that has been said in the last section about self-acting bearings applies equally to externally pressurized bearings. The term externally pressurized is used in preference to aerostatic in order to avoid the implication that aerodynamic gas film forces are not important. These, in fact, largely control the stability of this type of bearing. The effect of external pressurization is to modify the Reynolds equation as shewn in equation 3.3.2., and thus to modify the steady state performance and the dynamic stiffness matrix A(Q). However, a full scale solution of this equation would probably not yield very accurate information due to the lack of certainty about conditions of flow at the exit to the feeding areas, and would be expensive to compute due to the variety of feed hole configurations, and pressurization conditions. Thus it will be much more profitable to pursue an experimental investigation based on the insight provided by aerodynamic bearing analysis.

From experience with large clearance hybrid bearings (refs. 7, 20, 29) we have learned that when these have a load capacity at zero speed, they exhibit a resonant frequency to unbalance or impressed vibrations, controlled by the aerostatic stiffness of the gas film.

When the rotational speed is increased beyond this, a self excited whirl instability of approximately the resonant frequency is encountered at a speed of between two and six times this frequency.

Apart from some uncertainty about the whirl ratio - which can always conservatively be estimated at two - the vibration characteristics of large clearance hybrid bearings can be expected to behave in a predictable manner. The damping is known to be low but the magnitude has not been calculated and thus the amount of unbalance which can be tolerated at resonance cannot be predicted. However, since the system behaves approximately as a linear spring-mass-damper system, the response below resonance is very small, and rapid inversion from rotation about the geometric centre to the mass centre takes place after resonance.

The other extreme operating condition to that above where the aerodynamic forces are small compared to the aerostatic, is where there is no pressurization, i.e. pure aerodynamic operation. This condition also now has predictable characteristics given by the Marsh theory for free vibrations, and in Section 9 for forced synchronous vibrations. [a new development based on the work of Ausman[1,2] and Raimondi[21]].

There now remains an area in between these two extreme conditions where true hybrid bearing operation occurs, and here very little evidence has been presented in a conclusive manner. In fact the only

paper in the author's possession dealing with dynamic characteristics of hybrid journal bearings, is one by Gross[9], and the validity of this is doubtful since he used bearing sleeves flexibly mounted on rubber 'O' rings. A special type of externally pressurized bearing for high speed cryogenic applications has been comprehensively covered by Sixsmith. However, this bearing derived extra damping by the use of tuned cavities in the bearing wall.

4.2. The Scope of The Present Investigation.

A high speed digital computer suitable for the study of gas bearing dynamic characteristics is not available, and even had it been it is felt that more qualitative work is necessary to map out areas where full mathematical solutions are necessary. Also no attempt is made, in cases where simple theory does not correspond to the observed characteristics, to construct empirical formulae since it is felt that apparatus should be tailored to specific problems for this purpose, and here a general experimental rig has been used.

The purpose of this investigation is to present a review of the vibration characteristics of the hybrid bearing, and to test the relationship of these to simple theoretical predictions, and qualitative predictions based on the knowledge of the two extreme operating modes specified in 4.1.

Since the aerostatic stiffness is of prime importance in

vibration response, a method of calculating this is to be reviewed and checked against the measured stiffness obtained for the experimental bearings.

The first of the vibration characteristics is that of free vibrations. This is the most important since half-speed whirl is in fact a free vibration under the special condition of zero damping. Initially a comprehensive investigation will be made of the gas film stiffness and damping with no shaft rotation, and compared to the author's approximate theory and also to a computer solution of the exact mathematical model of the squeeze film forces, presented in ref. (17). The way in which these characteristics change as the shaft is rotated are to be examined and the terminal speed condition of the zero damping unstable whirl considered. Here the careful study made of the aerodynamic half speed whirl condition leads to the understanding of the manner in which it occurs in hybrid bearings.

The case where synchronous vibrations due to out of balance is present is known to affect the half speed whirl characteristics of self acting bearings. Also it has been suspected that aerodynamic bearings might exhibit a resonance to the out-of-balance forcing, but the conditions for the bearing system to be stable at the speed at which this might occur have not been developed. The condition for resonance in an aerodynamic bearing is theoretically examined and the validity of a simplified analysis of this compared to a full non-linear

solution. Similarly the relationship between the whirl onset speed and the resonance in a hybrid bearing has not previously been examined. One might expect the aerodynamic supplement to the aerostatic stiffness to raise the resonant speed, but due to circumstances discussed later not affect the whirl onset speed. It should be possible for whirl onset to occur before resonance - an occurrence not previously postulated. Thus a hybrid theory to calculate the stiffness and damping coefficients under conditions of synchronous loading is developed, and theoretical response curves calculated. Experimental response curves are obtained and the resulting stiffness and damping coefficients compared to theory.

The one major omission as far as recording the complete vibration characteristics of the hybrid bearing is concerned, is the response of the system to variable frequency imposed vibrations, at different running speeds. The experimental investigation has recorded the two most important vibration conditions - the free vibrations and synchronous forced vibrations - at any speed. More comprehensive results would be most easily achieved by mounting the whole test apparatus on a large shaker, a facility which is unfortunately not available.

5.

THE EXPERIMENTAL APPARATUS.

5.1. Introduction.

The original concept of this project was that it should be concerned with the high speed characteristics of hybrid journal bearings. A completely new experimental bearing apparatus was to be constructed incorporating a number of features not available in previous work within the University.

For the basic layout it was decided to use a two bearing, symmetric, rotating shaft system shown in Figure 5.1.1, as being the most versatile type of layout. A single bearing apparatus would have many advantages over this in that it is very difficult in a two bearing system to make the clearances the same, and to get the two bearings aligned parallel to the shaft. However, there are the disadvantages that a single bearing rig of the required rotor diameter would be very small to handle, and in general it would be very difficult to build a rotor with an inertia ratio such that cylindrical whirl instead of conical whirl could be obtained. Also the gas film stiffness to conical motions would be small, leading to low whirl onset speeds. Also the rig would not yield as much useful information about the behaviour of practical gas bearing machines which are almost universally of the two bearing type.

From the consideration of reaching high speeds a small diameter

rotor was desired, but against this had to be set the requirement of being able to monitor the motion of the shaft with accuracy. Using the Wayne-Kerr capacitance transducers it was decided that a 0.75 in diameter rotor was the smallest which could be used without impairing the accuracy of the measurements. A speed of 300,000 rpm should be possible at this diameter using a simple impulse turbine to drive the shaft.

This speed of 300,000 rpm is well above that which could be reached by the system without some external influence to provide stability from half-speed whirl. One method being used in practice is to provide external damping to the system by mounting the bearing sleeves in rubber 'O' rings which not only do this, but also seal the air supply to the bearing and allow a small amount of self-alignment. Accordingly the 'O' rings were initially installed and it was hoped that an experimental investigation could be made of their performance and characteristics.

Another small rig was constructed to apply forced vibrations to a pair of 'O' rings by means of an electromagnetic vibrator, in order to map their characteristics with change in vibration frequency and amplitude etc. However, this was to be only a subsidiary project, and it was discovered that a very elaborately designed rig would have been necessary to obtain useful information, so this piece of work was shelved in favour of a different approach. The other factors

which include material size variation of the 'O' rings, precompression, creep, ageing, groove size and pressure sealed, would make dynamic performance of rubber 'O' rings into a full project in itself.

The second approach considered was that it might be possible to investigate the 'O' ring performance on the actual gas bearing rig, using the gas film itself as a transducer. Provision was made for four probes to monitor the complete movement of each bearing sleeve as shown in Fig. (5.1). However, a closer look at the problem revealed that very little concrete information was available about the behaviour of hybrid gas films under dynamic conditions. In view of this, apart from one or two experiments which confirmed that 'O' rings could be effective in suppressing half speed whirl, the experimental effort was finally concentrated on gaining more knowledge of the gas film behaviour in rigid bearings.

The rig is quite suitable for this, except that in hindsight a larger rotor diameter might have been desirable - possible with lower speeds - to enable greater measurement and general accuracy to be obtained. The rig will be suitable for a wide range of further experimental work since its features include the possibility of varying bearing alignment, mass and length of rotor, bearing separation, bearing sleeve length to diameter ratio and type, provided that there is no more than one central row of feed holes. Also a slave bearing

could be used for steady state loading experiments.

5.2. The Test Rig Construction.

Since the gas bearing laboratory is situated on the upper floor of a two floor building, and the experiements were to be concerned with rotor vibrarions, it was considered desirable to mount the experiment on an anti-vibration bed. This was specially constructed and took the form of a two ton concrete block mounted on helical springs, which had a natural frequency of 4 c/s. Into this was set a milling machine table to form a test bed onto which a rig could be bolted. (Figure 5.1.2).

A two bearing system had been chosen and it was decided to mount each bearing in an independent block. This necessitated some means of adjusting the alignment of the bearing sleeves and this was achieved by mounting the complete bearing assembly inside the outer track of an 'INA' needle bearing self aligning spherical housing. The bearing sleeve housing could be locked rigidly once aligned by clamping up on the split mounting block. The air supply to the feed hole reservoir had to be fed in at the side and since the largest 'INA' self aligning unit had an inside diameter of only 2 inches, the bearing sleeve had to be placed eccentrically within its housing to accommodate the air intake which was positioned at the top. 'O' ring grooves were machined into the early bearing sleeves which had approximately a 0.005 in clearance in the housing,

but later sleeves had no grooves and were made a slight interference fit to achieve sealing of the air and eliminate any flexibility of the bearing sleeve system. All of the mounting blocks have a 1 in wide by 6 in long base ground flat and perpendicular to the face. The base covers three slots in the machine bed, and each block is located by a central tongue and clamped down by two $\frac{5}{8}$ in diameter bolts.

The rotor is driven by an impulse type turbine fed by three symmetric jets, to eliminate any resultant radial force on the rotor, and placed at the centre of the system. Since it is not possible to define the air flow direction as it leaves the bucket with such a small size, no theoretical design of the turbine is possible, but a small development programme indicated that the best jet angle for most purposes was such that it formed a tangent to a circle $\frac{3}{4}$ of the shaft diameter. The usual bucket is made by feeding a vertical end mill sideways into the rotor, but a more effective bucket was developed by using a slot cutter inclined at 15° to the vertical and feeding this in. This produced a bucket with the back wall sloping so that less air spilled over the top and more was turned around. The greater the angle the air is turned through the more momentum is transferred to the rotor, and ideally the air would all be turned around through 180° relative to the bucket with no spillage over the top at 90°.

The bearing blocks are spaced such that approximately $\frac{1}{4}$ in of rotor protrudes at each end, and this is used for the rotor motion monitoring probes. Wayne-Kerr capacity probes are used, having a diameter of $\frac{1}{4}$ inch beveled at the ends, two placed in quadrature at each end. These are mounted in cut-away brass rings inserted through steel mounting blocks, insulated by 1/16 in thick black nylon bushes and locked in position by grub screws. Extremely sensitive adjustment is possible: simply by twisting the probe carrier and pulling or pushing it is possible to set the probe distance from the shaft to better than 5μin from the desired position.

Special devices run through these probe mounting rings at each end. At the right hand end is a device for earthing the rotating shaft to the Wayne-Kerr meter. Originally an elaborate device was made for playing a jet of mercury, connected to earth, onto the end of the shaft, collecting it and recirculating it to a reservoir above the rig. However, this was not very safe since a certain amount of toxic mercury always escaped, and a much simpler idea was conceived. This was simply to fill mercury nearly to the open end of a glass tube which was then placed at a small angle above the horizontal close to the end of the shaft. The surface tension of the mercury held it in the tube and a small needle projecting from the end of the rotor into the mercury made the earth contact.

At the other end were the shaft location thrust bearing and the

phase-angle and speed measuring unit. The whole rig was tilted by 5° so that the rotor rested positively against the thrust bearing. This was 5/8 in diameter with a .013 in feed hold feeding into a small pocket, and normally had a supply pressure of 20 p.s.i.g. It was not easy to get this screwed in exactly parallel to the end of the rotor, so it was lapped in situ by a small disc of self adhesive abrasive paper stuck onto a spare rotor and run against the thrust face.

The thrust face was mounted in the body of the speed and phase measuring unit. This consisted of a photo diode which picked up the light reflected by a half black half white disc on to the end of the rotor from a light source in the body of the unit. Because of the thrust bearing, only the outside 1/16 in of the rotor end could be used but this proved to be quite sufficient. The signal was of square wave form and could not only be used for speed measurement, but the leading edge gave a reference point on the shaft corresponding to the black/white boundary. The body of the unit can be rotated so this reference enabled phase angle measurements to be made, reading off a scale on the outside edge of the body.

Since static loads could not be hung downwards from the shaft for aerostatic stiffness measurement, a loading gantry was built so that wires from the shaft could be passed over pullys and weights hung from them, thus loading the shaft upwards. This has the advantage

that by balancing the shaft weight a zero load can be applied to the bearings.

5.3. Rotor Design.

Again from the original standpoint of possible rotational speeds of up to 300,000 rpm a rotor length had to be chosen which would not exhibit a mechanical bending resonance within that frequency. In general the shaft will not behave as either a 'pinned-pinned' or a 'free-free' beam unless the centre of support happens to act at the free-free node. With the present layout the centre of the bearing was 1 in from the end of the shaft, and this would be outside the free-free node for all except very short rotors. As the pinned-pinned condition gives the lower critical frequency, the first calculation was to find the length of rotor which would have a critical at 5000 c/s, assuming it to vibrate as a pinned-pinned beam of length equal to the bearing centre distance.

The formula for the critical frequency is

$$f_c = \frac{\pi}{\ell^2} \left| \frac{EIg}{\pi D^2 \rho} \right|^{\frac{1}{2}} \quad c/s \qquad 5.1.$$

where E is Youngs Modulus

I is the polar moment of inertia

ρ is the density of the shaft material

g is the acceleration due to gravity

D is the shaft diameter

ℓ is the length between bearing centres.

From this is obtained a length ℓ of 4.2 in which represents a total shaft length of 6.2 in.

Now assuming a shaft length of 6 in the nodal points for the free-free case may be calculated (ref.28) and these are found to be stationed 1.4 in from the shaft end, i.e. 0.4 in inside the bearing centres. However, the restraint on the shaft by the gas film acting at the bearing centres would not be enough to shift the real nodal points very much, so that the free-free case must give a good representation of the critical frequency in this case.

The formula giving the critical frequency is now taken to be

$$f_n = \frac{3.56}{\ell^2}\left[\frac{4EIg}{\pi D^2 \rho}\right]^{\frac{1}{2}} \quad c/s \qquad 6.2.$$

which gives a calculated natural frequency of 5,300 c/s - above the desired speed of 300,000 rpm. The resonance would not be highly damped, so its effect would only be felt over a small frequency range close to the critical.

The rotor length and bearing spacing also determines whether the rotor will exhibit a resonance to translational or conical forcing first, and whether its free vibrations will be in the cylindrical or conical mode. In practice it is much easier to work with the

cylindrical mode since no problems then arise about the combined linear/angular properties of the bearing, even though with the geometry used here, the angular tilt of the rotor in conical motion is likely to be small.

A simple check may be made to determine the ratio of the natural frequency of one mode relative to the other.

We assume a stiff rotor supported in two discrete springs of stiffness K spaced a distance 2J, the bearing separation, apart.

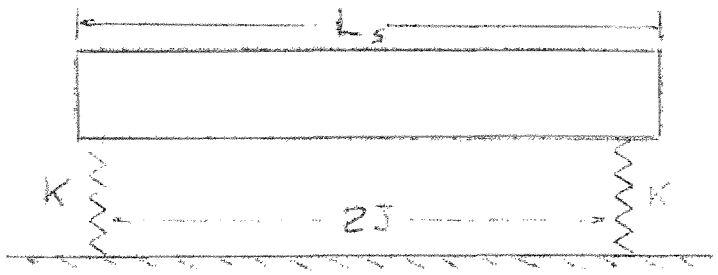

Neglecting damping in the bearings, we may write the equation of motion of the rotor for free vibrations in the translational and conical modes respectively

$$m\frac{d^2y}{dt^2} + 2Ky = 0 \qquad 6.3.$$

$$\left(I_T - \frac{I_o}{Q}\right)\frac{d^2\theta}{dt^2} + 2KJ^2\theta = 0 \qquad 6.4.$$

where m is the mass of the rotor

I_T is the transverse moment of inertia.

I_o is the polar moment of inertia.

y is the translational displacement of the rotor axis

θ is the angular displacement of the rotor axis

Q is ratio of vibration to shaft rotational frequency.

Solutions of these equations yield the natural frequencies of vibration

Cylindrical $$\omega^2_{nCYL} = \frac{2K}{m} \qquad 5.5.$$

Conical $$\omega^2_{nCON} = \frac{2KJ^2}{I_T - I_o/Q} \qquad 5.6.$$

Thus the ratio $$\frac{\omega_{nCYL}}{\omega_{nCON}} = \sqrt{\frac{I_T - I_o/Q}{J^2 m}} \qquad 5.7.$$

For the case of synchronous vibrations with a 6 in long 3/4 in diameter rotor

$$Q = 1$$

$$I_T = m\left[\frac{L^2}{12} + \frac{R^2}{4}\right]$$

$$I_o = \frac{mR^2}{2}$$

$$\frac{\omega_{nCYL}}{\omega_{nCON}} = \sqrt{\frac{(6)^2/_{12} - (.375)^2/_4}{(2)^2}}$$

$$\omega_{nCYL} = 0.86\ \omega_{nCON}$$

i.e. the natural frequency for synchronous conical motions should be 1.16 times higher than that for cylindrical. This would decrease as the rotor length was reduced, the two modes being superimposed on one another at a length of 4.6 in. This theory slightly underestimates the conical frequency since it does not count the additional bearing stiffness due to the small rotor tilt.

The onset of unstable vibrations also has its mode defined from this analysis in both the hybrid bearing case and the aerodynamic case, since it is by definition a condition of zero damping. Here the vibration frequency is usually half of the rotational frequency, i.e. $Q = \frac{1}{2}$ so for the rotor defined above the ratio becomes

$$\frac{\omega_{nCYL}}{\omega_{nCON}} = .732$$

The material used for the rotors was 'stubs' silver steel. The first rotors used were bought ready ground close to size, and just had buckets milled into them and final sizing with the external hone. However, this highlighted a problem associated with the rig design. The rotors rotate about an axis through the centres of the bearing sleeves, and any slight bend in a rotor produces a synchronous rotating shaft eccentricity under the shaft motion capacity transducers. This is not thought to seriously affect the bearing performance, but it makes measurements of rotor deflections within the bearing more difficult. It was thought that breaking the surface of the ready

ground material right in the centre was the principal cause of this bending, so all later rotors were machined out of 1 in diameter silver steel bar, the buckets cut and then allowed to age before final machining. This improved matters considerably, but did not cure the trouble, which had eventually to be overcome by electronic modification of the probe signals and also by straight measurement and subtraction. The final set of rotors used for the experiments were finish gound by Westwind Turbines Ltd. with an air bearing grinding machine, parallel within 0.00005 in. The straightness was such that an out-of-straight synchronous vibration of .00008 in was still present, but no out-of-round was detectable at all. Surface finish was measured on a Talysurf as 6μin C.L.A. Unfortunately whilst the journal dimensions were good there was up to 1/16 in variation in length which caused the mass of each to vary slightly.

The mean diameters as measured by Solex air gauging and masses of the rotors numbered from 1 - 6 are given in table 6.1.

Rotor No.	Mean Diameter.	Mass.
1	0.74945 in	.75 Lb
2	0.7492 in	.75 Lb
3	0.7489 in	.75 Lb
4	0.7486 in	.74 Lb
5	0.7482 in	.74 Lb
6	0.7459 in	.74 Lb

The balance of the rotors was extremely good after the grinding operation and they were not touched until it was required to unbalance them. Then holes were drilled at approximately 1/3 stations and tapped 4BA, the depth being adjusted until with standard 4BA socket head grub screws inserted to just below the surface, a rough state of balance was obtained.

The rotors were now placed in an aerostatic bearing rig similar in principle to the main experimental rig, but having capacity probes mounted at the centre of the bearing sleeve, and a large diametral clearance - between .004 in and .008 in depending on the rotor. This gives low damping which means that displacement is nearly in phase to the out-of-balance force for speeds below the resonance. The rotors were then run up and the angular position of the out-of-balance noted relative to the black/white disc on the end of the shaft. The principal out-of-balance was cylindrical (static) and the rotors were first treated for this, initially the grub screws being adjusted, and then metal removed at 90° stations in the plane of the grub screws. This was done until when checked at the cylindrical resonance the rotor appeared balanced. Since the damping was kept low, the two resonances of the cylindrical and conical vibration modes could be treated as if no interaction took place by approaching the cylindrical resonance from the low speed side and the conical resonance for the high speed side where the conical (dynamic) out-of-

——————— Cylindrical response to static unbalance.

- - - - - - - Conical response to dynamic unbalance.

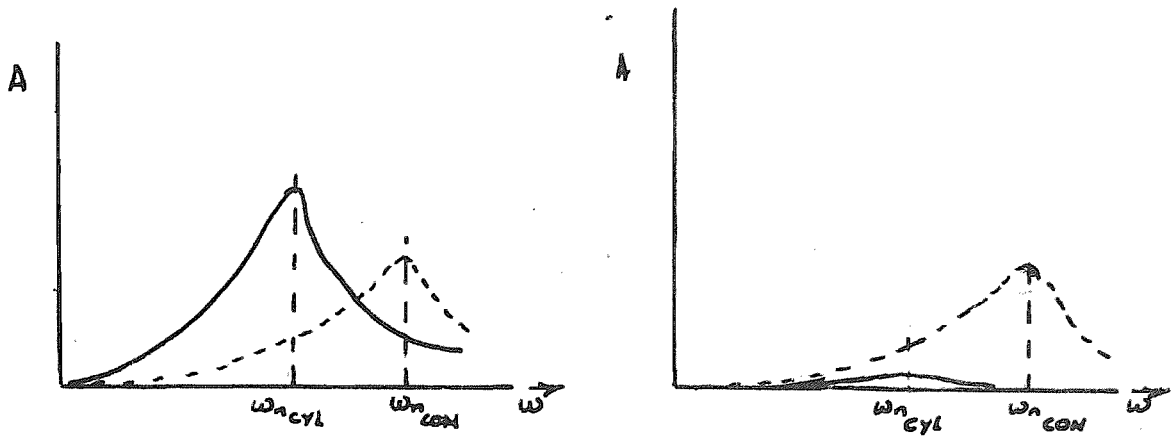

Initial

After static balancing.

balance forcing is 180^{o} out of phase with the displacement. Once the rotor is well balanced in the cylindrical mode, there is virtually no response at all from this mode above the conical resonance. By similarly adjusting the grub screws and removing metal the rotors were then dynamically balanced. The residual unbalance after this process was in all cases better than $0.75.10^{-5}$ Lb-in, equivalent to a mass shift of 10^{-5} in or 10% of the lowest unbalance used in the experimental work. It should be noted that for the purposes of balancing in a gas bearing, the further separated the modes are the better. Also the mode occurring first should always be treated first since after resonance its response amplitude tends to a constant value, equal to the distance between the geometric and mass axes.

5.4. Bearing Design.

The bearing sleeves (fig. 5.1.4.) were made of brass to give reasonable rubbing properties with the steel shafts. The length to diameter ratio was two and all tests were conducted with bearings using a central row of six annular, 0.014 in nominal diameter feed holes. It was recognised that the simple orifice feed holes exhibit a higher load capacity, but with a diameter of $\frac{3}{4}$ in they would be more difficult to manufacture. These holes were drilled with a No. 80 drill without a special drilling machine, and whilst an airflow check indicated that the mean of all six holes was approximately correct, there was some variation in the individual holes.

Originally the bearing bores were produced by boring close to size on the lathe, and then finishing with a honing machine. However, with this process it did not appear possible to produce bearing sleeves within 0.0003 in of roundness and parallel, or to produce pairs with matched mean diameters. This was overcome by the purchase of 'Ergis' internal laps, which are mechanite cylinders having a tapered bore. The cylinder has a helical slot down its length and by knocking it along a mandrel with a matched taper, the outside can be expanded perfectly round and parallel. Two grades of diamond lapping paste are used to give different cutting rates. Using these it became possible with some care to produce bores within .0001 in in roundness parallel and matching.

The first pair of lapped bearings not having the 'O' ring mounting shown in Fig.5.1.1. were an interference fit in the bearing housing. It was found that some distortion took place on clamping up and they were relapped in position. This then looked all right but two weeks later they were re-examined and found to have become .0005 in out of round. Thus the final bearing sleeves used had honed outer surface, and the bearing housing was honed to take them with a .0001 in interference, the bores finally lapped after clamping up again. This proved to be quite satisfactory, no further distortion taking place.

Two pairs of bearings sleeves have been used for this work since the first were wrecked when the air supply line blew off with the rotor running at high speed. Their mean diameters as measured by the Solex air gauge are as follows:-

		Mean diameter
1st Pair	Left Hand	0.75045 in
	Right Hand	0.75045 in
2nd Pair	Left Hand	0.7506 in
	Right Hand	0.75055 in

Thus the following radial clearances were available at the left hand bearing for the experiments, using the set of six rotors (i and ii refer to the two different bearings)

Rotor		Radial Clearance inches
1	i	0.00050
	ii	0.00057
2	i	0.00062
	ii	0.00070
3	i	0.00077
	ii	0.00085
4	i	0.00092
	ii	0.00100
5	i	0.00112
	ii	0.00120
6	i	0.00227
	ii	0.00235

Each time a new pair of bearings was installed, they had to be aligned in two planes, as parallel to the shaft as possible. The original intention had been to build an alignment bar of the same dimensions as the rotors, incorporating two capacity probes, one at each end of a bearing. This would have been floated on the gas film and slowly rotated, giving an exact measurement of the degree of misalignment. This was designed but never manufactured, and alignment was carried out by measuring the available side-to-side movement of a known diameter shaft in two planes, the bearings being moved in their spherical mountings by tapping in the direction giving larger movements. With patience it proved possible to

achieve between 80% and 90% of the available movement in all directions. This was probably not held at all times since replacing rotors could produce small bearing movements, but no change in performance was observed.

5.5. Instrumentation.

The objectives of the experimental work were to observe and measure the deflections and vibrations of the rotor under varying conditions, to know the speed of rotation and the phaseing of vibrations relative to the forces producing them.

The movements of the shaft were all measured using the Wayne-Kerr B731A capacity probe system, the principle of which is laid out in Appendix I. Two meters were used in conjunction with the four shaft probes, the left hand vertical probe being fed directly to one meter, whilst the other three were fed via a multi-way switch to the second. Probes having an electrode diameter of .063 in were used giving a full scale deflection on the output meters of 0.002 in, and the meters could easily be read to an accuracy of 2×10^{-5} in, although the quoted accuracy of the instrument is 5×10^{-5} in. Some care has to be taken when using flat surface probes relative to a curved surface. Reference 32 shows that the meter reading is considerably different from the actual spacing for small diameter shafts, but indicates that the difference is constant for all distances. Thus if only differences of distance reading are taken no inaccuracy

is incurred, and the vibration meter does this anyway. The information presented in ref. 32 does not quite go down to 0.75 in diameter so a probe was checked against a large diameter barrel micrometer with a piece of $\frac{3}{4}$ in diameter shaft attached, and the readings agreed exactly above 30% of the full scale meter reading. In practice, on the rig it was not possible to get the probe face parallel enough to the shaft to read below 30% of f.s.d.

The output of the vibration signal of the Wayne-Kerr meter is in the form of a 50 kc/s carrier wave modulated by the vibration waveform. In order to display this on an oscilloscope for observation or measurement, it is necessary to filter out the 50 kc/s signal leaving the vibration wave-form only. The filter circuit designed by Dr. McLachlan is shown in Appendix I, where it may be seen that the output amplitude is less than 2% below the input.

The signals were monitored and in some cases measured on a Tektronix 502A oscilloscope. The two series of vibration decay curves were photographed on Polaroid Land film, which gave a print of the oscilloscope trace within 10 seconds of exposure. Thus satisfactory recordings could be obtained at each condition before passing on to the next.

Accurate speed measurement was achieved by forming a lissajous figure on the oscilloscope between a synchronous shaft signal and the output of a 1% accurate Marconi TF1101 oscillator. By adjusting the

frequency of the oscillator to maintain a single loop lissajous figure, the exact frequency of an event such as the onset of half speed whirl could be obtained, and was recorded until the oscillator was adjusted again. It was also possible to measure the frequency of whirl where this was different to one half by following the rotor speed with a half-frequency lissajous loop, and at the onset of whirl searching back until a matched frequency loop was obtained. For constant monitoring of rotational speed, a Southern Instruments M48 tachometer was used, having scale readings 0 - 30,000 rpm 0 - 100,000 rpm and 0 - 300,000 rpm. The input signal was the square wave obtained from a photo-diode which was pulsed by reflected light from a half black half white disc on the end of the rotor. It was fed into the Southern tachometer from which it gets its power supply, but since the photo-diode output is very small a transistor amplifier stage is used at the back of the block before the transmission cable. For monitoring and other purposes the square wave signal is picked out of the tachometer after further stages of amplification within the instrument.

For phase measurement the technique used has been to feed the square wave, further amplified to 25 volts on to the C.R.T. cathode which modulates the trace brightness produding a bright spot on the trace when the rotating black/white disc changes from black to white or vice versa depending on the polarity of the amplification. In

fact the change from white to black, the trailing edge of the square wave, was used because the leading edge became ill defined at high frequencies. By rotating the body of the photo-diode unit the spot could be moved relative to the trace until it occupied the desired position, when the relative phasing could be directly read off the scale on the body.

The problem of the out-of-straight rotor synchronous amplitude signal was solved for tests not involving phase measurements by use of the square wave output from the tachometer. This was by using a tuneable filter which removed all the harmonics which make up a square wave, and left only the fundamental sine wave at rotor frequency. This could be attenuated to the same level as the out-of-straight Wayne-Kerr signal, and its phase adjusted to be the same by rotating the phase block. It is then fed into the second input on the oscilloscope and by switching in the common mode rejection facility, the out-of true signal is cancelled, leaving any other signal to be measured on its own. Without building one of these units for each end of the rotor, this method could not be used for out-of-balance testing since the unit is then required for phase measurement.

The air supply was obtained from either a small 100 psi or a larger 150 psi compressor. It passed through a filter-drier unit before being distributed to the various control valves. This meant that the turbine air passed through the filter unit together

with the bearing supplies making for more efficient filtration. All the valves used were Norgren regulator valves, small ones being used for the bearing and thrust supplies whilst a large sensitive regulator was used for the turbine for accurate control of speed. The bearings were arranged so that they could either be fed together on the same valve and pressure gauge or on two separate systems, and pressures between zero and 80 psig used. The turbine had three symmetrically spaced jets fed by a single input, an on-off tap being placed between the pressure regulator and the turbine for rapid control. A general view of the electronics and air control arrangements may be seen in Fig.5.15.

6.

THE AEROSTATIC BEARING PERFORMANCE

6.1. Introduction.

The theory for the aerostatic bearing as presented here is based on the work by Shires[24-27] and Robinson and Sterry[23]. This is by no means new and is only an approximate, lumped parameter analysis, but to the author's knowledge has not been superseded by anything more accurate. Distributed parameter analyses have been attempted assuming the feeding to be a line source around the bearing, but this also represents a considerable approximation unless large numbers of feed holes are being used. For hybrid bearings with low clearances, many feed holes mean the use of very small feed hole diameters which are not practicable. The claimed accuracy of the theory presented is around 10% on load capacity (Shires[27]), although since most experimental work has been performed on simple orifice bearings it is not clear whether this claim also relates to annular feed hole bearings. However, in general it will not be possible, without very special attention, to produce bearing systems having the physical accuracy to provide performance better than this.

The mode of operation of an aerostatic bearing has been given in Section 2.3. and the method of examining the performance of a

particular bearing sleeve with varying clearances and supply pressures will be presented in the next section. This is the type of analysis which would be necessary for selecting limits in a practical gas bearing machine. The performance aspect chosen for examination is the radial stiffness of the gas film, since this is required in the later work, and is far easier to measure in practice than load capacity.

6.2. Theoretical Analysis.

The method of analysis is to consider each of the feed holes round the bearing to feed into a discreet slot of width a and depth h. The shaft centre is displaced by the load W distance εc from the bearing centre where ε is the eccentricity c is the radial clearance. The local clearance at any point h can be approximated by $h = c(1-\varepsilon\cos\theta)$, θ being the angular displacement from the line of centres.

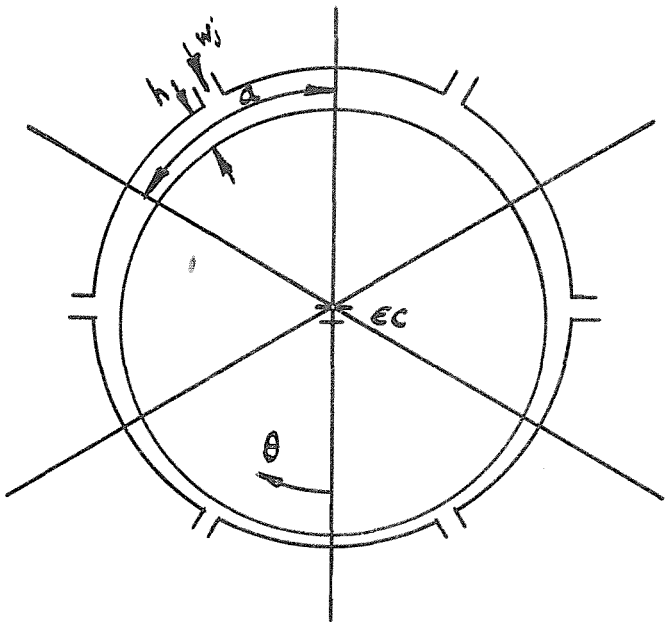

With a single row of feed holes, the air flow through a jet, W_j,

divides into two, half flowing each way through the slot (length ℓ) to atmospheric pressure. The pressure profile in each slot can be found, and thus the net pressure force acting to oppose the load, by equating the air flow in the clearance space to that in the jet. Initially only axial flow is considered, but clearly with a pressure differential around the bearing there will be circumferential flow. This will be accounted for by a semi-empirical expression derived in Ref (26) which is applied to the load capacity as found below.

If p_s is the air supply pressure to the feed hole and p_d is the exhaust pressure from the feed hole into the clearance space, the expression for the flow is

$$W_j = C_D A \rho_s \sqrt{2gRT_s} \left\{\frac{\gamma}{\gamma-1}\left[\left(\frac{p_d}{p_s}\right)^{2/\gamma} - \left(\frac{p_d}{p_s}\right)^{\frac{\gamma+1}{\gamma}}\right]\right\}^{\frac{1}{2}} \qquad 6.1.$$

where C_D is the discharge coefficient

A is the feed hole area

ρ_s, T_s are the upstream density and temperature

R is the gas constant

γ is the ratio of specific heats (1.41 for air).

For laminar flow the pressure drop along a slot length

ℓ, width a, height h for a gas flow $w_j/2$ is given by

$$p_d^2 - p_a^2 = \frac{12\mu RT\ell w_j}{ah^3 g} \qquad 6.2.$$

where μ is the viscosity of the gas.

With the jet and slot in series, we can substitute for w_j in equation 6.2 to get an expression for the pressure at the centre of the bearing, p_d, in terms of the local clearances h and the supply pressure p_s.

$$p_d^2 - p_a^2 = \frac{p_s \cdot 12\mu\sqrt{2gRT}}{g} \cdot \frac{\ell C_D A\sqrt{\gamma}}{ah^3} F(\gamma,K) \qquad 6.3.$$

where $$F(\gamma,K) = \left[\frac{1}{\gamma-1}\left\{(K)^{2/\gamma} - \left(K\frac{\gamma+1}{\gamma}\right)\right\}\right]^{\frac{1}{2}}$$

$$K = p_d/p_s$$

and $$p_s = \rho_s RT_s$$

Now for an annular orifice bearing the feed hole area

$$A = \pi\, d\, h$$

where d is the feed hole diameter.

The value of the discharge coefficient C_D is in some doubt, but it has been shown[5] that for the annular orifice bearing it is in the region of 0.9. With the following parameters specified as follows -

$$d = .014 \text{ in}$$

Bearing Diameter $D = 0.75$ in

Number of feed holes $n = 6$

$$a = \frac{\pi D}{n}$$

Bearing Length $L = 1.5$ in

$$\ell = \tfrac{1}{2}L = 0.75 \text{ in}$$

$$R = 53.3 \text{ ft Lb/lb } {}^{o}R.$$

$$T = 520 \ {}^{o}R$$

$$\gamma = 1.41$$

$$p_a = 14.7 \text{ Lb/in}^2$$

$$\mu = 2.62.\ 10^{-9} \text{ LbSec/in}^2$$

the pressure equation becomes :-

$$p_d^{\,2} - p_a^{\,2} = \frac{4.51\ 10^{-5}\ p_s\ F(\gamma K)}{h^2} \qquad 6.4$$

A useful parameter for gas bearing work has been found to be the gauge pressure ratio defined as

$$K_g = \frac{p_d - p_a}{p_s - p_a}$$

Thus a graph relating K_g to clearance can be constructed and is given in Fig. 6.2.1. for gauge values of supply pressure of 10, 30, 50 and 80 Lb/in^2, which are those used later in the experimental work.

The pressure in the slot falls parabolically from p_d to p_a, so

the mean pressure in each of the slots can be expressed in terms of the K_g for each slot. The vertical component of each slot pressure can now be summed to give the net load capacity. The general expression for this is given by ref.(23)

$$C_L = 2 \sin \frac{\pi}{n} \left(1 - \frac{2\ell}{3L}\right) \left[K_{g_1} \cos \frac{\pi}{n} + K_{g_2} \cos \frac{3\pi}{n} + \text{---} + \text{---} K_{g_{N/2}} \cos \left(\pi - \frac{\pi}{n}\right)\right] \qquad 6.5.$$

where C_L is the load coefficient

$$C_L = \frac{W}{LD\ (p_s - p_a)}$$

K_{g_1} is the gauge pressure ratio at the first feed hole round from the datum ($\theta = 0$) etc.

Up to this point the flow has been considered to be entirely axial. However circumferential flow will considerably reduce the load capacity and a semi-empirical formula relating the real load capacity C_{L_o} to the axial flow value C_L has been derived by Shires[26].

$$\frac{C_{L_o}}{C_L} = .315 \frac{\left[\dfrac{\cosh\ (6.36\ell/D) - 1}{\sinh\ (6.36\ell/D)} + \tanh\ \left(6.36\ \dfrac{L-2\ell}{2D}\right)\right]}{\dfrac{L-\ell}{D}} \qquad 6.6.$$

For the parameters used

$$C_{L_o} = 0.314\ C_L$$

Some caution should be exercised when using this for the multiplying factor was derived experimentally for an 8 feed hole bearing.

For convenience of computation of C_{L_o} the datum, $\theta = 0$, is taken in between the feed holes as shown in the diagram on p. 82. The result is plotted against a parameter K_{g_o} which is the gauge pressure ratio existing throughout the bearing at zero eccentricity (i.e. for $h = c$.) and represents the feeding parameter. Figure 6.2.2. shows this for three values of eccentricity, and for $\varepsilon = 0.9$ the effect of supply pressure variation is indicated. This is small at $\varepsilon = 0.9$ and is considered negligible at the lower eccentricity ratios.

Robinson and Sterry [23] stated that the position of the datum $\theta = 0$ had little effect on the load coefficient, but further work by Munday [18] indicated that for the six feed hole bearing at $\varepsilon = 0.9$ the maximum value of C_{Lo} can vary by 6% and can occur at anything between $K_{g_o} = 0.2 - 0.5$ depending on selection of θ. For smaller numbers of feed holes the distintion becomes marked, even for lower eccentricities where the six feed hole case is independent of datum selection. However, if this should be important experimentally, the test bearings were all orientated as shown on page 82.

From Figure 6.2.2. a load-deflection curve would show that stiffness is approximately constant up to an eccentricity of 0.6. The zero eccentricity stiffness is presented in non-dimensional form C_{L_o}/ε vs K_{g_o} in Figure 6.2.3., but this does not yield much informa-

tion about the variation of stiffness with changes of clearance or pressure, since both C_{L_o}/ϵ and K_{g_o} are functions of these.

$$\frac{C_{L_o}}{\epsilon} = \frac{W}{LD\ (p_s - p_a)} \frac{c}{e}$$

where deflection $e = \epsilon c$

Hence the actual stiffness

$$K_s = \frac{W}{e} = \left(\frac{C_{L_o}}{\epsilon}\right) \cdot \frac{LD\ (p_s - p_a)}{c} \qquad 7.7.$$

By considering only clearance to make K_{g_o} change (at each value of supply pressure) and using Figures 6.2.1. 6.2.3. a graph of stiffness vs K_{g_o} is constructed, Fig. 6.2.4. This shows clearly that maximum stiffness occurs at higher K_{g_o} the maximum load. This if of importance where feed holes are as small as can be made, and small clearances are required to minimise airflow or to increase hybrid properties. It should be noted that if the feed hole size is changed at fixed clearance also changing the value of K_{g_o}, the stiffness curve shape will be that shown in Fig.6.2.3. A $K_{g_o} = 0.8$ represents maximum stiffness for a given feed hole size but $K_{g_o} = .5$ gives maximum stiffness for any clearance where the feed hole can still be optimised, and now the smaller the clearance the higher will be the stiffness, since the maximum C_{L_o}/ϵ stays constant at .204.

Derived from Fig.6.2.4., Figure 6.2.5. shows how changing pressure affects the $K_s - K_{g_o}$ curve at various clearances. Increasing the supply pressure always increases the stiffness, the highest stiffness thus occurring, with fixed bearing parameters, as K_{g_o} tends to zero. However, readjusting the bearing parameters to bring K_{g_o} back to 0.55 always raises the stiffness back to its maximum value at that pressure. It is observed from equations 6.3. and 6.6. that changing L or D have a similar but not the same effect. Changing any other parameter not occurring in equation 7.6. may change the value of maximum stiffness but not the value of $K_{g_o} = 0.55$ at which it occurs. A three dimensional presentation derived from these two graphs shows the actual variation of stiffness with clearance and pressure (Fig.6.2.6.) over the range covered in the experimental work. It may be seen that as pressure is reduced the clearance for maximum stiffness increases, but also the sharpness of the peak diminishes, so that if a bearing is designed for maximum stiffness at the highest pressure to be used, it will be fairly close to the optimum for all lower pressures.

6.3. Experimental Measurement of Stiffness.

Apart from the fact that stiffness is specifically needed for later experiments, it provides by far the easiest parameter with which to compare theoretical predictions with practical bearings. This is because of the necessity when measuring load capacity to be able to

define a zero eccentricity and for this to represent the zero load condition. The first is relatively straightforward since the mean of the top to bottom movement of the rotor gives the zero eccentricity at the centre of the bearing. However, with a misaligned bearing it should be remembered that the effective eccentricity increase will be greater than with one parallel to the shaft, and non-linearities will become apparent sooner. The second condition is more difficult since without special equipment some variation in feed hole size is inevitable, and at zero load the shaft will assume an eccentric position. It is now difficult to relate experimental results to the theory.

Stiffness, on the other hand, being constant up to medium eccentricities does not suffer from a small zero load displacement. Some misalignment will alter the eccentricity at which the stiffness starts to fall off, but again will not affect it at low eccentricities.

Experimentally therefore it is neither necessary to know the initial load e.g. in a self loaded system, provided that this is small, nor the initial eccentricity, subject to the same condition. All that is necessary is to know the change in deflection that this produced.

This was done for each new set of bearing sleeves used for all the rotors at the four test pressures - 10, 30, 50 and 80 psig. A

gantry was used and the load applied upwards by wires passing over pullys and attached to dead weights. Thus the initial load was negative (the shaft weight) so stiffness was measured through the zero load position. It was soon discovered that due to feed hole errors the stiffness could differ considerably. Later a bearing sleeve was dissected and the feed hole sizes measured using a travelling microscope. A set of six revealed a 10% variation about the mean which was slightly below .014 in. For the first pair of bearings specified on page 74 independent loads were applied to each end of the shaft to ensure that each bearing was being loaded uniformly. This was found not to be necessary for the second pair. This time, however, it was considered important that the aerostatic performance of each bearing be as similar as possible, so the pressure of the right hand bearing was adjusted to give uniform stiffnesses at each end; the overall stiffness was then the same as that of the left hand bearing.

A sample set of readings out of more than a dozen such sets is presented in table 6.1. (for the first pair of bearings). The applied load is that for each bearing, so that the stiffness of each is calculated from the delfections and this load.

Table 6.1.

Load - Deflection readings for rotor 4

Bearing Diameter 0.75045 in.

Mean Clearance = .0009 in.

Using .002 in probes, a meter reading of 10 represents .002 in deflection. The probes were always set at 10 for zero applied load.

Applied Load Lb	Left Hand Bearing Meter Reading	Left Hand Bearing Deflection in x 10^{-5}	Right Hand Bearing Meter Reading	Right Hand Bearing Deflection in x 10^{-5}
p_s = 30 psig				
0	10	0	10	0
1	9.25	15	9.3	14
2	8.2	36	8.6	28
p_s = 50 psig				
0	10	0	10	0
1	9.55	9	9.6	8
2	9.05	19	9.2	16
3	8.55	29	8.8	24
4	8.0	40	8.3	34
5	7.0	60	7.8	44
p_s = 80 psig				
0	10	0	10	0
1	9.7	6	9.75	5
2	9.35	13	9.4	12
3	9.0	20	9.1	18
4	8.6	28	8.8	24
5	8.15	37	8.45	31
6	7.9	42	8.15	37
8	7.1	58	7.4	52

These figures are plotted in Fig.6.3.1a and the stiffnesses calculated from the linear portion of the load deflection curves are as follows.

Table 6.2.

Supply Pressure psig	Stiffness Lb/in Left Hand Bearing	Right Hand Bearing
30	6×10^3	7×10^3
50	10.3×10^3	$1[illegible].5 \times 10^3$
80	14.4×10^3	16.7×10^3

These are plotted against pressure in Fig.6.3.1.b. The complete set of stiffness results obtained by this method, for the first pair of experimental bearings is presented in Table 6.3.

Table 6.3.

Supply Pressure psig	Stiffness Lb/in ($\times 10^{-3}$) 10		30		50		80	
BEARING Clearance in	L-H	R-H	L-H	R-H	L-H	R-H	L-H	R-H
.0005							15	25
.0006			2.2?	6.0	13.2	27.2	30.0	
.0007			8.7	8.7	15.5	21	25	32.7
.0009			6.0	7.0	10.3	12.5	14.4	16.7
.0011	1.25		5.25		7.0		9.25	
.00235	0.6		1.26		1.8		2.46	

The results for the second pair of bearings are presented in table 9.1. page 160.

Clearly at low clearances, some of the stiffnesses are very different between the two ends. Since this pair of bearings had very well matched bore diameters, and the alignment allowed better than 80% of movement in all directions, it is reasoned that feed hole differences must cause the variations. At large clearances where the feed holes are mostly choked little effect on stiffness is noticed.

The mean of these results, the results obtained for the second pair of bearing sleeves, and some other stiffness results obtained during preliminary experiments with the rig are compared to the theoretical prediction in Figure 6.3.2. The correlation is good at low pressures and large clearances, but in general agreement is within 20% which is not as good as that claimed by Shires[27], but not surprising in view of the uncertain feed hole sizing.

7.

FREE SHAFT VIBRATIONS WITH NO ROTATION.

7.1. Introduction.

The first set of dynamic vibration measurements follows from the static loading tests and concerns the response to an impulse loading with the rotor floating on an aerostatic air film but not rotating. This case is not of great practical importance except in certain limited cases, but it leads on to the very important section concerning the free vibrations of rotating shafts under hybrid conditions. The vibrations for the non-rotating case will be only in the plane of the impulse load since it is only with rotation that a film force is generated normal to the displacement, causing an orbital vibration.

It has been postulated that a possible approach for the analysis of the externally pressuzed hybrid bearing is to consider the aerostatic and aerodynamic pressures to be generated independently of one another and their effects to be additive. This can also be applied to the externally pressurized bearing with vibration where the aerodynamic component is considered as the pure squeeze film force. It is thus possible to calculate theoretical stiffness and damping values for the translational vibration mode of the experimental system, and compare these with actual measured values. With

the bearings loaded only by the rotor weight these results would be at low eccentricities, but it had been found during the static loading tests that provided the applied loads were effectively decoupled from the rotor, the film stiffness and damping properties could be found also at the various eccentricities provided by the applied loads.

7.2. Theoretical Analysis.

The aerostatic stiffness, required for the postulated method of analysis, need not be calculated since measured values are available, and it is assumed that the pressure feeding does not contribute to the damping. This leaves the aerodynamic squeeze film force to be calculated.

The mathematical model governing all bearing film conditions is the Reynold's equation, already derived in its general form (equation 3.2.6.). Ignoring the effects of pressure feeding and assuming the condition of planar vibrations and no shaft rotation the Reynold's equation becomes

$$\frac{\partial}{\partial\phi}\left[\bar{h}^3\bar{\rho}\,\frac{\partial\bar{p}}{\partial\phi}\right] + \left(\frac{R}{L}\right)^2 \frac{\partial}{\partial\zeta}\left[\bar{h}^3\bar{\rho}\,\frac{\partial\bar{p}}{\partial\zeta}\right] = \frac{\sigma}{\omega_1}\frac{d}{dt}\,(\bar{\rho}\bar{h}) \qquad 7.2.1.$$

where $\sigma = \dfrac{12\,\mu\omega_1}{p_a}\left(\dfrac{R}{C}\right)^2$ the Squeeze Number

$\bar{h} = c(1-\varepsilon\cos\phi)$

where $\varepsilon = \varepsilon_o + \varepsilon_1 e^{i\omega_1 t}$

ε_o being the static eccentricity ratio and ε_1 a small dynamic variation at vibration frequence ω_1

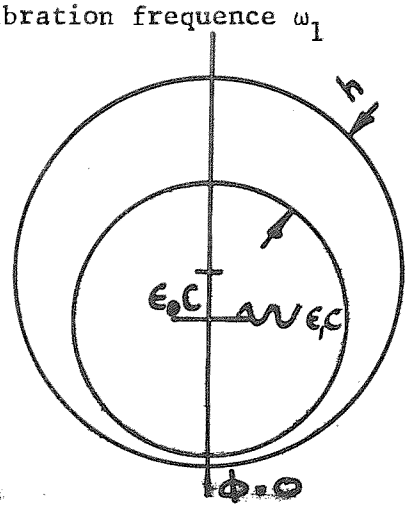

For the low squeeze numbers expected in the experimental system it is possible to assume the lubricant to be incompressible and the Reynold's equation then reduces to

$$\frac{\partial}{\partial\phi}\left[\bar{h}^3 \frac{\partial\bar{p}}{\partial\phi}\right] + \left(\frac{R}{L}\right)^2 \frac{\partial}{\partial\zeta}\left[\bar{h}^3 \frac{\partial\bar{p}}{\partial\zeta}\right] = \frac{-\sigma}{\omega_1}\left[\frac{d\varepsilon}{dt}\cos\phi + \varepsilon\sin\phi \frac{d\phi}{dt}\right] \qquad 7.2.2.$$

Now with only planar motion $\frac{d\phi}{dt} = 0$

Also $\frac{d\varepsilon}{dt} = \varepsilon_1 \, i \, \omega_1 e^{i\omega_1 t}$.

$$\therefore \quad \frac{\partial}{\partial\phi}\left[\bar{h}^3 \frac{\partial\bar{p}}{\partial\phi}\right] + \left(\frac{R}{L}\right)^2 \frac{\partial}{\partial\zeta}\left[\bar{h}^3 \frac{\partial\bar{p}}{\partial\zeta}\right] = -\sigma \, \varepsilon_1 i \, e^{i\omega_1 t} \cos\phi \qquad 7.2.3.$$

Since both positive and negative pressures exist in an aerodynamic journal squeeze film, the pressure gradients circum-

ferentially are greater than the axial gradients where all flow is to ambient. Thus to obtain a closed analytic solution the further assumption is made that no axial pressure gradients exist: i.e. the infinitely long bearing solution.

$$\frac{\partial p}{\partial \zeta} = 0$$

$$\frac{\partial}{\partial \phi}\left[\bar{h}^3 \frac{\partial \bar{p}}{\partial \phi}\right] = -\sigma \varepsilon_1 i e^{i\omega_1 t} \cos\phi \qquad 7.2.4.$$

for convenience let $\sigma \varepsilon_1 i e^{i\omega_1 t} = q$ and integrate equation 7.2.4. with respect to ϕ

$$\bar{h}^3 \frac{\partial \bar{p}}{\partial \phi} = -q \sin\phi + C_1 \qquad 7.2.5.$$

where C_1 is a constant

Now by symmetry at $\phi = 0$ and π, $\frac{\partial \bar{p}}{\partial \phi} = 0$

i.e. $C_1 = 0$

Integrating a second time

$$\bar{p} = \int \frac{-q \sin\phi}{(1-\varepsilon\cos\phi)^3} d\phi$$

$$\bar{p} = \frac{+q}{2\varepsilon(1-\varepsilon\cos\phi)^2} + C_2$$

For zero velocity the pressure is ambient throughout the bearing

i.e. $\bar{p} = 1 \quad \therefore \quad C_2 = 1$

$$\text{Hence} \quad \bar{p} = 1 + \frac{q}{2\varepsilon(1-\varepsilon\cos\phi)^2} \qquad 7.2.6.$$

The net force in the vertical direction is given by

$$\bar{W} = \frac{W}{LDp_a} = \int_{\pi}^{0} \bar{p} \cos\phi \, d\phi$$

$$\bar{W} = \int_{\pi}^{0} \frac{q\cos\phi}{2\varepsilon(1-\varepsilon\cos\phi)^2} \, d\phi$$

Now in Gross[10] p 383 it is shown that if

$$A_k^{i,j} = \int_{\beta_2}^{\beta_1} \frac{\sin^i\phi \cos^j\phi}{(1-\varepsilon\cos\phi)^k} \, d\phi$$

where $i = 0$, $j = 1$, $k = 2$, $\beta_1 = \pi$, $\beta_2 = 0$

$$A_2^{01} = -\frac{1}{1-\varepsilon^2}\left[\frac{\sin\phi}{1-\varepsilon\cos\phi} + \varepsilon\left\{\frac{2}{(1-\varepsilon^2)^{\frac{1}{2}}} \tan^{-1}\left[\frac{1+\varepsilon}{1-\varepsilon}\tan\tfrac{1}{2}\phi\right]\right\}\right]_{\phi}^{\pi}$$

Hence

$$\bar{W} = \frac{q}{2\varepsilon}\left[A_2^{01}\right]$$

which reduces to

$$\bar{W} = \frac{-q}{2} \frac{\pi}{(1-\varepsilon^2)^{3/2}}$$

$$\text{or} \quad \bar{W} = \frac{-i\,\pi\,\sigma\,\varepsilon_1\, e^{i\omega_1 t}}{2(1-\varepsilon^2)^{3/2}} \qquad 7.2.7.$$

the significance of -i is that this force lags 90° behind the dis-

displacement, and there is no force component in phase with the displacement. Thus, this aerodynamic force is all damping for the incompressible case.

We may consider this force as the product of a damping coefficient C and the velocity $i\varepsilon_1\omega_1 e^{i\omega_1 t}$.

Hence the damping coefficient is

$$C = \frac{12\,\mu\,\pi\,L}{(1-\varepsilon^2)^{3/2}}\left(\frac{R}{c}\right)^3 \qquad 7.2.8.$$

Vibrations are linear with amplitude provided that $\varepsilon_1 << \varepsilon_o$ making ε^2 constant. If this condition is not satisfied the damping constant varies in magnitude throughout the cycle.

The equation enables the functional dependance of the damping on the parameters involved to be demonstrated, but since the assumptions of infinite length and incompressible fluid have been made, the values obtained will not be accurate for the real case.

This needs a solution of the full equation 7.2.1. involving an approximate analytic or numerical method. The latter has been used by Mullan and Richardson[17] where the zero eccentricity case has been calculated. The compressible fluid condition results in both in-phase stiffness and quadrature damping force components, the damping being reproduced in Fig.7.2.1. It is seen that the damping is independent of vibration frequency for squeeze numbers of less than

1.0, but after that reaches a maximum and then falls. At the same time the squeeze film stiffness increases with squeeze number, but as will be seen later, never becomes significant compared with the aerostatic stiffness.

The change in the damping coefficient with radial clearance is given in Fig.7.22 where the incompressible curve proportional to $(1/c^3)$ is shown, and also the effects of higher vibration frequency reducing its magnitude. This is seen more clearly in Fig.7.2.3. where large clearances operate almost incompressibly whilst small clearances show a large reduction as frequency increases.

7.3. Experimental Method.

This set of experiments was carried out using the first pair of bearings detailed on p. 74. The clearance at each end was exactly the same, but as shown by the results on p 93, the static stiffnesses differed in the high gauge pressure ratio cases. Thus it would be expected that the damping at each bearing would be the same, but that the vibration frequency could differ resulting in a beating amplitude. However, this effect was not significant enough to be observable and measurements were all taken at the left hand bearing only.

Free shaft vibrations in the translational mode were induced by shock loading. A piece of wood was used to strike the shaft

since this excites only the low frequency resonance of the shaft on the gas film. A striker with a high 'ring', such as a piece of metal, would be likely to excite mainly the high frequency bending resonance of the shaft. The shock response - a decaying simple harmonic motion - was observed on the Tektronix oscilloscope and photographed to give a record which could subsequently be analysed. This was arranged simply by setting the trigger level such that the impulse response signal triggered the oscilloscope time base. The camera shutter was opened prior to the impulse and closed at leisure, use being made of the 'single shot' facility which enables the oscilloscope to trigger for one sweep of the time base only. It was arranged that four traces could be recorded on one print by multiple exposures.

Zero to .002 in. probes were used giving good sensitivity and signal to noise ratio, but care had to be taken to ensure that the probe was within .002 in. of the surface. Loading or changing to a smaller diameter shaft could result in it being outside the range which makes the Wayne-Kerr output non-linear. However, since it was so easy to adjust the probe clearance with the system used, the distance reading was checked or reset before each reading, a usual distance being .0015 in. The actual vibration displacements induced by the shock loading were usually extremely small, being of the

order 10^{-5} in.

At each condition of clearance and pressure, the eccentricity was altered by adding decoupled loads acting vertically upwards. It was assumed for simplicity that when the shaft weight was exactly belanced, zero eccentricity conditions existed. Due to feed hold variations this was not exactly true but the errors involved in assuming this were not considered to have a large effect on the results. The eccentricity produced by the added loads was thus calculable from the previously measured stiffness. This system was used because in some cases the movement of the shaft was too great for one setting of the 0 - .002 in. probe.

The decoupling of the shaft mass from the applied weight had to be quite carefully considered. It was found for low loads that the kinks in the loading wires provided sufficient low stiffness decoupling springs, but as the applied weights were increased these kinks were straightened out, the weights being no longer decoupled. This was overcome by interposing low stiffness helical springs into the loading wires, which then appeared to be satisfactory under all conditions.

Results could only be obtained under conditions at which the shafts would float on the gas film, since no forced vibrations were employed. At the very high values of gauge pressure ratio the shafts

will not float even under zero load conditions due to a 'lock-up' effect where the film stiffness is very low and once the shaft is on the bearing wall high pressure keeps it there.

The damping coefficient C controls the rate at which the shock imposed vibrations die away and as the clearances get smaller the damping increases rapidly, and it soon becomes difficult to analyse the response curves. The controlling parameter is the damping ratio ξ which is the ratio of the actual to the critical damping. This is defined by

$$\xi = \frac{C}{2}\sqrt{\frac{1}{Km}}$$

where K is the total stiffness

m is the vibrating mass.

When the damping becomes critical, i.e. $\xi = 1$, the response curve is an exponential decay curve and is a function of both the stiffness and damping. With low values of ξ these two may be obtained almost independently by measuring the vibration frequency and the rate of decay respectively. Hence for the high damping cases we must look for a method of reducing ξ, and referring to the equation, it is clear that the way to do it is to raise the vibrating mass. The masses of the shafts are normally in the region .74 - .75 Lb but it was found possible to affix the brass mass shown in Fig. 5.1.5, increasing their masses to 4.26 - 4.27 Lb. This normally

reduces the damping ratio some 2½ times, but exceptions to this will be discussed later. Sets of results taken with the two mass conditions at the larger clearances gave good agreement. At the lower clearance only the larger mass was used, it being possible to obtain results at zero eccentricity for a clearance of .0005 in and up to .5 eccentricity for a clearance of .0007 in.

Besides varying clearance and eccentricity, the supply pressure was changed. This altered the feeding conditions, changing the stiffness, natural frequency and hence, at the higher frequencies, the damping coefficient.

7.4. Results.

The method chosen for analysing the results was to use an analogue computer rather than measure the logarithmic decrement, as the latter method becomes impossible when the damping ratio gets large and motion ceases to be recognizably periodic. The sets of photographed decay curves, examples of which are given in Fig.7.4.1. were analysed by setting up a free vibration equation for a damped spring - mass system

$$\ddot{x} + 2\xi\omega_n \dot{x} + \omega_n^2 x = 0$$

on a Solartron analogue computer, and imposing an initial velocity condition. This is not the exact input given to the experimental system but was a better representation than an initial displacement.

The experimental case appears to be a combination of both, but after the first half cycle the response is the same in any case. The response output signal from the computer was displayed on an oscilloscope and repeated every second so that a visual match between the photograph and computer solution could be obtained. This was done by adjusting the stiffness, damping and initial condition potentiometers until the two curves matched exactly for size and form.

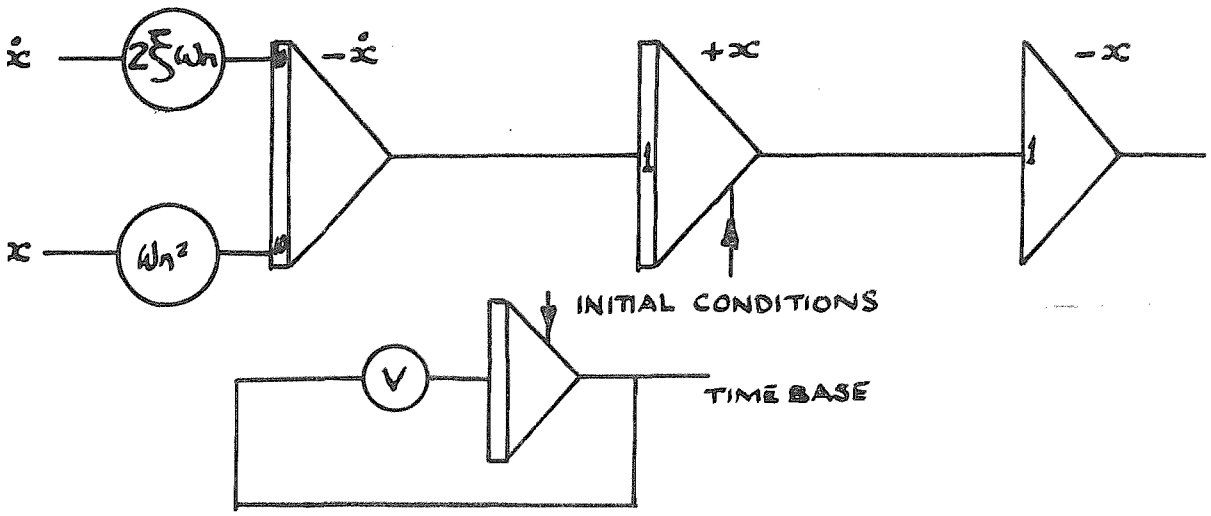

A good match was simply obtained for the low damping ratio cases. Here the technique was first to match the vibration frequency, and then to adjust the damping to get the correct decay rate.

However, in the cases where the damping ratio became greater than about 0.7 it was very difficult since, as explained previously, a match involved simultaneous adjustment of both stiffness and damping. It was made feasible by the fact that it is usually possible to gauge the natural frequency to a fair degree of accuracy from other results. It is possible that a least squares fit would have been more satisfactory in these cases, but as far as possible these conditions were avoided, and not many cases had to be analysed. Under these conditions accuracy of damping was thought to be down to about 15%, much worse than the low damping results.

The sweep rate (T/B cm/sec) of the experimental oscilloscope was recorded, but not the vertical sensitivity which was made just large enough for easy observation but not so large as to amplify the noise component of the signal too much. The analogue computer was so arranged that only three potentiometers were used - damping $2\xi\omega_n$ = a volts, time base voltage v volts, and the initial condition size. The stiffness control was set permanently at a voltage of 100, and the frequency of the response controlled only by the timebase speed. The horizontal input sensitivity M of the computer monitoring oscilloscope was usually fixed at 5v/cm.

The damping ratio and natural frequency ω_n could now be obtained for the scaling used.

$$\xi = \frac{100\ a}{63.2}$$

$$\omega_n = \frac{4960\ M}{V.\ T/B}$$

These relationships satisfied all the experimental results analysed.

A specimen set of the tabulated results obtained for more than 80 differing conditions are given below in Table 7.1. for rotor 3. The radial clearance = .0007 in, and the mass 4.27 Lb.

TABLE 7.1.

Photograph number	Supply Pressure Lb/in^2	Actual Load Lb	Eccentricity	Oscilloscope Time Base T/B ms/cm	Computer Volts V	Computer Volts a	ξ	ω_n c/s	$\xi\omega_n$ c/s	C Lb sec/in
56A	30	0	.12	5	.243	.352	.56	204	114	15.7
B		2	.29		.245	.358	.57	202	115	15.8
C		4	.46		.245	.566	.89	202	180	24.8
D		5	.55		.245	1.0	1.6	202	330	45.6
57A	50	0	.12	5	.170	.232	.37	292	118	16.3
B		2	.18		.168	.282	.45	295	133	18.4
C		6	.31		.168	.36	.57	295	168	23.2
D		10	.44		.168	.98	1.55	295	458	64.7
58A	80	0	.12	5	.153	.20	.32	324	104	14.4
B		4	.21		.167	.208	.33	298	98	13.5
C		8	.31		.140	.209	.33	350	115	15.9
D		12	.4		.161	.246	.39	308	118	16.3

In this particular case the zero eccentricity error was 0.12 and is added to the calculated values.

Two specimen records are presented in Fig.7.4.1.(a) is for rotor 3 clearance .0007 in, supply pressure 30 psig, with eccentricities between .12 and .55 (b) is for rotor 4, clearance .0009 in with a supply pressure 80 psig, the eccentricities ranging between .39 and .07.

The complete results are plotted in Figures 7.4.2. - 7.4.7. The first shows values of damping coefficient plotted against the eccentricity for the various rotors and differing pressures. Fig. 7.4.2. also contains some results taken using the two different vibrating masses for rotors 5 and 6. Except for the smallest clearance condition, the scatter band is quite small considering the measurement techniques, and the function of the damping change with eccentricity reasonably well defined. The effects of pressure are not marked in these graphs but the effects - if any - are examined in more detail in Fig. 7.4.3. where the zero eccentricity damping is plotted against supply pressure, indicating that under the conditions of the experiment no significant change is observable. Since the increased mass content of the air in the film and the change in vibration frequency as the pressure is increased would not theoretically be expected to have any effect on the damping at low values of the

squeeze number σ, it can be concluded that the annular orifice method of feeding air into the clearance does not modify the damping in the system.

The effect of change in radial clearance at zero eccentricity on the damping is examined in Fig.7.4.4., where it is compared with a theoretical damping curve derived from Fig.7.2.1. The theoretical curve is the pure squeeze film damping component for compressible air in a plain journal bearing of L/D=2. The curve is corrected for vibration frequency effects on compressibility from Fig.7.2.2., noting that the actual frequency of vibration $\omega_1 = \omega_n\sqrt{1-\xi^2}$ where ω_n is the measured natural frequency. The experimental scatter is indicated, and in general, agreement with the theory appears to be excellent. Of course at the lower clearance the theoretical curve is rising almost vertically so that the relatively large experimental scatter is only to be expected, but when plotted against the theoretical curve, either of the extreme points seem to agree.

The last damping curve is given in Fig.7.4.5. where the experimental damping change with eccentricity for rotor 6, the largest clearance, is compared to infinitely long bearing incompressible theory plotted from equation 7.2.8. Rotor 6 gives the closest approximation to incompressible conditions and it is seen that the curve shapes agree well. The difference in magnitude is because the theory is not for a finite length bearing and thus axial pressure profiles are not accounted

for. However, this difference is of the same order as that shown at zero eccentricity between finite and infinite length theory in Fig.7.2.2. Also a small difference in shape would be expected since as the eccentricity becomes large, the fluid film on one side of the shaft must enter the compressible regime, and again the finite length bearing curve will be slightly different to infinite theory in this respect.

It should be noted that it is generally not possible to align bearings perfectly. The effect of this is to induce an eccentricity which is zero at the centre of the bearing, and increases positively and negatively on either side. If the eccentricity at each end exceeds 0.5, then due to the non-linear form of the damping change with eccentricity, the damping will be modified. Even if the misalignment is not of this magnitude, as would be expected, the misalignment will still affect the damping when, due to shaft deflection, the eccentricity value reaches 0.5 at one end.

The second important set of measurements obtained were the variation of the natural frequency or film stiffness with supply pressure, (or if desired, these pressures could be translated into gauge pressure ratio using figure 6.2.1.) and eccentricity for the various clearance rotors. Fig.7.4.6. shows the measured dynamic natural frequencies plotted together with the values predicted from the static load-deflection determined stiffnesses for the left hand bearing. The

agreement is good except for the two curves presented for rotor 5 where the dynamic stiffness seems to be high. Also the measured natural frequency for rotor 1 was measured as 400 c/s at a supply pressure of 80 psig whilst the prediction was 251 c/s.

It may be considered that significant squeeze film stiffness could be generated and may account for at least part of the increased magnitude. However, using the curve of stiffness vs squeeze number presented by Mullen & Richardson[17] it can be shown that for a clearance of .0011 in and frequency of 450 c/s the additional stiffness in one of the experimental bearings is likely to be only some 30 Lb/in if a linear superposition works. This compares to the aerostatic stiffness of 7000 Lb/in at a supply pressure of 50 Lb/in^2. The maximum squeeze film stiffness which can be obtained for a given bearing geometry is limited by compressibility to an assymptotic value as the squeeze number is increased. For the clearance of .0005 in this value is 2.6×10^3 Lb/in, but is only approached to within 10% at a vibration frequency of 1300 c/s. At a more realistic practical frequency of 130 c/s the squeeze film stiffness would be 520 Lb/in which compares to a value of 5800 Lb/in at 60 Lb/in^2 supply pressure. This represents a change in the natural frequency of 3%, and so may be neglected.

The effect of eccentricity on the natural frequency is presented somewhat tentatively in Fig.7.4.7, since in all cases, as the eccen-

tricity became appreciable the damping became high and it was difficult to determine the frequency accurately. The results are again only plotted for the largest clearance case where the measurements were easiest. A full set of results is presented for the .74 Lb mass and a : set at 80 psig supply pressure for the 4.26 Lb mass. The results do seem to indicate that for eccentricities greater than 0.5 the squeeze film stiffness begins to become significant, and that at the higher frequencies, its component may become larger in relation to the aerostatic stiffness. It is thought that much greater effects would be present in the smaller clearance bearings as eccentricity is increased due to the much larger compressibility effects.

7.5. Comments.

It is indicated by this set of experiments that a first order design evaluation of the damping for planar vibrations in an inherently compensated gas bearing can be simply obtained from a pure squeeze film analysis. The relevant curves for this at zero eccentricity ratio are presented in ref. (17). At relatively large clearances for the sort of frequencies to be expected with this type of bearing, the conditions are incompressible, and excellent agreement between theory and experiment can be obtained. When the clearance is reduced, compressibility effects become apparent and the

calculation of damping becomes more difficult, as the frequency of vibration is now an important factor, and this frequency is a function not only of the stiffness and mass, but also the damping. The point at which compressibility becomes important for the L/D=2 bearing is seen from Fig.7.2.1. to be a squeeze number of approximately 1.0, after which the damping coefficient C falls rapidly. The external pressurization increases the mass content of the bearing, effectively lowering the squeeze number and this might be expected to raise the damping. An analysis in ref. 17 predicts that the damping will decrease by 20% as supply pressure is increased from 10 psig to 80 psig. However, no evidence of any significant change has been found in practice. This is not a definite conclusion, but it is suggested that design estimates based on the normal squeeze number will be approximately correct provided that bearing pressures do not become very large.

In cases where it is necessary or possible to design for optimum damping, the question arises as to what should be chosen as optimum, since the condition of critical damping does not effect the most efficient return of the displaced rotor to its initial position. The return will be exponential, and probably the best criteria to use is to specify that the vibration envelope of the displaced rotor returns to within a certain proportion of its excursion in one cycle of vibration. It should be noted that the optimum value of damping

for free vibrations will not necessarily give the best forced vibration conditions.

The response of a lightly damped system may be expressed as

$$x = A\ e^{-\xi\omega_n t} \sin(\omega_1 t - \phi)$$

The exponential $e^{-\xi\omega_n t}$ defines the envelope in which we are interested, and the sine function the actual periodic motions.

Thus at time $t = 0$, the amplitude

$$x_o = A$$

after one cycle $\quad t = 2\pi/\omega_1$

where $\quad \omega_1 = \omega_n\sqrt{1-\xi^2}$

The amplitude now is

$$x_1 = A\ e^{-\frac{2\pi\xi\omega_n}{\omega_1}}$$

$$\frac{x_o}{x_1} = e^{\frac{2\pi\xi\omega_n}{\omega_1}}$$

$$\ln \frac{x_o}{x_1} = \frac{2\pi\xi}{\sqrt{1-\xi^2}}$$

Now if we choose that the amplitude should reduce to 0.1% of the initial excursion after 1 cycle

$$\frac{2\pi\xi}{\sqrt{1-\xi^2}} = \ell n\ 1000 = 6.9$$

i.e. $$\xi = 0.74$$

For the amplitude to reduce to only 1%

$$\xi = 0.59.$$

Another approach which is not subject to any imposed boundaries, is to find the value of the damping ratio for which the total summed area between the periodic vibration curve and the axis has a minimum value. This yields a damping factor (Ref.(13)).

$$\xi = 0.663$$

which is between the two given above. These stringent conditions require a damping ratio considerably less than unity, which is the criterion often suggested.

The method of obtaining a designed value of damping at low clearance is not straightforward. The best technique would be to find the damping for the incompressible case first, calculate the aerostatic natural frequency and arrive at a first estimate of vibration frequency. Since the damping is likely to be high, the vibration frequency may well be much less than the natural frequency and close to the incompressible region. This value of vibration frequency can now be used to obtain a better estimate of damping from

which the process could be repeated until a satisfactory solution is obtained.

The effect of increasing the vibrating mass is worth noting since it reduces the natural frequency and hence the damping ratio if the damping were constant. But at low clearances a reduction in natural frequency may lead to an increase in the damping which further reduces the actual vibrating frequency, resulting in a much higher damping constant. Thus the overall effect on the damping ratio is by no means clear, and in fact under some conditions it could increase rather than decrease.

Hence the design of a machine with a fixed gas film geometry would require a very careful selection of the vibrating mass in order to achieve an optimum damping ratio. This might also have to be tempered by requirements related to other aspects of the machine performance, normally its stability in the rotational mode.

The results presented should also be equally applicable to forced vibration conditions, although it would be necessary to redefine the optimum damping ratio which could be specified as that which reduces the resonant frequency to zero

$$\text{i.e.} \quad 1 - 2\xi^2 = 0$$

$$\xi = .707.$$

8.

FREE VIBTATIONS WITH SHAFT ROTATION.

8.1. Introduction.

In the last section the gas film properties have been examined for the experimental bearing system with no shaft rotation. This is of limited interest, more important being the effects of journal rotation on the dynamic bearing damping and stiffness characteristics. This is all the more important due to the occurrence of self excited rotor instability which can completely preclude operation at any higher rotational speed. The onset of instability may be considered as the speed at which the effective gas film damping to free vibrations becomes zero, and it is of some interest to examine the rate at which damping changes at this boundary to get an idea of the 'violence' of the whirl instability i.e. the rate of growth of vibration after the onset.

In this section only free vibrations are considered, and for rotating systems these will not normally yield information useful in examining response to forced vibrations. The most common case of the latter, out-of-balance forcing, will be examined in the next section. However certain uses of hybrid journal bearings lead to imposed vibration which is not of a periodic nature, and which can most easily be considered as discreet shock loads. It is desirable to examine the rotor response to such loading to see if it will be

possible to obtain quantitative or qualitative information on how to design bearings with the best damping properties.

The problem is much more complicated than the non-rotational case due to the presence of the radial and tangential film forces generated by the shaft rotation. Also, due to the tangential force, the vibration will not be planar but a decaying elliptical orbit about the steady state position, this being in the limiting case of zero eccentricity a circular spiral. These radial and tangential forces are, for a given bearing geometry, functions of rotational speed, eccentricity, orbital motion and the ratio of orbital frequency to rotational frequency. It has been shown by Marsh[14] that no simple analytic method can be used to exactly determine these forces for the pure aerodynamic case, and this will also be true for the hybrid bearing except possibly at large clearances, where near to incompressible conditions occur.

For near incompressible conditions where the aerostatic pressure force, in phase with the displacement is much greater than the in phase component of the aerodynamic force, it is possible to use a simple mathematical model to describe the bearing dynamic behaviour in free vibrations. In an orthogonal set of x-y axes two equations are necessary to define the elliptical orbit.

$$m\ddot{x} + C\dot{x} + Kx - n_c y = 0$$

$$m\ddot{y} + C\dot{y} + Ky + m_c x = 0.$$

In the first equation $C\dot{x}$ represents the direct squeeze film damping, and is assumed to be independent of rotational speed. The stiffness force Kx is independent of the aerodynamic film pressures. The force $n_c y$ is the tangential aerodynamic force produced in the x-direction due to a deflection in the y-direction, and is in phase with the squeeze film force. In this simple model the coefficient n_c is assumed to be directly proportional to the rotational speed ω. The forces are similarly derived in the y-direction. Now for the lightly loaded bearing system used, eccentricities will generally be low and hence the whirl will be circular

$$|x| = |y| \quad \text{or} \quad y = ix.$$

Thus the two equations reduce to the same thing and only the first will be considered.

This may now be written

$$m\ddot{x} + [C\dot{x} - in_c x] + Kx = 0$$

where the effective damping coefficient is

$$C' = [C - n_c/\omega_1]$$

for a periodic vibration $x = A\, e^{i\omega_1 t}$

where ω_1 is the vibration frequency.

Since the self excited instability sets in when damping becomes zero, the condition for stability can be written

$$C \geq \frac{n_c}{\omega_1}$$

and since we take n_c proportional to speed

$$n_c = N_c \omega \quad \text{where } N_c \text{ is in Lbsec/in}$$

The condition becomes

$$C \geq N_c \left(\frac{\omega}{\omega_1}\right)$$

where (ω/ω_1) is a frequency ratio $\frac{1}{Q}$.

In practice for lightly loaded systems instability sets in when $Q = 1/2$ and so we may deduce that at the onset of instability the pure squeeze film damping coefficient C is equal to twice the direct tangential coefficient N_c.

This may be checked using simple infinitely long bearing incompressible theory. The equations for the gas film forces are presented in Gross[10] p 340 for dynamic conditions.

Using an ε,θ set of coordinates the non dimensional forces along and perpendicular to the displacement are

$$W'_{o\,e\infty} = W'_{o\,\infty} \cos\phi = \frac{\pi\Lambda\varepsilon'}{(1-\varepsilon^2)^{3/2}}$$

$$W'_{o\,\theta\infty} = W'_{o\,\infty} \sin\phi = \frac{\pi\Lambda\varepsilon(1-2\theta')}{(2+\varepsilon^2)(1-\varepsilon^2)^{1/2}}$$

where $\varepsilon' = \frac{d\varepsilon}{d(\omega_1 t)}$ and $\theta' = \frac{d\theta}{d(\omega_1 t)}$

It may be seen that within these coordinates a steady circular whirl at half of the rotational speed gives $\varepsilon' = 0$ and $\theta' = 1/2$

whence there is no net gas film force.

However, transformed into an x-y set of fixed coordinates, one pair of such equations exists for each plane, and none of the individual equations equals zero. Now ε' becomes $\dot{x}/c\omega$ and θ' becomes zero resulting in force components

$$W'_{o\,x\infty} = \frac{\pi\Lambda}{c\omega}\dot{x} \equiv C'\dot{x}$$

$$W'_{o\,y\infty} = \frac{\pi\Lambda}{2c}\,.\,y. \equiv N_c\omega y$$

when the steady state eccentricity tends to zero.

The first is the squeeze film component identical to that obtained previously and the second the tangential force due to rotation. If the orbit is circular $|x| = |y|$ and the motions must be simple harmonic so that $\dot{x} = \omega_1 x$.

Hence for the condition of half frequency whirl the squeeze film component $C\omega_1 x$ is exactly the same as the tangential component $N_c\omega y(=N_c\omega x)$, since $2\omega_1 = \omega$.

It is emphasised that this only applies to infinitely long incompressible complete films, at low eccentricities. Under these conditions, it is seen that no other forces operate in the self acting bearing i.e. it has no stiffness, and is thus inherently unstable. However, it was shown in the previous chapter that incompressible conditions exist for the larger clearances used.

The infinitely long condition is a small limitation since we are concerned with relative magnitudes. This simple analysis only applies to the very large clearance bearing, and as soon as compressibility becomes apparent, no easy analytical approach exists. However, one or two features can be discussed for the limiting case of zero eccentricity. Due to the external pressurization, the system will be stable at low speeds, and will have a stiffness which is a combination of the aerostatic and aerodynamic in phase force components. The damping will be a function of vibration frequency and rotational speed as in the incompressible case, and should become zero when the frequency ratio reaches the critical value of 1/2. It is also very interesting to note that for the condition of a circular half frequency whirl about zero eccentricity no aerodynamic pressure is generated at all, which means that as well as no damping (assuming as before that no damping component exists due to the external gas flow), there is also no aerodynamic stiffness component, and consequently the whirl frequency should be exactly the aerostatic natural frequency. Thus whirl onset occurs at exactly twice the aerostatic natural frequency.

at $\epsilon = 0$ no stiffness

Due to the non-linearity of the tangential and squeeze film force components with rotational speed and frequency, in the finite compressible case, the overall damping would no longer follow the

simple linear relation with speed of the incompressible case.

8.2. Experimental Technique.

The method of obtaining the gas film properties is much the same as that outlined in the last section.

The rotor response to a shock load was photographed and analysed. Results were obtained for six values of clearance, varying this time, supply pressure and speed between the limits of zero speed and the onset of half-speed whirl.

For this set of experiments an extra mass as added for the non rotational cases to reduce the damping ratio could not be used owing to the severe problems of balance and growth at high speed. Thus for the smaller clearances the results taken at low speeds where high damping conditions exist were subject to the same uncertainties as described in the last chapter. A complete set of zero speed damping and natural frequency values having already been obtained, the lowest speed at which results were taken was in general around one fifth of the whirl onset speed. Four traces could be recorded on one photograph, and thus for each value of supply pressure the response was defined by six points, the last being the onset of whirl. The usual method was to first increase the shaft speed to the whirl onset which is known to be of the order of twice the aero-static natural frequency. From this value speed was increased very slowly until the whirl was detected. Speed measurement was by

stationary Lissajous figure formed between a 1% accuracy oscillator and the small out of balance/out of true vibration component measured by the capacity probes. In this way accurate measurement of whirl onset speed was possible although hysteresis effects were noticed and some small deviation is probable from the true speeds. Vibration amplitude growth was rapid and so speed was reduced immediately. The oscillator was now tuned to half frequency and speed again increased but at the first sign of whirl a search was made with the oscillator to detect the actual frequency of whirl which in some cases was considerably below half the rotational frequency. The shape of the whirl orbit was observed in each case by forming a Lissajous figure, between the quadrature capacity probes, which displays the motion of the shaft centre. This always appeared to be circular. It had been intended to photograph a small self excited orbit for each test case and make an exact analysis of the orbit shape, but unfortunately before this the last experiment could be conducted a bearing air supply pipe blew off and the rotor running at very high speed, seized on to the bearing sleeve. However, a record of typical damped orbits had been made in preliminary tests and figure 8.2.1. shows the orbital response at three stable speeds, the last being very close to the stability boundary.

The rotor eccentricity was monitored for changes with speed and was found always to be low, the maximum change within the speed

range being less than 15% in the worst case which was with a 10 Lb/in^2 supply pressure and mostly less than 5%. The effects of misalignment would normally be expected to contribute as much to the effective eccentricity as the shaft weight.

A major experimental difficulty which had to be overcome was the presence of an out of balance/ out of true synchronous displacement which was superimposed on the shock response signal. The shafts (except rotor 3) were all balanced to an accuracy better than that available on a precision commercial balancer and the main contribution was from the slight amount of bend in all the rotors. The measurements were taken at a point almost one inch from the centre of the bearing which would also represent the axis of rotation of the shaft. The magnitude of this, while only of the order 5×10^{-5} in peak to peak was still significant in comparison to the shock response, and rendered analysis virtually impossible.

A sinusoidal variable phase variable amplitude voltage locked to rotor frequency was required, to subtract from the unwanted synchronous signal. A variable phase oscillator was not suitable since the rotor speed could not be maintained constant whilst the shock impulse was applied. The problem was solved by converting the square wave output of the light pick-up unit at the end of the rotor into a sine wave which was amplified with variable gain. The phase could be varied by rotating the photo-diode.

Signal substraction is a feature of the Tektronix oscilloscope used, and proved to be no problem. The synchronous signal component was eliminated for each reading separately leaving only the high frequency surface roughness effects, and enabling photographic records to be obtained, exactly similar to those in Fig.7.4.1.

8.3. Results.

A sample of the 60 readings taken on the rig is presented in table 8.1. for rotor 5, at four different supply pressures and four speeds in each case. The limiting speed giving zero damping is recorded and also the actual whirl frequency so that the whirl ratio may be derived.

Table 8.1.

Rotor 5. C = .0011 in m = .74 Lb.

Photograph No.	Supply Pressure Lb/in^{2}g.	Speed rpm	Time Base Speed ms/cm	Whirl Onset rpm	Whirl Freq. c/s	Whirl Ratio
74 A	10	9500	5			
B		14000	5	29400	215	.44
C		18900	5			
D		24000	10			
75 A	30	15000	2			
B		24200	2	48900	398	.49
C		32000	5			
D		44700	10			
76 A	50	15000	2			
B		27000	2	60000	462	.46
C		40700	2			
D		53000	5			
77 A	80	18000	2			
B		34000	2	69000	522	.45
C		48200	5			
D		66000	10			

These photographed decay traces were now analysed on the analogue

computer in the same way as the last chapter, and the results for the above conditions are presented in table 8.2.

Table 8.2.

Rotor 5.

Photograph No.	Supply Press Lb/in^2	Speed rpm $\times 10^{-3}$	V / v	M v/in	T/B ms/cm	a / v	ξ	ω_n c/s	measured ω_{res} c/s	$\xi\omega_n$ c/s	C' Lbsec/in
74 A	10	9,5	.246	5	5	.364	.575	202	190	102	2.46
B		14	.253	5		.214	.338	196	190	66.4	1.6
C		18,9	.241	5		.131	.207	206	200	42.7	1.03
D		24	.240	10	10	.052	.082	206	205	16.9	.41
75 A	30	15	.31	5	2	.187	.295	400	415	118	2.8
B		24,2	.31	10	2	.135	.213	400	385	85.2	2.05
C		32	.292	10	5	.094	.148	365	3.80	54.0	1.31
D		44.7	.137	10	10	.025	.040	362	3.82	14.5	.35
76 A	50	15	.555		2	.208	.330	447	500	125	3.53
B		27	.279		2	.130	.205	444	455	91	2.19
C		40,7	.276		2	.083	.131	449	452	58.8	1.41
D		53	.228		5	.026	.041	435	452	17.8	.43
77 A	80	18	.227		2	.153	.241	546	500	132	3.0
B		34	.249		2	.107	.169	497	512	84	2.02
C		48,2	.1		5	.064	.102	496	505	50.6	1.22
D		66	.102		10	.010	.016	486	512	7.8	.19

The complete damping and natural frequency results are presented in Figures 8.3.1 - 8.3.6 in descending order of radial clearance,

plotted against speed, each curve representing a different value of supply pressure.

For the largest clearance Fig.8.3.1. the results are close to those indicated by the incompressible film theory outlined in the first section. The natural frequency (or stiffness) shows less than 5% increase over the speed range, which is within the experimental accuracy. The damping with no rotation was shown in the previous chapter to be little affected by the pressure but the indications here are that at small rotational speed the effect of pressure becomes noticeable before the linear fall off to zero at the whirl onset. The same considerations apply to rotor 5 where the highest compressibility number referred to ambient pressure is approximately 4 which is the edge of compressible regime in pure aerodynamic bearings. Going down in clearance to rotor 4, Fig. 8.3.3. the three higher pressure curves are the same as before but at the lowest pressure the first case of supercritical damping is reached and unexpected events occur. The stiffness drops initially as speed is increased until the vibration frequency equals half the rotational frequency from whence the frequency ratio remains more or less constant up to the onset of whirl, which is what one might expect in a purely aerodynamic bearing. The damping is also different to the previous forms, falling very rapidly until the condition of the half-frequency vibrations exist and then falling in a linear manner to zero

at the whirl onset.

For the final three curves it must be remembered that the damping ratio at low speeds was usually greater than unity and that the results cannot be regarded as precise. However, it is felt that they do show the trends in this region since a zero assymptote is available and at moderate speeds results become quite acceptable again as the damping ratio decreases. For rotor 3 the same effects as for rotor 4 occur at the lowest stiffness, but for higher pressures. Whilst a drop in the stiffness occurs, the natural frequency does not become a constant half rotational frequency, but tends to it as whirl onset approaches. The whirl onset is still close to twice the aerostatic natural frequency as expected. Also for the damping at the lowest pressure similarity exists with rotor 4, but now this trend occurs (to a lesser extent) at the higher pressures. The variation of both natural frequency and damping with speed continue their trends as the clearance is decreased with rotors 2 and 1. The apparent assymptote is pure aerodynamic chacteristics for free vibrations, the degree of pressurization affecting only the onset speed of half speed whirl and the zero speed conditions.

It is indicated on page 121 that the overall damping C' is a function of the frequency ratio only, for a given clearance under incompressible conditions. The damping results for rotor 6 have

been plotted against the frequency ratio to examine this. The zero speed value which was taken from the previous chapter's results is below the extrapolated line joining the other readings which indicates that the zero damping was approximately 10.5 Lb sec/in. Also the mean frequency ratio for which damping became zero was not 2 but approximately 2.5. Thus the damping curve was shifted up by a value of the order of 2-4 Lb/sec/in at all frequency ratios. This could possibly be explained by the effects of bearing misalignment (and small shaft eccentricity) which could combine to increase the magnitude of the overall damping which as seen, effectively moves the curve to the right on the graph. The damping results for the other rotors also indicate that the zero speed damping for this set of tests was higher than that predicted before, and the plot of overall damping to frequency ratio for rotor 5 follows exactly the same trends, although less pronounced than for rotor 6.

As the clearance is reduced, the effects of compressibility become important, the linear incompressible relations no longer hold and also the combination of mass, stiffness and damping leads to greater than critical damping conditions resulting in non-periodic motions. This makes the frequency ratio unsuitable as a parameter against which to present results, direct speed or compressibility

number now being the best choice.

The set of experiments also yields information about the actual whirl onset, which is summarized in Table 8.3.

Table 8.3.

Supply Pressure Lb/in^2	Rotor 1		Rotor 2		Rotor 3		Rotor 4		Rotor 5		Rotor 6	
	ω_n	ω_w	ω_n	ω_w	ω_n	ω_w	ω_n	ω_w	ω_n	ω_w	ω_n	ω_w
10								172	230	215	125	137
Whirl Ratio							.48		.44		.46	
30			326	320	475	470	410	465	370	398	181	190
Whirl Ratio			.49		.5		.48		.49		.44	
50		270	587	630	688	680	544	560	426	462	217	223
Whirl Ratio	.49		.49		.5		.48		.46		.41	
80	720	740	883	860	865	900	635		490	522	253	258
Whirl Ratio	.47		.48		.5				.45		.39	

The whirl ratios are presented and measured whirl frequencies (ω_w) are compared to the natural frequencies (ω_n) calculated from the mean load deflection stiffnesses of both bearings.

Also measured were the whirl onset speeds and frequencies of whirl for rotors 4 and 5 with no external pressurization. The onset speeds of 43 and 46 c/s are found from Marsh[14] to correspond

to calculated eccentricities of 0.18 and 0.2 respectively. The frequency ratios found from this agree almost exactly with the measured values. Since the calculated eccentricity for the shaft weight at the onset speed is slightly less than that indicated by the stability boundary, the misalignment effect is deduced to be small.

The whirl ratios were in all cases equal to or less than 1/2, as described by many authors both experimentally and theoretically. The lowest ratio was 0.39 - which represents an onset speed of 2.56 times the actual whirl frequency - for the largest clearance bearing at its highest pressure. Whirl ratios well below half frequency have been recorded for large clearance bearings in previous work by the author (ref. 29) where ratios as low as 1/7 were obtained. The results for the small clearances are all much closer to 1/2 and all results for rotor 3 are exactly half frequency. Generally the presence of ratios other than 1/2 must indicate that some static eccentricity was present or possibly that 'external' damping was provided by the pressurization. Slight evidence for this is seen in the reduction of the whirl ratio with increasing supply pressure. Also observation of the actual whirl orbit indicated no significant departure from a pure circular orbit.

The special case of rotor 3 where exact half frequency whirl

is seen is thought to be due to the fact that this rotor was not quite as well balanced as the rest of the set. The effect of out-of-balance on the whirl instability will be examined in the next chapter.

The vibrations measured at the left hand bearing have previously been considered for the non rotational case in terms of the stiffness of the left hand bearing. But for the onset of shaft cylindrical whirl, the motion is controlled by both bearings and unfortunately the two bearings used possessed different stiffnesses at low clearances. An approximation to the overall effect can be obtained by taking the controlling stiffness to be the mean of the two bearings. These values generally agree to within 10% with the actual measured frequencies of whirl, there being no set pattern of the discrepancies.

8.4. Comments.

The free vibration performance of a hybrid bearing system has been examined. Certain known aspects - the self excited whirl onset data - have been confirmed but the free vibrations in the speed range below whirl onset have yielded some predictable results at large clearances and some unpredictable ones at the smaller clearances. The experience so far has indicated that all aspects of free vibration response in large clearance bearings can be predicted to a working

accuracy using incompressible theory.

At small clearances the damping diminishes very quickly at low speeds before reducing steadily to zero at the whirl onset. The effect would probably be less pronounced with a larger rotor mass, but still present. The vibration frequency at the same time falls below the value representing the aerostatic stiffness, tending to an aerodynamic-type half frequency value over a large speed range.

These results at low clearances cannot be explained specifically within the scope of the present work since it is felt that the only comprehensive method would be to derive a full theoretical solution either along the lines developed by Marsh and described earlier or preferably by the "Finite Orbit Program" developed by Castelli and Elrod[4] where complete response orbits are theoretically computed. The Marsh method involves investigating the force components within the gas film under specified conditions of speed orbit and frequency ratio and is very much cheaper to perform than the Orbit Program.

If the results are considered in terms of the Marsh approach certain deductions can be made. Using an orthogonal set of axes x, y the forces set up by a displacement in the x-direction are radial F_{xr} and tangential F_{xt} and similarly in the y-direction F_{yr} and F_{yt}. The net force in the x-direction is

$$F_{xr} + F_{yt}$$

Now these forces are complex, containing in-phase and quadrature components and may be written

$$F_{xr} = A + iB$$

$$F_{yt} = C + iD.$$

The net radial force will be

$$A + iD$$

and the net quadrature force

$$iB + C.$$

where these represent the stiffness and damping components of the film force. Each of these coefficients A, B, C, D, is an independent function of speed and frequency ratio and orbit, A also containing the aerostatic force. In general the dynamic response of hybrid bearings can only be predicted by obtaining each of the coefficients and examining their sums. This problem is very much greater than that of the aerodynamic gas bearing where the frequency ratio is always known to a first approximation, and in fact a more complex analysis of the finite orbit type may well prove to be the only tenable method of solution.

An experimental attack on the problem could be launched to measure the values of the coefficients of the radial and tangential forces using the orbital vibration experiment described on page 38

for the determination of stability bounds of aerodynamic bearings. For a general small elliptic orbit considered in the terms described above, there exist eight independent coefficients. For a given orbit, normal vibration measurements of force, displacement and phase would enable four coefficients to be found, and making the assumption of the linearity of the forces to small perturbations a change in the shape of the orbit will allow the other four coefficients to be found. However, it is felt that the experimental difficulties would be enormous and that the prevailing American practice of the computer experiment will prove more satisfactory even considering the high cost.

Within the limitations of the experimental equipment, the continuation of the exploratory experiments could be made by standing the rig on end to achieve a zero load system, and varying the mass of the rotor to alter the frequency of vibtation. However, this would involve a series of special rotors and is not possible within the time available.

However, although the stiffness and damping values cannot be accurately calculated, the trends shown here should be bourne in mind when designing at low clearance ratios.

The whirl onset may be predicted to be above twice the aerostatic natural frequency. The ratio will be close to one half for lightly loaded systems, but may decrease by a large amount under high eccentricity conditions.

A general method for experimentally predicting the unstable whirl onset speed of journal bearing systems without actually encountering the unstable condition has been described on page 46. It now appears possible in the light of the experimental results obtained, to postulate a simpler method of performing the same task.

It is seen that in every case, including the low clearance tests where the vibration behaviour is aerodynamic in character, that the damping falls linearly with speed as it tends to zero. In all cases this linear region occupies more than half of the speed range, and since the damping ratio is low in this region, all measurements are of good accuracy. Thus by plotting the damping against speed, it is possible to extrpolate to zero damping as soon as a linear portion of the curve has been well established enabling the whirl onset speed to be obtained.

This method would avoid many of the practical problems associated with the Marsh method[15] where the stationary member has to be forced and its amplitude measured as well as the relative amplitude between it and the rotor. The impulse excited free vibration method would need only one measurement of vibaation of the rotor relative to the sleeve in one plane, and would avoid the expensive vibration generation equipment. The method would be exactly that described in section 8.2, but where damping ratios were very small a simple logarithmic decrement measurement would yield very accurate measurement

of damping.

This free vibration damping approach perhaps lacks the logical exactness of Marsh's proposed method, and as laid out above has not been demonstrated for anything except the hybrid bearing. However, it is clear that any bearing system must exhibit high damping at low speed and zero damping at the whirl onset, even if this does not turn into a linear relationship, it should be possible to predict whirl onset without encountering unstable whirl but running close to it. The whirl ratio is easily extracted by the same method of extrapolation of the actual vibration frequency.

9. FORCED SYNCHRONOUS VIBRATIONS.

9.1. Introduction.

An early investigation by Brix[3] produced a theory and some experiments on synchronous forced vibrations in self acting bearings. However, since that time much new information relevant to the topic has become available, and in view of the increasing use of small clearance hybrid bearings, a new examination of the vibration response in both types of bearing will be made.

The response of gas lubricated systems to synchronous forced vibrations is very important, the most common source being out of balance of the rotor. This to some extent will always be present, although careful balancing will normally avoid any observable vibrations. As balancing is an expensive procedure it is desirable to know the level of vibration produced by the residual unbalance and to ensure that this does not exceed, say, half of the bearing clearance at the maximum speed or at resonance, whichever occurs at the lower speed. Hybrid bearings are widely observed to display a resonance, but no clear information has been published concerning resonance in an aerodynamic bearing. This is because hybrid bearings usually become unstable in half speed whirl after resonance, whereas the conditions for the aerodynamic bearing to run through a resonance before the onset of whirl have never, to the author's knowledge, been observed or defined. It is well known that out-of-

balance loading can produce an offset of the half speed whirl (Ref.30,15) but again the conditions have not been defined under which it is possible to have sufficient out-of-balance to produce whirl offset, but not lead to bearing failure before resonance.

For the analysis of synchronous vibrations, it is possible to use either a set of axes fixed in space, or a set which revolve with the bearing/rotor line of centres. The result in either case will be essentially the same, leading to the position that steady state theory can be used to predict synchronous vibration response. Marsh[15] has pointed out that this is only strictly true for an inertialess fluid, which air is normally assumed to be. It was also observed that in practice it is easier to measure vibration amplitude than distance so a convenient way of simulating gravity loading of a bearing might be to apply an out-of-balance to a vertical rotor system. However, since it is a dynamic system, some care must be exercised to use the total resultant force acting on the gas film, and not just on the rotor, i.e. the vector sum of the forcing term and the rotor inertia as shown in Fig.9.1.1.

9.2. The Aerodynamic Bearing.

That the load capacity of a bearing is the same whether the load is steady or rotating at shaft speed can also be deduced from the form of the Reynolds equation for unsteady loading where there is a $(1 - 2Q)$ term. The only difference is the attitude angle: for

steady conditions the load vector leads the line of centres, and in the dynamic state it lags the line of centres. This is true for all gas lubricated bearings subject to the condition that fluid inertia does not become significant (which would also invalidate Reynold's equation).

It is now possible to examine the rotor response in a zero steady load system using Ausman's Ist order Perturbation Theory[1] and his 'Linearized 'ph' Theory'[2], and also the numerical solutions of Raimondi[21], all of which are for steady state conditions.

For the aerodynamic bearing an estimate may be obtained of the dynamic rotor response to an out-of-balance loading in a closed form. We use the infinitely long bearing solution to Ausman's Ist order Perturbation theory which is valid for small eccentricities and high compressibility numbers where end effects are small. This is based on a private communication from Dr. Marsh[16]. The load capacity and attitude angle are given by -

$$\frac{W}{\pi p_a RL} = \frac{\Lambda\varepsilon}{\sqrt{\Lambda^2+1}} \qquad 9.1.$$

$$\tan\phi = \frac{1}{\Lambda} \qquad 9.2.$$

Referring to Fig.9.1.1. where b is the distance between the mass centre and the geometric centre of the rotor, ec is the displacement and r is the distance of the mass centre from the centre of rotation,

the load is given by

$$W = \frac{Mr\ \omega^2}{g} \qquad M \text{ is the shaft wt}$$

It should be noted that a couple acting against the driving force is also present but this is very small.

Equation 9.1. now becomes

$$\frac{Mr\ \omega^2}{\pi p_a RL} = \frac{\Lambda\varepsilon}{\sqrt{\Lambda^2+1}} \qquad 9.3.$$

This may be written in terms of the stability parameter

$$\gamma = \frac{Mc\ \omega^2}{4\pi g p_a RL}$$

$$4\gamma\left(\frac{r}{c\varepsilon}\right) = \frac{\Lambda}{\sqrt{\Lambda^2+1}} \qquad 9.4.$$

But

$$b^2 = r^2 + (\varepsilon c)^2 - 2r\ \varepsilon c \cos\phi \qquad 9.5.$$

$$\therefore \quad \left(\frac{b}{\varepsilon c}\right)^2 = \left(\frac{r}{\varepsilon c}\right)^2 + 1 - \frac{2r}{\varepsilon c}\ \frac{\Lambda}{\sqrt{\Lambda^2+1}}$$

$$\left(\frac{b}{\varepsilon c}\right)^2 = 1 + \frac{\Lambda^2}{16\gamma^2(\Lambda^2+1)} - \frac{\Lambda^2}{2\gamma(\Lambda^2+1)} \qquad 9.6.$$

Now we can write $\gamma = A\Lambda^2$ where Λ is a constant $= \frac{M\ p_a}{144\pi g\mu^2 L}\left(\frac{c}{R}\right)^5$

$$\left(\frac{b}{\varepsilon c}\right)^2 = 1 + \frac{1}{16A^2\Lambda^2(\Lambda^2+1)} - \frac{1}{2A(\Lambda^2+1)} \qquad 9.7.$$

to obtain the condition for ε_{max} differentiating w.r.t.A gives

$$(1+A^2)^2 = (1+8A)A^4 \qquad 9.8.$$

$$\text{or} \qquad 4\gamma_{(MAX)} = \frac{1}{2}\left[1 + \sqrt{1+8A}\right] \qquad 9.9.$$

For small clearances where $8A << 1$ the condition for resonance reduces to

$$\gamma_{(MAX)} = 1/4$$

Substituting equation 9.8. into 9.7, the maximum eccentricity is given by

$$\varepsilon_{MAX} = \frac{b}{c}\sqrt{\frac{1}{1 - \frac{1}{16\gamma^2_{(MAX)}}}} \qquad 9.10.$$

The constant A is proportional to rotor mass and (clearance)^5 and from 9.9., 9.10 ε_{MAX} decreases with increasing A for a given out-of-balance. Also the compressibility number for resonance, $A_{(MAX)}$ decreases with increasing A.

The other parameter of interest is the dynamic phase angle α being the angle between the out-of-balance forcing vector b and the displacement vector εc (Fig. 9.1). It is possible to obtain an expression for the condition $\alpha = 90^o$ when

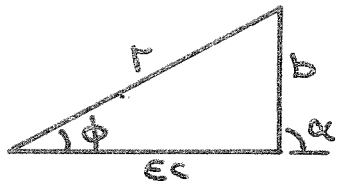

$$\frac{\varepsilon c}{r} = \cos\phi$$

but $$\frac{\varepsilon c}{r} = \frac{4\gamma\sqrt{A^2+1}}{A}$$

and $$\cos\phi = \frac{A}{\sqrt{A^2+1}}$$

$$\therefore 4\gamma = \frac{A^2}{(A^2+1)}$$

i.e. for $\alpha = 90^{\circ}$ $\quad A^* = \left[\frac{1}{4A} - 1\right]^{\frac{1}{2}}$ $\qquad$ 9.11.

also it is deduced that for

$$0 < A < A^*, \quad \alpha < 90$$

$$A > A^*, \quad 180 > \alpha > 90$$

In general

$$\sin\alpha = \frac{r}{b}\sqrt{A^2+1}.$$

The 90° phase point always occurs at a compressibility number below $A_{(MAX)}$ for values of A up to 0.25, when the phase angle does not go below 90° at all. For the geometry used by the author, at a clearance of 6.10^{-4} in the value of A is .0375,

becoming .25 at a radial clearance of 9.0 10^{-4} in. Thus the 90^{o} phase shift condition does not conform to the normal linear spring-viscous damping - mass model, displaying resonance at a speed below the 90^{o} phase shift which is taken to denote the natural frequency.

The first order perturbation theory is non-linear in compressibility number i.e. speed, but gives linear stiffness, and should be adequate for low eccentricities.

The use of the linearized 'ph' solution enables more accuracy to be obtained at high eccentricities, but looses the merit of analytic criteria for resonance and 90^{o} phase shift.

The linearized 'ph' solution for the infinitely long bearing load capacity and attitude angle is

$$\frac{W}{\pi p_a RL} = \frac{\Lambda}{\varepsilon(\Lambda^2+1)^{\frac{1}{2}}}\left[\frac{1-(1-\varepsilon^2)^{\frac{1}{2}}}{(1-\varepsilon^2)^{\frac{1}{2}}}\right]\left[1-\frac{\varepsilon^2}{(\Lambda^2+1)}\right]^{\frac{1}{2}}$$

$$\tan\ \phi = \frac{(1-\varepsilon^2)^{\frac{1}{2}}}{\Lambda}$$

substituting the out-of-balance loading and considering the triangle of forces in Fig.9.1.1. the following expression is obtained for the eccentricity

$$\left(\frac{b}{\varepsilon c}\right)^2 = 1 + \frac{1}{4A^2\Lambda^2\varepsilon^4(\Lambda^2+1)}\left[\frac{1-(1-\varepsilon^2)^{\frac{1}{2}}}{(1-\varepsilon^2)^{\frac{1}{2}}}\right]^2\left[1-\frac{\varepsilon^2}{(\Lambda^2+1)}\right]$$

$$-\frac{1-(1-\varepsilon^2)^{\frac{1}{2}}}{\Lambda\varepsilon^2(\Lambda^2+1)}\left[1-\frac{\varepsilon^2}{(\Lambda^2+1)}\right]^{\frac{1}{2}} \qquad 9.12.$$

No direct solution for ε is possible, and it would be necessary to use an iterative technique to find ε at a given value of Λ. Alternatively the expression could fairly conveniently be set up in an analogue computer and response curves obtained over a wide range of operating conditions.

Both the above analyses are only strictly valid for the infinite length bearing, but are not greatly in error, for a length to diameter ratio of two, at $\Lambda = 2.0$ (order 10% which improves at higher values). If accurate response magnitude is required at low values of compressibility or at high values of eccentricity, then the most convenient method, apart from a full computer solution of Reynold's equation, is to use the steady state load design charts of Raimondi[21].

There is no simple method of obtaining the eccentricity and again an iterative process must be used. The technique used was for a given value of Λ, to guess an eccentricity which enables a value of the attitude angle ϕ to be obtained from the chart. For the given value of out-of-balance vector 'b', a graphical construction on polar graph paper was used to find the radius of whirl 'r' (see Fig.9.1.1.). The load experienced by the gas film could now be calculated and checked against the predicted load for that Λ and ε on the chart. If not correct ε was modified until all the conditions were satisfied. The phase angle α is also obtained from

the graphical construction. This method yields results up to an eccentricity of 0.8, but it should be noted that theoretically the aerodynamic gas bearing would never fail due to synchronous loading and should always run though resonance since it possesses infinite load capacity as $\varepsilon \to 1$. Thus solutions from the charts may not be available over a range of compressibility numbers, but there will always be a solution at higher values. In practice of course due to misalignment, surface asperities etc., eccentricity ratios greater than 0.8 are seldom achieved without failure.

Illustrative response and phase angle curves are given in Figs. 9.2.1. - 9.2.3. Figure 9.2.1. shows the comparison between the Ausman first order theory and the full non-linear theory obtained from the Raimondi design curves, for the same out-of-balance at two different bearing clearances. Agreement is seen to be fairly good whilst the eccentricity ratio is below 0.5, but to differ markedly at high eccentricities. It is also noted that the maximum eccentricity predicted by the Ausman theory is fairly good at the large clearance where the constant 'A' is relatively large, but as 'A' decreases the maximum becomes much larger than the clearance. This will be so whatever the value of the out-of-balance.

Figure 9.2.2. is an eccentricity-phase angle plot of Raimondi solutions for a range of clearances at one out-of-balance. Figure 9.2.3.shows the same data plotted against the compressibility number.

The first figure well illustrates that there are two regimes depending whether the ratio b/c is small (large clearance) or large. When it is small, the eccentricity does not rise above 0.6 and a closed loop resonant curve is obtained. But if b/c is large, the response curve instead of undergoing a resonance, increases towards $\varepsilon = 1$ whilst the phase angle instead of crossing the 90° axis at finite eccentricity continues to decrease from its initial 90°. It has already been pointed out that in theory the aerodynamic bearing has infinite load capacity as $\varepsilon \to 1$, so at high eccentricity a very rapid phase change occurs accompanied by a rapid drop in eccentricity as speed is increased. The response then becomes close again to that predicted by the linear theory. In practice this would mean that the bearing cannot run through resonance, but will fail. It is clear from Fig.9.2.2. that there is a critical b/c ratio (in the region 2.04/6.8 for this case) between failure and safe operation at speeds through resonance. However, it would be necessary to use a digital computer to obtain a comprehensive set of critical b/c values under various conditions.

The behaviour can be fairly readily understood if we consider the non linearity effects. As the compressibility number increases, the ratio between the in-phase and quadrature force components increases (i.e. ϕ decreases). In terms of the dynamic vibration

model Fig.9.1.1. the stiffness increases at a much greater rate than the damping. The same is also true at a given value of Λ if eccentricity is increased. This leads in dynamic terms to a greatly reduced damping ratio, signified by a large resonant amplitude, very rapid phase change from a low value to one approaching 180°. Also the 90° phase change occurs at the same frequency as resonance. Thus the effects shown for high b/c ratios in Figs. 9.2.2., 9.2.3., are due to the fact that high b/c ratios lead to high eccentricities and high compressibility numbers at resonance. Also resonance is above that predicted by the first order solution since the stiffness is greater. The critical b/c ratio would occur when the relation of ε to Λ was such that an increase in speed just leads to sufficient damping to run through resonance, with the phase angle not displaying a maximum point before resonance. (See Fig.9.2.3.).

Finally Fig.9.2.4. shows an experimental result plotted together with the 1st order solution and the Raimondi solution. The method by which the experimental results were obtained will be outlined in a later section. However, it should be noted that the lack of points in the range $\Lambda_{\ } = .24 - 1.65$ is the region of half speed whirl, and it was only the ability to attain a whirl offset which made it possible to obtain a useful set of points. This was the only aerodynamic case where it proved possible to run

through half speed whirl. The points plotted are the mean of the deflections in the vertical and horizontal directions. The curves are plotted for a clearance of .00062 in, but judging from the form of the experimental amplitude and phase angle curves, a Raimondi solution plotted for a greater than critical clearance would give much better agreement. However, the open feed holes in the bearing may in practice have the same effect as enlarging the clearance.

9.3. Theoretical Aspects of The Hybrid Bearing.

The aerodynamic bearing subjected to synchronous rotating loads has been examined in the last section, and much of what has been discussed is relevant to the hybrid case, where the aerodynamic pressure profile is modified by a supply of pressurized air.

The aerodynamic gas film force is conveniently split up into radial and tangential components W_r, W_t acting along and perpendicular to the line of bearing centres. OO' Fig.9.1.1.

Now the aerostatic film force W_s acts along the line of centres, and thus it is postulated that a first order estimate of hybrid radial force W_{Hr} is the sum of the independent aerostatic and aerodynamic radial forces, and the hybrid tangential force W_{Ht} is the same as the aerodynamic force.

For calculation of hybrid steady state load capacity Powell[19] used a vector method encompassing the above idea. In common with other workers e.g. ref.9. he recommends the use of a compressibility

number Λ_m, based not on ambient pressure but on a mean pressure defined as

$$p_m = \frac{1}{2}(p_s + p_a)$$

The idea behind this is that the added mass of gas in the film due to the aerostatic supply has the same effect on the aerodynamic components as increasing the ambient pressure. However, the use of p_s takes no account of the feeding restriction characteristics and the downstream pressure p_{do} would be more realistic. Calculation of hybrid load capacity and attitude angle can be stated more simply than by Powell, as follows:-

For a particular Λ_M, ε

Aerostatic: Find W_s ---------- Shires

Aerodynamic: Find W_D, ϕ_D ---------- Ausman, Raimondi

$$W_r = W_D \cos \phi_D$$

$$W_{Hr} = W_r + W_s$$

$$W_{Ht} = W_D \sin \phi_D$$

$$\therefore \quad W_H = \sqrt{(W_{Hr}^2 + W_{Ht}^2)}$$

$$\tan \phi_H = \frac{W_{Ht}}{W_{Hr}}$$

This method copes perfectly well with the non-linear form of the aerostatic load W_s with eccentricity since use of the full

Shires theory[27] enables this to be found. However, since the assumption that a direct superposition can be made is not likely to be rigorous, it will normally be quite sufficient to use the linear Ausman 1st order solution for the aerodynamic component and a linear W_s equal to the zero eccentricity stiffness times the eccentricity.

The present work is concerned with the response to out-of-balance loading and this can be tackled as for the aerodynamic bearing in a simple analytic or a more rigorous iterative manner. The latter method would be to use the procedure given above to obtain a set of hybrid load and attitude angle curves in the same form as the Raimondi charts. The dynamic response and phase angle are then found as for the aerodynamic case. But this would be extremely laborious since for each different aerostatic load component a different set of charts would be needed.

The analytic approach is based as before on the Ausman 1st order perturbation solution for an infinite length bearing. The aerodynamic film force components along and normal to the line of centres are given by

$$\overline{W}_r = \frac{W_r}{\pi p_m RL} = \frac{\Lambda_m^2 \varepsilon}{\Lambda_m^2+1}$$

$$\overline{W}_t = \frac{W_t}{\pi pmRL} = \frac{\Lambda_m \varepsilon}{\Lambda_m^2+1}$$

The aerostatic force component is

$$\overline{W}_s = \frac{W_s}{\pi p_m RL} = \frac{K\varepsilon c}{\pi p_m RL} = k\varepsilon$$

where (K is aerostatic stiffness Lb/in

($k = \frac{Kc}{\pi p_m RL}$ non dimensional stiffness based on p_m.

The hybrid radial component can now be written

$$\overline{W}_{Hr} = \frac{W_{Hr}}{\pi p_m RL} = \frac{\varepsilon}{\Lambda_m^2+1} \left[\Lambda_m^2+k(\Lambda_m^2+1)\right]$$

and the tangential component

$$\overline{W}_{Ht} = \frac{\Lambda_m \varepsilon}{\Lambda_m^2+1}$$

Total load

$$\overline{W}_H = \frac{W}{\pi p_m RL} = \frac{\varepsilon}{\Lambda_m^2+1}\left[\{\Lambda_m^2 + k(\Lambda_m^2+1)\}^2 + \Lambda_m^2\right]$$

The attitude angle is given by

$$\tan \phi_H = \frac{\Lambda_m}{\Lambda_m^2 + k(\Lambda_m^2+1)}$$

or

$$\cos \phi_H = \frac{\Lambda_m^2 + k(\Lambda_m^2+1)}{\sqrt{\{\Lambda_m^2 + k(\Lambda_m^2+1)\}^2 + \Lambda_m^2}}$$

Now for out-of-balance loading

$$\overline{W}_H = \frac{Mr\omega^2}{\pi p_m \sigma RL} = 4\gamma' \left(\frac{r}{c}\right)$$

where γ' is based on p_m.

$$\therefore\ 4\gamma' \frac{r}{c\varepsilon} = \frac{1}{\Lambda_m^2+1}\left[\{\Lambda_m^2 + k(\Lambda_m^2+1)\}^2 + \Lambda_m^2\right]^{\frac{1}{2}} .$$

From Fig.9.1.1.

$$\left(\frac{b}{\varepsilon c}\right)^2 = 1 + \left(\frac{r}{\varepsilon c}\right)^2 - 2\left(\frac{r}{\varepsilon c}\right) \cos \phi_H .$$

This reduces to

$$\left(\frac{b}{\varepsilon c}\right)^2 = \{\frac{1}{4A'}\left(\frac{1}{\Lambda_m^2+1} + \frac{k}{\Lambda_m^2}\right) - 1\}^2 + \{\frac{1}{4A'\Lambda_m(1+\Lambda_m^2)}\}^2$$

where $\gamma' = A'\Lambda_m^2$

There is no simple direct expression for maximum eccentricity, but the first term in the equation displays a minimum in Λ_m whilst the second term decreases rapidly with Λ_m. A criterion for ε_{MAX} can thus be established when the second term is small - say

$$\{\frac{1}{4A'\Lambda_m(\Lambda_m^2+1)}\}^2 < .001$$

This occurs for large A' and Λ_m.

This yields the condition for ε to be a maximum

$$\Lambda_m^2 + k(\Lambda_m^2+1) = 4A'\Lambda_m^2(\Lambda_m^2+1)$$

or

$$4A'\Lambda_m^4 + \Lambda_m^2[4A' - (k+1)] - k = 0$$

In fact this is the condition for the 90° phase shift $\alpha = 90^\circ$ since referring to the sketch on page 130

$$\frac{\varepsilon c}{r} = \cos \phi_H$$

$$\therefore \frac{4A'\Lambda_m^2(\Lambda_m^2+1)}{\sqrt{\{\Lambda_m^2 + k(\Lambda_m^2+1)\}^2 + \Lambda_m^2}} = \frac{\Lambda_m^2 + k(\Lambda_m^2+1)}{\sqrt{\{\Lambda_m^2 + k(\Lambda_m^2+1)\}^2 + \Lambda_m^2}} .$$

which leads to the expression above.

As for the aerodynamic case the maximum eccentricity or resonant condition always occurs at a speed above that for the 90° phase angle, although for high values of A'/Λ_m, the two practically coincide. It is important to note this, since an approach based on considering the system to be a mass linear spring - viscous damped type, leads to the expectation that the resonant frequency will always be below that for the 90° phase change, and as A' gets large, will approach it from the opposite side to that stated by this theory.

The phase angle may be zero or 180° when ϕ_H is zero, and an examination leads to the conclusion that

when $\Lambda_m = 0$, $\alpha = 0$

$\Lambda_m \to \infty$, $\alpha \to 180$

Also, since ϕ_H is zero for low and high values of Λ_m we can examine the expression to obtain the condition for the maximum value of ϕ_H.

This is given when

$$\Lambda_m = \sqrt{\frac{k}{1+k}}.$$

A sample set of curves are given in Fig.9.3.1. showing the variation of generalised eccentricity, phase and attitude angles with compressibility number. The static stiffnesses chosen are those obtained experimentally for rotor I at supply pressures of 30 Lb/in^2 and 80 Lb/in^2 gauge.

9.4. Hybrid Bearing Experiments.

A series of experiments have been carried out for synchronous unbalance loading, basically with the apparatus described previously. As before one pair of bearing sleeves was used for all the tests, being of the same design but having a different bore diameter.

The parameters varied were the bearing clearance using the set of rotors to give a clearance range initially from 0.00057 in to 0.00235 in radial. For each clearance a range of supply pressures gave varying aerostatic stiffnesses, and also the magnitude of the out-of-balance was changed to test the effect of varying amplitude. The direct variables obtained from each test were the amplitude of vibration and the phase angle between the load and displacement

vectors at each chosen value of rotor speed. In all tests half-speed whirl was experienced and the onset and offset speeds were noted and also the whirl ratio.

The first operation was to measure the new aerostatic stiffnesses. In this case an attempt was made to equalize the aerostatic stiffnesses of the two bearings by measuring the load-deflection of the left hand test bearing at standard supply pressures, and adjusting the right hand bearing pressure until the stiffness at low eccentricities was the same. The most marked difference occurred at small clearances, high pressures, where the gauge pressure ratio is high, up to 20 Lb/in^2 differential being applied. The resulting measurements are summarised in Table 9.1. which gives the measured system stiffnesses, together with the calculated aerostatic natural frequency in cycles/second and r.p.m.

Table 9.1.

Rotor Number			1	2	3	4	5	6
Mass Lb.			.74	.737	.735	.730	.730	.732
Supply Pressure								
10 psig	Stiffness	Lb/in			4000	3750	4000	1400
	Nat.Freq.	c/s			230	224	232	136
		rpm			13800	13400	13900	8150
30 psig	k			19500	18500	10000	7500	1900
	ω_n	c/s		508	495	366	314	159
		rpm		30500	29700	21900	18800	9540
50 psig	k		29000	34500	28200	14500	14500	2800
	ω_n	c/s	618	674	612	427	375	193
		rpm	36100	40300	36700	26200	22300	11600
80 psig	k		72000	49000	41500	20000	13750	3900
	ω_n	c/s	974	805	740	517	428	228
		rpm	58300	48300	44400	31000	25700	13700

The unbalance loading could be arranged in a fairly accurate manner by two methods. The first and most simple was to tape a known

weight of 20g wire at two stations just inside the bearings with Selotape. This had the advantage of simplicity and would certainly be used where the rotor cannot be mutilated, but for the present purpose the disadvantages ruled it out. These are that at high speeds the out-of-balance loading is greater than the Selotape will bear (for force could become as large as 60 Lb at the largest unbalance finally used), which was rather dangerous. Also it was difficult to determine the angular position of the weights relative to the phase measuring system. The method adopted was to drill and tap the rotors with a 4 B.A. thread at two stations just inboard of the bearings. Grub screws were inserted ensuring that the threads were a tight fit, and positioned roughly near the balanced position. The rotors were then balanced in a separate large clearance air bearing rig and the 'residual' unbalance checked at the system resonance by putting a known unbalance and measuring the relative amplitude between the residual and the new total unbalance. The residual in all cases was better than $0.75.10^{-5}$ Lb-in in both the cylindrical and conical mode. The unbalance could be altered by screwing the grub screws, of known mass, in or out by a known amount, positional accuracy being better than 5%. Unbalance of up to $20.57.10^{-5}$ Lb-in could be attained, but was only used for one test, most being conducted at $7.5.10^{-5}$ Lb-in or $15.02.10^{-5}$ Lb-in representing 2 or 4 turns of the screws from balance.

The bowed shafts again presented a problem in extracting the required data from the capacity probe signals which included the synchronous out-of-true signal component. This time the common mode rejection technique used for the free vibration was not feasible since the output from the photo-diode light pickup was needed for phase angle measurement.

The vector diagram shows the out-of-true signal T at an angle ψ to the out-of-balance force vector. The signal actually measured is of magnitude R at an angle β to the force vector.

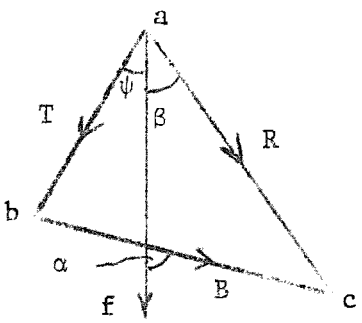

The required information is the out-of-balance response B and phase angle α.

Angular position monitoring was achieved by feeding the amplified square wave output from the photo-diode on the Z-mod of the oscilloscope, arranged such that the bright up operated off the trailing edge of the square wave. The trailing edge cut off remained sharp at all speeds whilst the leading edge deteriorated at high speed. Hence a bright spot was obtained on the oscilloscope representing a known angular position of the rotor.

The method used was to measure the phase angle of the force relative to a fixed displacement vector by rotating the body of the light unit so as to always maintain the bright-up spot at the top of the sinusoidal signal. The angle could be read off the body of the unit, overall accuracy being about $\pm 5^{o}$. A more accurate way to use the light unit would be to use the square wave output as a switch so that the sinusoidal signal can be examined over half a cycle

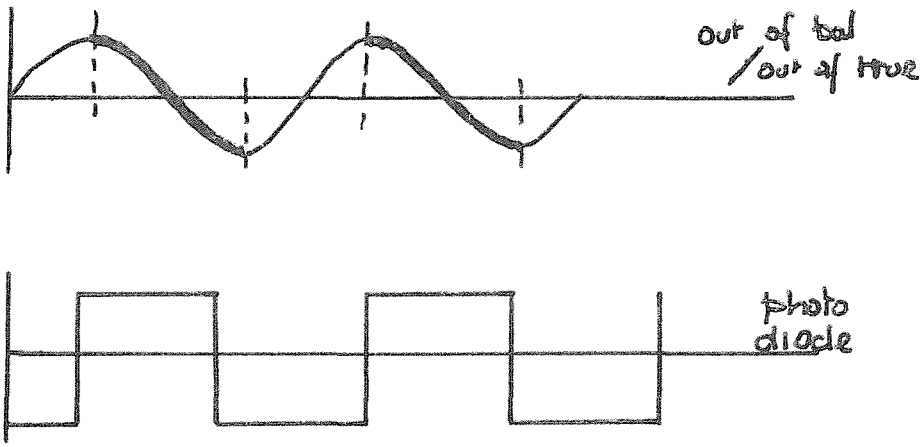

If the resulting wave form consisting of the sections shown in full is fed into an integrating meter, and the light unit adjusted for a null meter reading an exact position is obtained. Since this method works on the fundamental synchronous component only, it is not affected by out-of-round or other spurious signal components

The out-of-true vector T and its phase angle ψ were found for each (balanced) rotor at about 10 c/s which is the low

frequency limitation on the Wayne-Kerr vibration meter. The amplitude was read off the meter and the angle found as described above. Unbalance was then applied by screwing out the grub screws by a certain number of turns, and amplitude R and phase angle β read at discreet speeds up to the onset of half speed whirl or synchronous whirl failure. A graphical method was devised to obtain the required vector B and angle α, using polar graph paper. The point (T,ψ) was plotted on a transparent graph sheet and this was placed over a normal sheet of the same scale such that the tip of the (T,ψ) vector was at the origin of the lower sheet. The vectors at various speeds (R,β) were now plotted on the transparent sheet and the vectors (B,α) read directly off the graph paper below. Examples of the final polar plot are given in Fig. 9.5.1.-9.5.5. and these are transcribed on to a linear presentation with speed, Fig. 9.5.6.-9.5.11.

By measuring vibrations with two probes and the phase unit, the amplitudes of vibration in two directions could be monitored simultaneously. The results for the aerodynamic case are the mean of the vertical and horizontal response but the hybrid are for the vertical direction only. This becomes important only if significant static load is applied resulting in a non-circular orbit.

A method of obtaining a direct plot of B,α was evolved, but

this would only be suitable for an unloaded vertical rotor system since it measured a rotating displacement vector relative to a fixed load vector. This means that if the initial displacement vector mas measured in the vertical plane, as speed was increased it would be measured in planes which rotated forwards 180^{O} from vertical. Thus any difference in the characteristics of the gas film in each plane would serve to cloud the main effects of speed (compressibility number).

The technique was to form a Lissajous figure on the oscilloscope using two quadrature capacity probes at one end of the rotor. The trace bright-up was again used giving one bright spot on the circle, and at low speed this was placed at the centre of the graticule. The line joining the centre of the Lissajous circle to the spot represents the vector T in the diagram, point b being the spot. The brightness control was dimmed so that only the spot was visible, and as speed increased, the spot traced out the out-of-balance eccentricity - phase angle locus i.e. the locus of point 'c' relative to point 'b'. This can be scaled and the spot photographed at discreet speeds to give a direct record in exactly the same form as the derived graph Fig.9.5.1. No measurements were made by this method, but it was extremely useful for obtaining a rapid visual picture of the system behaviour; this could best be achieved by running the shaft up to full speed and then stopping it rapidly.

9.5. Results.

Readings were taken with various unbalances for five different rotors. Due to the half speed whirl encountered during this series of experiments, considerable rubbing took place and the bearing clearances at the time the results were taken were as follows.

Table 9.2.

Rotor Number	Radial Clearance
1	.00062 in
2	.00075
3	.0009
5	.00124
6	.00235

The principal variables used were clearance pressure and speed. Unbalance was varied at each clearance, but since it was not intended to examine eccentricity effects, only one value at each clearance is in general recorded. The pressures used were, as before 10, 30, 50 and 80 Lb/in^2 gauge. In Table 9.3. below, a typical set of results is given for rotor 3 with supply pressure 30 psig. Tabulated against speed are A and β, the measured half peak amplitude and phase angle which include the out-of-true shaft component, and the derived values of synchronous unbalance amplitude e, eccentricity ratio ε and phase angle α.

Table 9.3.

Speed rpm 10^{-3}	Measured Amplitude A in x 10^{4}	Measured Phase Angle β^{0}	Unbalance Amplitude e in 10^{4}	Unbalance Eccentricity Ratio ε	Actual Phase Angle α^{0}
0	0.6	-30	0	0	0
10	.65	-27	.1	.011	0
15	.8	-15	.3	.033	20
20	1.05	0	.65	.072	30
25	1.4	20	1.12	.125	45
30	1.7	50	1.7	.19	70
35	1.8	80	2.1	.23	95
40	1.7	100	2.1	.23	112
45	1.4	110	1.9	.21	122
50	1.3	120	1.75	.195	130
55	1.4	130	1.9	.21	136

Whirl →

The complete set of 16 results are presented in graphical form. Figures 9.5.1. — 9.5.5. show an eccentricity - phase angle plot as derived directly from the measured amplitude - angle plot. The unbalanced used is marked on each graph in terms of the mass axis shift b. The same information is given in Figures 9.5.6. - 9.5.11. plotted against speed. The reason why these have not been plotted

against the hybrid compressibility number Λ_m will be given later.

9.6. Analysis of Results.

In order to examine the correlation between the experimental results and the simple theory presented in Section 9.3. it is either possible to plot out theoretical response curves for each value of measured aerostatic stiffness as shown in Fig.9.6.1., or to break down the experimental results and examine in phase and quadrature components in the light of the theory. Not only would the former method be immensely laborious to do for a finite L/D ratio, but it would also yield less useful information than the latter.

Since the system is considered to be a vibrating one, the gas film force in phase with displacement will be considered the stiffness force, and to consist of the direct superposition of the aerodynamic and aerostatic stiffness forces. The quadrature film force is considered to be entirely due to the aerodynamic component and can be called the damping force. Since the vibration measured is the the planar representation of a circular orbit the motion seen must be simple harmonic. Thus an analysis based on linear spring - damping characteristics is quite valid. The actual stiffness controlling the vibrations is not the tangent to the load-eccentricity curve at any part, but is given by the line joining that part to the datum i.e. $\frac{W_{rH}}{\varepsilon c}$.

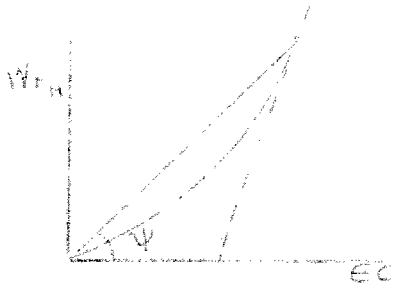

Also it should be noted that the static stiffness for steady state loading is not the same as the dynamic stiffness. The former is given as $\frac{\text{Total Load}}{\text{deflection}} = \frac{\sqrt{(W_{rH}^2 + W_{tH}^2)}}{\epsilon c}$ whilst the dynamic stiffness is controlled by the radial force only $\frac{W_{rH}}{\epsilon c}$

It is now possible to consider the results in terms of Fig.9.1.1.b. The radial force W_r is represented as

$$W_r = (K_s + K_D)\ \epsilon c. \qquad 9.6.1.$$

where K_s is the aerostatic stiffness Lb/in

K_D is the aerodynamic stiffness Lb/in

and the tangential force W_t by

$$W_t = C\ \epsilon c \omega \qquad 9.6.2.$$

where C is the damping constant $\left(\frac{\text{Lb sec}}{\text{in}}\right)$

Now for one bearing

$$W_r = (K_s + K_D)\ \epsilon c = \frac{M\epsilon c\omega^2}{2g} + \frac{Mb\omega^2}{2g} \cos\alpha$$

$$(K_s + K_D) = \frac{M\omega^2}{2g}\left[\frac{b}{c}\ \frac{\cos\alpha}{\epsilon} + 1\right] \qquad 9.6.3.$$

and

$$W_t = C\varepsilon c\omega = \frac{Mb\omega^2}{2g} \sin\alpha$$

$$C = \frac{Mb\omega \sin\alpha}{2cg\varepsilon} \qquad 9.6.4.$$

Thus the experimental results can be reduced to values of stiffness and damping for each speed, and since the aerostatic stiffness K_D is considered constant, aerodynamic theory can be used to examine the results.

Theoretical plots of aerodynamic stiffness and damping can be derived from the Ausman 1st order perturbation solution. For improved accuracy the finite length theory, for L/D = 2, will be used taken from Fig.4. of Ref. (2) where $\frac{W}{\pi p_m LR\varepsilon} = \left[\frac{\overline{W}}{\varepsilon}\right]$ and attitude angle ϕ are plotted against compressibility number.

Now $\frac{\overline{W}}{\varepsilon}$ can be split up into components

$$\frac{\overline{W}_r}{\varepsilon} = \frac{\overline{W}}{\varepsilon} \cos\phi \,, \quad \frac{\overline{W}_t}{\varepsilon} = \frac{\overline{W}}{\varepsilon} \sin\phi$$

$$\frac{\overline{W}_r}{\varepsilon} = \frac{W_r}{\pi p_m RL\varepsilon} = \frac{K_D \varepsilon c}{p_m RL\varepsilon}$$

$$\therefore \quad K_D = \frac{\overline{W}_r}{\varepsilon} \propto \frac{\pi p_m RL}{c} \qquad 9.6.5.$$

Also $$\frac{\overline{W}_t}{\varepsilon} = \frac{W_t}{\pi p_m RL\varepsilon} = \frac{C\varepsilon c\omega}{\pi p_m RL\varepsilon}$$

$$C = \frac{\overline{W}_t}{\varepsilon} \div \frac{\pi p_m RL}{\omega c}$$

$$C = \frac{\overline{W}_t}{\varepsilon\Lambda} \div 6\mu\pi L \left(\frac{R}{c}\right)^3 \qquad 9.6.6.$$

Nondimensional stiffness $K_D^* = K_D \cdot \frac{c}{\pi p_m RL}$, and nondimensional damping $C^* = C \cdot \frac{1}{6\pi\mu L} \left(\frac{c}{R}\right)^3$ are plotted against compressibility number Λ_m in Fig.9.6.1.

These curves are accurate at low eccentricities and their validity at other eccentricities has been examined by looking at the subsequent Ausman linearized 'ph' theory. This indicates that at $\varepsilon = 0.5$ the quadrature component or damping is only 7% higher than the linearized value, whilst the in-phase stiffness component is 24% higher. Now it is observed that the non-dimensional stiffness curve is almost linear with compressibility number for $\Lambda_m < 3$ and also that both K_D^* and Λ_m have the same functional dependence on pressure p_m. Hence radial stiffness is independent of p_m for low values of Λ_m. Thus only the damping is dependent on the pressure and combined with its independence on eccentricity, this should make it ideal for the examination of the best, if any, value of pressure p_m to use with the theory.

The results from figures 9.5.6. - 9.5.11. were reduced to values of damping and stiffness are previously outlined, and a sample set of calculations is given in Table 9.4.

Table 9.4.

Rotor 5 $\quad M = 0.73$ Lb $\quad c = .0012$ in

$b = 1.53\ 10^{-4}$ in $\quad b/c = .127$

$$C^* = 1.26\ 10^{-3}\ \frac{N \sin\alpha}{\varepsilon}$$

$$(K_D + K_s) = 1.04\ 10^{-5}\ N^2 \left[\frac{.127}{\varepsilon} \cos\alpha + 1\right]$$

Pressure Lb/in^2 g	Speed Nrpm	Ecc ε	Phase Angleα	sinα	cosα	Damping C*	Stiffness $(K_s + K_D)$
10	0	-	-	-	-	-	$.2 \times 10^4$
	5000	.0085	20	.342	.94	1.12	.393
	10000	.12	17	.292	.956	.135	.206
	15000	.32	98	.99	-.139	.258	.221
	20000	.292	140	.643	-.766	.245	.277
	25000	.25	160	.342	-.937	.19	.341
	14000	.31	90	1.0	-	.258	-
30	0	-	-	-	-	-	$.375.10^4$
	10000	.025	0	0	1	0	.633
	15000	.11	16	.276	.961	.21	.496
	20000	.397	68	.927	.375	.260	.466
	25000	.4	125	.819	-.574	.286	.533
	30000	.3	149	.515	-.875	.287	.588
	40000	.15	161	.326	-.946	.484	.568
	21500	.43	90	1.0	-	.27	-
50	0	-	-	-	-	-	$.502.10^4$
	15000	.15	4	.07	.918	.039	.432
	20000	.305	28	.47	.883	.171	.56
	25000	.555	89	1	.017	.257	.653
	28000	.485	126	.809	-.588	.26	.69
	35000	.335	150	.5	-.866	.291	.733
	25000		9.0	1.0	-	.25	-

Table 9.4. (continued)

Pressure Lb/in^2 g	Speed Nrpm	Ecc ε	Phase Angleα	sinα	cosα	Damping C*	Stiffness ($K_s + K_D$)
30	0	-	-	-	-	-	$.687.10^4$
	10000	.021	0	0	1	0	.734
	20000	.185	15	.259	.966	.156	.694
	25000	.5	48	.743	.669	.207	.76
	30000	.58	119	.875	-.485	.252	.838
	37000	.47	150	.5	-.866	.219	1.09
	45000	.295	156	.407	-.913	.345	1.28
	55000	.26	157	.391	-.92	.46	1.74
	27500	.62	90	1.0	-	23	-

The damping values for rotor 5 are plotted against speed in Figure 9.6.2. and it is seen by comparing with Fig. 9.6.1., that instead of the non-dimensional damping decreasing with speed (or A_m), it increases. However, a brief consideration of the dependence of C* in the phase angle yields that this is quite possible with the errors assumed in the determination of α. The damping is dependent on a sine function of α and this is extremely sensitive to error for low and high values of α. A 10° negative error was assumed and a result replotted, giving the dotted line shown in Fig.9.6.2. for the supply pressure 30 psig., which has the correct dependent form on A_m. Thus perhaps no reliance should be placed on the overal curves, but the sine function is conversely insensi-

tive to errors around the 90° value, so if the values of C* are found for $\alpha = 90^{\circ}$ they will essentially depend only on the accuracy of the eccentricity measurement.

The values of non-dimensional damping obtained in each case at the 90° phase change are summarised in Table 9.5. From these is calculated the value of pressure p_m which would give the correct C* from theory, and this is compared to p_m based on the downstream aerostatic pressure p_d.

Table 9.5.

Rotor No.	Supply Pressure p_s Lb/in^2	Speed N rpm	Damping C*	A_m	Practical p_m Lb/in^2	$p_m = \left(\frac{p_d+p_a}{2}\right)$ Lb/in^2
1	30	25000	.55	*	-	28
	50	50000	.50	*	-	35.2
	80	62000	.46	.5	133	44.7
2	30	35000	.458	.5	46.8	26
	50	45000	.450	.5	60	31.2
	80	52000	.446	.6	58.6	37.5
3	10	18000	.462	.45	16	18.7
	30	35000	.368	1.02	16.35	23.2
	50	42[illegible]	.408	.82	25	26.9
	80	48000	.383	.94	24.8	30.7
5	10	15000	.258	1.65	2.5	17.9
	30	21500	.27	1.57	3.78	21.3
	50	25000	.24	1.8	3.8	23.5
	80	27500	.23	1.88	4.0	26.7
6	10	7600	.785	*	-	15.3

* C* is higher than theory indicates that it can be.

It is immediately apparent from the above results that no simple rules exist about the calculation of the quadrature gas film force in the hybrid bearing, such as the theory postulates. However, the results show two marked trends. The first is that as would be expected, as supply pressure is increased the effective compressibility number is reduced due to the greater mean pressure in the bearing simulating a higher ambient pressure. This means that the ratio of aerodynamic damping to stiffness decreases as well as their actual magnitudes. Secondly the damping is much higher than the theoretical value at low clearance (rotor 1) becoming the same order of magnitude for rotor 3, and continuing the trend by reducing below theory for the larger clearance of rotor 5. The result for rotor 6 is against this trend but has to be considered against the firm indications of the other four clearances.

Further experimental evidence showing the same trend has been obtained from Dr. Powell who has privately loaned the author attitude angle measurements obtained at the same time as the eccentricity - steady load experiments reported in Ref[19]. These figures can also be reduced to the same constants $(K_D + K_S)$ and C* as the author's experimental analysis. In this case the smallest clearance C = .00062 in already has C* below the theoretical, and again the damping is found to get further below the theoretical values as clearance is increased.

In the previous set of experiments on the shock response of a rotating shaft, a condition exists in each experiment where the vibration frequency and the rotation frequency coincide - a condition of free synchronous vibrations. A simple expression was obtained for the infinitely long incompressible squeeze film damping constant, and if the damping constant for synchronous vibrations under the same conditions is examined, it is found to be exactly half of the zero speed squeeze film value. This serves to confirm the previous conclusions that under incompressible conditions, the damping falls linearly from the zero speed vibration value to zero at a rotational speed equal to twice that vibration frequency, by giving a further check at the mid speed range.

A new look at the damping results in Chapter 7 in the light of the synchronous theory now begins to shed some light on their shape in the low clearance tests. Due to the natural frequency (which is also approximately the vibration frequency at this condition) reducing from the aerostatic value at low speeds, the synchronous vibration condition occurs at much less than half of the whirl onset speed. Thus the damping must reduce to half of its zero speed value very rapidly, and thence to the zero damping whirl onset condition much more slowly. Also due to compressibility effects it might be expected to be less than half of the zero-speed value at the synchronous condition.

The stiffness curves plotted in Figures 9.6.3., 9.6.4. show that in general the stiffness increases from the aerostatic value K_s as speed increases. Agreement with theory is again not good but this time the smaller clearance stiffnesses tend to be too low and the larger too great, whilst rotor 3 gives something like the correct rise with speed. It should be noted that comparisons have been made at high values of the phase angle where the errors in α do not unduly affect the cosine function. It does mean, however, that another error is introduced since the eccentricity is usually significant, but from the point of view of examining the results it was felt that nothing further could belearned by resorting to the linearized 'ph' theoretical analysis instead of the lst order analysis.

The steady state results of Powell yield stiffness results which are less than the theoretical prediction, but again this is much more marked at the lowest clearance. As is also seen in the free vibration experiments the hybrid stiffness in one or two cases falls below the aerostatic value, before recovering, but it is difficult to offer an explanation for this phenomenon.

9.7. Comments.

These stiffness and damping results lead to the tentative conclusion that the ratio of damping to stiffness predicted by the theory is incorrect possibly to a greater degree than the actual

magnitude of the resultant. Thus when the stiffness is too high the damping is too low, and vice-versa, but the vector sum of the two tends to even out. The steady state hybrid results of Powell[19] support this view, the theoretical load capacities being higher, but of the same form as the experimentally measured values. The situation would also have been slightly improved if Powell had used a mean pressure p_m based on p_d rather than on supply pressure p_s. But the attitude angle results which he obtained were not in good agreement with the theory.

It is felt that the author's experimental rig would have confirmed the simple hybrid bearing theory presented if it had represented conditions in the gas film, but this does not appear to be the case. The rig is not, however, suitable for producing the very accurate results needed to form a modified theory or a complete empirical theory. This should be of fairly large dimensions so that all parameters can be controlled to high accuracy. From the point of view of producing practical information for the steady and out-of-balance loading of hybrid bearings, the aerostatic/aerodynamic superposition approach is still considered to be the best, but empirical laws concerning the derivation of a mean pressure p_m would have to be worked out separately for the aerodynamic in-phase and quadrature film forces. The result should then be fairly simple to use but would not give a very good physical

picture of the film behaviour.

9.8. Half Speed Whirl.

Each test was either teminated, or interrupted by the onset of half speed whirl, except in the few cases where insufficient power was available to drive the rotor as fast as the first onset speed. It has been observed by a number of workers [30, 9, 15] that synchronous unbalance whirl can inhibit the growth of the developed half speed whirl and sometimes lead to an offset back to plain unbalance synchronous whirl, so some notes were made during the present series of unbalance experiments.

For the three larger clearances examined in detail, rotors 2, 3, 5, no significant effects due to out-of-balance were found, beyond some degree of stabilization of the half-speed whirl orbit with unbalance mass centre shifts of up to $2.79.10^{-4}$ in.

Rotor I, however, gave interesting results both in aerodynamic operation and hybrid. The initial radial clearance was .00057 in but due to rubbing during large amplitude whirl this had enlarged to .00062 in by the completion of the experiments.

The aerodynamic experiments needed a small amount of pressure jacking to start the rotor, which then had to be switched off quickly. The technique of running up to a stable speed above whirl offset and then turning off the jacking did not work for synchronous unbalance loading since some form of lock-up seems

to occur as the pressure is turned down. However, aerodynamic operation was quite satisfactory and in all cases the rotor could be run at speeds well above the half speed whirl onset.

The measured onset and offset speeds are given in table 9.6. below.

Table 9.6.

Unbalance mass centre shift (in)	Whirl Onset Speed rpm	Whirl Offset Speed rpm
0	6000	None
1.02×10^{-4}	6000	
1.53	5900	
1.78	5900	*
2.04	5750	30000
2.3	5900	34000
2.55	5600	30000

(* half speed whirl did not fully develop from synchronous whirl up to 90,000 rpm.) With zero unbalance the bearing failed at 60000 rpm, and with $1.02.10^{-4}$ in unbalance axis shift at 30000 rpm. No touching occurred with any other unbalance up to the maximum speed available. The above figures are plotted in Fig. 9.8.1.(a) which has the same form as a similar graph in Ref.15. It

indicates that an unbalance mass centre shift of $4.5\ 10^{-4}$ in would ensure that no half-speed whirl occurred at all in the low speed region. The factor controlling half speed whirl onset and offset is eccentricity, and at the onset speed of approximately 6000 rpm, the eccentricity is in all cases not significant, so the onset is not here affected by the amount unbalance. As the speed increases, the unbalance load increases and in some cases becomes such that it would produce an eccentricity in the stable state such that the speed again becomes below the onset for that eccentricity. Half-speed whirl offset now occurs, and so long as the eccentricity continues to increase with speed at a greater rate than the whirl onset condition, no further instability is encountered. It is surmised, however that in a resonant system, the eccentricity will decrease again to a point where half speed whirl again sets in. In Fig. 9.3.1 it is seen that as the larger unbalances produce larger eccentricities, the whirl offset speeds fall, until onset and offset speeds merge. A photograph is presented Fig.9.3.2. showing four stages in the development of half speed whirl from synchronous whirl as shaft speed is decreased at 30000 rpm.

With the system subjected to significant synchronous unbalance loading it is observed that the 'half speed whirl' is exactly half frequency unlike the normal condition where the ratio is always just less than 0.5. This is explained in terms of the inertialess fluid

coordinate transformation which enables a system with a rotating synchronous load to be analysed from a rotating set of coordinates, when it is exactly the same as the fixed system. But the whirl ratio in each system is known to be either equal to or less than 0.5. The only whirl ratio which enables the half-speed whirl to satisfy both systems simultaneously is the exact half frequency ratio. This will only be seen in practice of course where the static load is small.

Whilst the speed was increasing through the region of stabilized half-speed whirl the circular half speed whirl orbit trace shown in Fig.9.8.2. was observed in several cases to break up into a complex pattern. Unfortunately no measurements were taken at the time, but it is now surmised that this was caused by the onset of conical whirl, existing at the same time as the cylindrical mode. However, no proof of this was obtained.

Half-speed whirl onset and offset were also observed for rotor 1 operating as a hybrid bearing with a supply pressure of 30 psig. These are presented in Table 9.7 and plotted in Fig.9.8.1.b.

Table 9.7.

Unbalance mass shift in	Onset Speed rpm	Offset speed rpm
0	36000	)
		)
1.02×10^{-4}	36000	)
		)
1.53	37000	)
1.78	42000	*
2.04	47000	52000
2.3	No Whirl < 90,000	

* as for Table 9.6.

In the three cases where no whirl offset was observed no touching occurred up to 90,000 rpm.

All speeds are below the resonant speed for this case so that eccentricity increases with speed here also. But the onset speed here is quite high and eccentricities already significant so that increasing the unbalance has a marked effect on the onset speed. Only one offset speed was obtained very close to the tip of the whirl envelope. Thus not only does the small amount of pressure feeding give a higher balanced half speed whirl onset but it reduces the amount of unbalance needed to avoid low speed whirl onset altogether.

However, the amount of unbalance below which whirl cannot be run through is just the same as for the aerodynamic case.

Unbalance loading can only affect the half-speed whirl offset characteristic where the offset speed is below the resonant frequency to synchronous unbalance vibrations, and eccentricity is still increasing. On the other hand whenever eccentricity is significant the onset speed may be delayed. In the case of bearing systems designed for hybrid operation, the aerostatic component is normally large and it would be expected that the resonance will occur before any whirl offset.

10.

CONCLUSIONS.

10.1. General.

Several important aspects of hybrid journal bearing performance have been examined, interrelations defined, and areas of difference outlined. Also where these fell into the general scheme of the work, one or two aspects of aerodynamic performance are included. When possible 1st order theoretical evaluations have been made, backed by experimentation, and these have indicated that in certain cases, simple aerodynamic-aerostatic superposition is possible while in other cases it is not. The experimental equipment is capable of proving or disproving theoretical indications, but has not been designed to perform the highly accurate experiments needed to formulate design laws where theory is inadequate. However, the results presented offer a design guide to virtually all performance aspects of hybrid bearings using annular feed holes.

10.2. Aerostatic Performance.

From a theoretical analysis of the single row annular feed hole bearing it is indicated that the best load capacity is obtained around $K_{go} = 0.5$, and if feed hole diameter is fixed, the best stiffness around $K_{go} = 0.0$. These support the findings by other

workers using pocketed feed holes. An experimental evaluation of stiffness supports this conclusion, but at high supply pressures, the relationship with changing clearance is found to be much more sharply peaked than theory suggests. Thus the optimum stiffness is very critically dependent on clearance. The measured stiffness is generally within 20% of the theory but this may have been due to the uneven feed hole sizes in the bearings used. Since accurate feed holes are difficult to make, reports not specifying feed hole sizes exactly should be considered with some care.

10.3. Free Vibrations.

For the case of free planar vibrations with no shaft rotation a simple analysis is developed based on the assumption that all damping is due to self acting squeeze film effects and all stiffness due to aerostatic stiffness, since squeeze film stiffness is comparatively small. The theory predicts that damping increases as $(1/c)^3$ at small vibration frequencies, but stays approximately constant with clearance at high frequencies. It might be expected that increasing the supply pressure, which increases the density of the gas in the film, would increase the damping. An analysis in ref.17 suggests that damping decreases with pressure. However, the author's experimental damping results agree remarkably well in all aspects, with a theory based on no external pressure effects, and

no changes are observed with supply pressures from 10 psig to 80 psig. It is shown that the damping ratio for the effective return of the shaft to its equilibrium position need be no higher than 0.59, which is well below the critical value often cited.

With rotation the vibration becomes orbital, but provided the static eccentricity is low this is circular and may be treated in the same way as a planar vibration. It is predicted that under infinitely long incompressible operating conditions the damping in a hybrid bearing decreases linearly to zero. The vibration frequency remains constant and the damping curve is defined at zero speed, a speed equal to the frequency of vibration, and a speed twice the vibration frequency which produces a neutral stability half speed whirl. This linear damping decrease is shown experimentally at the largest clearance used.

At smaller clearances compressibility effects set in and the constant natural frequency changes not as might be expected to a value which increased with speed, but one which initially decreases. In the lowest clearance case examined, the natural frequency reduces rapidly until it is approximately half of the rotational frequency, and thereafter behaves in a similar manner to an aerodynamic bearing, This is not explicable in terms of simple theory, but a solution of the time dependent Reynolds equation may well predict it.

The damping also decreases very rapidly, but this is expected since at the synchronous whirl condition which occurs at low speed, it should be rather less than half of the initial value. Thus very small clearance hybrid bearings will have, except at very low speeds, the same weakness to half frequency vibrations as exhibited by aerodynamic bearings, even though they have a very much higher unstable whirl onset speed. In large clearance bearings imposed half speed vibrations will produce very low damping, but unless the vibration frequency is close to the resonant frequency (i.e. the rotational speed close to the whirl onset), the response will not be excessive.

The forgoing has all related to the onset of half speed whirl at a speed equal to twice the aerostatic natural frequency. It may be deduced from Reynold's equation that this will occur since with zero applied load and an exact half frequency vibration, no aerodynamic pressure forces are generated at all. This leaves only the aerostatic stiffness to govern the natural frequency of vibration. In practice eccentricity or misalignment effects may slightly make the whirl ratio lower than one half.

In the unbalance loading tests it is demonstrated that unbalance above a certain threshold value is capable of producing sufficient eccentricity to effect a half speed whirl offset.

This is demonstrated for both aerodynamic and hybrid bearings, and whilst the onset characteristics are quite different, the offset threshold unbalances and characteristics appear to be the same. In both cases if sufficient unbalance is applied no half speed whirl occurs, but in the hybrid case this is only half of that needed for the aerodynamic bearing. The whirl ratio is always exactly one-half with unbalance present.

Free vibration results must not be generalised from the annular feed hole case to cover simple feed hole bearings. These latter can under certain circumstances exhibit a self excited (or zero damping) resonance at zero speed, and will probably have a different damping response to the annular type.

The damping measurements lead to the proposal of a simple method of evaluating the whirl onset speed without encountering it, by measuring the damping to a shock vibration at stable speeds, and extrapolating the curve to zero. This needs only one capacity probe, and for systems like the one considered by the author, three readings, since the damping decreased linearly to zero when the speed was greater than the synchronous vibration speed.

10.4. Forced Synchronous Vibrations.

Theoretical analysis of both aerodynamic and hybrid operation is presented, based on the assumption that when the fluid is inertialess and the static eccentricity zero, a rotating unbalance load

response may be calculated using steady load theory, the only difference being that the attitude angle lags instead of leads the line of centres.

For the aerodynamic bearing a 1st order perturbation gives an analytical expression for the resonance which for small clearances approximates to $\gamma = 1/4$. However, examination of this approach using full non linear solution shows that its accuracy is limited except for large clearances and small unbalances. An important indication of this full theory is that there exists a critical value of unbalance/clearance. If this is exceeded bearing failure occurs, but if not it should be possible to run through resonance at quite moderate eccentricities. One experimental case was found where whirl offset allowed high speeds to be obtained and in this case gave reasonable agreement with theory. However, there were open feed holes in the bearing wall and if these could be considered to enlarge the effective clearance, agreement would be much better. The full theory is not likely to be in error since it has been well proved for steady loading conditions.

A hybrid theory based on the assumption that aerostatic film-force is directly additive to the aerodynamic radial force component, and that damping is entirely due to the aerodynamic quadrature force component is developed. It indicates that the resonant speed will be higher and amplitudes in general lower than the aerodynamic bearing.

Also that the 90^{o} phase change between force and displacement occurs before the resonance, not after as suggested by the linear spring theory often used to describe such bearings.

However, a comprehensive investigation does not back the detailed predictions of the theory, and in particular it appears that the damping cannot be assumed to be the aerodynamic quadrature force component, as was possible in the free vibrations case. However, the theory serves to illustrate hybrid bearing trends, and it is found that the prediction of overall load capacity is closer than the prediction of its components.

11.

RECOMMENDATIONS FOR FURTHER WORK.

The whole field of externally pressurized bearings is open to more exact mathematical analyses than have been obtained up to now. But the complexity of these bearings is such that any theory is unlikely to give exact the dependance on all parameters, and a semi-empirical approach using experiments to produce modifications to the theory would probably be best.

Aerostatic bearing design needs more empirical work especially in the areas not covered by Robinson and Sterry. The free vibration experiments reported here on annular orifice bearings should all be repeated with simple orifice feed holes, but a mathematical analysis of free vibrations under hybrid conditions would have to be undertaken in order to achieve a better understanding of the phenomena encountered. Also whilst the worst or resonant conditions have been examined, forced vibration facilities are needed to examine vibration response at other frequencies.

The conditions for whirl offset due to unbalance and the definition of critical unbalance/clearance boundaries, are further areas which would stand full investigation in the plain aerodynamic journal bearing.

Finally much experimental and mathematical work remains to be done on predicting the load capacity of hybrid journal bearing, which

has not proved amenable to a simple approach.

REFERENCES

1. Ausman, J. S. — 1957. 'The Finite Gas Lubricated Journal Bearing'. Proc. I.Mech.E. Conference on Lubrication and Wear.

2. Ausman, J. S. — 1960. 'An Improved Analytical Solution for Self-Acting, Gas Lubricated Journal Bearings of Finite Length'. A.S.M.E. Paper No. 60 - Lub.9.

3. Brix, V. H. — 1959. 'Shaft Stability in Gas Film Bearings'. Engineering London 187, No.4848 p. 178.

4. Castelli V. and Elrod, H. G. — 1963. 'Solution of the Stability Problem for 360^{o} Self-Acting, Gas-Lubricated Bearings of Infinite Length'. Franklin Institute Report I - A2049 - 20.

5. Dwight, P. R. — 1962. 'Static Characteristics of Pressure Fed Air Lubricated Journal Bearings'. University of Southampton Honours Project Report.

6. de Ferranti, J. Z. — 1905. 'Improvements in and Relating to Air Bearings for High Speeds' U.K. patent No.16, 716B.

7. Fischer, G. K., Cherubim, J. L. and Decker, O. — 1959. 'Some Static and Dynamic Characteristics of High Speed Shaft Systems Operating with Gas-Lubricated Bearings'. First Int. Symp. on Gas-Lubricated Bearings ONR/ACR 49.

8. Grassam N. S. and Powell J. W. — 1964. 'Gas Lubricated Bearings' Butterworth London.

9. Gross, W. A. — 1962. 'Investigation of Whirl in Externally Pressurized Air Lubricated Journal Bearings'. J. Basic Eng.(March).

10. Gross W. A. — 1962. 'Gas Film Lubrication'. Wiley. New York.

11. Harrison, W. J. — 1913. 'The Hydrodynamical Theory of Lubrication with Special Reference to Air as a Lubricant'. Trans. Camb. Phil. Soc. 22 (1913) p.39.

12. Hirn, G. A. — 1854. 'Etudes Sur Les Principaux Phenonenes que Presentant les Frottements Mediats'. Soc. Ind. Mulhouse Bull. 26 p.188.

13. Magnus, K. — 1965. 'Vibrations'. Blackie, London.

14. Marsh, H. — 1963. 'The Stability of Aerodynamic Gas Bearings'. Cambridge Ph.D. thesis.

15. Marsh, H. — 1964. 'The stability of Aerodynamic Gas Bearings Pt. II'. Cambridge University Report.

16. Marsh, H. — 1965. Private Communication.

17. Mullan, P. J. and Richardson H. H. — 1964. 'Plane Vibration of the Inherently Compensated Gas Journal Bearing: Analysis and Comparison with Experiment'. A.S.L.E. Trans. 7. p.277.

18. Munday, A. J. — 1965 Private Communication.

19. Powell, J. W. — 1964. 'Experiments on a Hybrid Air Journal Bearing'. A.S.M.E. paper 64-WA/LUB-11.

20. Powell, J. W. and Tully, N. — 1962. 'Whirl Instability of Externally Pressurized air Lubricated Journal Bearings'. Engineer Lond.213 No.553. p.1121.

21. Raimondi, A. A. — 1961. 'A Numerical Solution for the Gas Lubricated full Journal Bearing of Finite Length'. A.S.L.E. Trans. 4.

22. Reynolds, O. — 1886. 'On the Theory of Lubrication and its Application of Mr. Beauchamp Towers Experiments including an Experimental Determination of its Viscosity of Olive Oil'. Phil. Trans. Roy.Soc. London. Ser. A.177 p.157.

23. Robinson C. H. and Sterry F. 1958 'The Static strength of pressure fed gas journal bearings. Jet bearings'. A.E.R.E. report R/R 2642.

24. Shires G. L. 1949 'Experiments with an air Lubricated journal bearing'. N.G.T.E. Memo No. M49.

25. Shires G.L. 1949 'On a type of air lubricated journal bearing'. N.G.T.E. Report No. R.61.

26. Shires G.L. 1962 'The vented pressure fed gas journal bearing'. A.E.E.W. R.111.

27. Shires G.L. 1964 'The design of externally pressurized bearings'. Chapter 4 p.110 of 'Gas Lubricated Bearings' ed. Grassam & Powell.

28. Timoshenko S. 'Vibration Problems in Engineering'.

29. Tully N. 1962 'Dynamic Characteristics of hydrostatic gas bearings' University of Southampton Honours Project Report.

30. Tully N. and Powell J.W. 1963 'An investigation of half speed whirl in an air bearing gyroscope' University of Southampton Report.

31. Vohr J. H. and Pan C.H.T. 1964 'On the Spiral Grooved Self Acting Gas Bearing'. M.T.I. Report No. 63TR52.

32. Wayne Kerr Laboratories Ltd. Instruction Manual for the B731A Vibration meter.

LIST OF FIGURES.

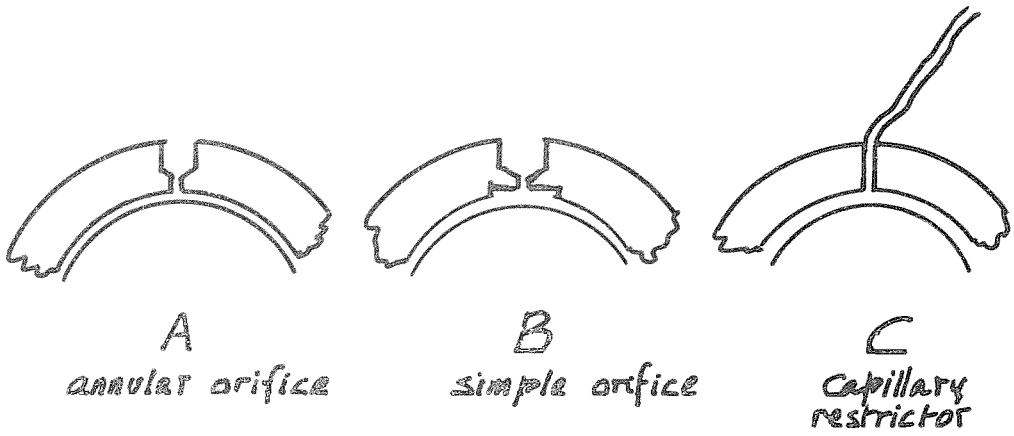

TYPES OF FEED HOLE RESTRICTOR

FIG. 2.3.1. a

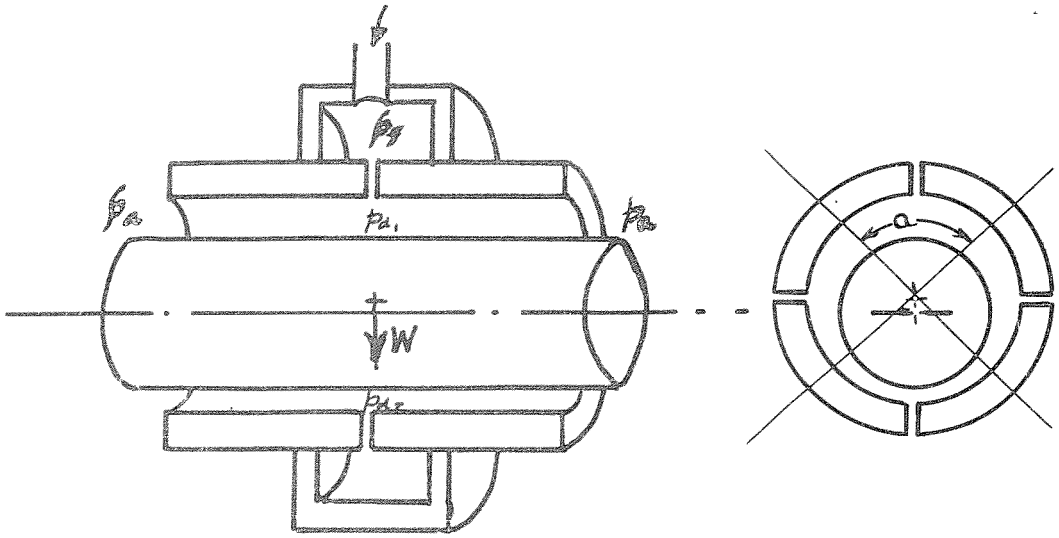

AEROSTATIC BEARING

FIG. 2.3.1. b

FIG 3.2.1.a

COORDINATES FOR NAVIER STOKES EQUATIONS

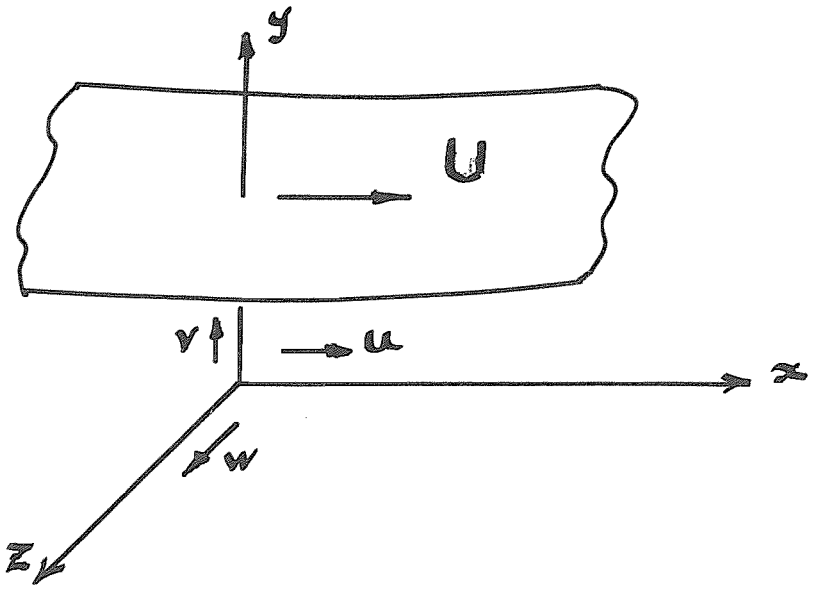

FIG 3.2.1.b

COORDINATES FOR JOURNAL BEARING

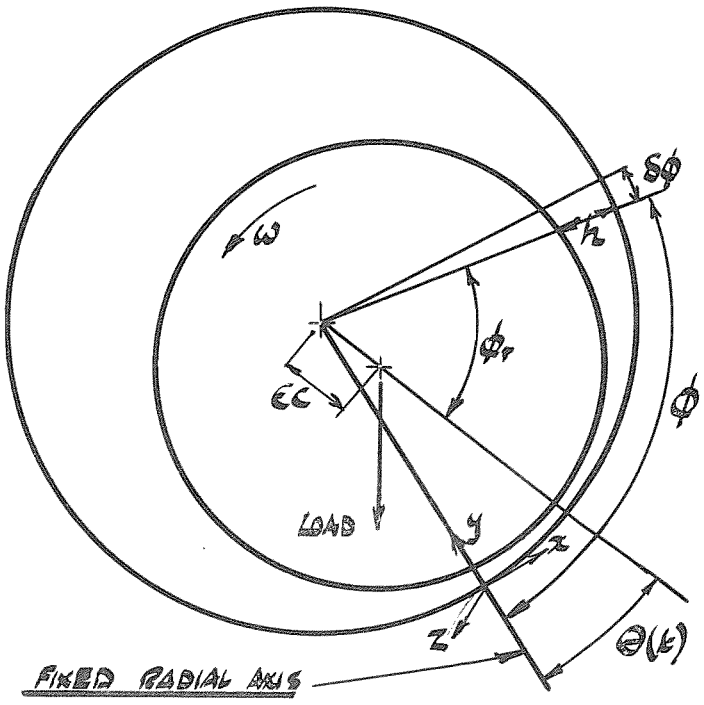

FIG 5.1.1.

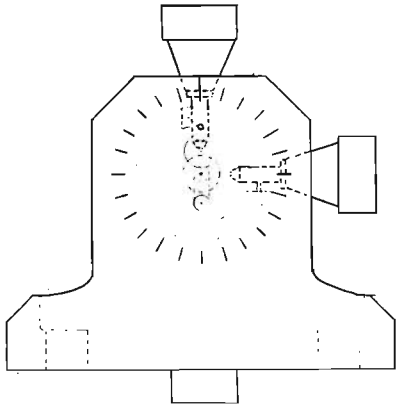

MOUNTING BLOCK 'A'
CONTAINING
① SHAFT MONITORING PROBES
② THRUST JET
③ PHOTO-DIODE PICK UP. SPEED & PHASE MEASUREMENT

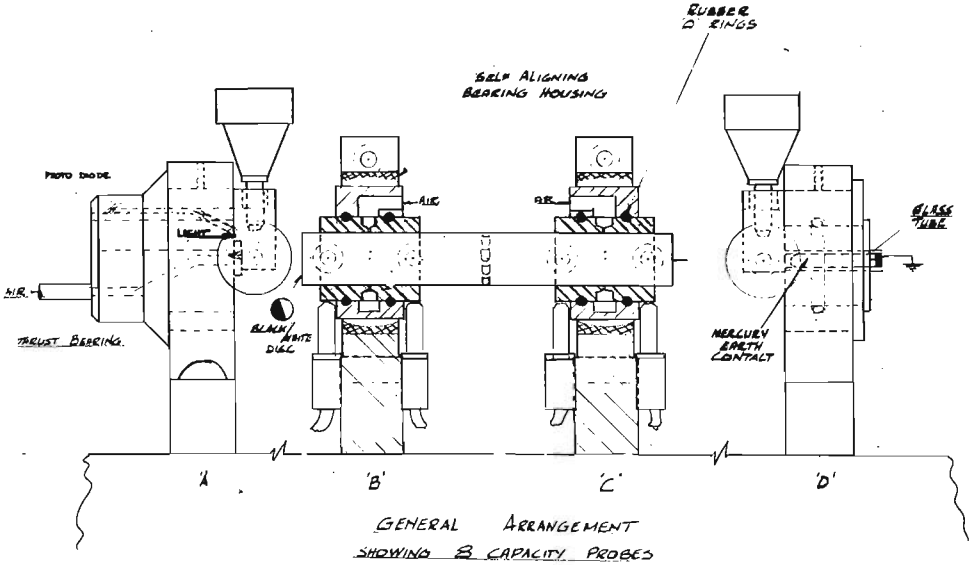

GENERAL ARRANGEMENT SHOWING 8 CAPACITY PROBES MONITORING THE BEARINGS AND 4 MONITORING THE SHAFT

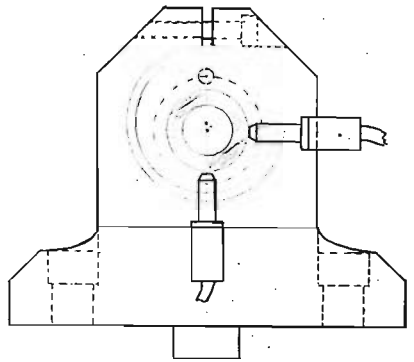

BEARING MOUNTING BLOCKS 'B' & 'C'

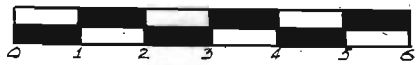

SCALE - INCHES

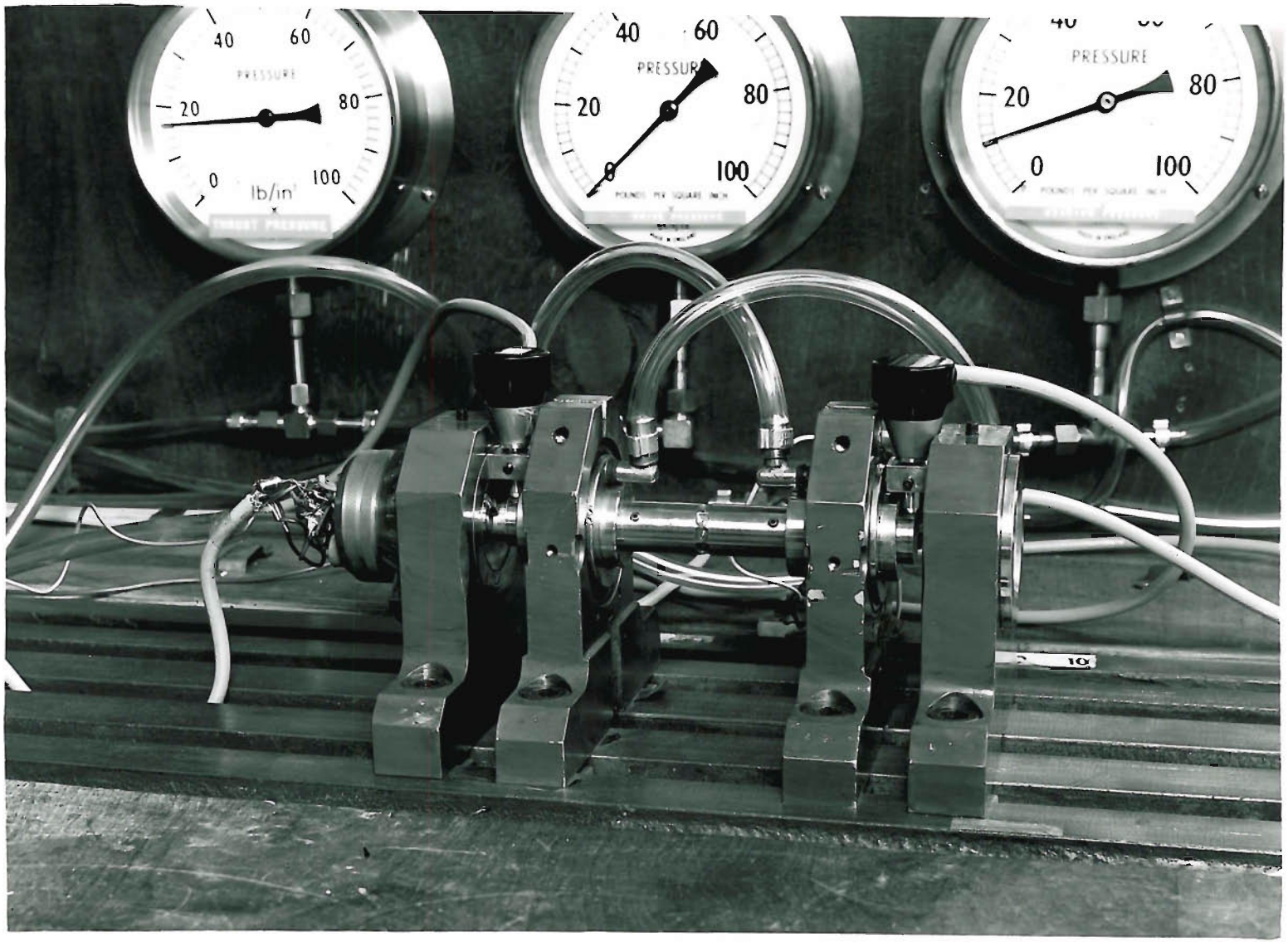

FIG 5.12. TEST RIG

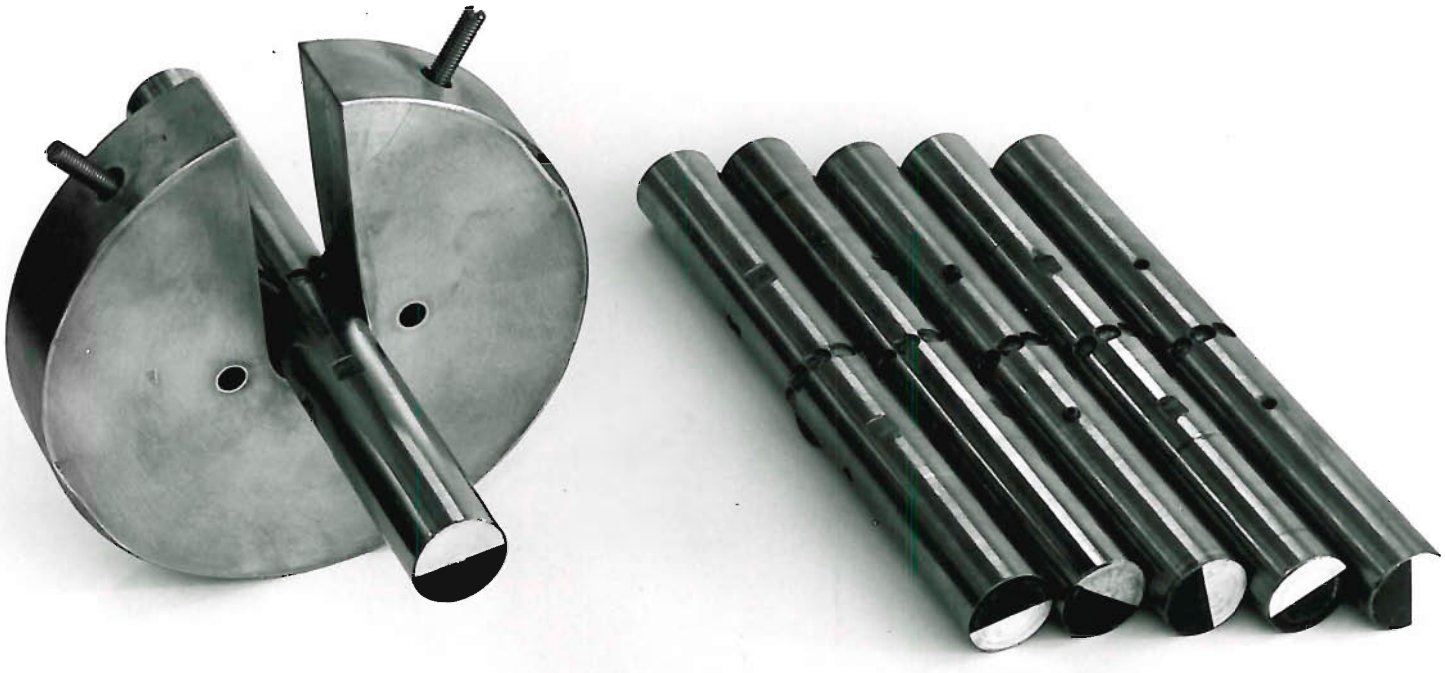

FIG 3.1.3 ROTORS

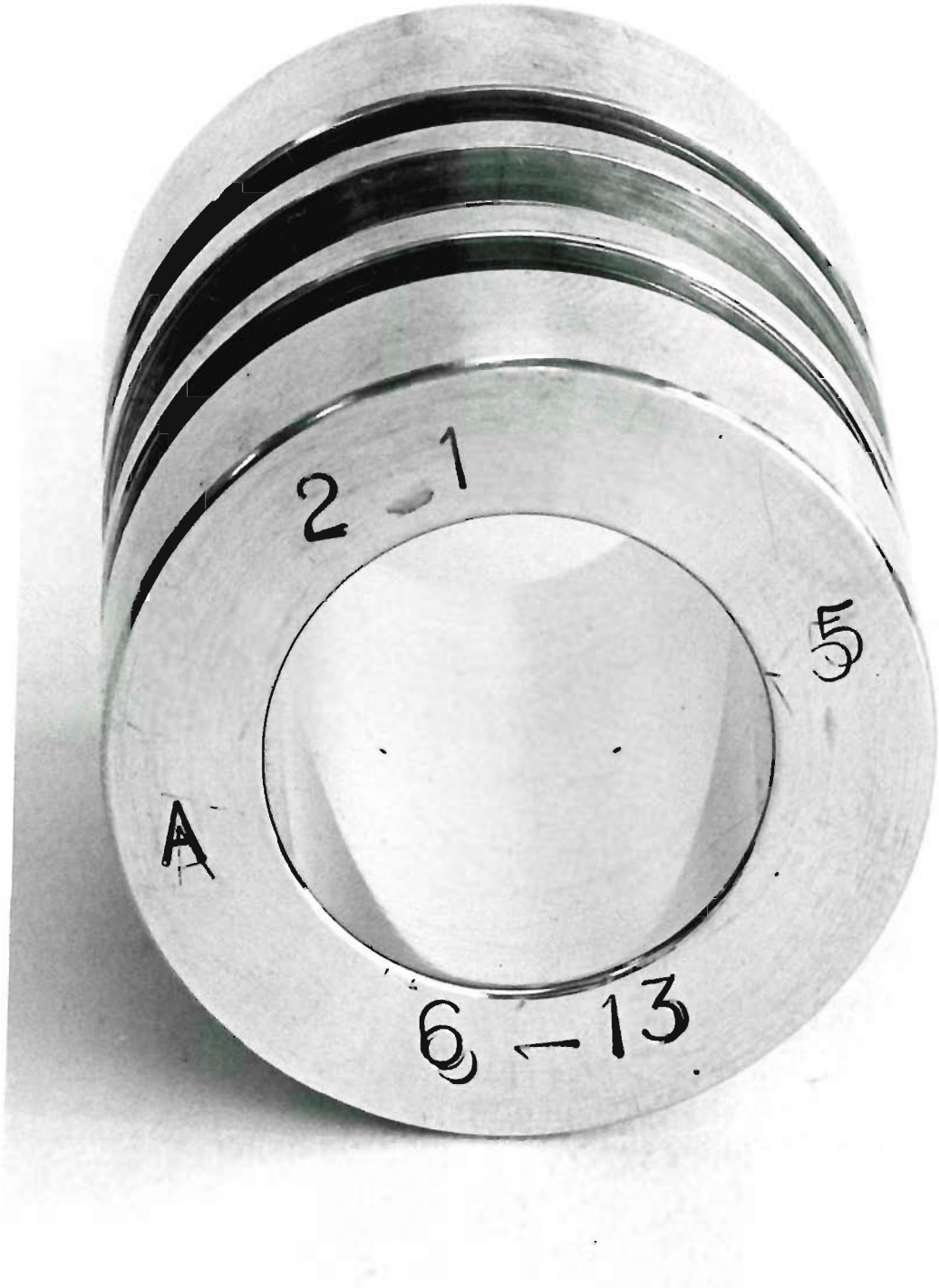

FIG 5.14. BEARING SLEEVE

Fig 6.13 Instrumentation and Control

FIG. 6.2.1

GAUGE PRESSURE RATIO VS CLEARANCE

SIX FEED HOLES .014in DIAMETER

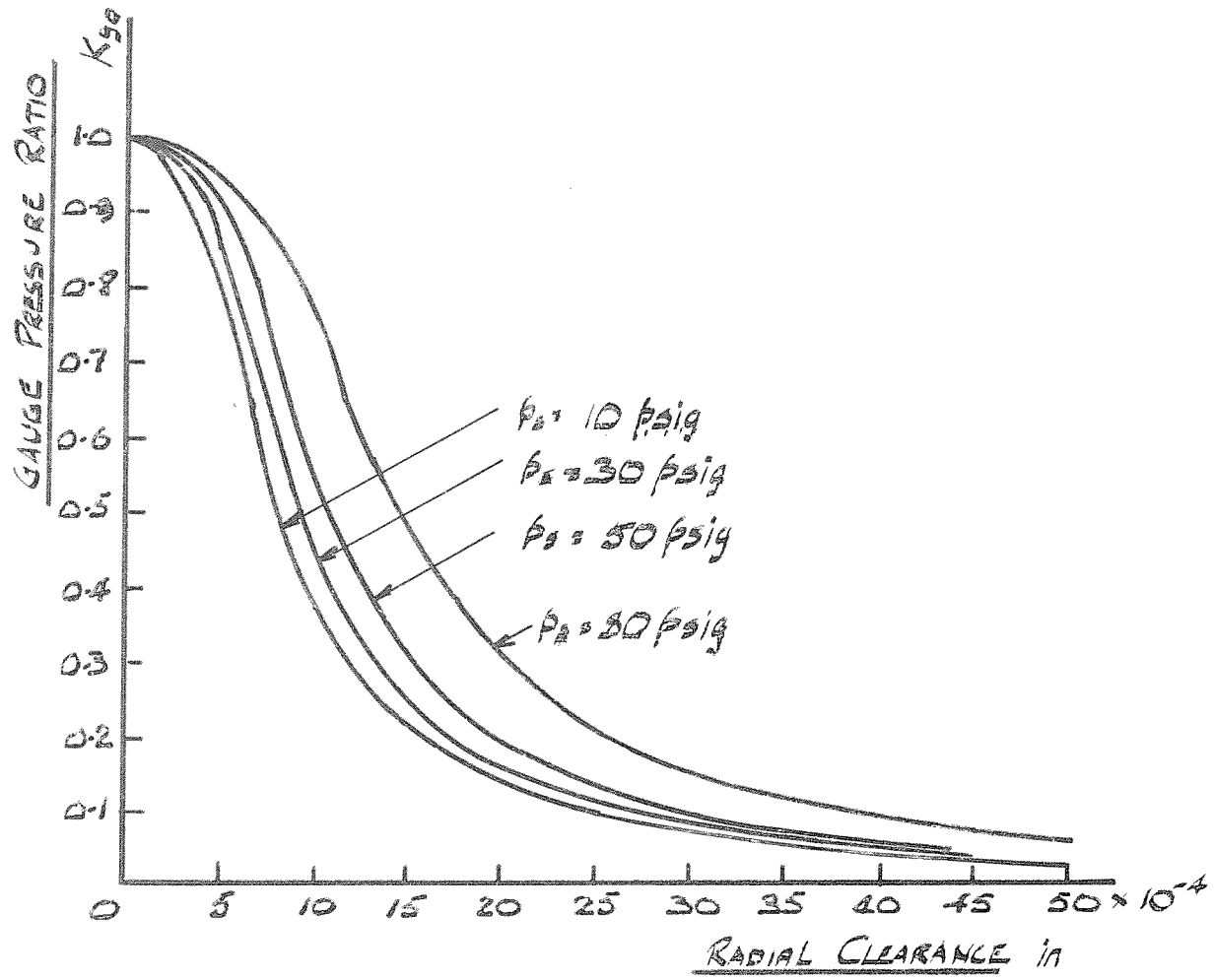

FIG 6.2.2.

LOAD COEFFICIENT
VS
GAUGE PRESSURE RATIO

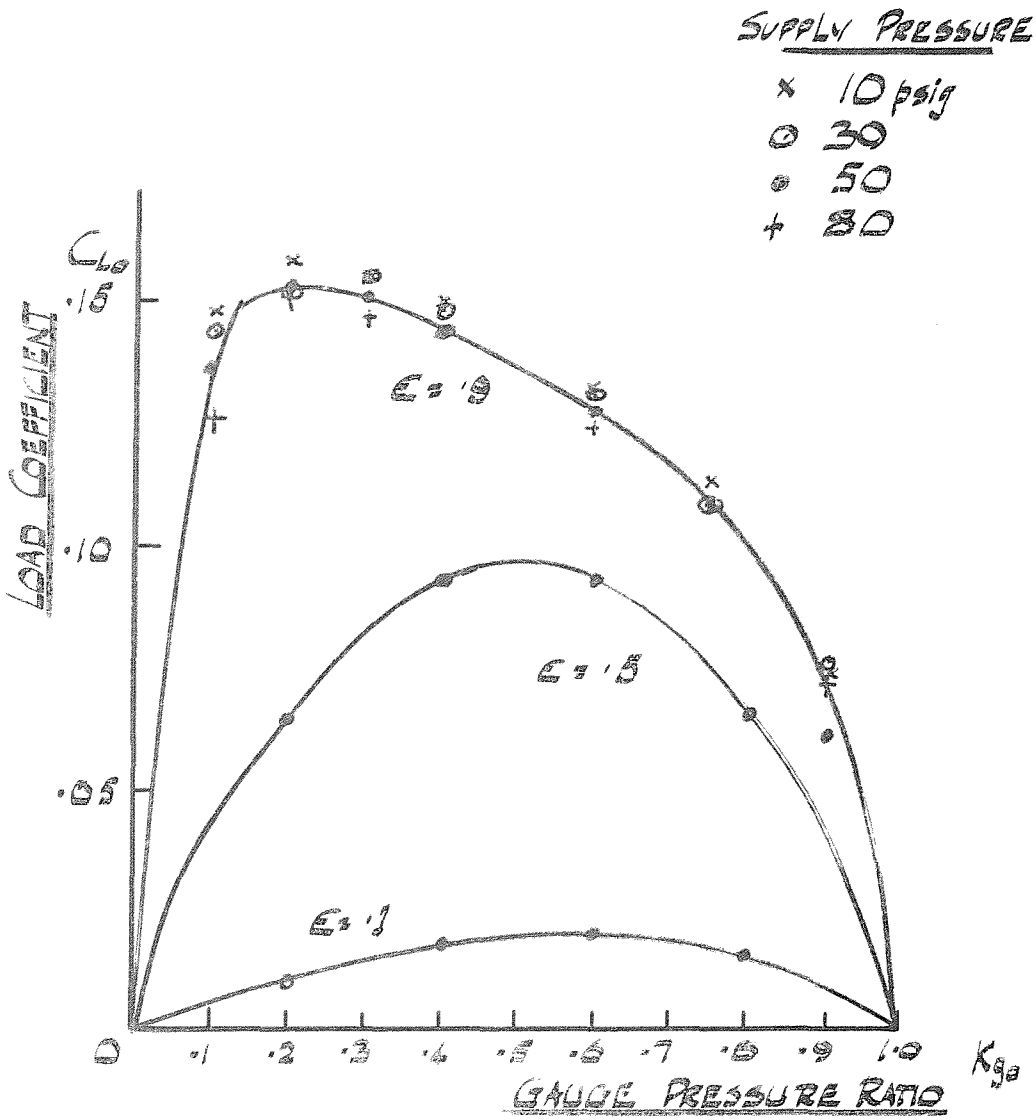

FIG 6.2.3.

NON-DIMENSIONAL STIFFNESS AT ZERO ECCENTRICITY VS GAUGE PRESSURE RATIO

P_s = 50 psig

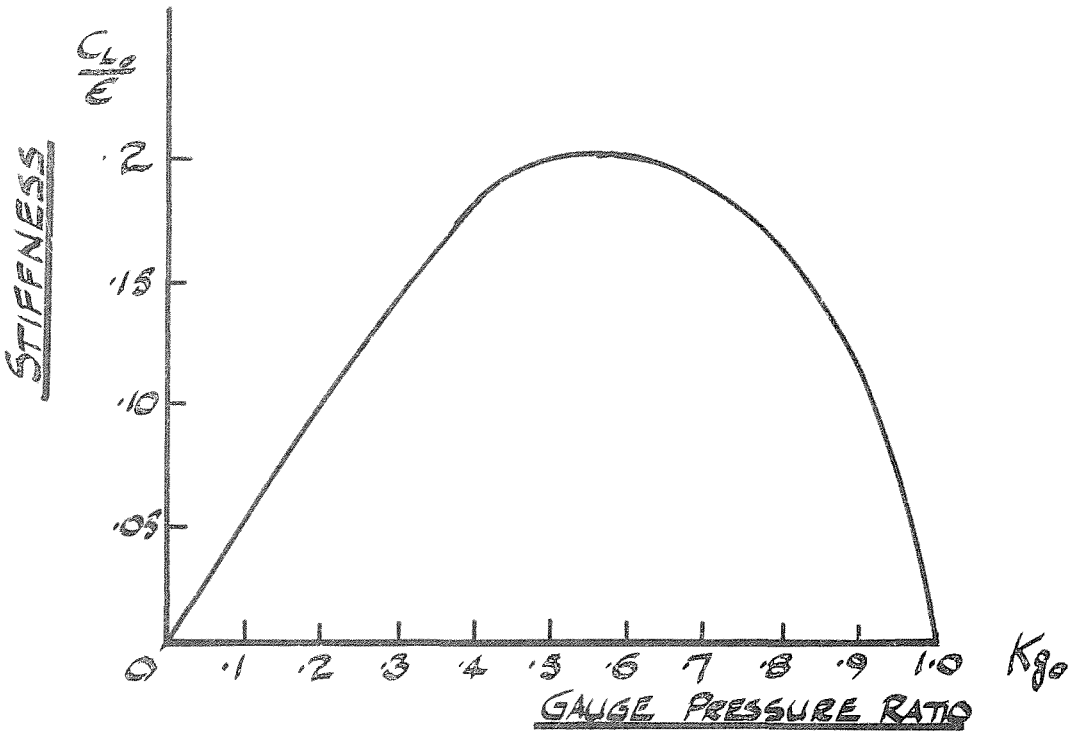

FIG 6.2.4.

STIFFNESS vs GAUGE PRESSURE RATIO

FIXED PRESSURE VARIABLE CLEARANCE

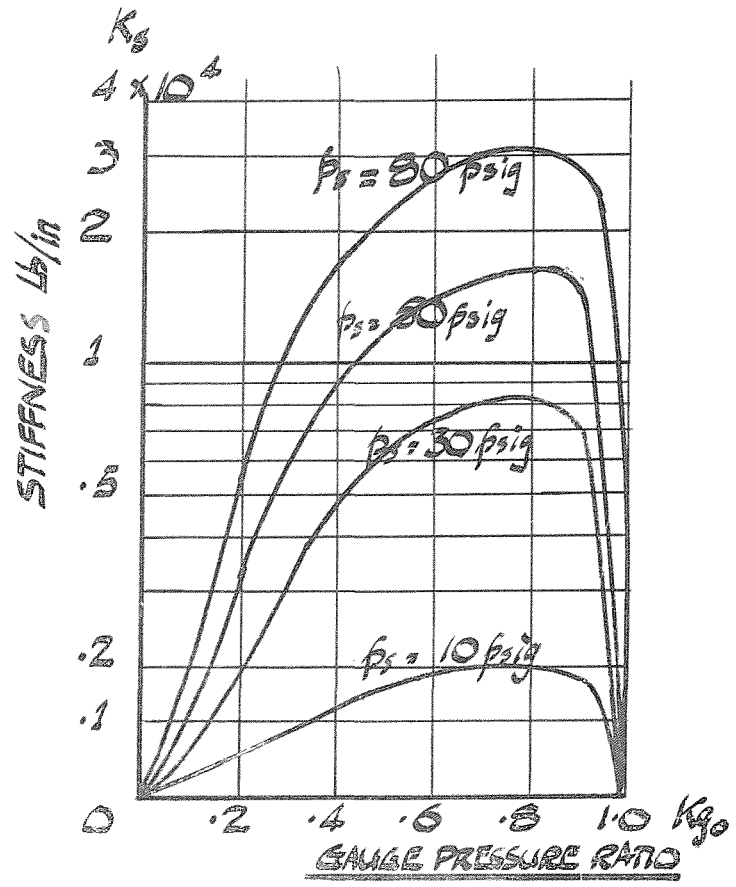

FIG 6.2.5.

STIFFNESS vs GAUGE PRESSURE RATIO

FIXED BEARING PARAMETERS VARIABLE PRESSURE

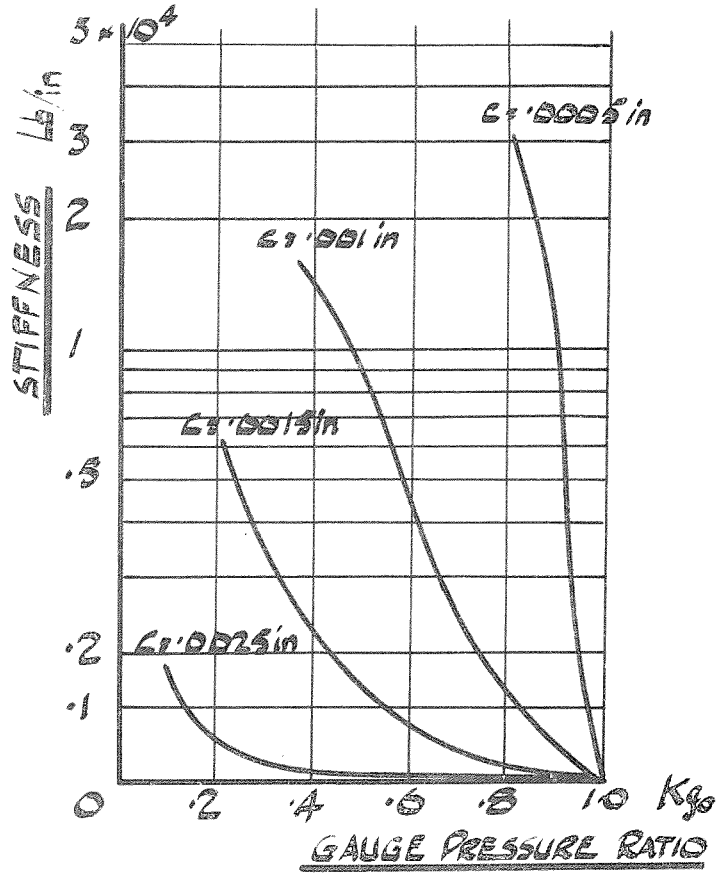

Fig 6.2.6.

STIFFNESS
vs
CLEARANCE and SUPPLY PRESSURE

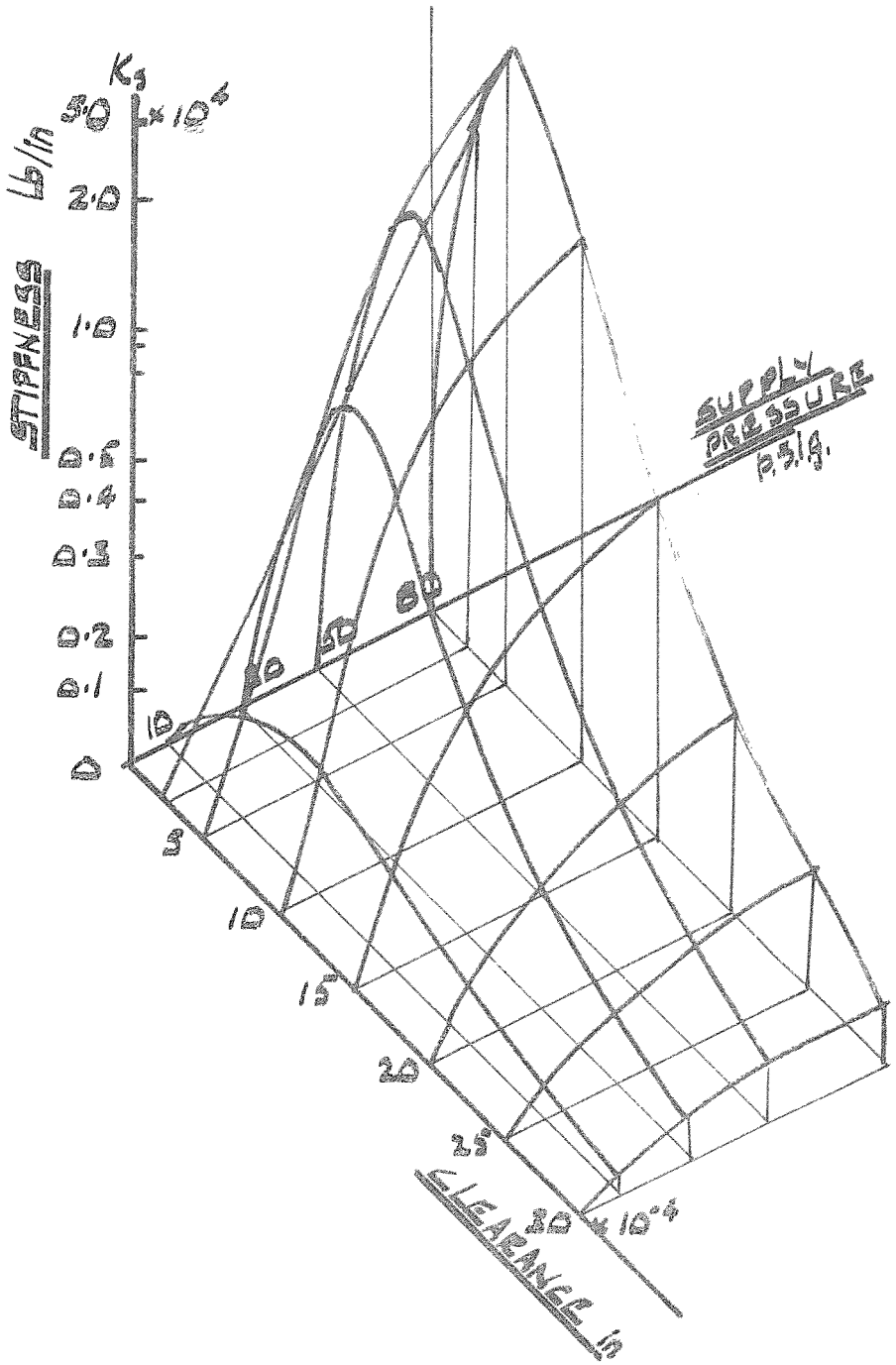

FIG 6.3.1.

EXPERIMENTAL DETERMINATION OF STIFFNESS

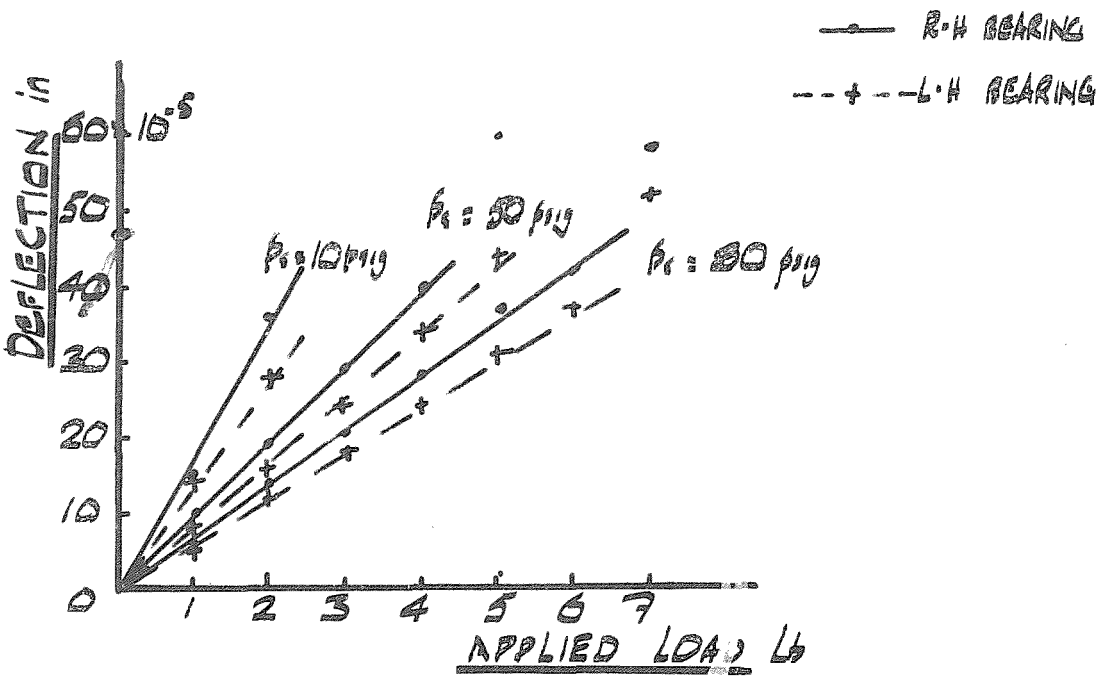

a

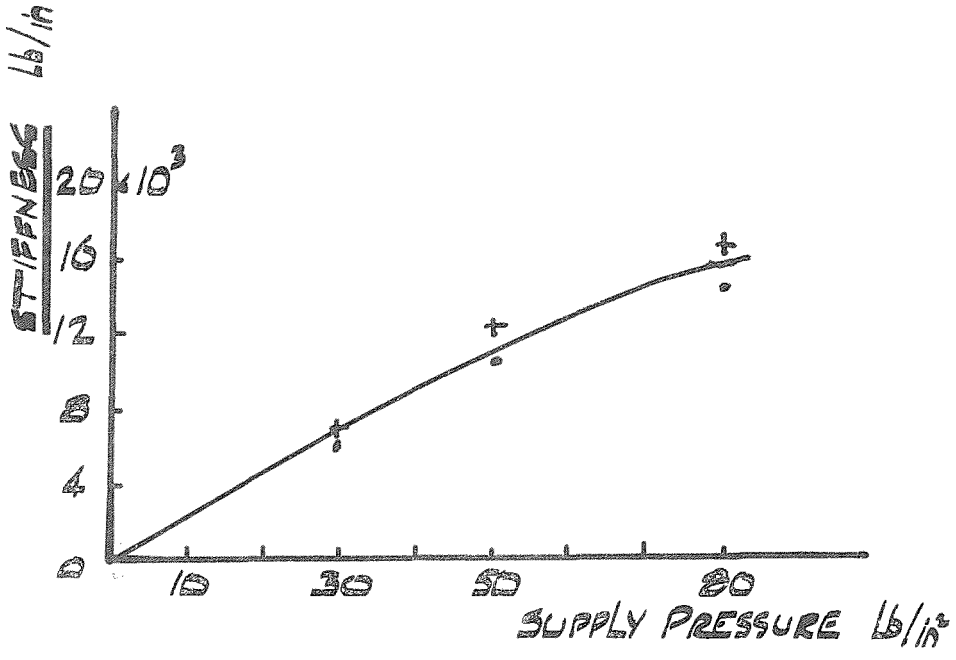

b

Fig 6.3.2

Comparison of Experimental Stiffness with Theory

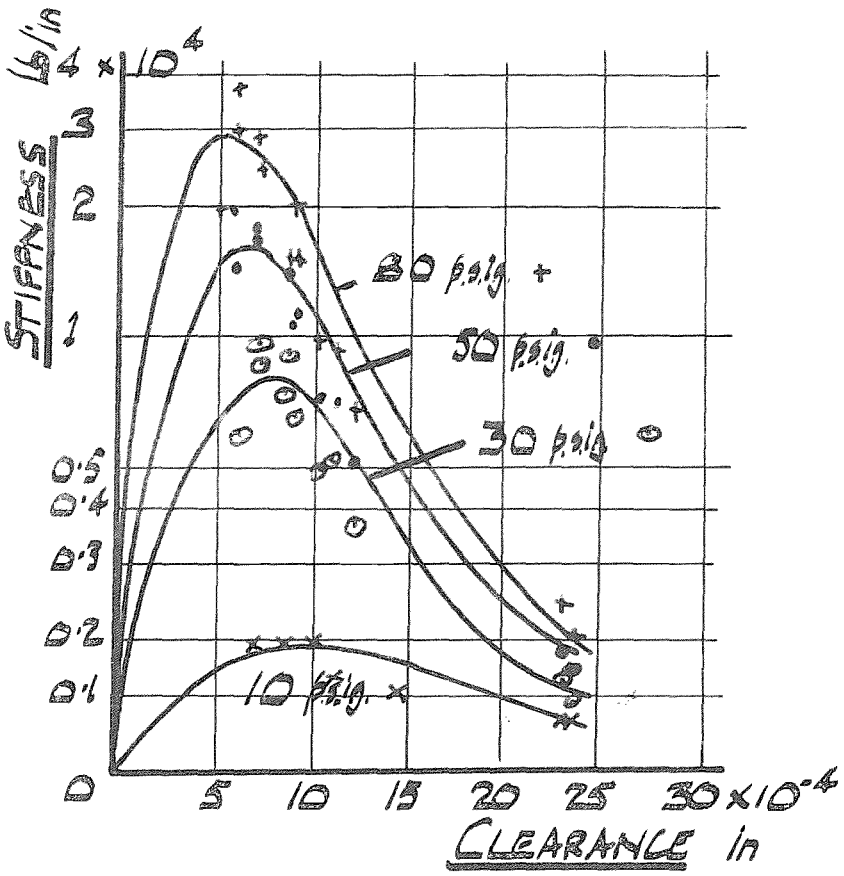

FIG 7.2.1.

THEORETICAL SQUEEZE FILM

DAMPING

L/D = 2

ε = 0

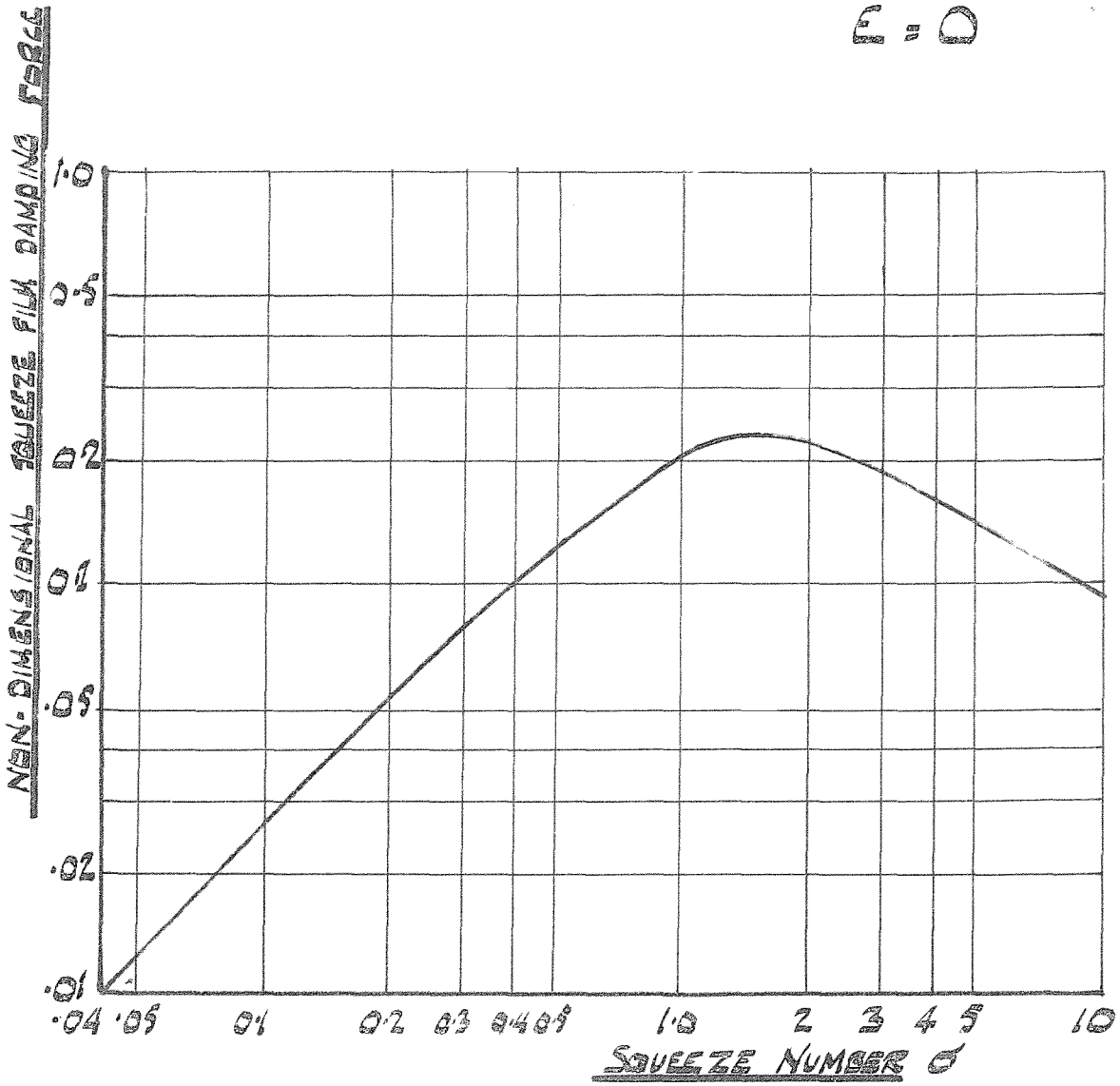

FIG 7.2.2.

THEORETICAL DAMPING COEFFICIENT FOR VARYING CLEARANCE AND VIBRATION FREQUENCY

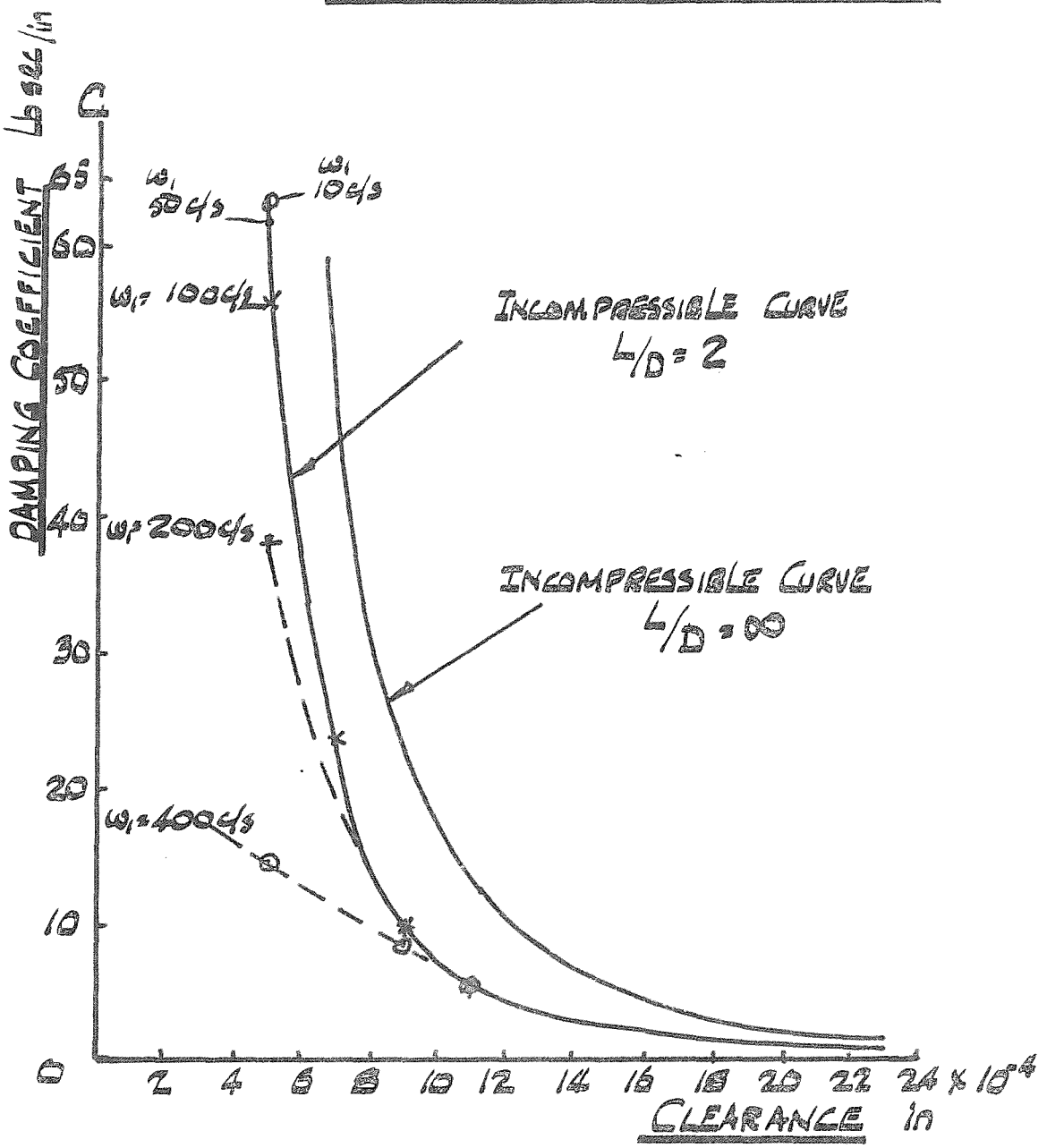

FIG 7.2.3

THEORETICAL VARIATION OF DAMPING COEFFICIENT WITH VIBRATION FREQUENCY AT DIFFERENT CLEARANCES

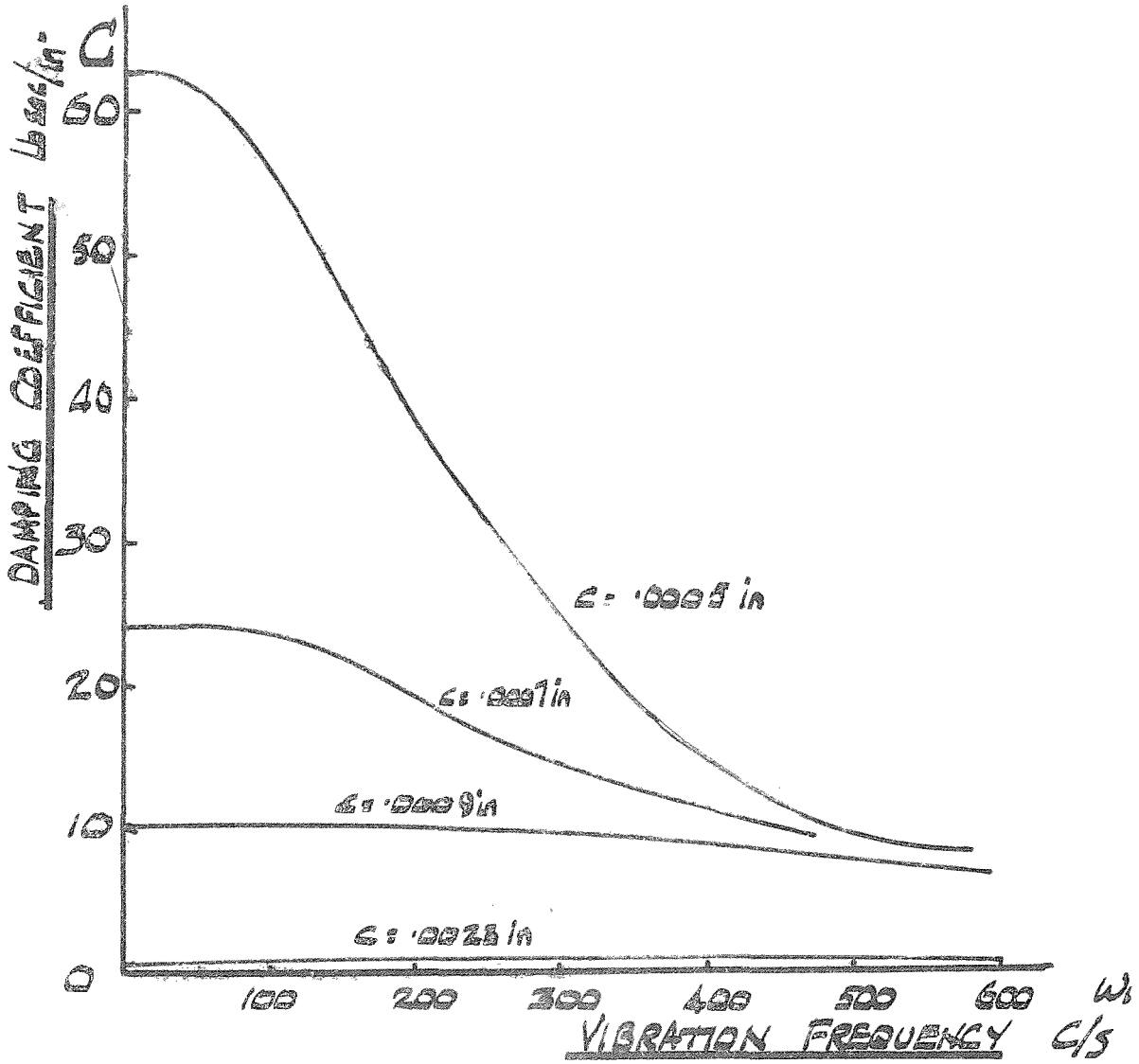

FIG 7.3.1

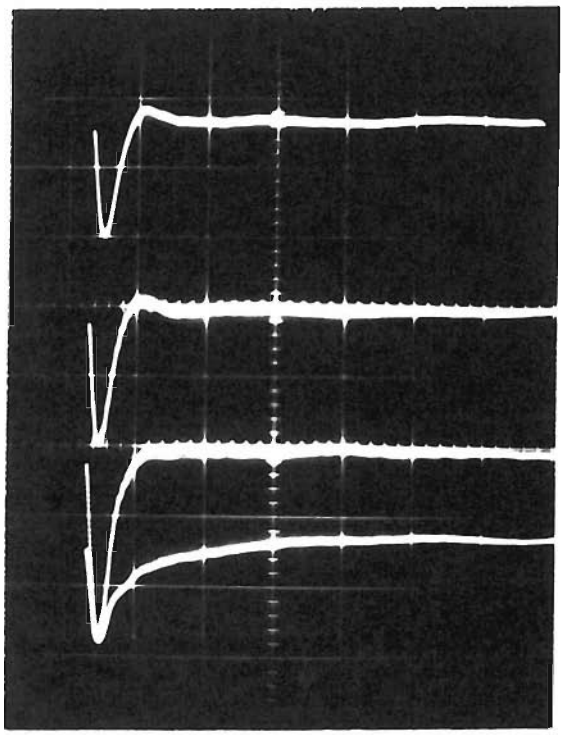

ROTOR 4

P_s = 80 psig

DAMPED FREE

PLANAR

VIBRATIONS

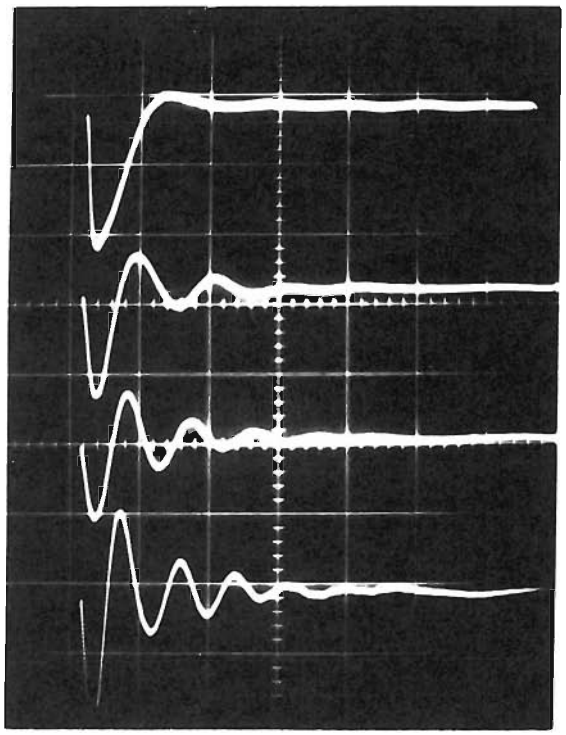

ROTOR 3

P_s = 30 psig

FIG 7.4.2

EXPERIMENTAL DAMPING RESULTS

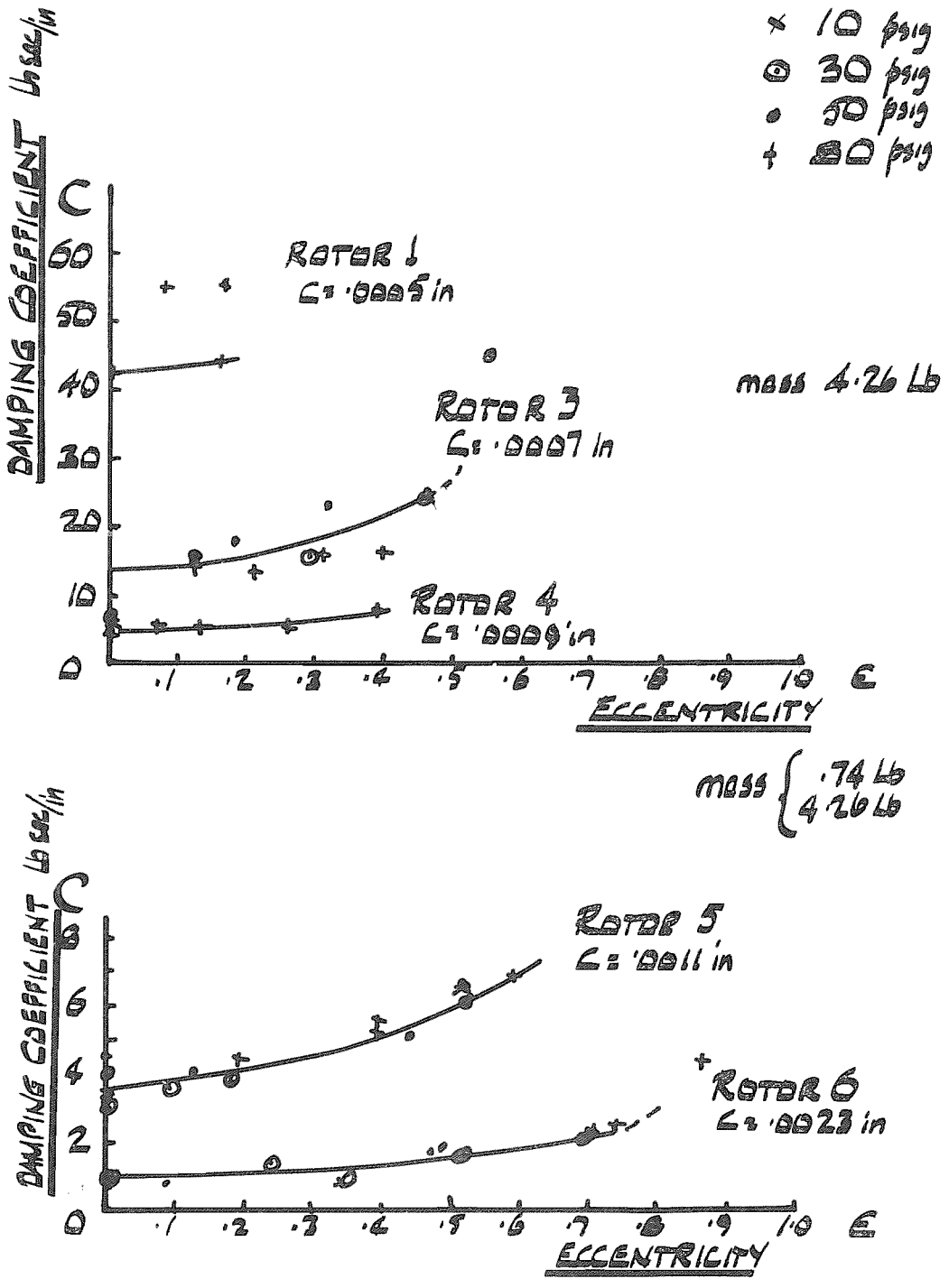

FIG 7.4.3

EFFECT OF SUPPLY PRESSURE ON DAMPING

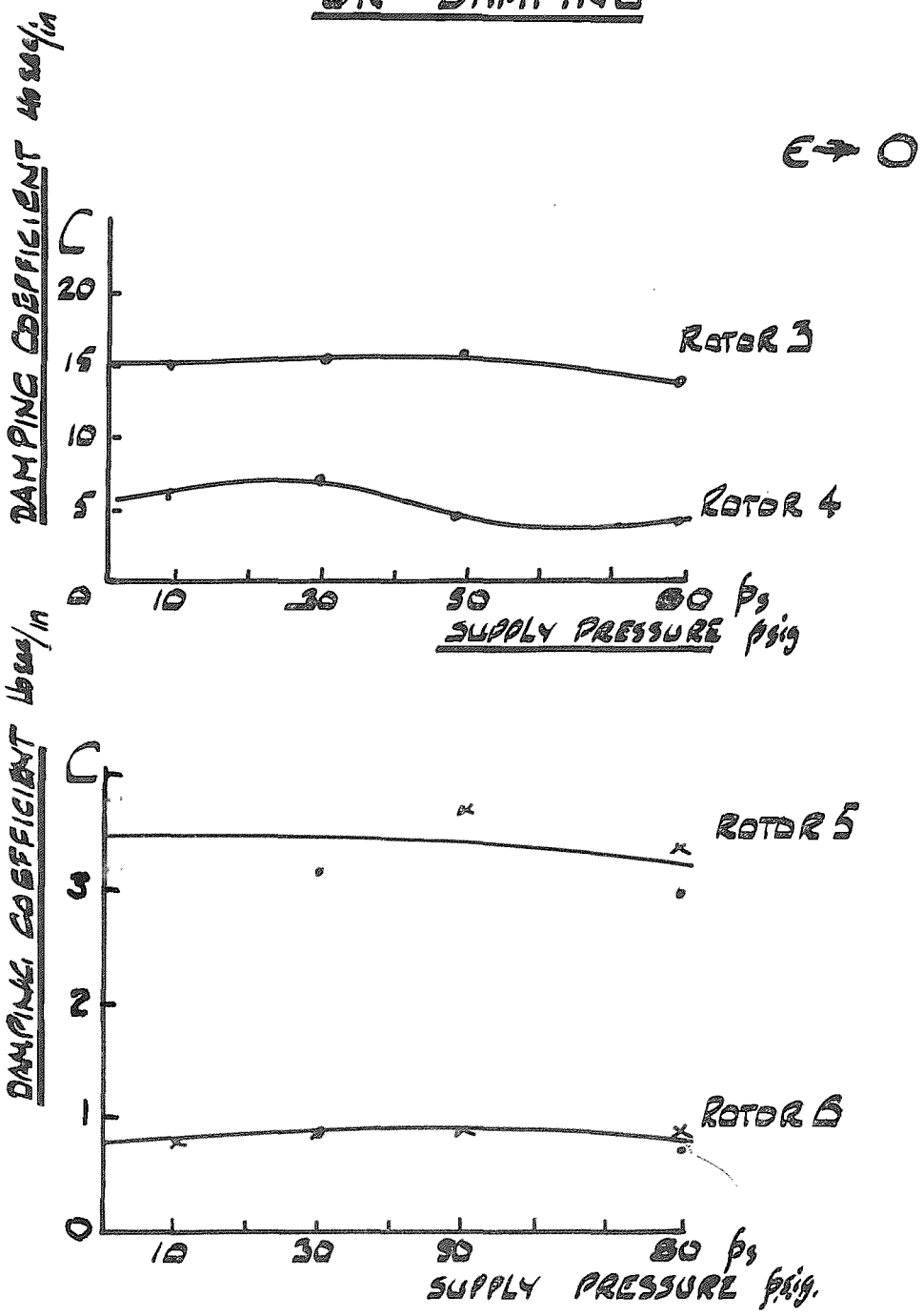

FIG 7.4.4

DAMPING VS CLEARANCE

E.O

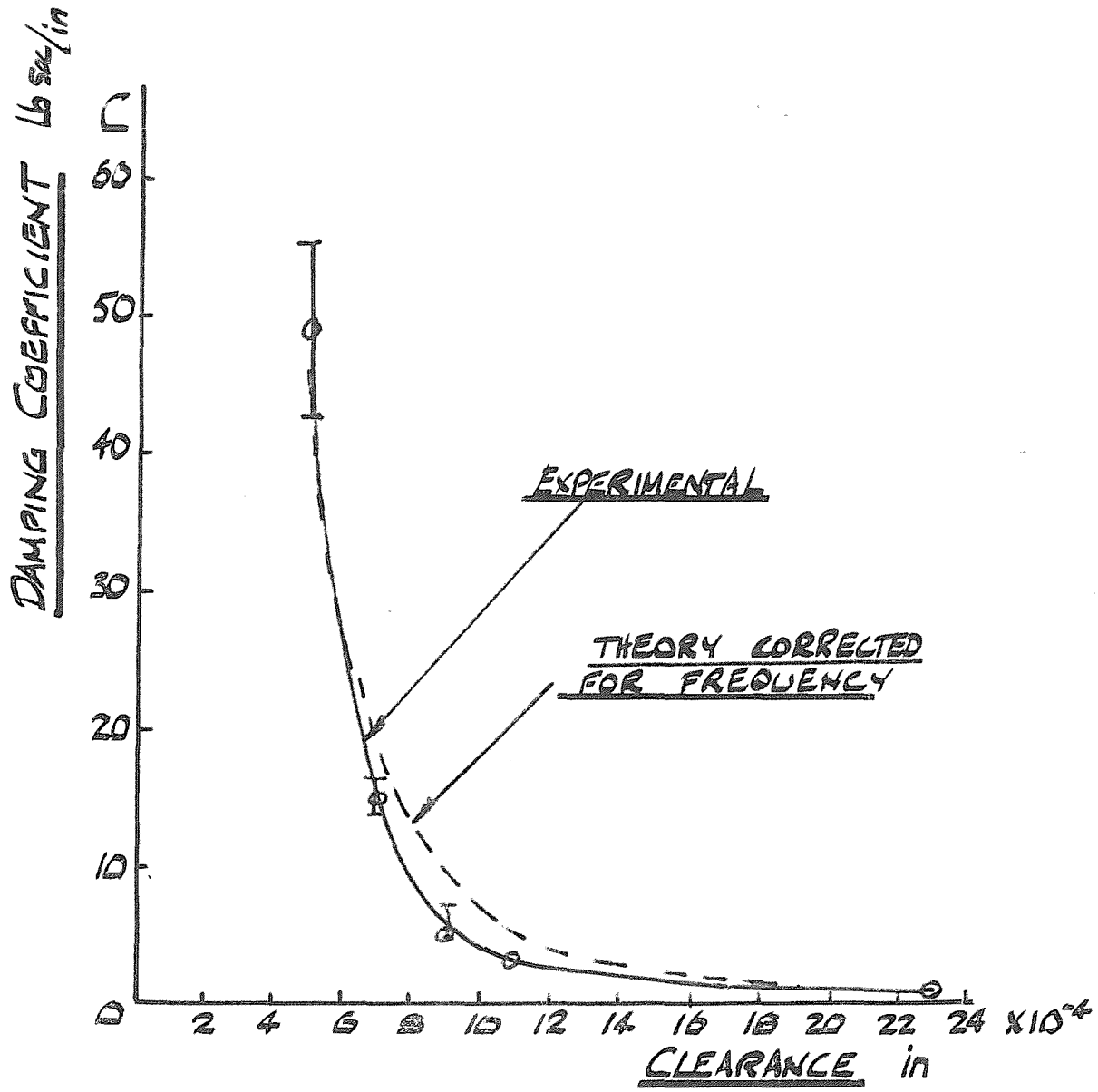

FIG 7.4.5

DAMPING VS ECCENTRICITY RATIO

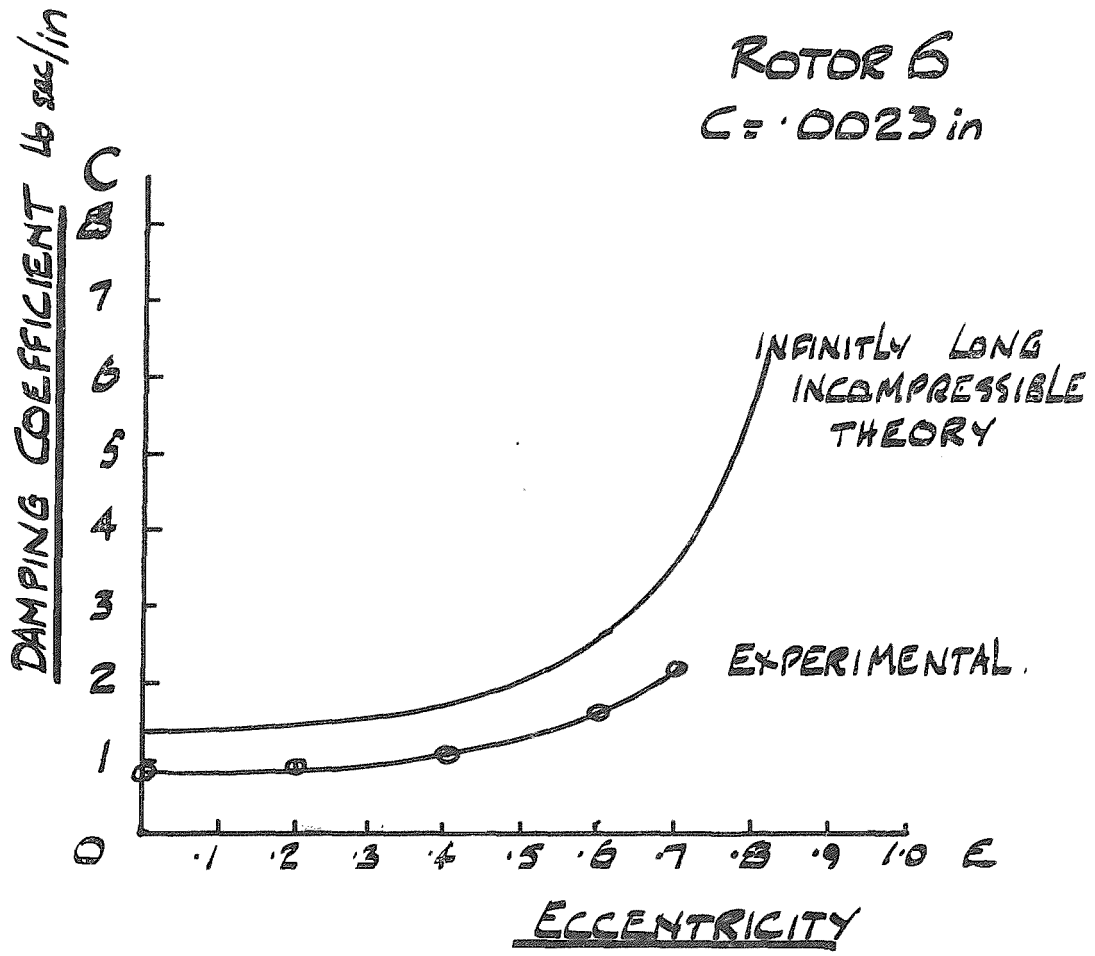

FIG 7.4.6.

COMPARISON OF NATURAL FREQUENCY CALCULATED FROM STATIC STIFFNESS AND MEASURED

$\epsilon = 0$

* STATIC

● DYNAMIC.

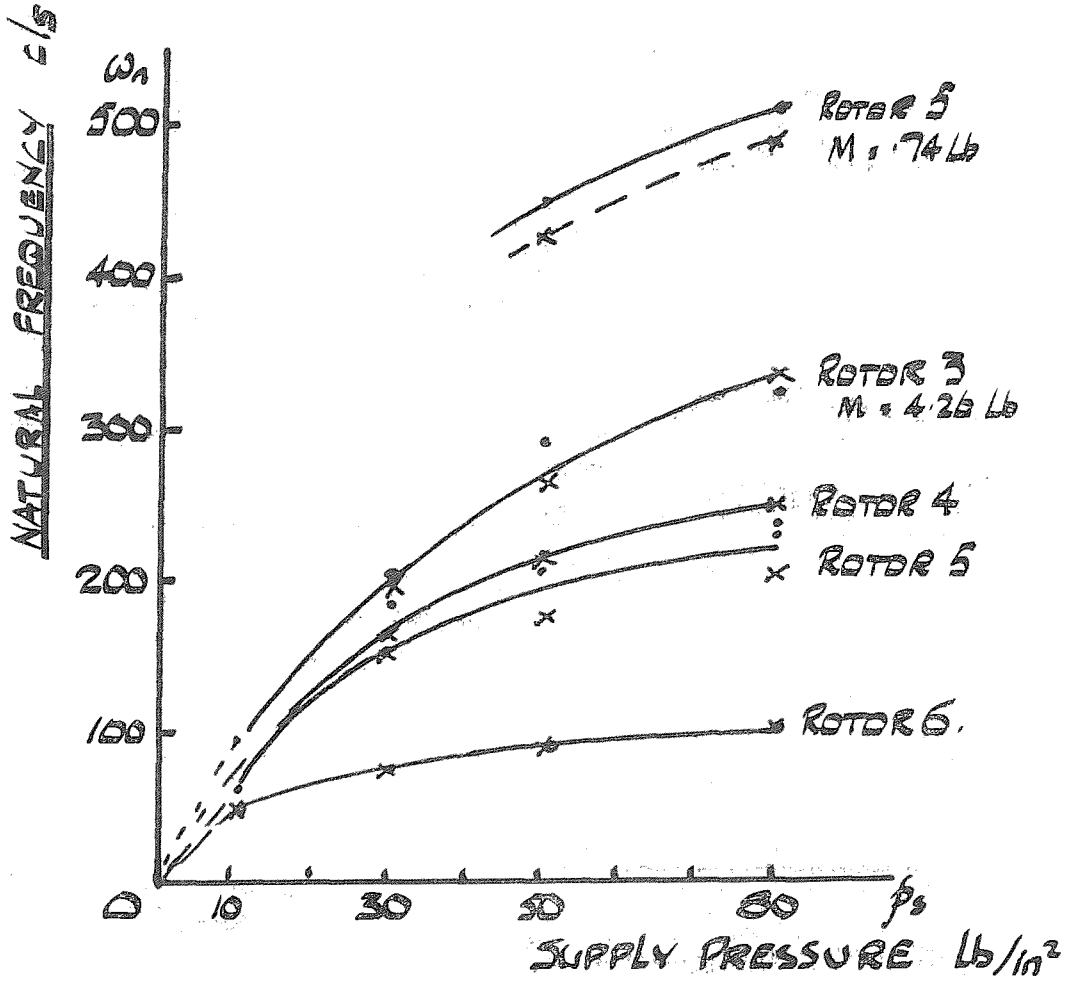

FIG 7.4.7.

MEASURED EFFECT OF ECCENTRICITY ON NATURAL FREQUENCY

ROTOR 6
C = .0023 in
M = .74 lb

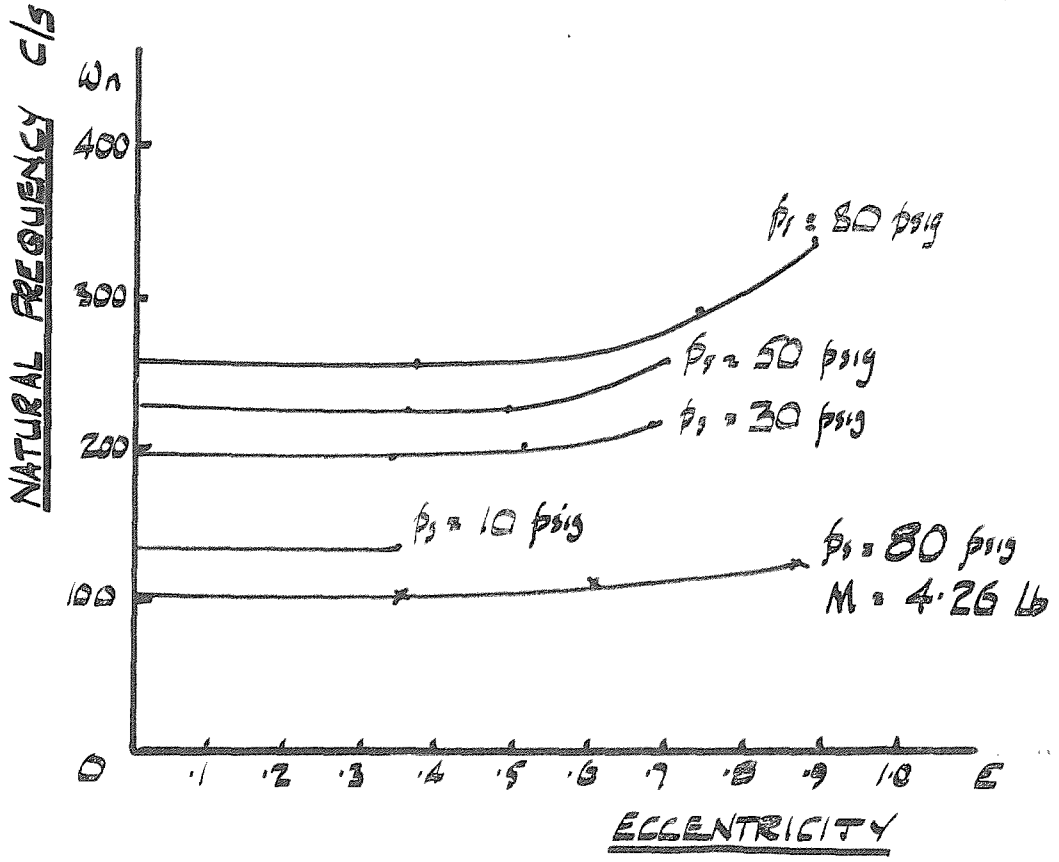

Fig 3.2.1

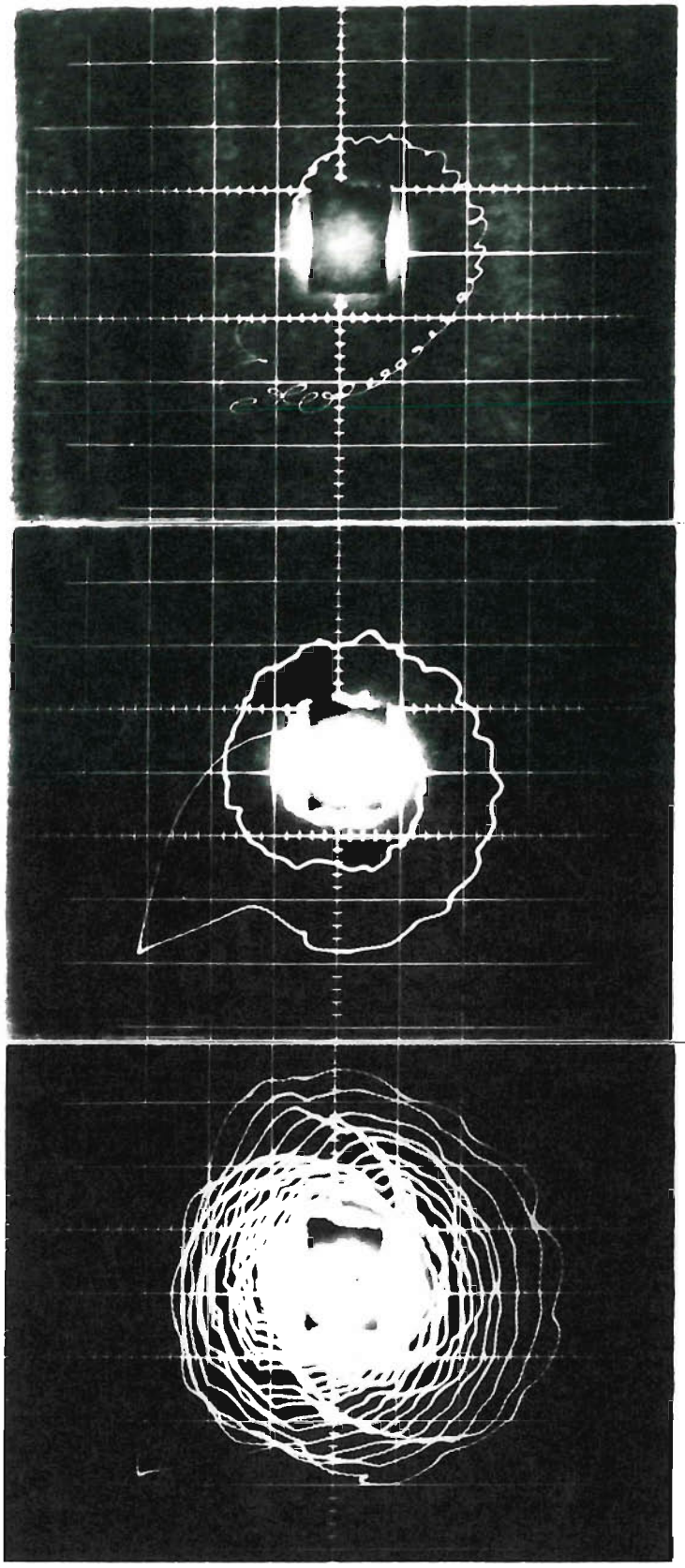

10000 rpm

19700 rpm

30000 rpm

DAMPED VIBRATION ORBITS.

FIG 8.3.1.

DAMPING AND NATURAL FREQUENCY VS SPEED

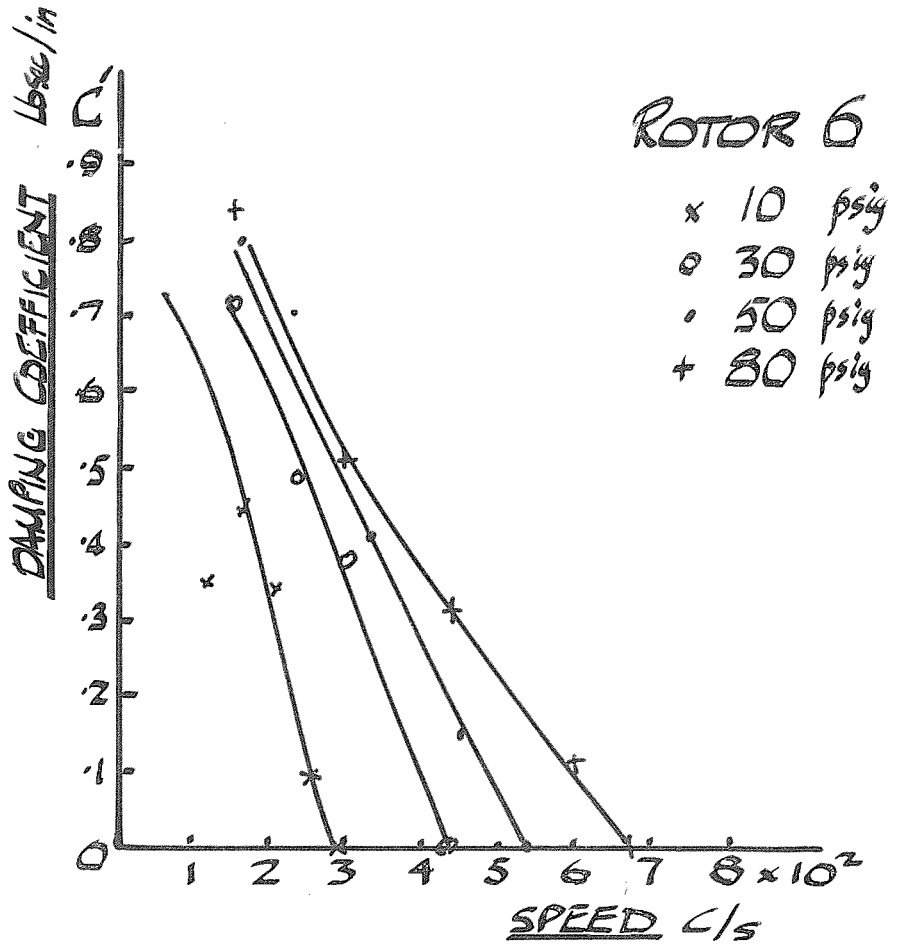

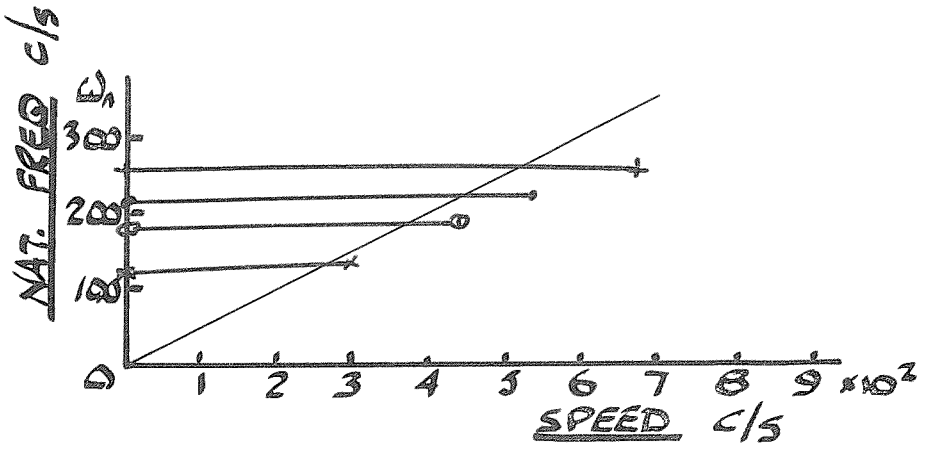

FIG 8.3.2.

DAMPING AND NATURAL FREQUENCY VS SPEED

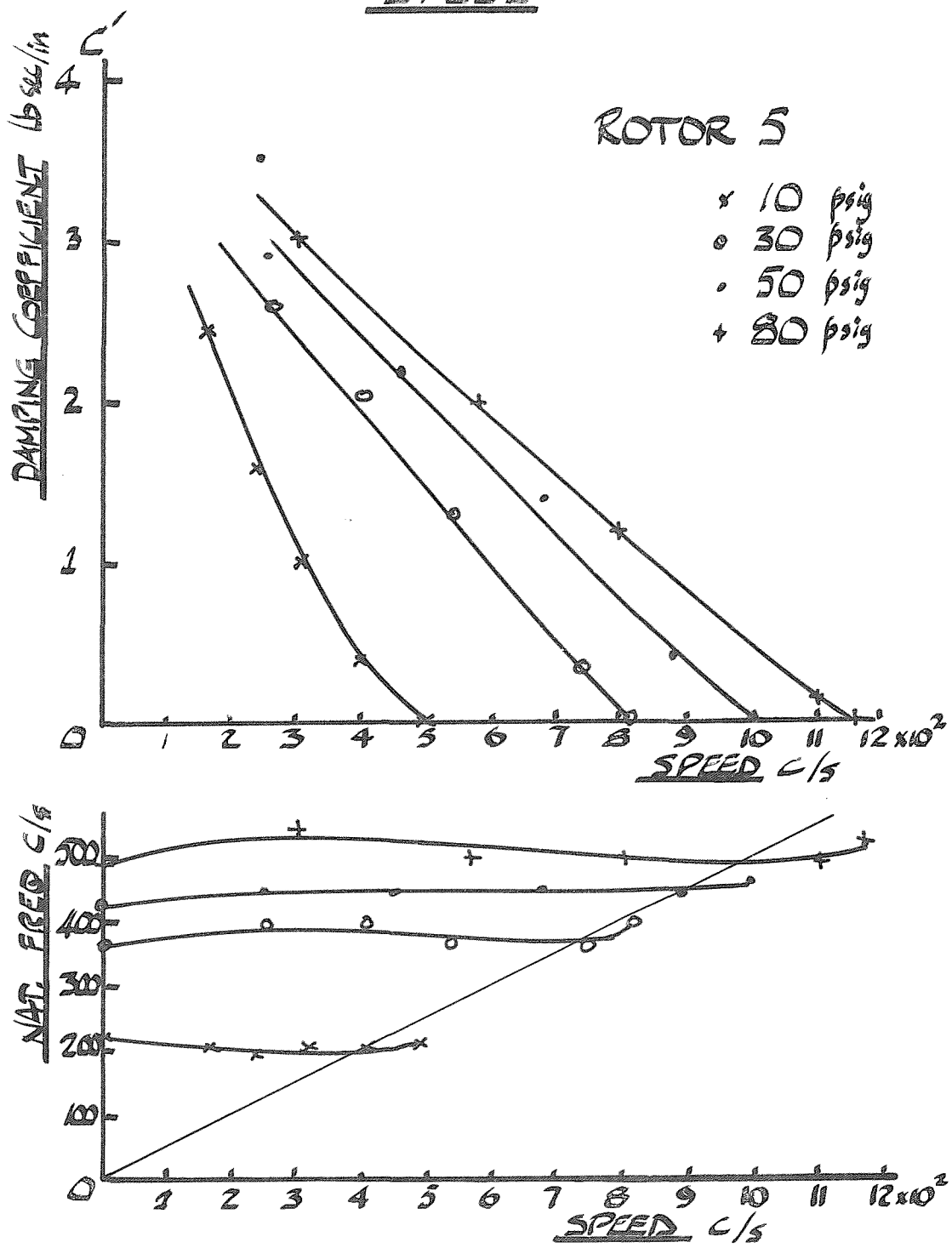

FIG 8.3.3.

DAMPING AND NATURAL FREQUENCY VS SPEED

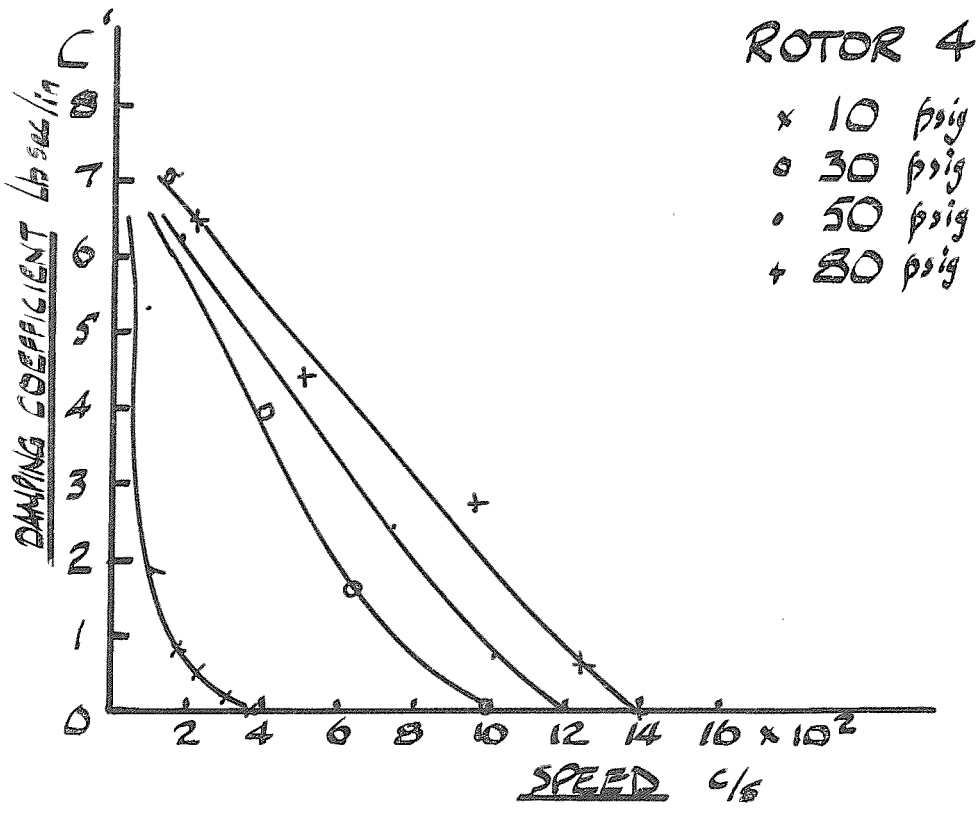

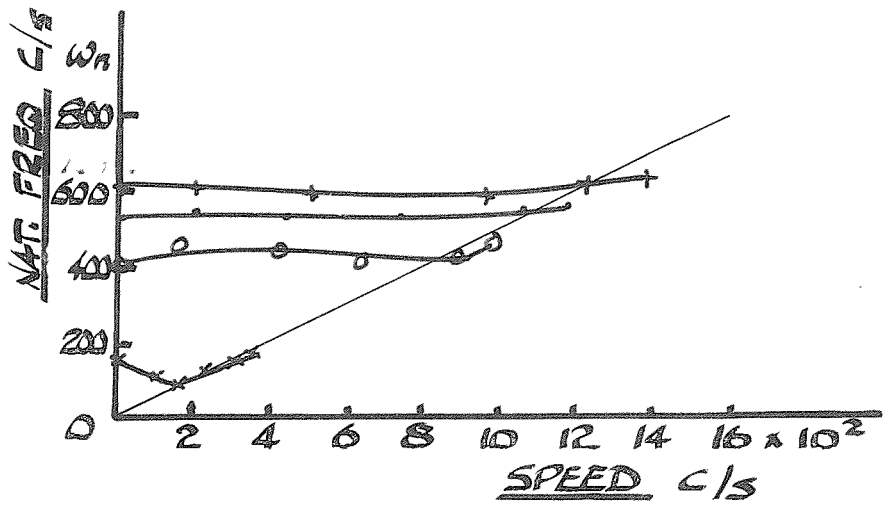

FIG 8.3.4.

DAMPING AND NATURAL FREQUENCY VS SPEED

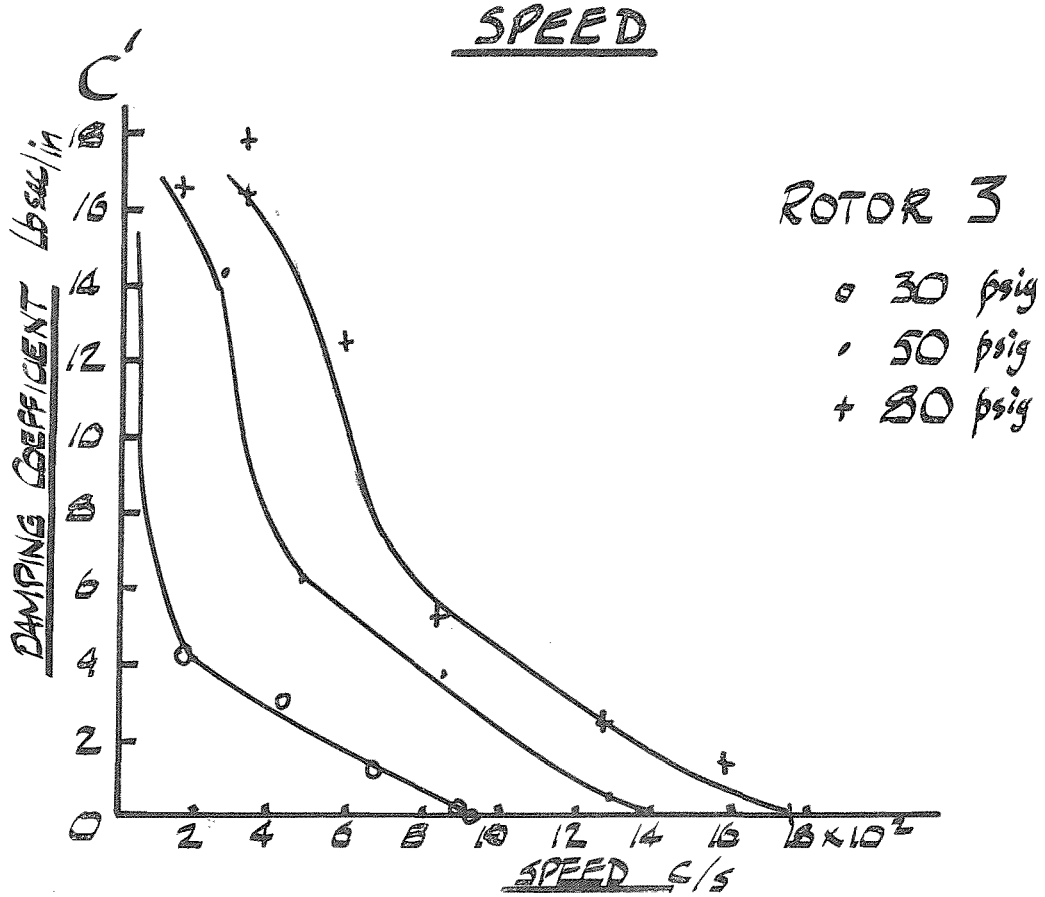

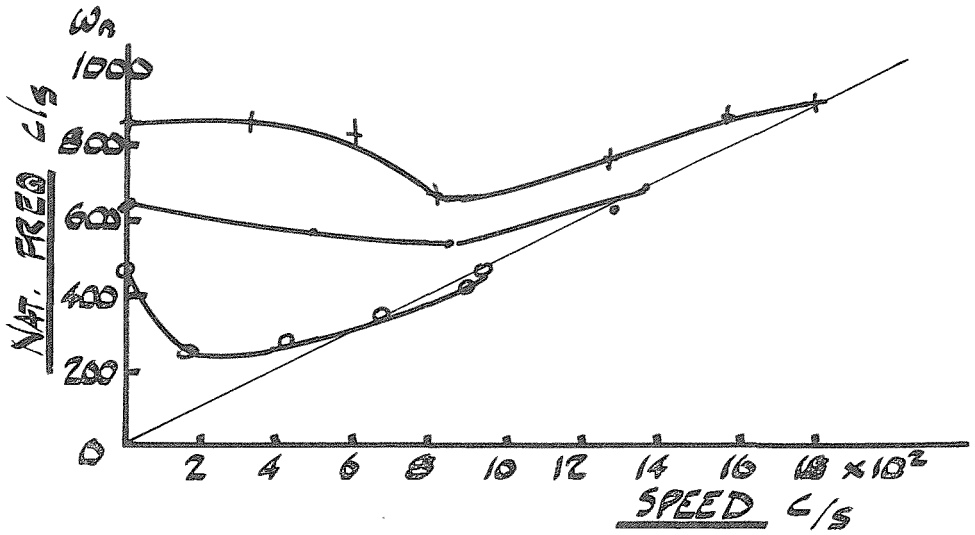

FIG 8.3.5.

DAMPING AND NATURAL FREQUENCY VS SPEED

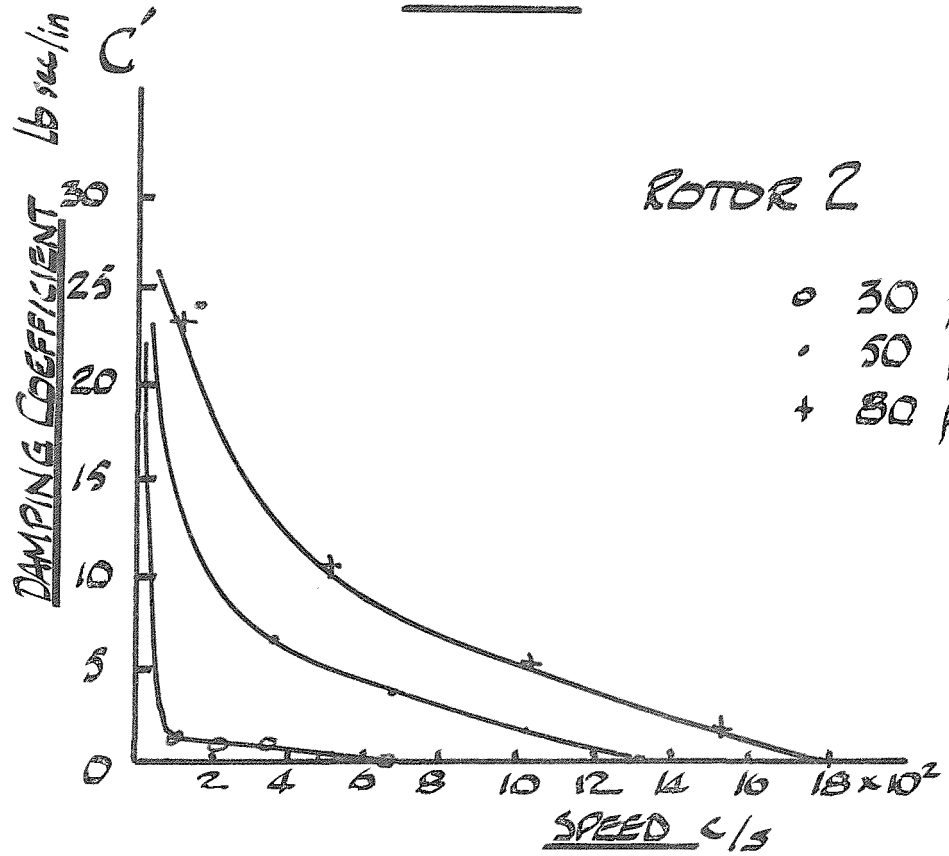

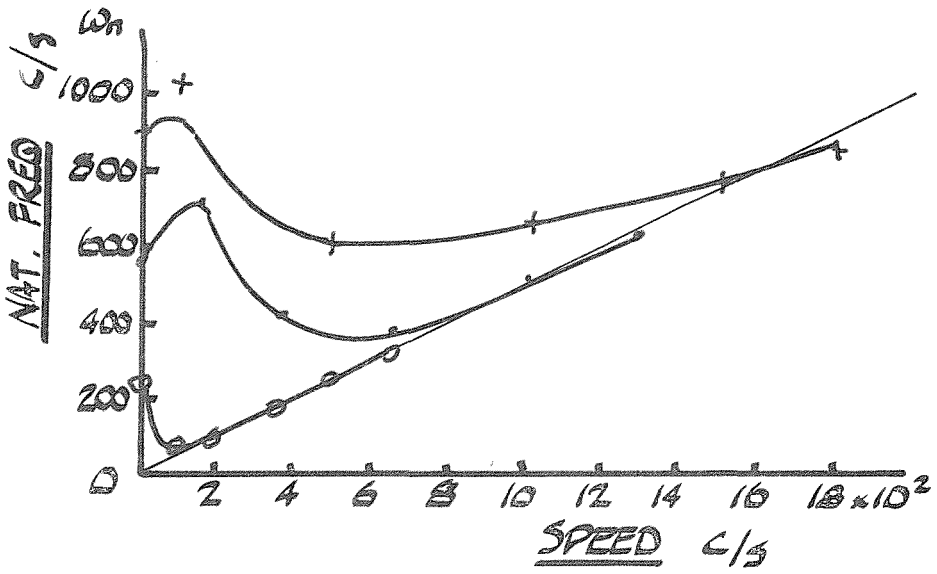

FIG B.3.6.

DAMPING AND NATURAL FREQUENCY VS SPEED

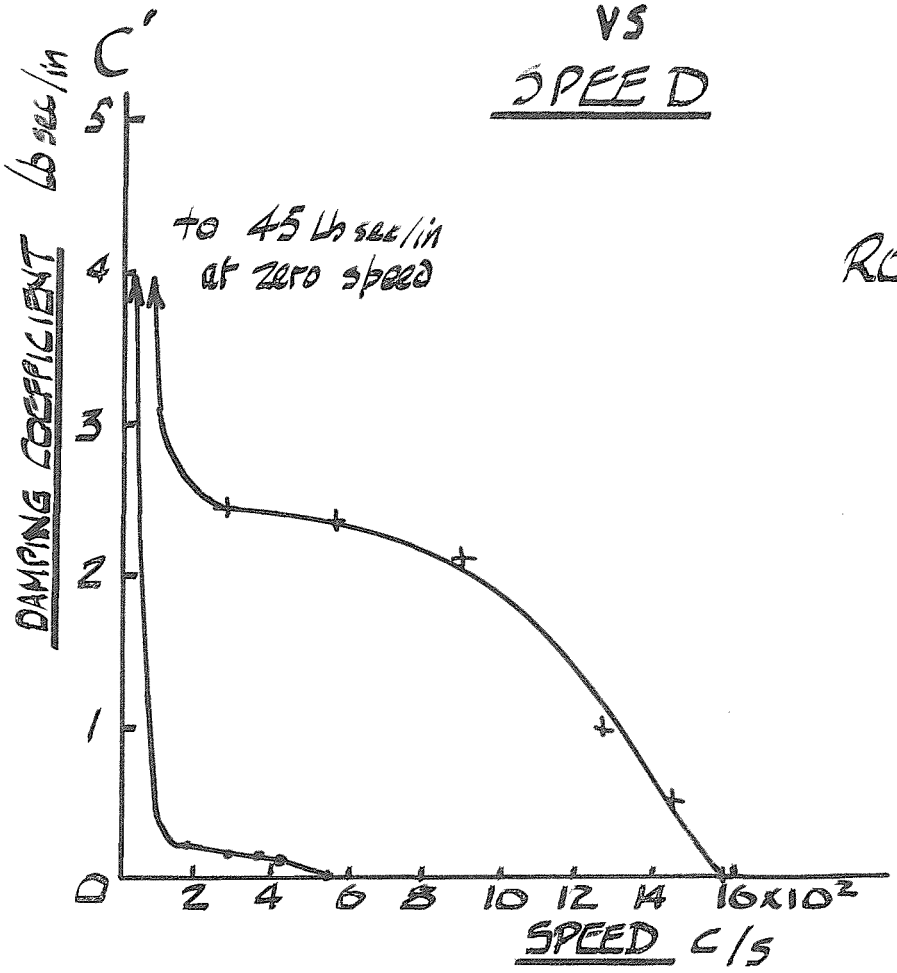

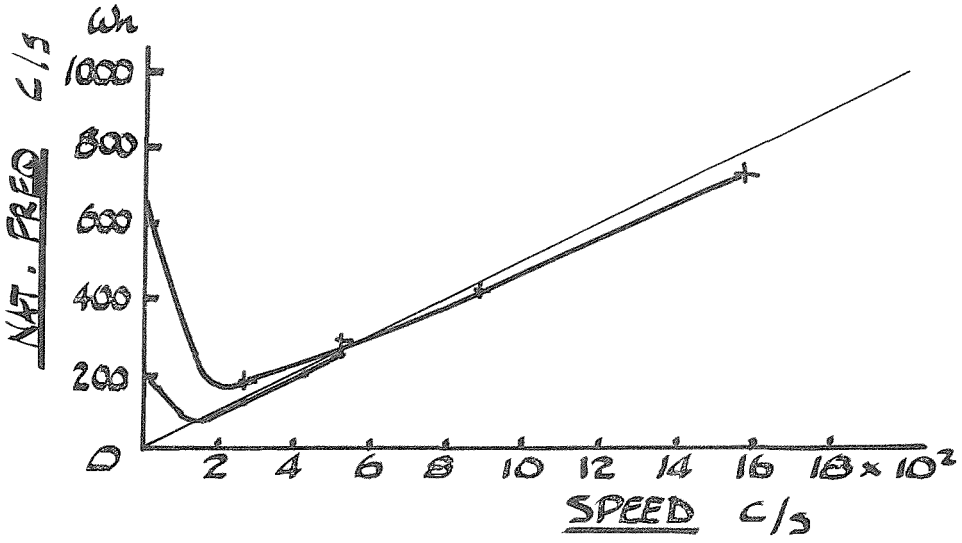

FIG 9.1.1.

OUT OF BALANCE FORCE SYSTEM

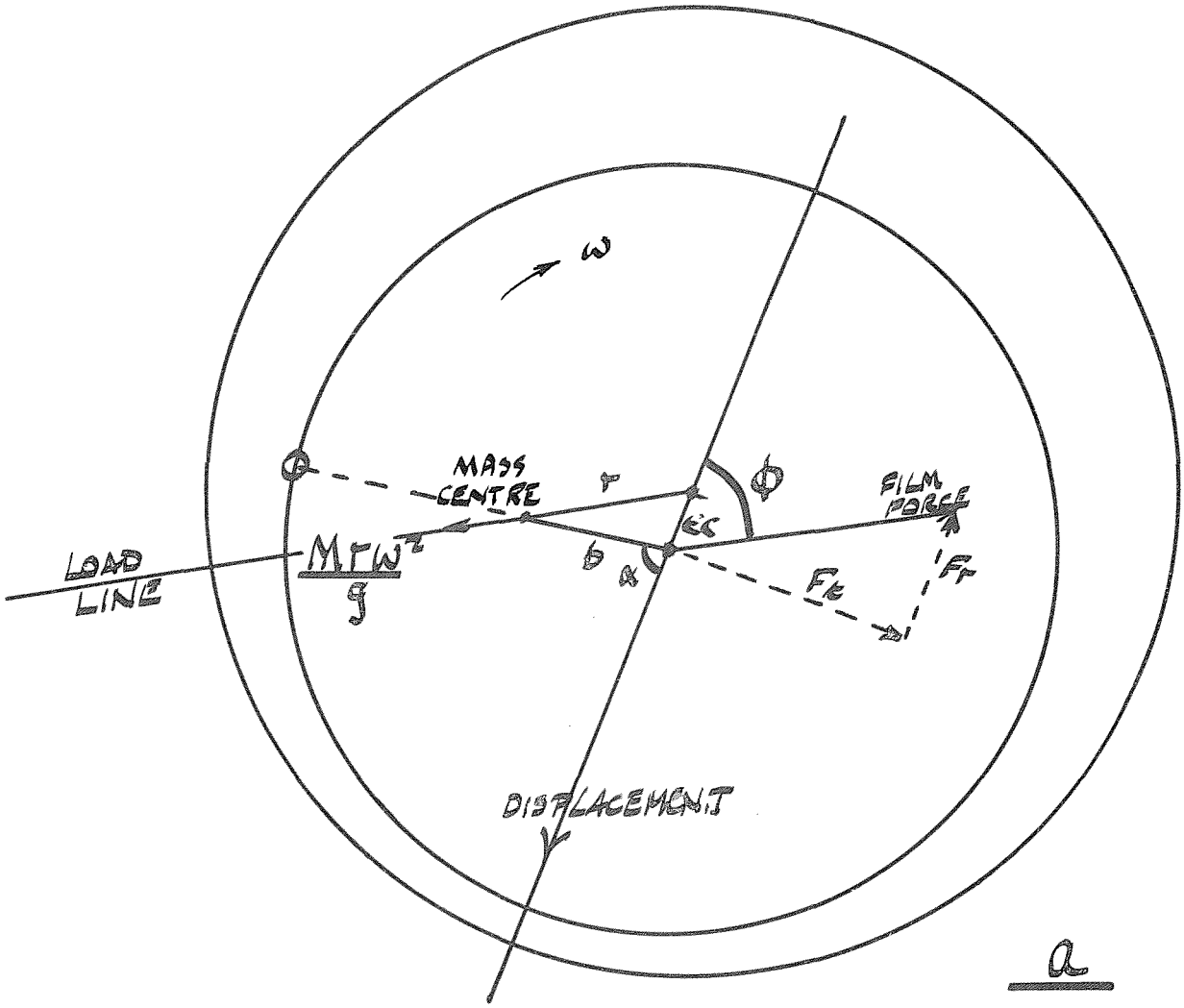

a

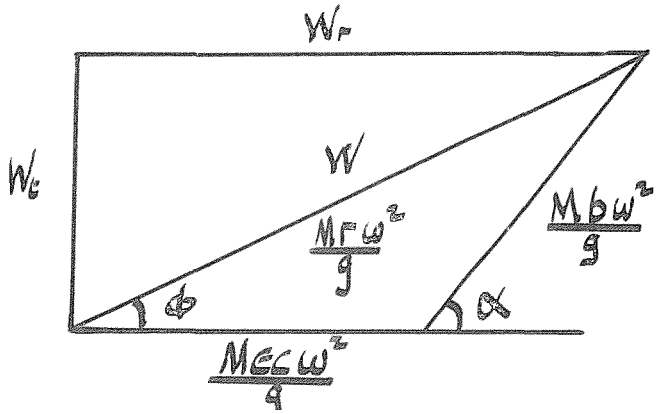

b

FIG 9.2.1

THEORETICAL AERODYNAMIC BEARING RESPONSE TO UNBALANCE LOADING

R = .75 in L = 1.5 in M = .746 δ = .000204 in

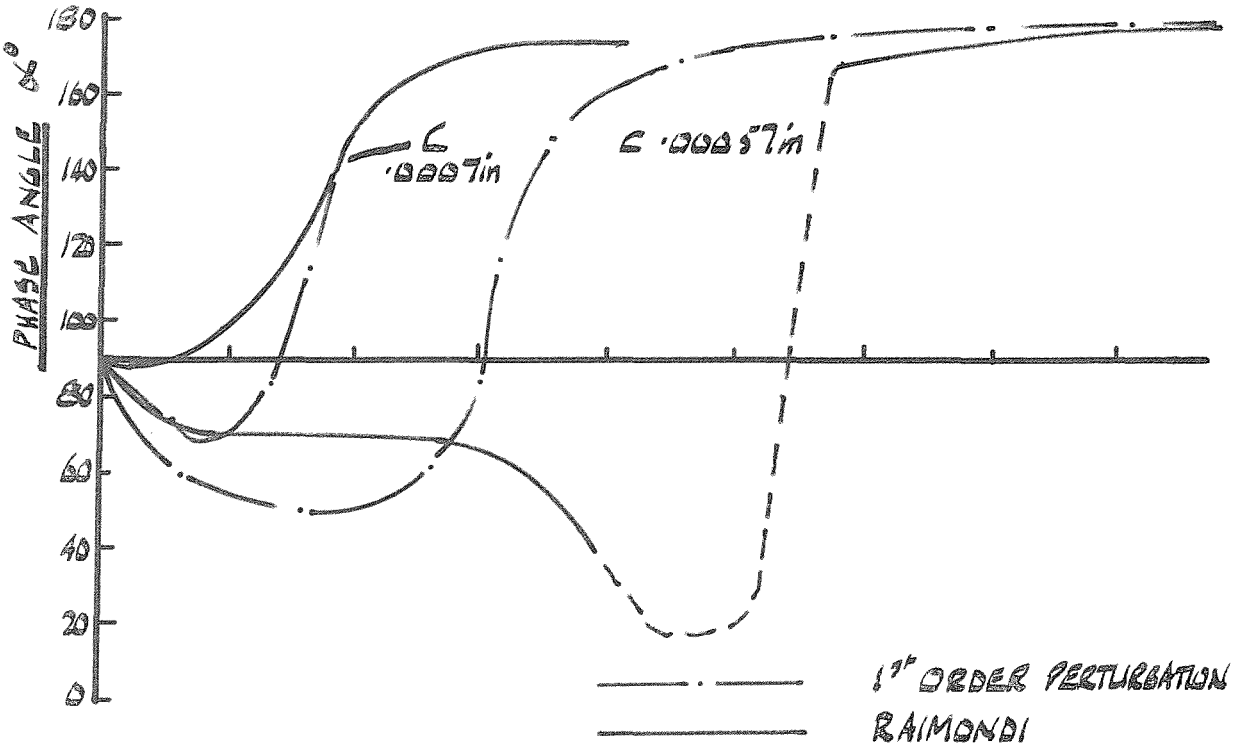

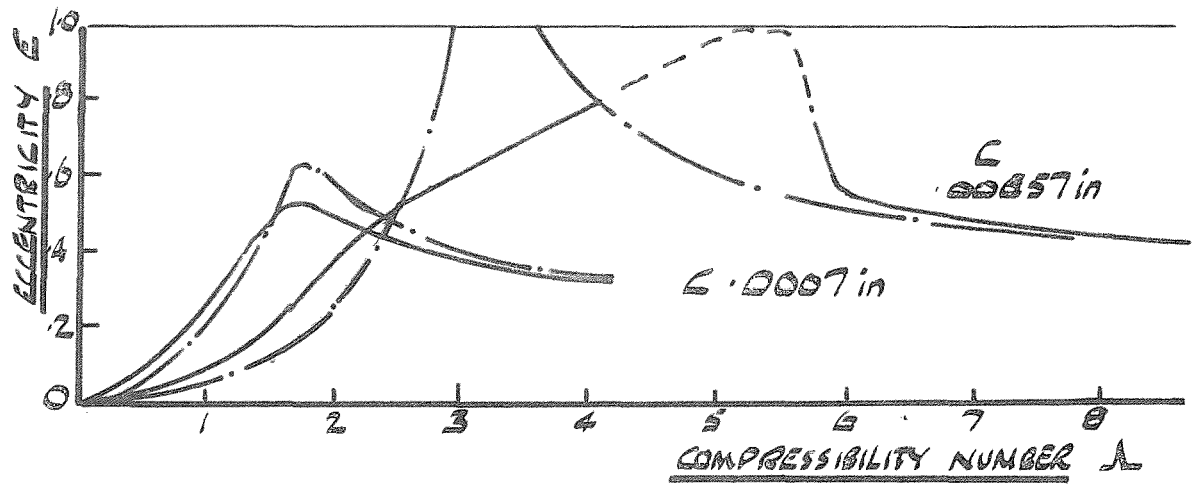

FIG 9.2.2.

THEORETICAL

AERODYNAMIC BEARING ECCENTRICITY — PHASE ANGLE RESPONSE CURVES

VARIOUS CLEARANCES $b = 2.04\ 10^{-4}$ in

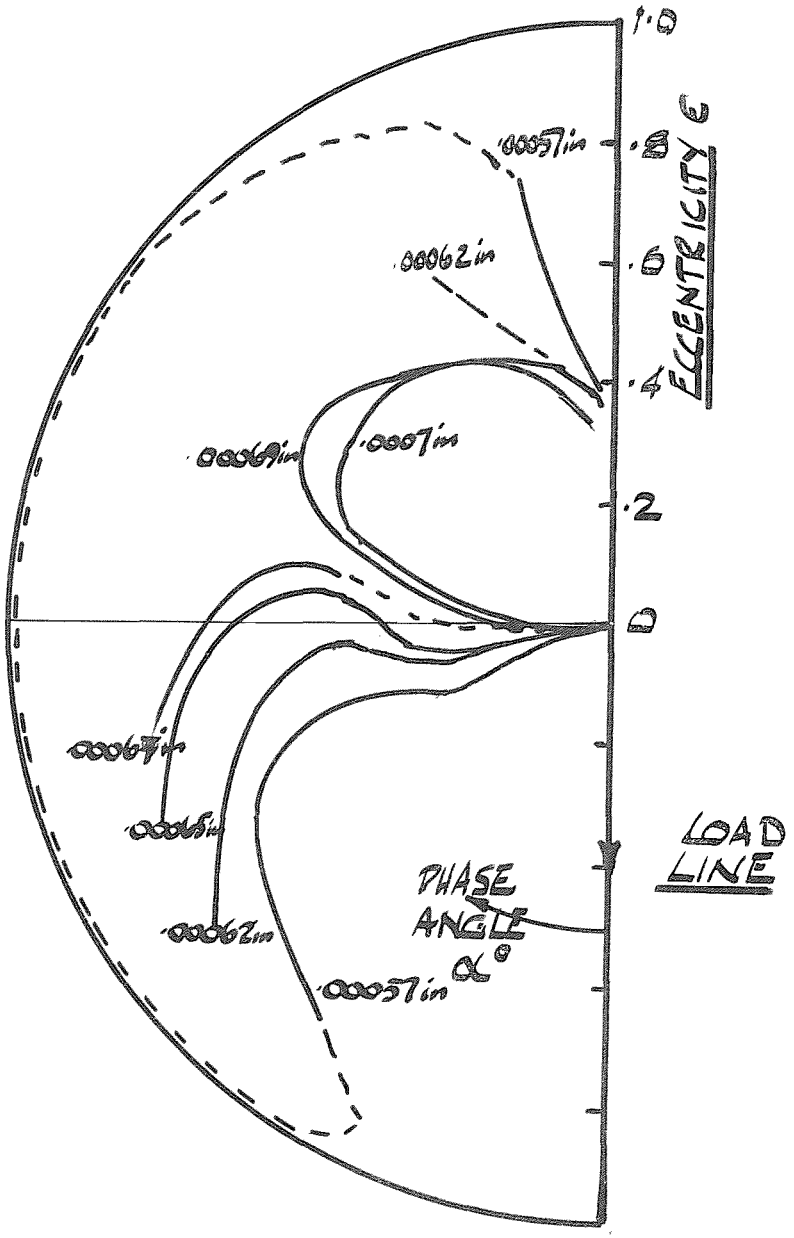

FIG 9.2.3.

AERODYNAMIC BEARING AMPLITUDE AND PHASE ANGLE RESPONSE CURVES

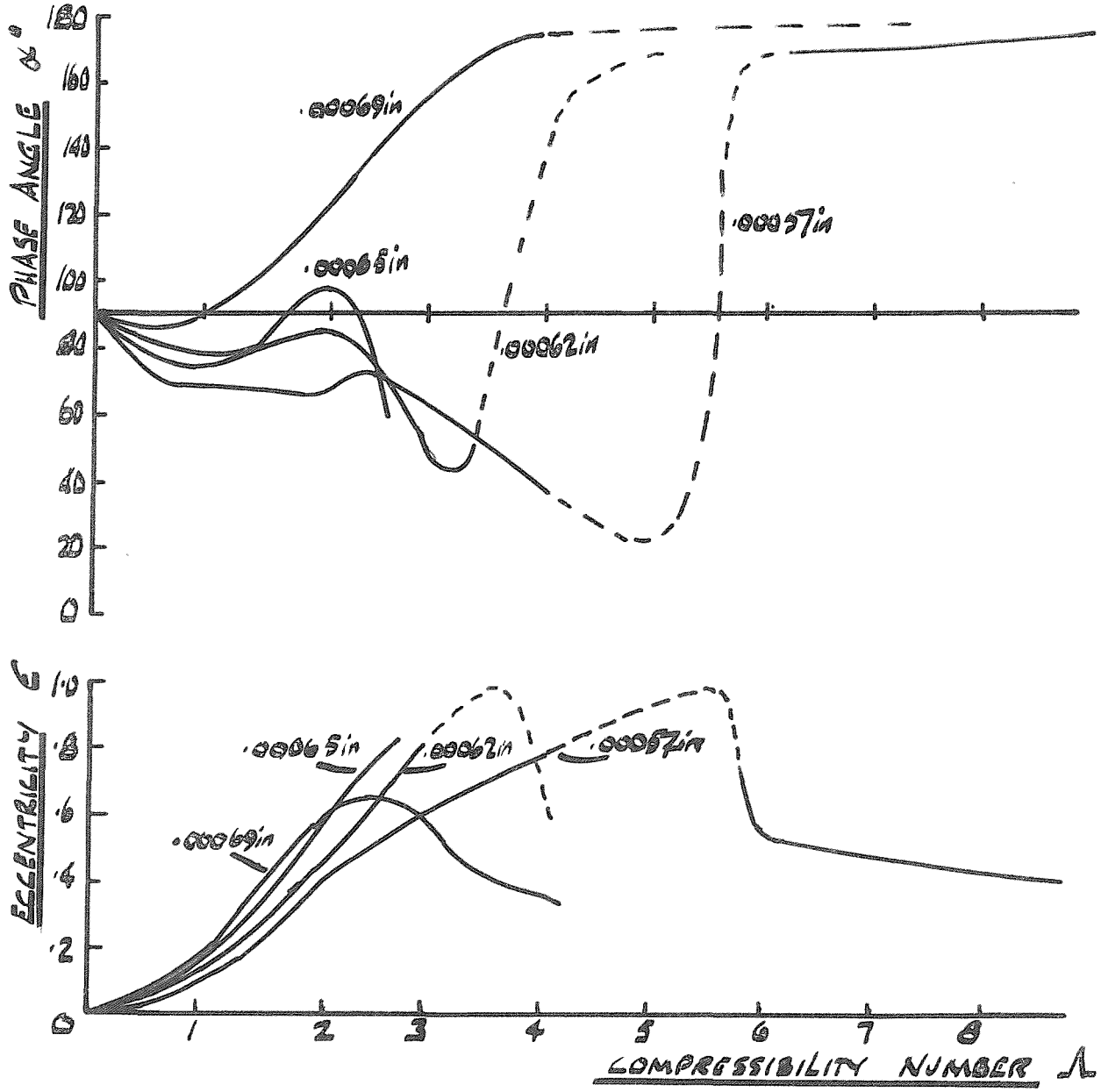

FIG 9.2.4.

COMPARISON OF THEORY (RAIMONDI) WITH EXPERIMENT FOR AERODYNAMIC BEARING

ROTOR 1 $c = .00062$ in
$b = .000204$ in

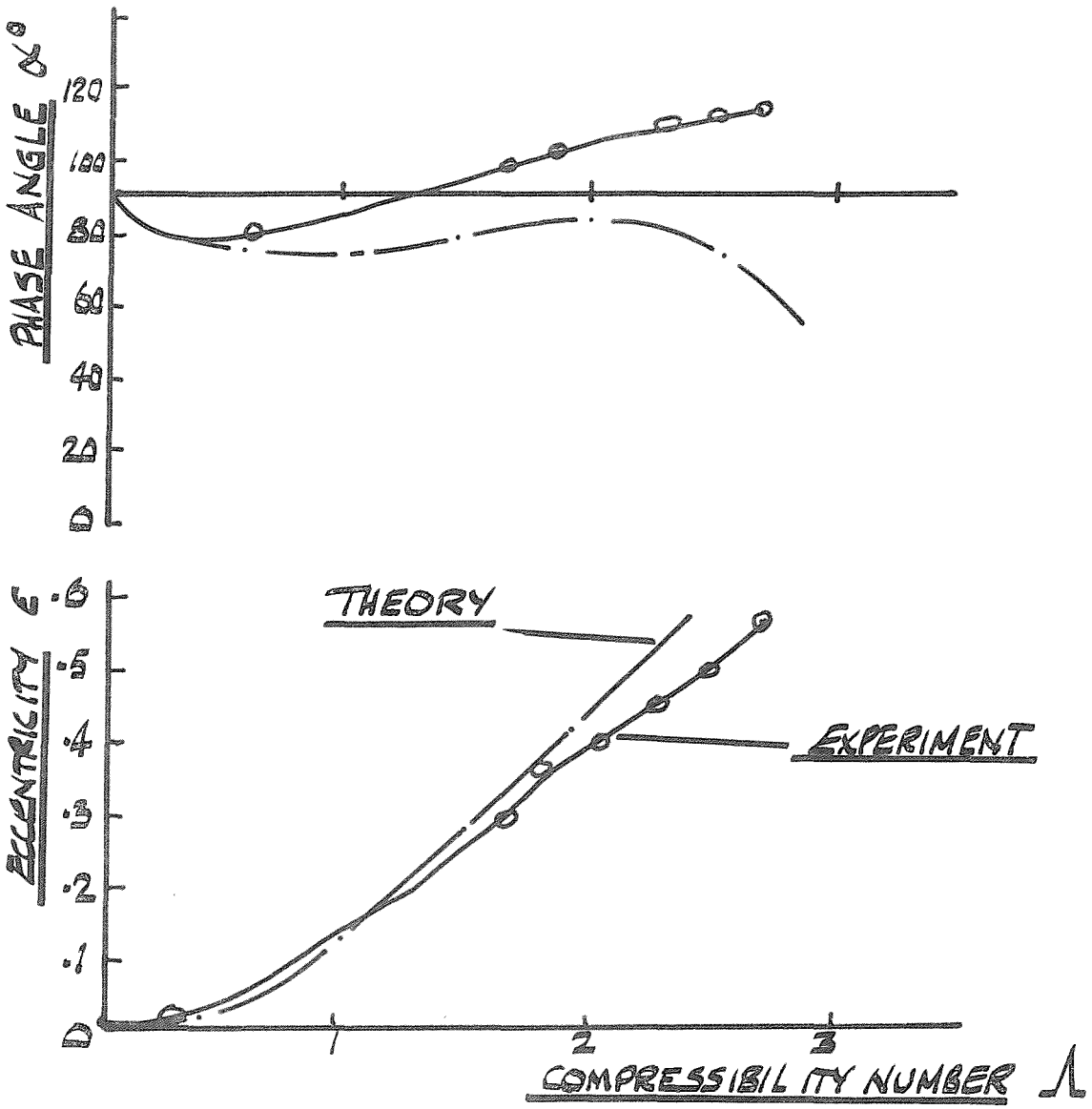

FIG 9.3.1.

THEORETICAL HYBRID BEARING RESPONSE TO UNBALANCE LOADING. 1ST ORDER PERTURBATION INFINITE LENGTH SOLUTION

$C_r = .00062$ in

AEROSTATIC STIFFNESS

① $p_s = 50$ psig $K_s = 1.45 \times 10^4$ lb/in

② $p_s = 80$ psig $K_s = 3.6 \times 10^4$ lb/in

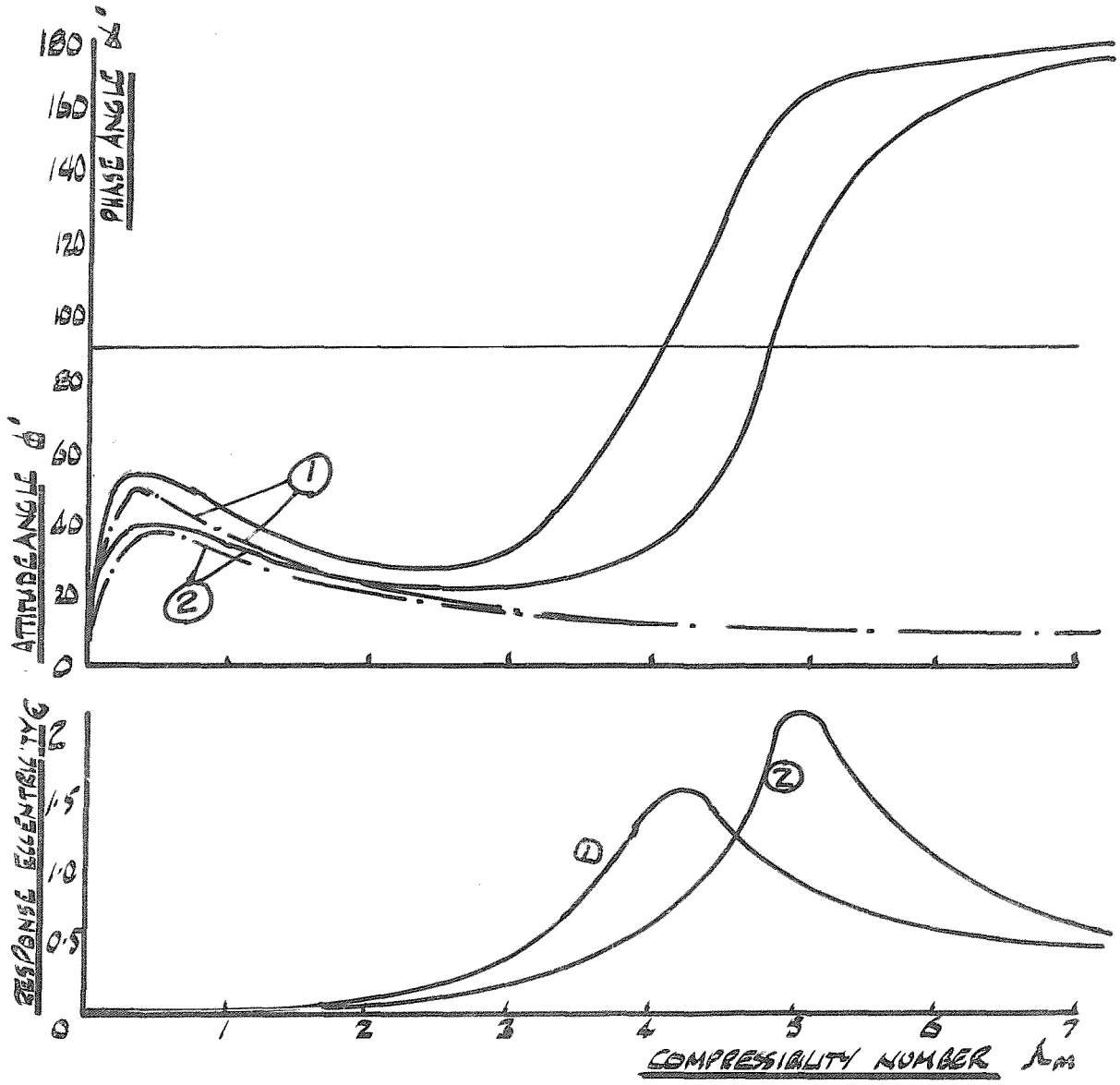

FIG 9.5.1.

HYBRID BEARING

EXPERIMENTAL PHASE ANGLE — ECCENTRICITY CURVES

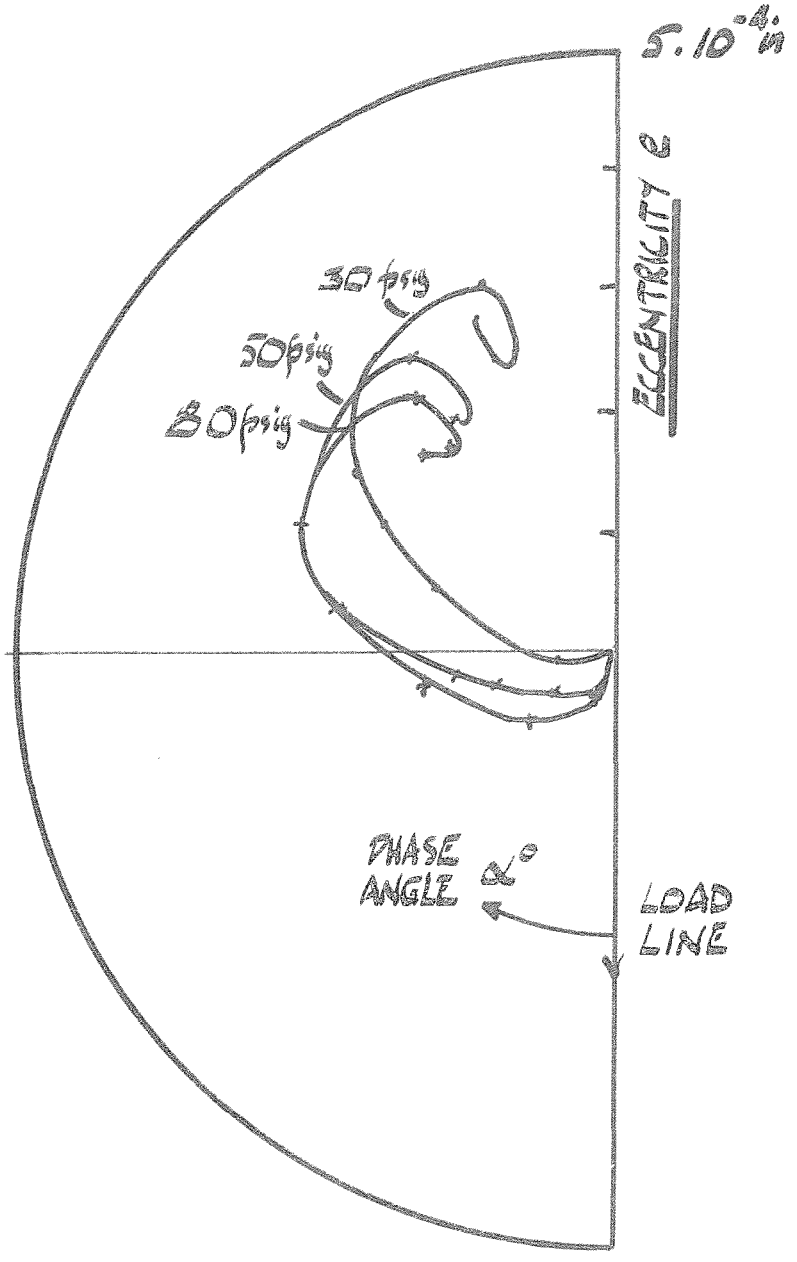

ROTOR 1

b = 2·0410⁻⁴in

FIG 9.5.2.

PHASE ANGLE — ECCENTRICITY

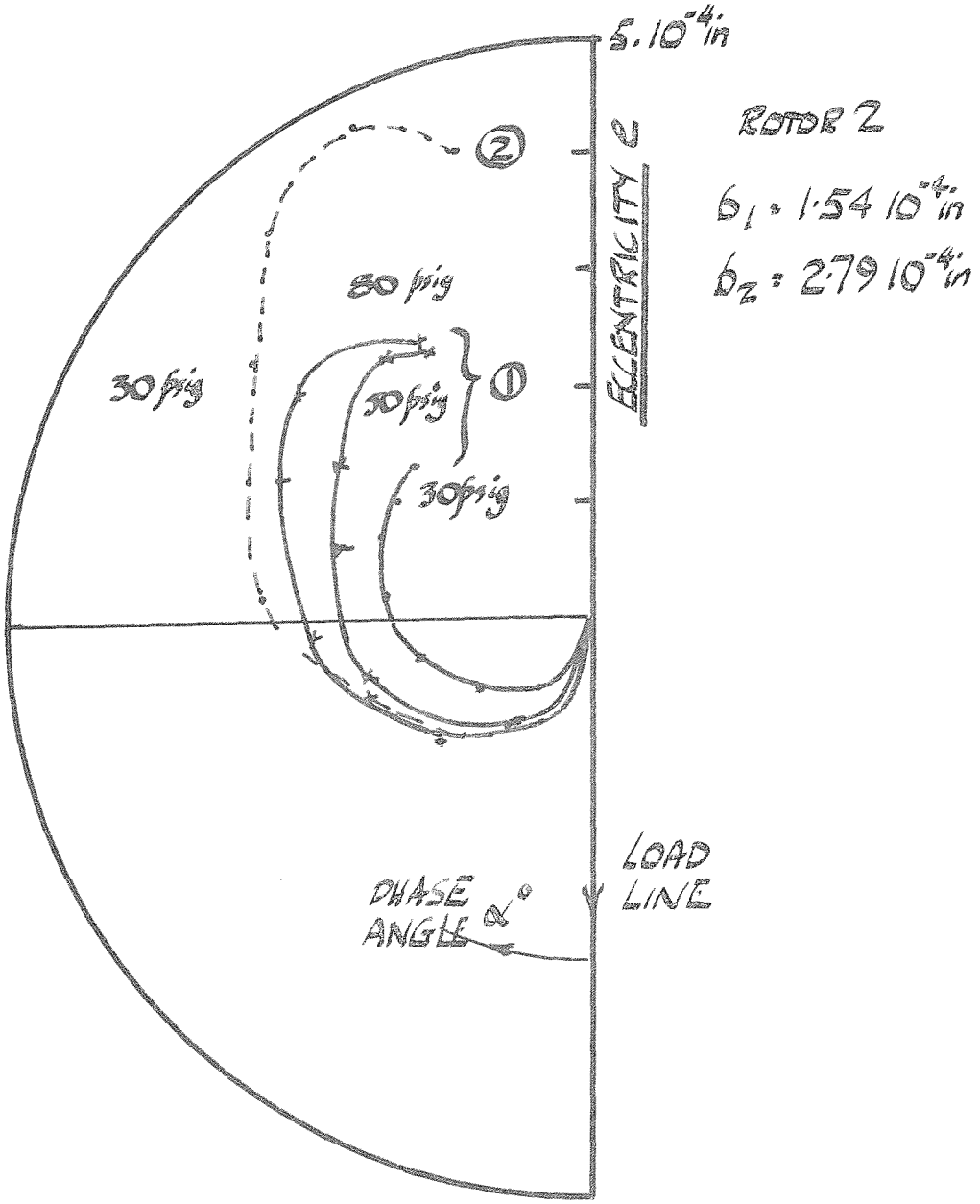

FIG 9.5.3

PHASE ANGLE — ECCENTRICITY

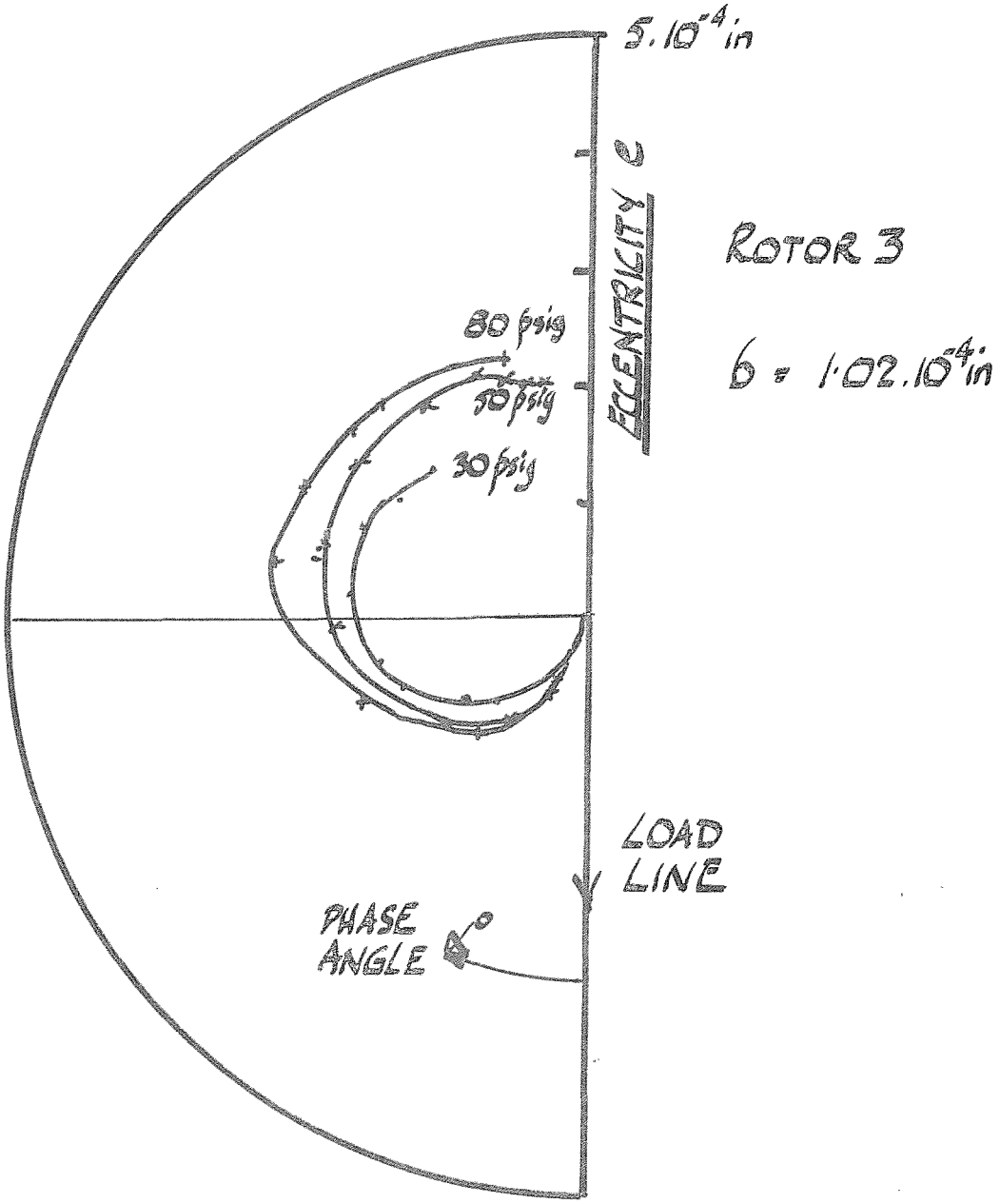

FIG. 9.5.4.

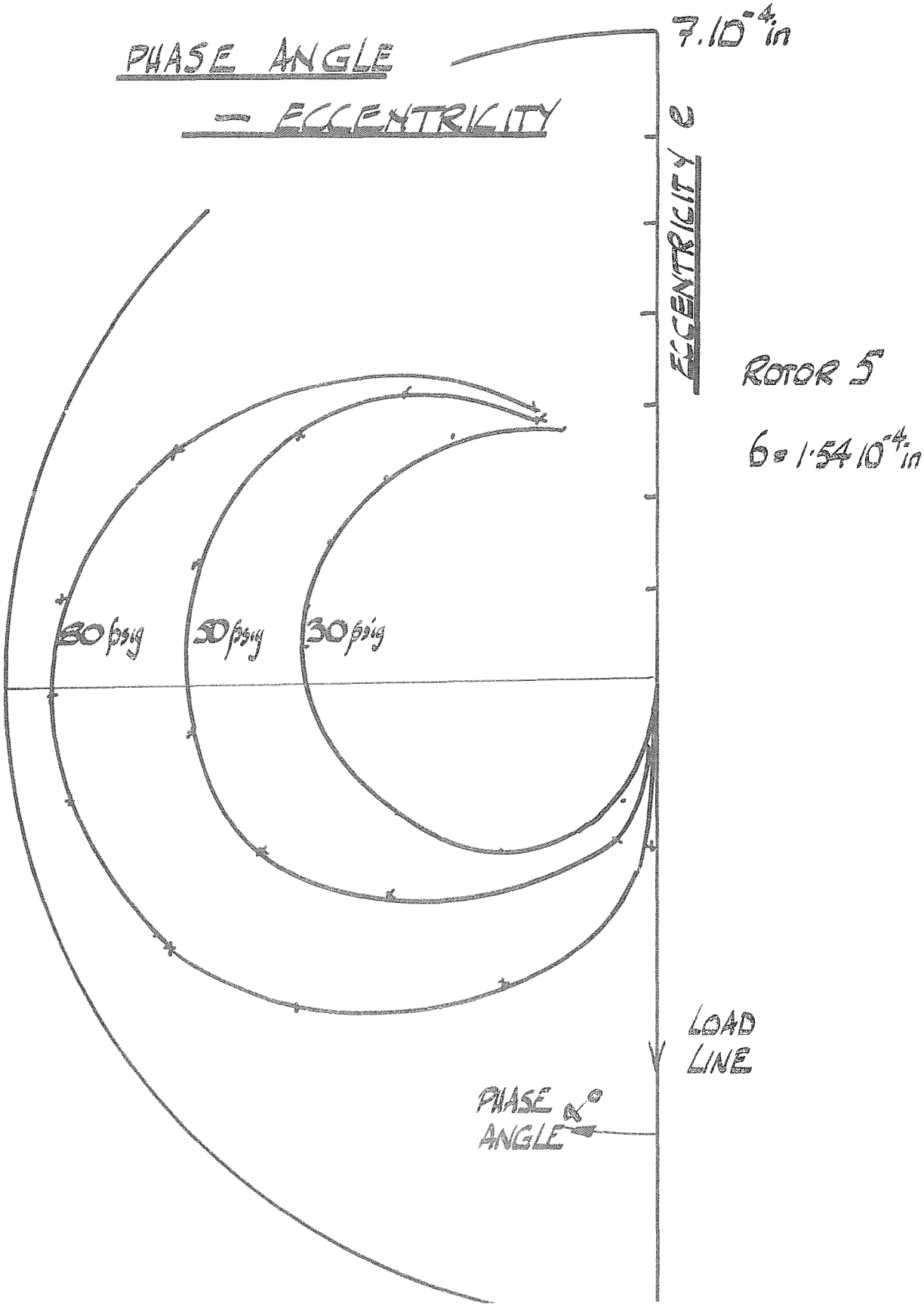
7.10⁻⁴ in
PHASE ANGLE
— ECCENTRICITY
ECCENTRICITY e
ROTOR 5
δ = 1.54 10⁻⁴ in
30 psig
50 psig
30 psig
LOAD LINE
PHASE ANGLE φ°

Fig 9.55.

PHASE ANGLE — ECCENTRICITY

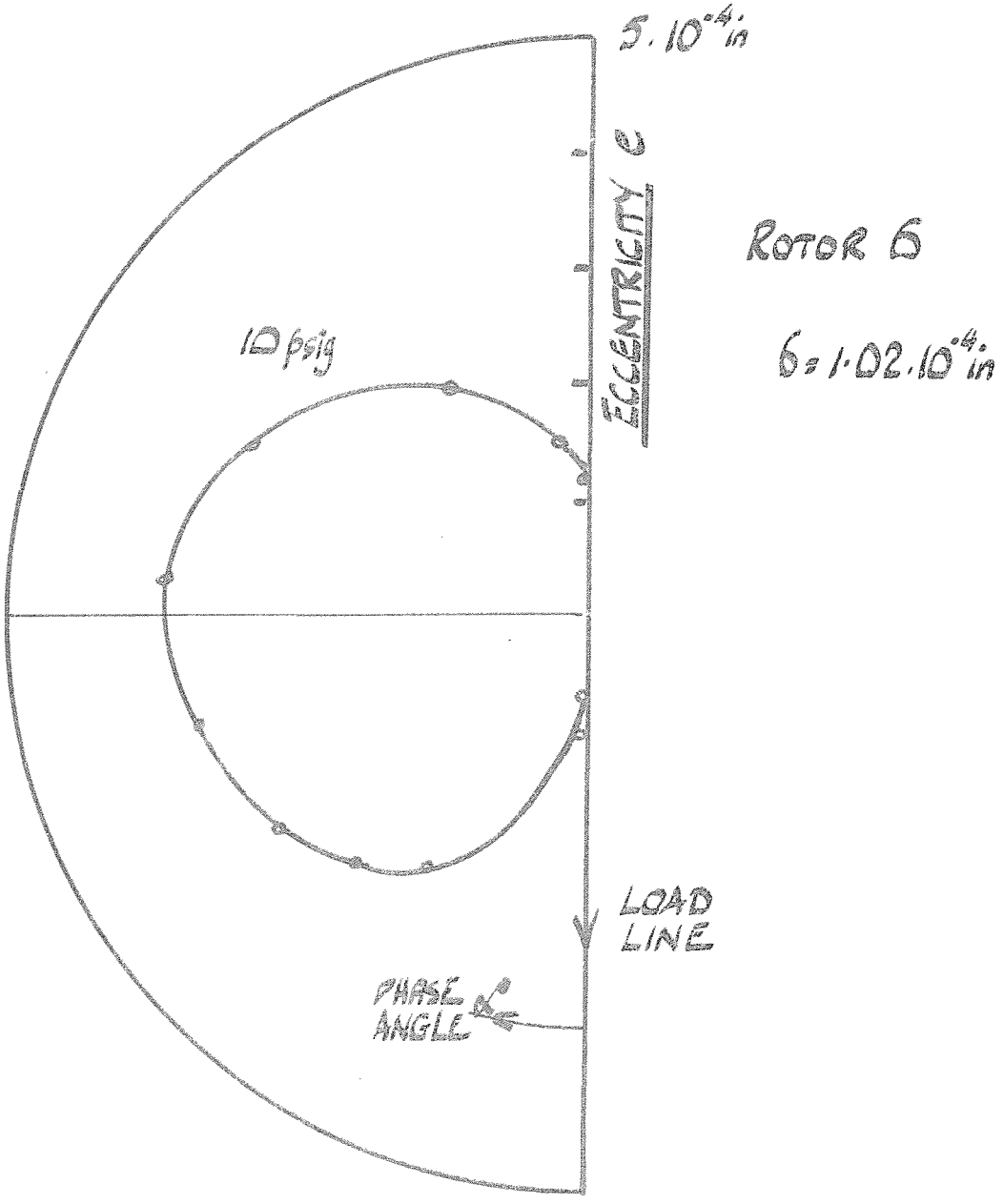

FIG 9.56.

EXPERIMENTAL PHASE ANGLE AND ECCENTRICITY vs SPEED

ROTOR 1 $\delta = 2.04 \cdot 10^{-4}$ in

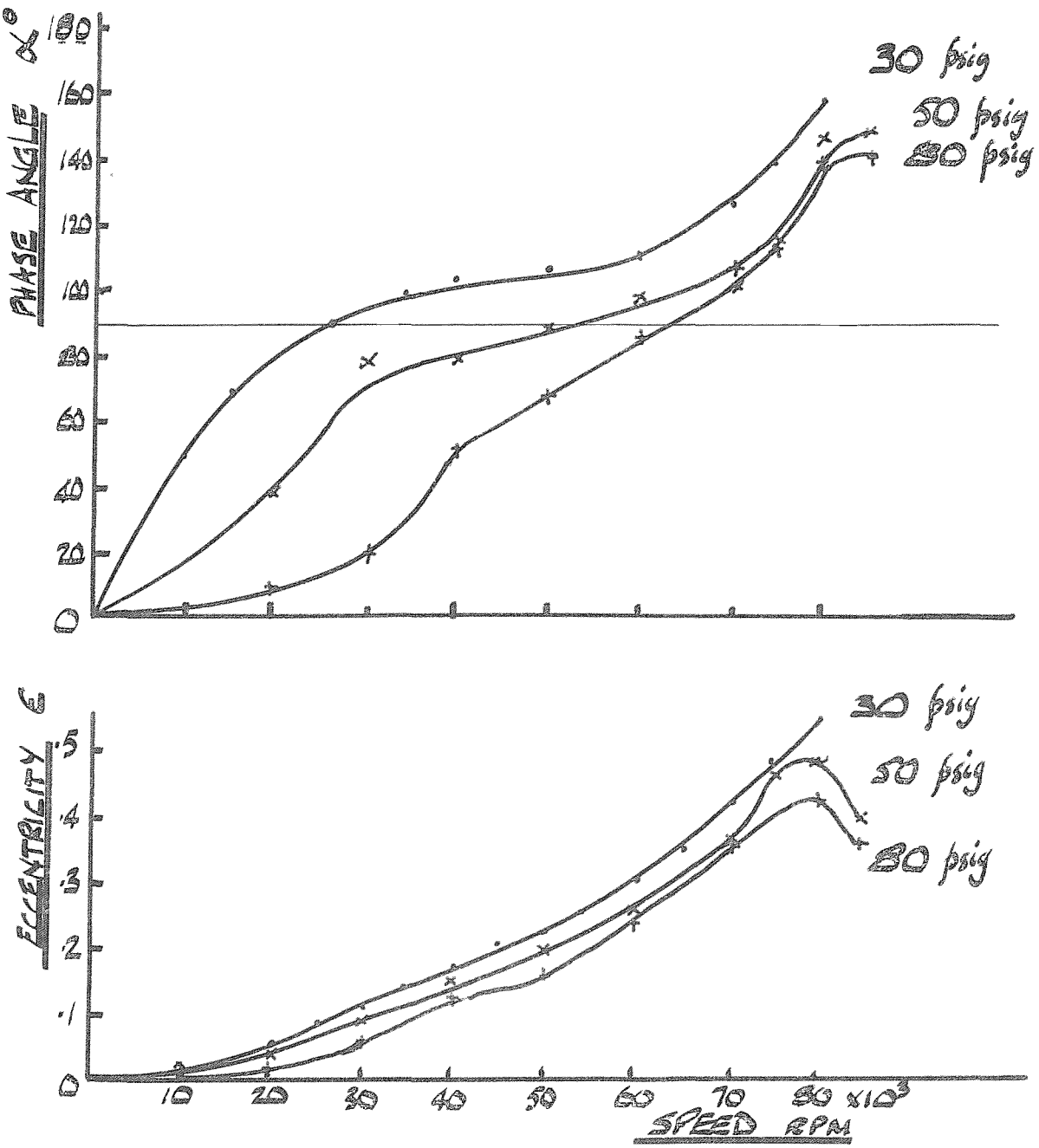

FIG 9.5.7.

PHASE ANGLE AND ECCENTRICITY VS SPEED

ROTOR 2. $\delta = 1.54.10^{-4}$ in

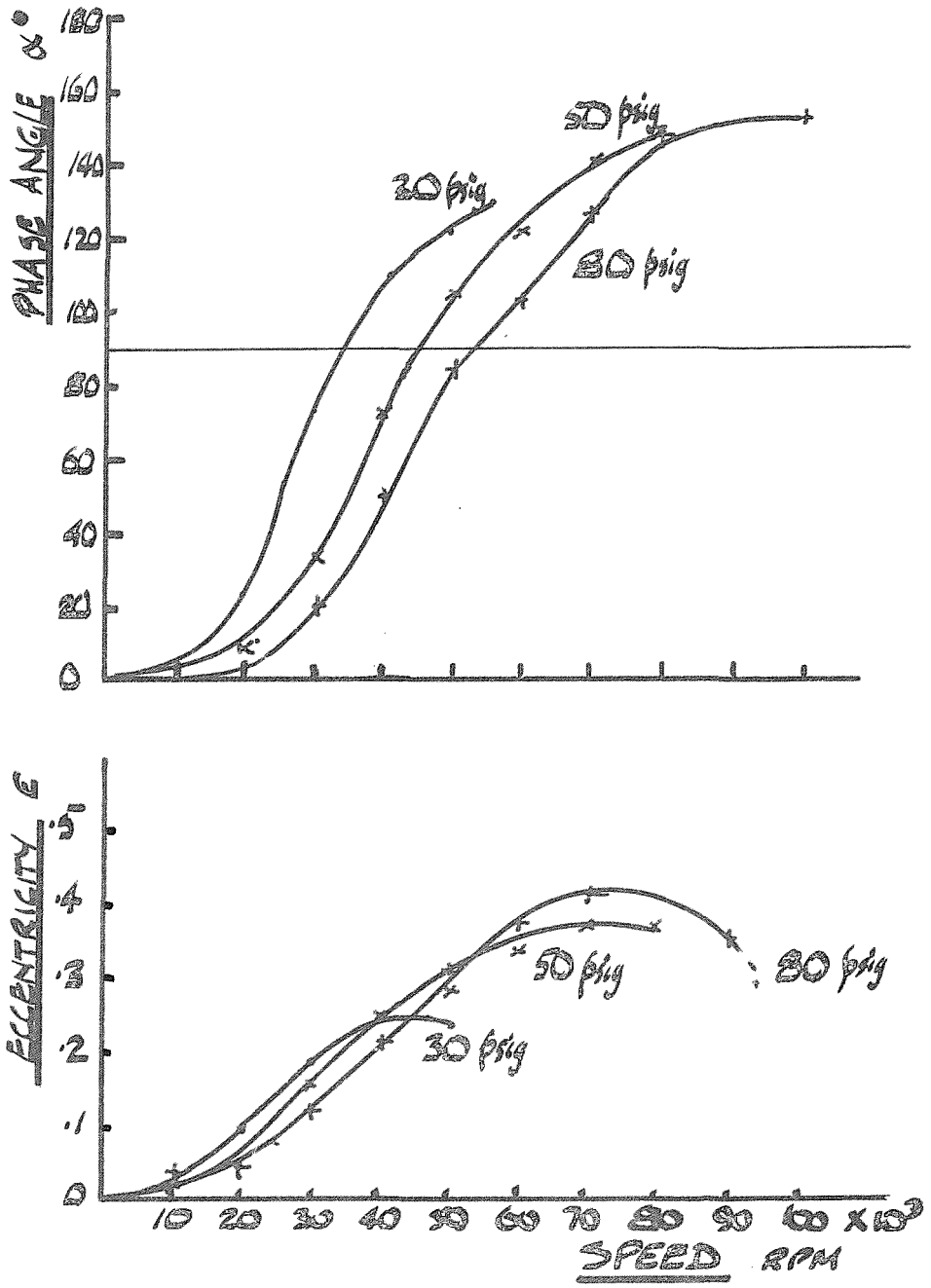

FIG 9.5.8.

PHASE ANGLE AND ECCENTRICITY VS SPEED

ROTOR 2 $\delta = 2.79.10^{-4}$ in

30 psig

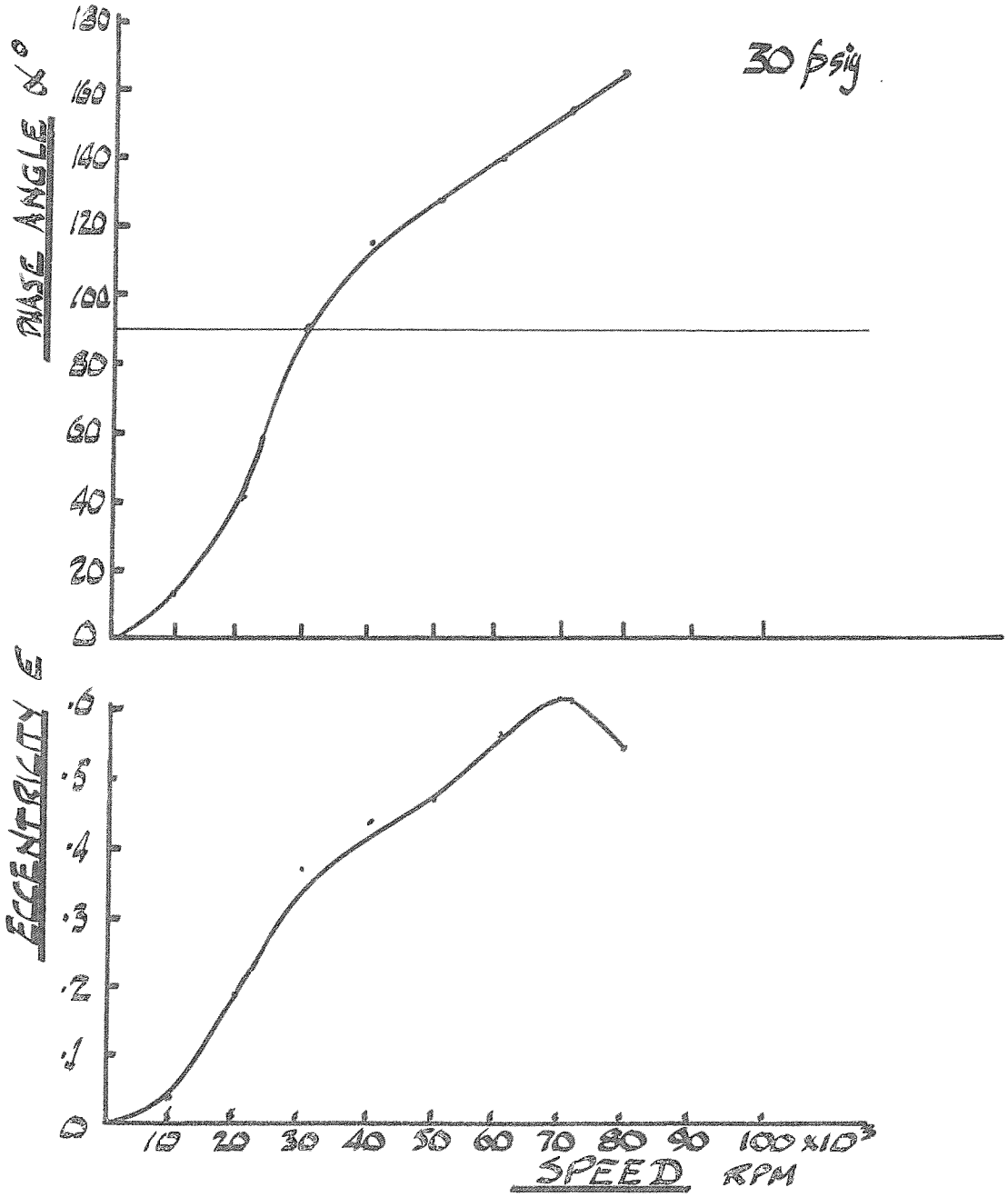

FIG 9.59.

PHASE ANGLE AND ECCENTRICITY VS SPEED

ROTOR 3 $b = 1.02.10^{-4}$ in

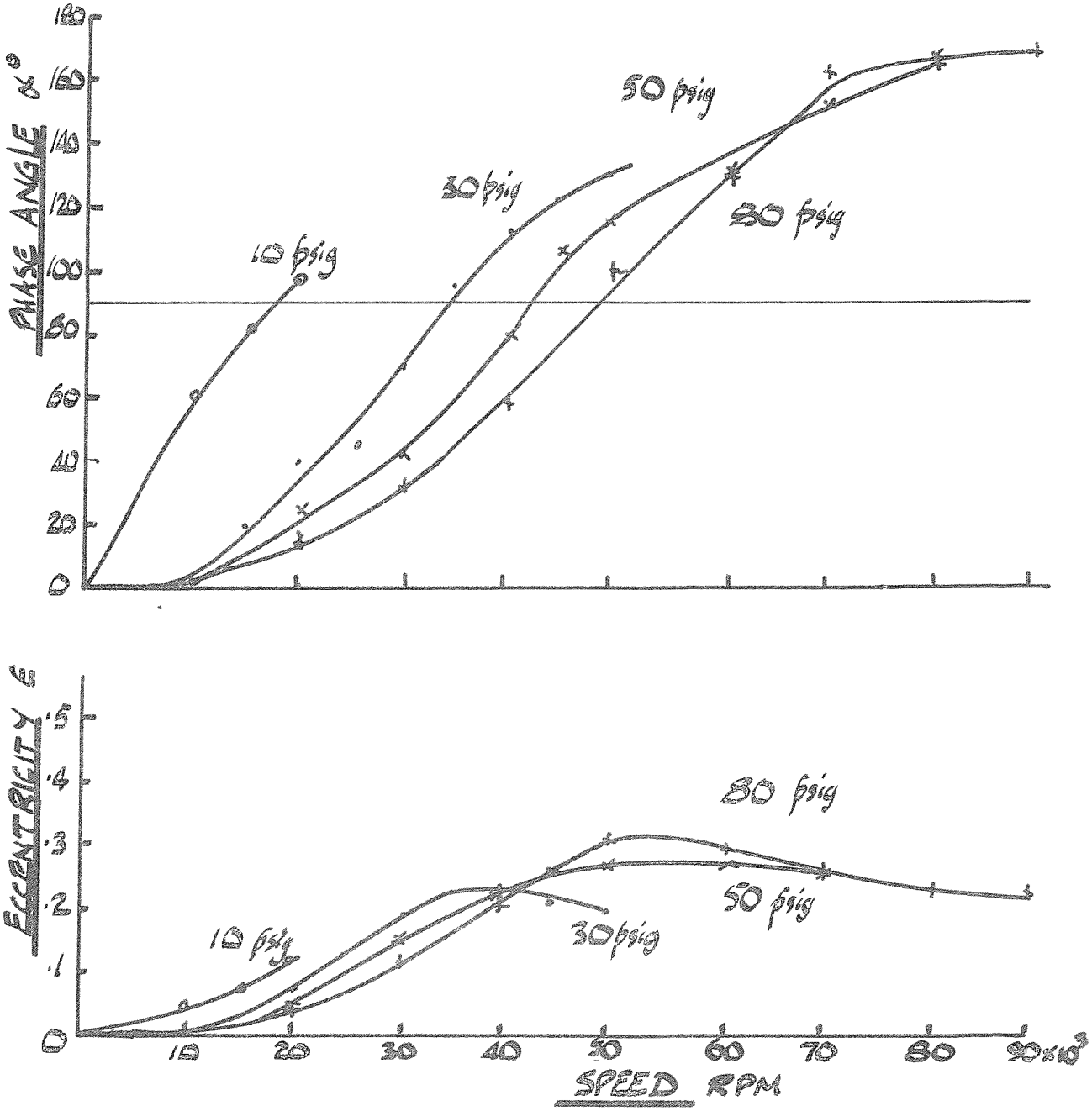

Fig 9.5.10.

PHASE ANGLE AND ECCENTRICITY VS SPEED

ROTOR 5 $\delta = 1.54 \cdot 10^{-4}$ in

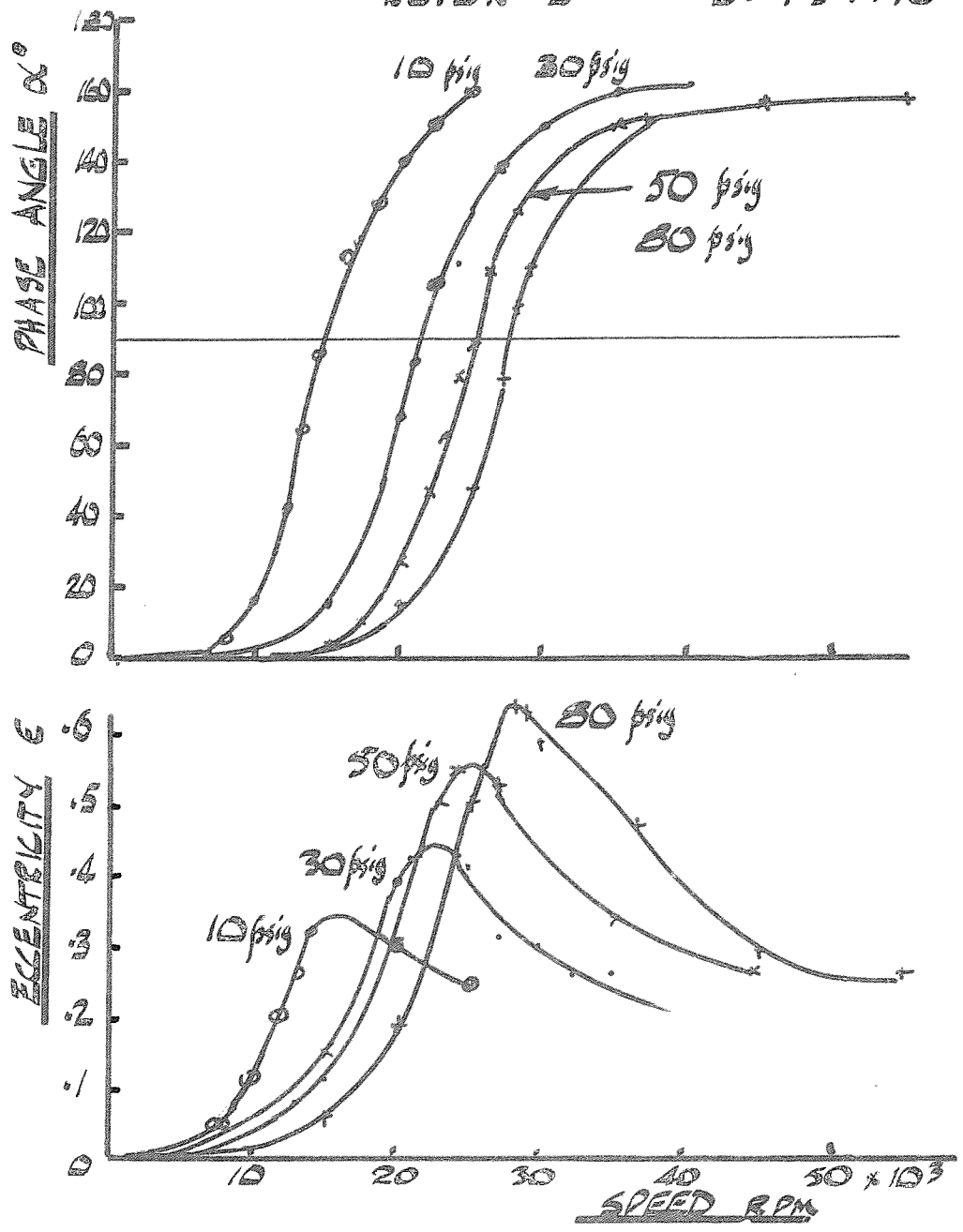

FIG 9.5.11.

PHASE ANGLE AND ECCENTRICITY VS SPEED

ROTOR 6. $b = 1.02.10^{-4}$ in

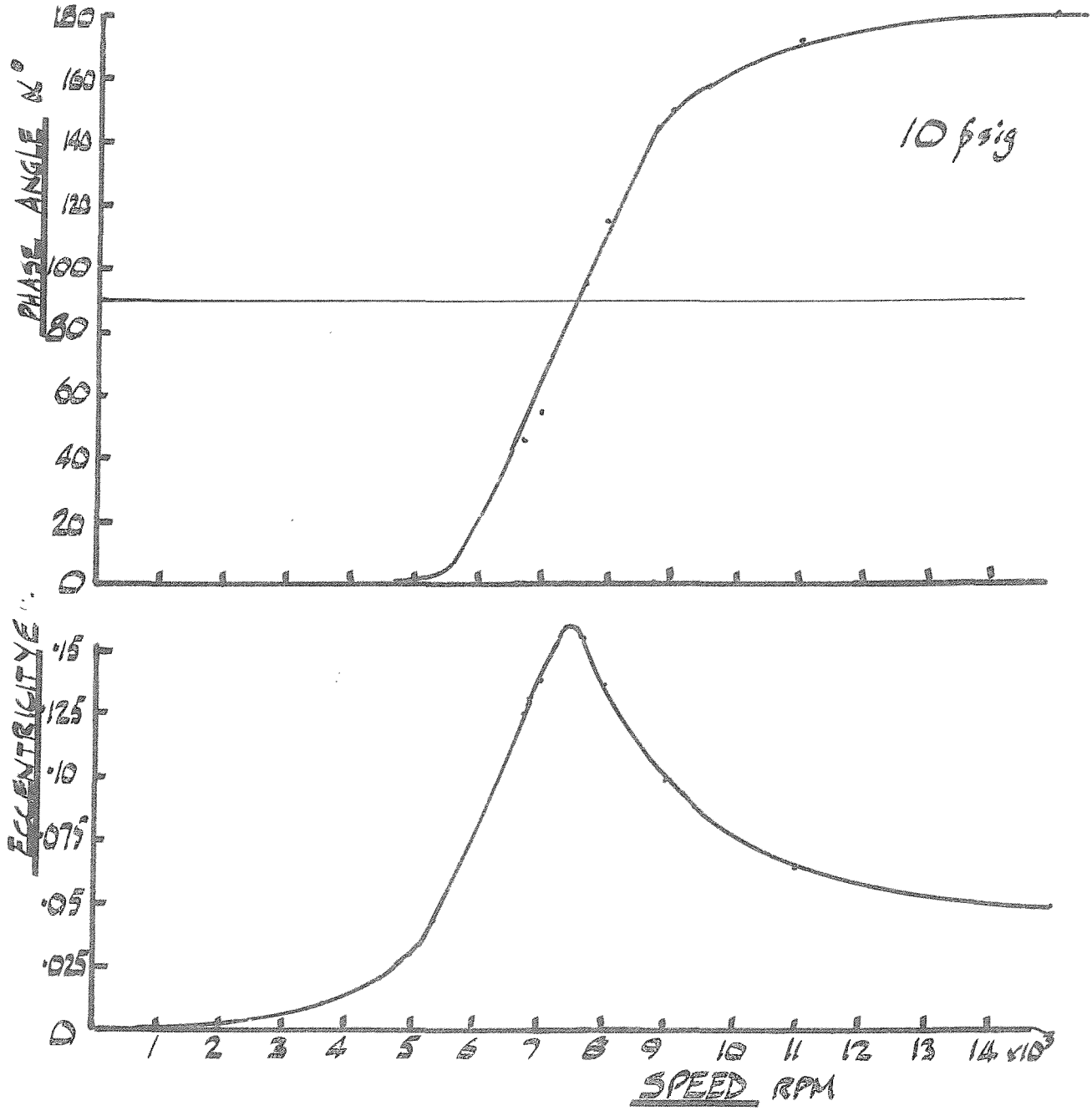

FIG 9.6.1.

AERODYNAMIC STIFFNESS AND DAMPING

(1ST ORDER PERTURBATION $L/D = 2$ $\epsilon \to 0$)

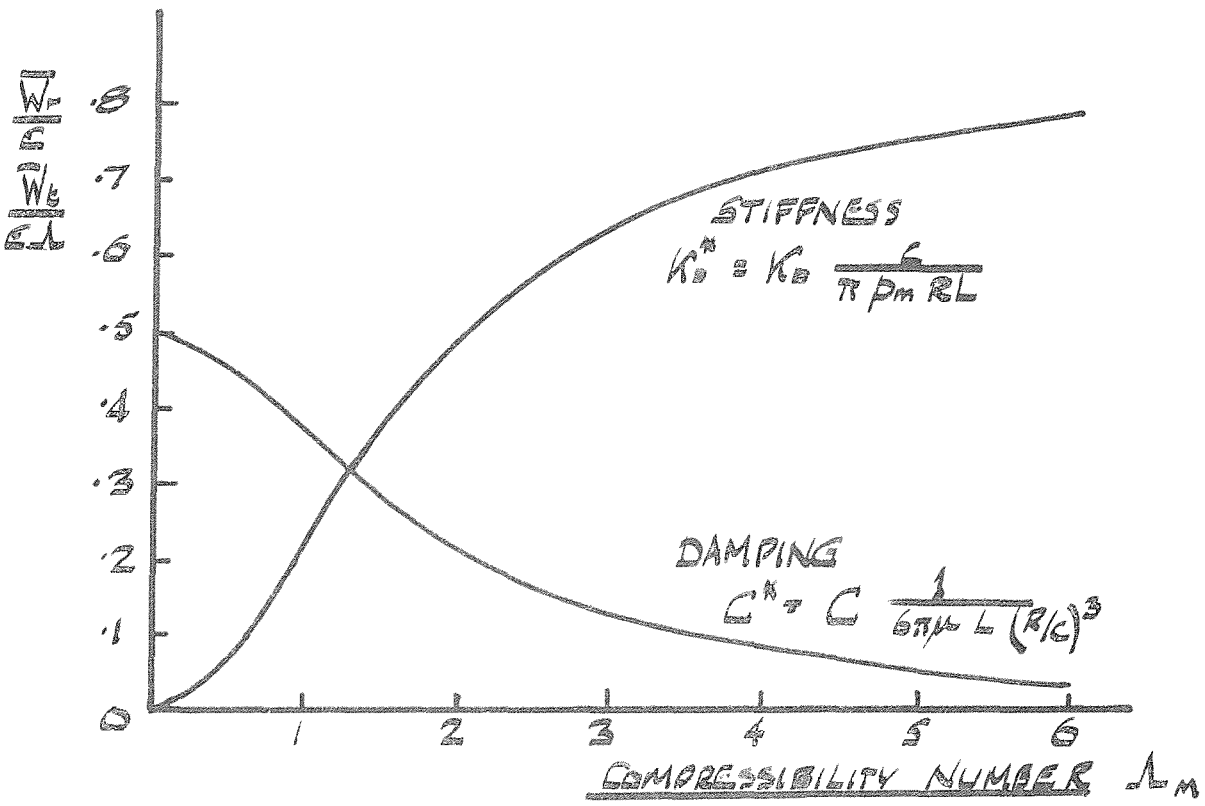

FIG 9.6.2.

NON-DIMENSIONAL DAMPING VS ROTATIONAL SPEED

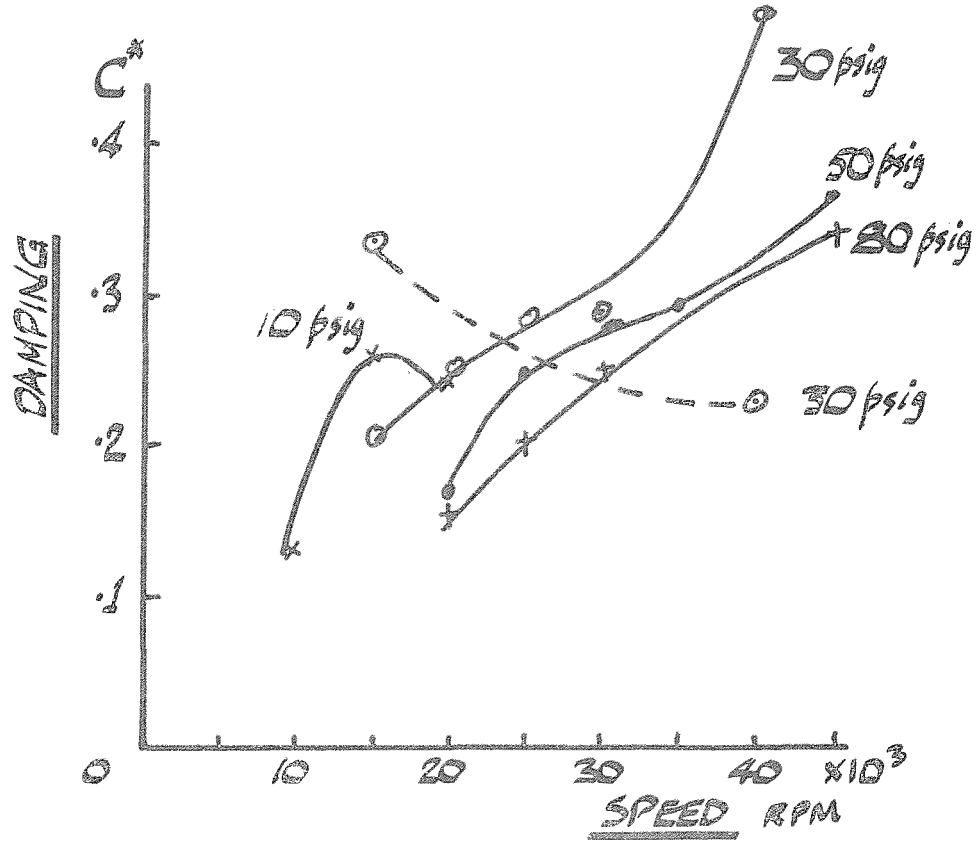

FIG 9.6.3.

TOTAL RADIAL STIFFNESS vs SPEED

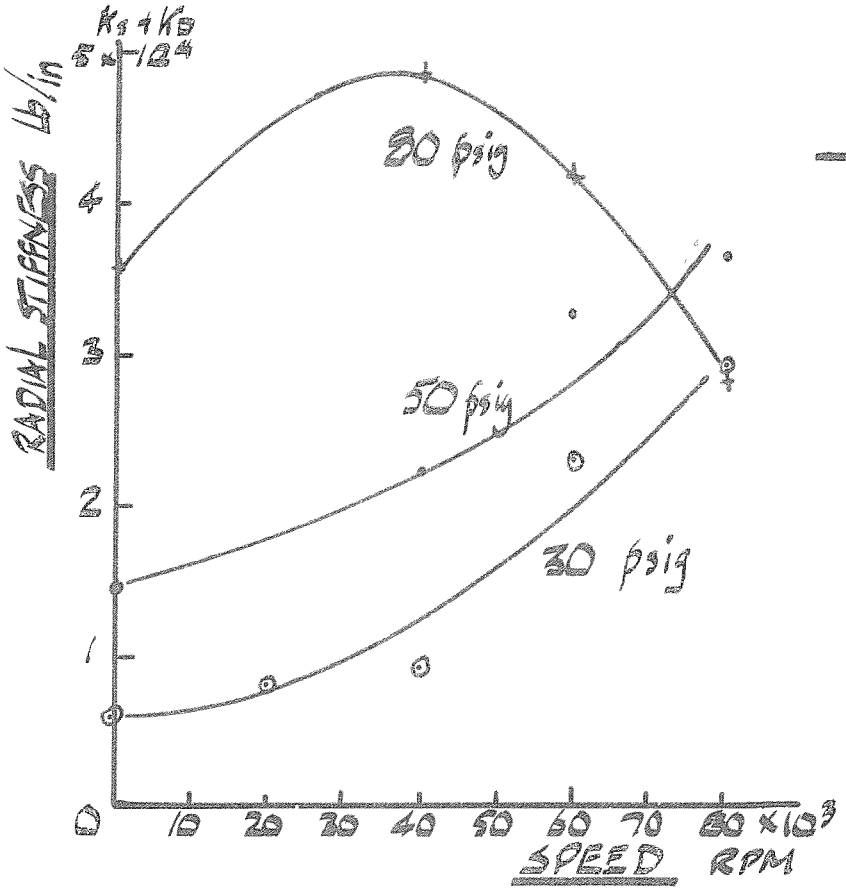

ROTOR 1

δ = 2.04 10⁻⁴ in

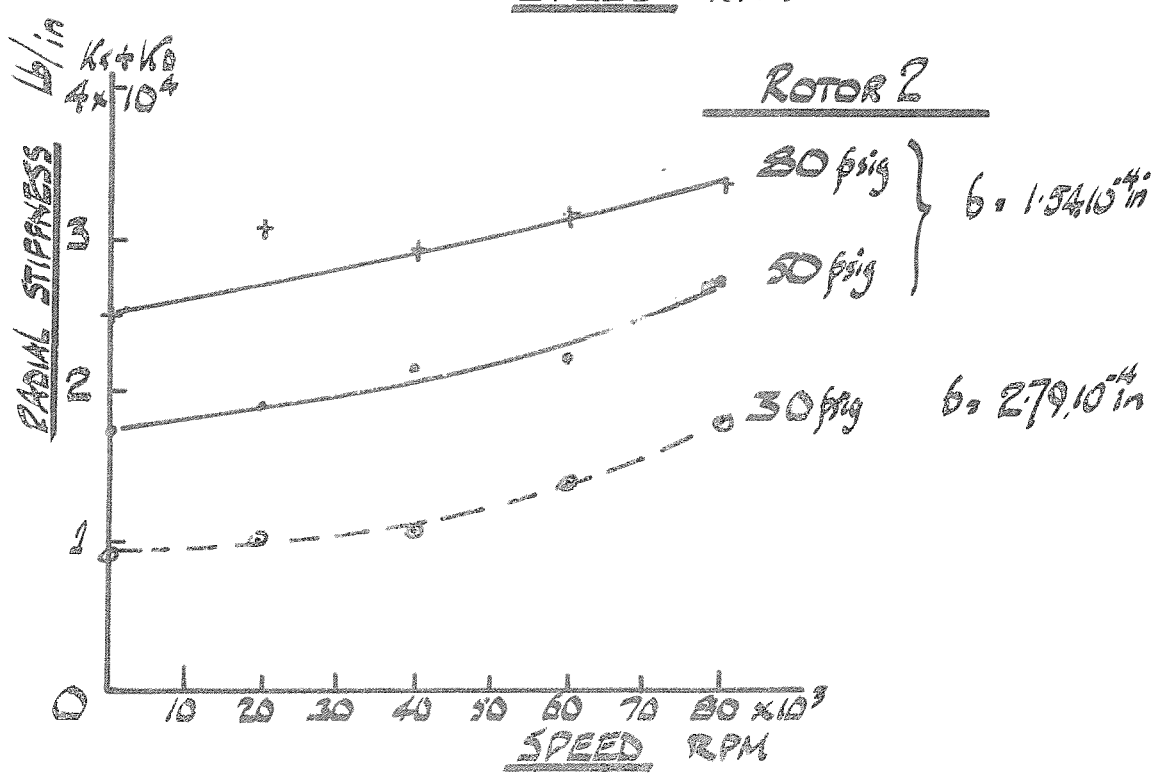

ROTOR 2

80 psig, 50 psig: δ = 1.54 10⁻⁴ in

30 psig: δ = 2.79 10⁻⁴ in

FIG 9.6.4.

TOTAL RADIAL STIFFNESS vs SPEED

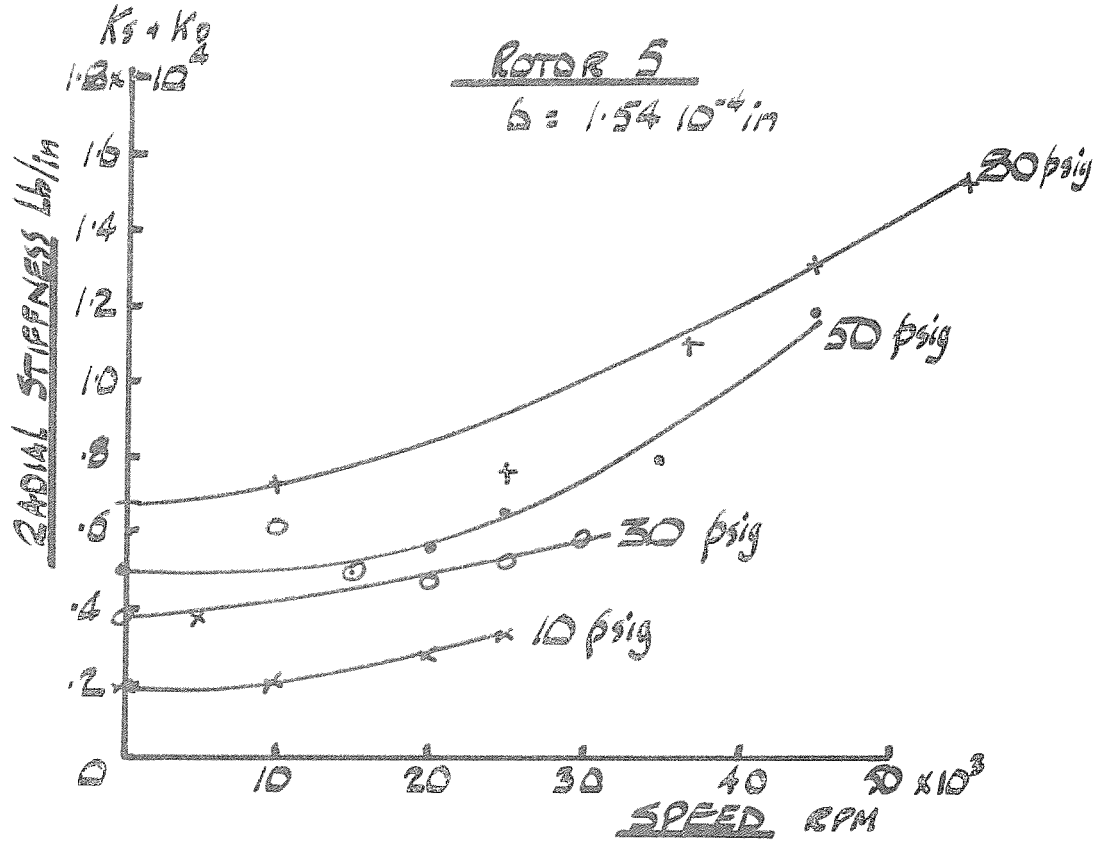

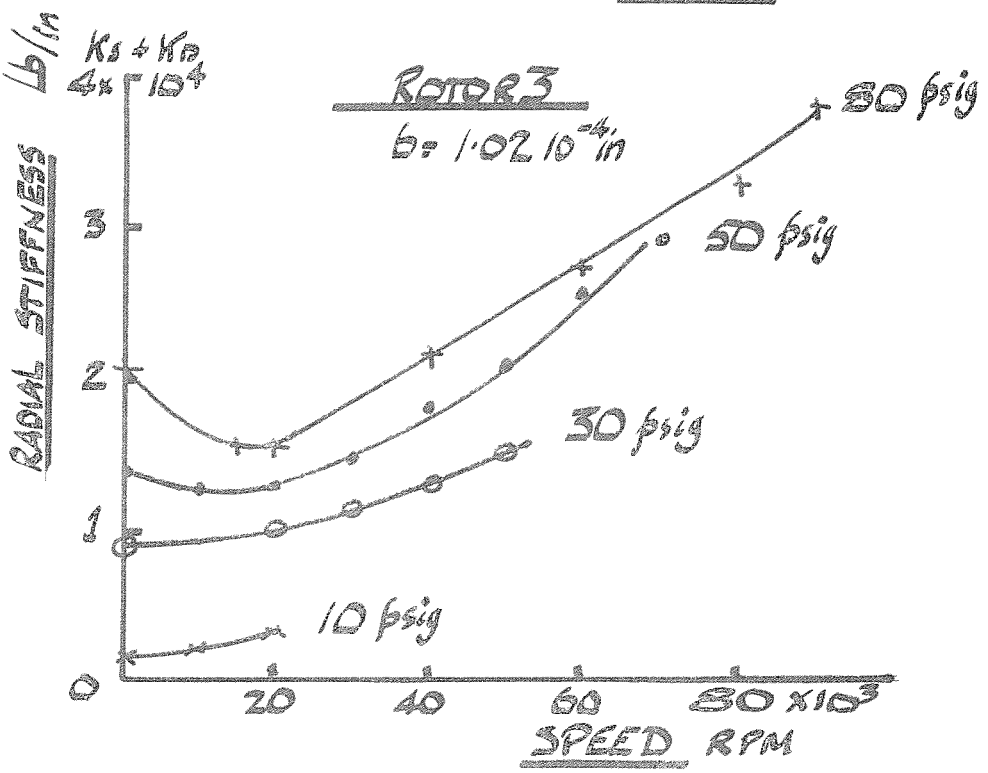

FIG 9.B.1

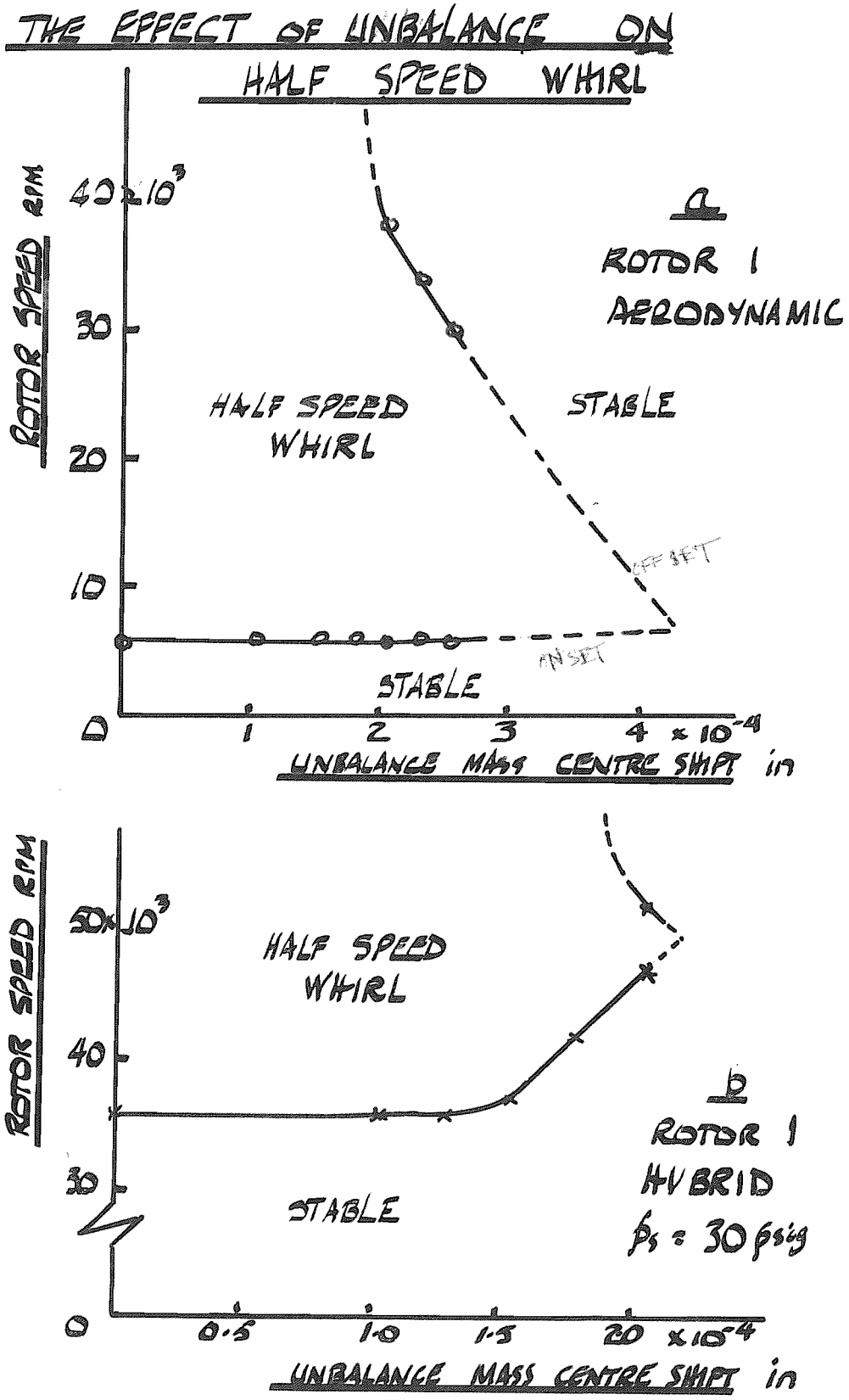
THE EFFECT OF UNBALANCE ON HALF SPEED WHIRL
ROTOR SPEED RPM
40 x 10³
30
20
10
0
HALF SPEED WHIRL
STABLE
OFF SET
ON SET
STABLE
1
2
3
4 x 10⁻⁴
UNBALANCE MASS CENTRE SHIFT in
a
ROTOR 1
AERODYNAMIC
ROTOR SPEED RPM
50 x 10³
40
30
0
HALF SPEED WHIRL
STABLE
0·5
1·0
1·5
2·0 x 10⁻⁴
UNBALANCE MASS CENTRE SHIFT in
b
ROTOR 1
HYBRID
p_s = 30 psig

Fig 9.B.2.

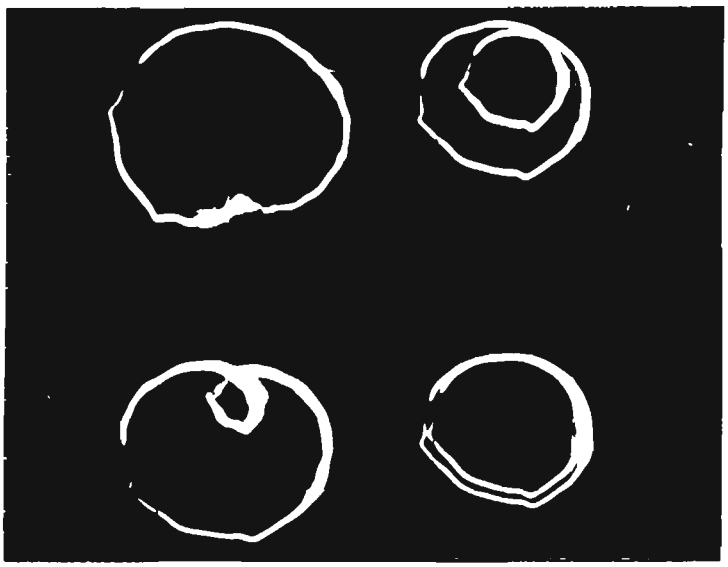

DEVELOPMENT OF HALF SPEED WHEEL

APPENDIX I.

The Principle of Operation of the Wayne-Kerr Distance and Vibration Meter B731A.

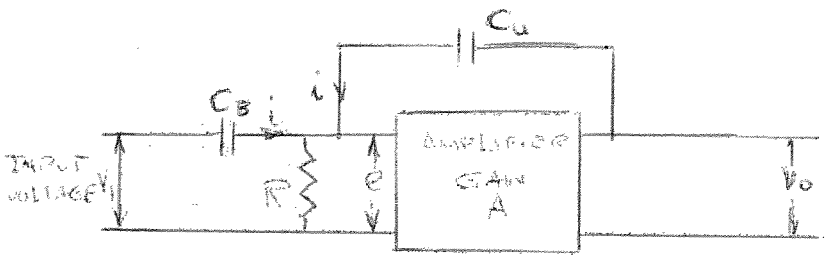

The input reference signal i_1 to a high gain amplifier is the current passed by a standard capacitor C_8 connected to the output circuit of a stable 50 Kc/s oscillator. A current i_2 dependent on the amplifier output voltage Vo is fed back to the input through the capacitance C_u between the shaft and the probe. The capacitance C_8 is chosen to be comparable to C_u and the gain of the amplifier is made very high. Under these conditions the amplifier output voltage is inversely proportional to the capacitance between the shaft and the probe, and thus this output voltage is directly proportional to the separation of the probe from the shaft.

$$Vo = Ae = A(i_1 - i_2)R \quad \{180^\circ \text{ phase difference between } i_1 \text{ and } i_2\}$$

But C_u is comparable with C_8 and the amplifier gain A is so high that e << Vo

$$\text{i.e.} \quad e \to 0$$

$$\therefore \quad i_2 - i_1 \to 0$$

$$\text{or} \quad i_2 = i_1 \quad \text{in the limit}$$

$$\therefore \quad Vo = i_2 X_u \text{ and } V_1 = i_1 X_8$$

$$Vo/v_1 = \left(\frac{i_2}{i_1}\right) \cdot \left(\frac{X_u}{X_8}\right)$$

$$Vo = \frac{V_1}{X_8} \cdot X_u = \frac{V_1}{X_8} \left(\frac{1}{\omega C_u}\right)$$

$$\text{i.e.} \quad Vo = K \left(\frac{1}{C_u}\right) \quad \text{where K is a constant } \frac{V_1}{\omega X_8}$$

but $C_u = \frac{a}{d}$

where a is c.s.a. of probe

d is separation of shaft and probe

$$\therefore \quad Vo = \frac{k}{a} \cdot d$$

$$\text{i.e.} \quad Vo \propto d$$

Thus the 50 kc/s output from the high gain amplifier has a mean amplitude dependent on the distance of the probe from the shaft, and a modulation amplitude dependent upon the peak-to-peak

vibtation of the shaft.

A meter, fed by a metering circuit which rectifies the modulation 50 kc/s output from the high gain amplifier indicates the mean distance between the shaft and the probe.

A vibration metering circuit demodulates the 50 kc/s output and feeds a meter through a peak to peak detector. The meter then gives the peak-to-peak vibration amplitude of the shaft.

An output from the meter is provided which is, however, the modulated 50 kc/s signal. To view the vibration wave form on an oscilloscope, the 50 kc/s carrier is filtered using the filter shown in the accompanying figure.

PERFORMANCE OF 50 Kc REJECTION FILTER FOR USE WITH WAYNE KERR VIBRATION METER

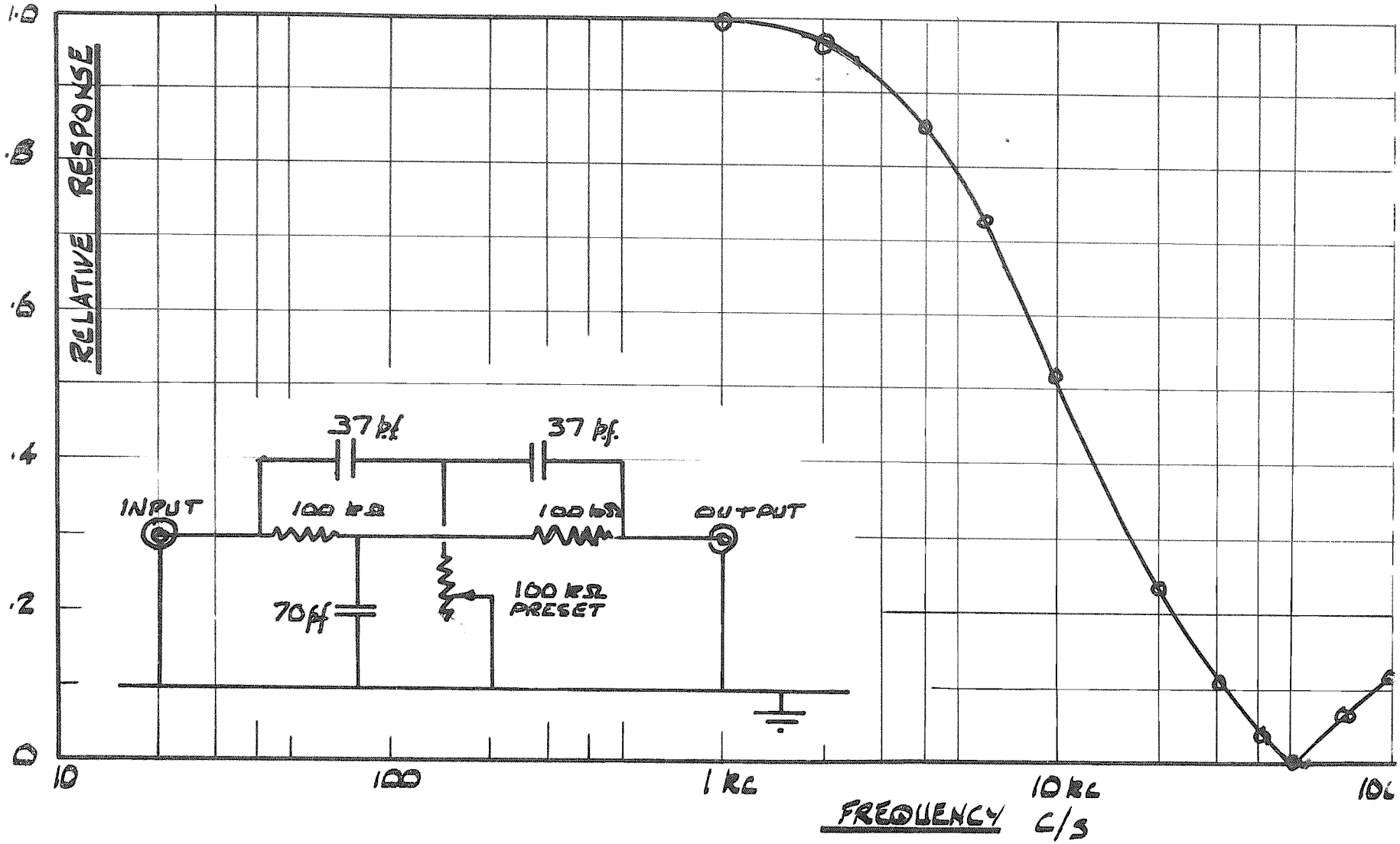

APPENDIX 2.

After the main body of this report had already been completed, it has been realized that the 50 kc/s rejection filters used with the Wayne-Kerr meters and detailed in Appendix 1, lead to a small phase lag between the measured and true phase angles at the higher frequencies. This only affects the results obtained for the synchronous unbalance loading and presented in Chapter 9.

It is not considered, however, that this materially alters the conclusions reached, since for the damping the main conclusions were based on results taken only at the 90° phase change between force and deflection where the frequencies were low and phase lag in the filter negligible. One curve presented, Fig. 9.6.2. will be changed, where instead of the damping coefficient increasing with speed as shown, it will turn over at high speeds and begin to reduce. The stiffness results will be little affected since the filter phase lag only becomes noticeable at high speeds where the system is normally approaching inversion. The derived stiffness is a sine function of phase angle and errors of $10\text{-}15^{\circ}$ have little effect in this region.